Development of Magnetic Resonance Based Spin Labeling Techniques for Functional Brain Imaging

Dissertation

der Mathematisch-Naturwissenschaftlichen Fakultät

der Eberhard Karls Universität Tübingen

zur Erlangung des Grades eines

Doktors der Naturwissenschaften

(Dr. rer. nat.)

vorgelegt von

Mustafa Çavuşoğlu

aus Kayseri

Tübingen

2012

Tag der mündlichen Qualifikation: 02.04.2012

Dekan: Prof. Dr. Wolfgang Rosenstiel

1. Berichterstatter: Prof. Dr.Dr. Fritz Schick

2. Berichterstatter: Prof. Dr.Kamil Uludağ

I hereby declare that the dissertation entitled:

"Development of spin labeling techniques for functional brain imaging"

submitted for the degree of 'Doctor of Philosophy' has been completed by me the undersigned and that I have not used any other than permitted reference sources or materials nor engaged in any plagiarism. All references and other sources used by me have been appropriately acknowledged in the work. All the figures reprinted in the context of the thesis were clearly cited and the peer-reviewed papers published as I am the co-author were placed in the thesis with the permission of the corresponding authors.

December 6, 2011   Mustafa Çavuşoğlu
Tübingen

Acknowledgements

Starting from the first day of being a member of Max Planck Institute, I realized the spectacular scientific environment with many excellent scientists and engineers and with such state-of-the-art equipment. I will always carry the pride of doing my PhD at such a fantastic team doing a 'real science' on the governing dynamics of the Magnetic Resonance Imaging. This work would have not been possible without the help and support of many individuals.

First and most importantly, I would like to thank my supervisor Prof. Kâmil Uludağ for his constant input, enthusiasm, trust and guidance. He supported me at every stage of my PhD study. I have had a particularly rewarding experience under his tutelage and consider myself lucky to have such a brilliant and encouraging mentor. My work benefited immensely from his scientific guidance and innovative ideas. His (ultra-) fast analytical skills and great memory made our discussions very efficient and helpful. His collaborative leadership styles have profoundly impacted how I myself lead and act as part of a team, and also how I approach toward ones work. Through his suggestions, I improved my presentation and writing skills a lot.

I am very fortunate to have the opportunity to work with Prof. Kâmil Uğurbil. Not only his tremendous scientific knowledge but also his great personality made every discussion with him inspiring and motivating for me. I am grateful to Prof. Uğurbil for his invaluable suggestions and support in my carrier planning. He is always an excellent model in my future research.

I would like to express my thanks and gratitude to Prof. Fritz Schick for being "Doktorvater" of me. He is one of the kindest and friendly people I have ever met and his supports and guidance in my PhD study are invaluable. I also would like to thank Prof. Bernd J. Pichler and Prof. Heinz Clement, the members of my advisory and review committee, for showing their keen interest to the subject matter, reading and commenting on the thesis.

I met Prof. Nikos Logothethis in 2007 when I arrived to Tübingen. It was a great pleasure for me to have the opportunity to discuss about the principal components of neuroscience with him. I also enjoyed a lot and will never forget our talks in Turkish. I would like to thank Prof. Klaus Scheffler for his guidance on my academic life and his precious ideas that are lighten of my future studies. It was a great honor for me to meet them.

I was very lucky to have great collaborators each individually excellent and outstanding scientist. Particularly, I thank to Dr. Rolf Pohmann for introducing me many aspects of pulse programming and MR engineering. His valuable comments on my projects supported me a lot and showed me new directions. Dr. Andreas Bartels tremendously contributed in my perfusion fMRI studies with his great experience and amazing sense of humor. I cannot overemphasize his support and friendship. Dr. Ralf Veit and Dr. Balint

Varkuti from Institute of Medical Psychology and Behavioral Neurobiology, Tübingen have great contribution in application of arterial spin labeling to address several challenging questions in functional brain imaging.

Dr. Baris Yesilyurt and Dr. Hannes Wiesner have special importance for me. I am so lucky to have such great team members and friends. I could never forget our discussion on almost every aspect of MRI in our coffee breaks and late night pizza sessions. I would like thank both of them for their invaluable supports and friendship.

I was also so lucky to work with Mr. Mihai Vintiloiu whom I believe worlds one of the best network administrators. I do not remember even a single time that he was not able to solve any technical problem I faced. I also would like to thank our great department secretary Mrs. Tina Schröder for her endless support in any case I went to her office including my bad mood recoveries.

The High-Field MR group at Max Planck Institute made coming to work a pleasure. I would like to thank current and former colleagues Marius, David, Shajan, Jens, Aneta, Mirko, Denis, Frank, Axel, Juliane, Hildegard, Saskia, Jonas, Sabrina, Joshi, Frank, Markus, Sung-Tak, Deepti, Ritu, Bernd, Gunter, Jörn and Nataila for their friendship and helpfulness. I feel privileged to have gotten to know you. Thank you for the incredible support and friendship over the years.

Finally, I would like to thank my parents for their unconditional love and support. Without them none of this would have been possible.

Max Planck Institute   *Mustafa Çavuşoğlu*

December, 2011, Tübingen

Abstract

Since its invention in 1992, arterial spin labeling (ASL) has become a widely used tool for noninvasively investigating brain function. Because ASL provides a direct and repeatable measurement of CBF, these methods are highly applicable in studies of cognitive neuroscience, in the evaluation of pharmacological treatments and in the diagnosis of CBF related diseases. The focus of this dissertation is on the development and implementation of arterial spin labeling techniques ultimately with applications in neuroscience. On the technical side, the systematic errors in ASL experiments such as transit delay time artifacts are investigated for various ASL methods including pulsed, pseudo-continuous and dual coil continuous sequences. Magnetization dispersion effects on quantitative CBF estimation are explored and the regional bias that occurs as a result of varying transit delay times is characterized. Different pulsed ASL encoding schemes are compared from the aspects of their relative signal-to noise ratio (SNR) and absolute CBF estimates. A new method is proposed to calculate the equilibrium magnetization of arterial blood which is required for absolute CBF quantification and compared with those other methods. Taking the advantage of better spatial localization and sensitivity profile of ASL compared to blood oxygenated level dependent (BOLD) signal, retinotopic mapping of human brain with perfusion contrast is performed and variations of hemodynamic delay times across the visual areas in BOLD and perfusion activations are investigated. Further on the application side, a number of neuroscience projects performed in collaboration are presented: i) The covariation of local anatomical connectivity, gray matter volume and perfusion is quantified by conducting an integrative MRI study utilizing a combination of diffusion tensor imaging, arterial spin labeling and anatomical imaging ii) Differential effects of intranasal insulin and caffeine on cerebral blood flow is investigated iii) the spatial sensitivities of widely used fMRI sequences such as gradient echo-BOLD, spin echo-BOLD and arterial spin labeling are compared with respect to optimal transcranial magnetic stimulation (TMS) sites for evoking highest motor responses. Overall, the results presented in this thesis are addressing the questions related to the technical and methodological problems in arterial spin labeling and its applications in functional brain imaging.

Contents

Introduction

Cerebral blood flow (CBF) is an important physiological quantity that is crucial for proper maintenance of normal metabolic rates in animals and humans as the supply of oxygen and nutrients and the removal of waste products. CBF is also a well-established correlate of brain function and a significant parameter reveal the complex neurobiology of healthy and disordered brain functions [1]. Recent developments in magnetic resonance imaging (MRI) have made possible the non-invasive measurement of regional CBF. Arterial spin labeling (ASL) is a promising non-invasive MRI-based method to directly measure CBF by utilizing arterial blood water as an endogenous diffusible tracer [2, 3]. ASL has been demonstrated to provide highly reproducible and reliable quantitative CBF measurements enabling it for clinical applications and the repeatability and high temporal resolution features makes it suitable for functional MRI (fMRI) studies [4]. The development of ASL techniques is an active research area and although they are not yet widely available on standard MR scanners, applications of ASL both in clinics and neuroscience are steadily growing [1].

The focus of this dissertation is on the development and implementation of arterial spin labeling techniques ultimately with applications for functional brain imaging. The outline of the thesis is as follows:

Chapter 1 presents a brief introduction to perfusion imaging and basic physical principles of arterial spin labeling techniques. I described the pulsed (PASL) and continuous ASL (CASL) sequences and the absolute perfusion quantification methods associated with these methods. In addition, to motivate the subsequent chapters, I discussed the potential limitations of the PASL and CASL techniques and discusses relatively new approaches such as pseudo-continuous ASL (pCASL) and velocity selective ASL (VS-ASL).

Chapter 2 is reserved for describing the magnetization dispersion effects on quantitative perfusion imaging using PASL, CASL and pCASL. Arterial transit delay time maps were created to and a general framework is presented to characterize the magnitude of the magnetization dispersion effects on regional CBF estimate for varying distances between the tagging and imaging regions. This work is published as reference [5].

Chapter 3 compares the PASL encoding schemes from the aspects of relative signal-to noise ratio (SNR) all in the control, tag and average difference images and their ultimate CBF estimates. We proposed a new method to calculate the equilibrium magnetization of arterial blood which is required for absolute CBF quantification and we compared it with those other methods. This work is published as reference [6].

Chapter 4 serves as a brief review of the previous studies on perfusion based functional magnetic resonance imaging to form a basis for further chapters. The strong and the

weak features of arterial spin labeling (ASL) and blood oxygenation level dependent (BOLD) functional magnetic resonance imaging (fMRI) are compared and discussed. The principles of ASL signal processing are explained from the aspects of signal and noise characteristics.

Chapter 5 presents the retinotopic mapping of human brain with perfusion contrast using arterial spin labeling and investigation of variations of hemodynamic delay times across the visual areas in BOLD and perfusion activations. This is the first study showing the delineation of visual areas from CBF weighted images and the work is published as reference [7].

Chapter 6 covers there examples of applications of ASL in neuroscience research as I performed in collaboration. I found more convenient to compose this chapter from the published papers where I am the co-author. The first study, "Quantifying the Link between Anatomical Connectivity, Gray Matter Volume and Regional Cerebral Blood Flow: An Integrative MRI Study" is published as reference [8], the second study "Differential effects of intranasal insulin and caffeine on cerebral blood flow (CBF)" is published as reference [9], and the third study, "Functional Localization in the Human Brain: Gradient-Echo, Spin-Echo, and Arterial Spin-Labeling fMRI Compared with Neuronavigated TMS" is published as reference [10].

References

1. Buxton, R.B., *Introduction to Functional Magnetic Resonance Imaging: Principles and Techniques*2002, Cambridge: Cambridge University Press.
2. Detre, J.A., et al., *Perfusion imaging.* Magn. Reson. Med., 1992. **23**: p. 37-45.
3. Williams, D.S., et al., *Magnetic resonance imaging of perfusion using spin-inversion of arterial water.* Proc. Natl. Acad. Sci. USA, 1992. **89**: p. 212-216.
4. Liu, T.T. and G.G. Brown, *Measurement of cerebral perfusion with arterial spin labeling: Part 1. Methods.* Journal of the International Neuropsychological Society, 2007. **13**(3): p. 517-525.
5. Cavusoglu, M., Pohmann, R., Burger, C., Uludag, K., *Reginoal effects of magnetization dispersion on quantitative perfusion imaging for pulsed and continuous arterial spin labeling.* Magnetic Resonance in Medicine, 2011. **(submitted)**.
6. Cavusoglu, M., et al., *Comparison of pulsed arterial spin labeling encoding schemes and absolute perfusion quantification.* Magn Reson Imaging, 2009. **27**(8): p. 1039-45.
7. Cavusoglu, M., Bartels, A., Yesilyurt, B., Uludag, K., *Retinotopic maps and hemodynamic delays in human visual cortex measured using arterial spin labeling.* Neuroimage, 2011 (doi: 10.1016/j.neuroimage.2011.10.056).
8. Varkuti, B., et al., *Quantifying the link between anatomical connectivity, gray matter volume and regional cerebral blood flow: an integrative MRI study.* Plos One, 2011. **6**(4): p. e14801.
9. Grichisch, Y., et al., *Differential effects of intranasal insulin and caffeine on cerebral blood flow.* Hum Brain Mapp, 2011.
10. Diekhoff, S., et al., *Functional localization in the human brain: Gradient-Echo, Spin-Echo, and arterial spin-labeling fMRI compared with neuronavigated TMS.* Hum Brain Mapp, 2011. **32**(3): p. 341-57.

Chapter 1

Principles of Arterial Spin Labeling

Overview

Basic physical principles of the arterial spin labeling MRI are described. The early methods for perfusion imaging based on PET and CT scans are summarized. The contrast mechanism of the perfusion measurement, potential limitations and drawbacks and quantification of cerebral blood flow are discussed for continuous arterial spin labeling. Underlying motivation and physical principles of dual-coil arterial spin labeling are explained. Different versions of pulsed arterial spin labeling techniques are described. Problems arising due to the lack of well-defined bolus duration in pulsed arterial spin labeling are discussed and the methods developed to overcome those problems are demonstrated. Basic principles of pseudo-continuous arterial spin labeling and velocity selective arterial spin labeling are described.

1.1 Perfusion Imaging

Perfusion is the physiological process of nutritive delivery of arterial blood to a capillary bed in the biological tissue by means of blood flow. Adequate blood flow is survival for the tissues as the supply of oxygen and nutrients and the removal of waste products. Abnormalities of perfusion account for most of the leading causes of medical disorders and mortality. Thus, measurement of perfusion yields great information about the tissue viability, metabolism and function. Several methods have been developed for *in vivo* perfusion measurements typically based on the wash-in and wash-out kinetics of exogenously administered tracers. These notably include radioactive tracers such as [^{15}O] water and ^{18}F detected by positron emission tomography (PET) [1] and ^{133}Xe detected by computerized tomography (CT) [2]. Recently, a number of NMR detectable tracers have been used for measuring the brain perfusion such as ^{2}H, ^{19}F and gadolinium DPTA [3, 4]. The common approach in calculating the perfusion rate is the application of the principles of tracer kinetics to a serial measurement of tissue tracer levels and creating the time/activity curves where activity refers to the concentration of the tracer. To minimize the exposed radiation and to reduce the radioactive inference between the

consecutive scans, repeated CBF measurements using radioactive tracers must include delays up to the order of an hour [5]. Such delays not only mitigate the effectiveness these methods as measures of short term CBF dynamics but also limits the usefulness of them in clinical routines and in scientific experiments. In recent years, the developments in magnetic resonance imaging (MRI) enabled the non-invasive measurement of the local tissue perfusion based on arterial spin labeling (ASL) [6]. Relative to the other imaging modalities, perfusion measurements with ASL has the advantages of not exposing ionizing radiation, providing quantitative measures of local tissue blood flow, blood volume and mean transit time with better spatial and temporal resolution than any other technique, including nuclear medicine methods [7]. ASL techniques have already become a standard tool in exploring the underlying physiological mechanisms during brain activation, in studies of disease progression, in the evaluation of pharmacological treatments and in several neuroscience and cognitive experiments [8].

1.2 Physical principles of arterial spin labeling

ASL uses the magnetically labeled proton spins of arterial water as an endogenous diffusible tracer [6]. 'Labeling' refers to an alternation in the magnetic state of the spins in the blood by either saturation or inversion. Before acquiring the image of the slice of interest, a 180° radiofrequency (RF) inversion pulse is applied to flip the magnetization of the water in arterial blood. The labeled spins flow in to each tissue element in proportion to the local cerebral blood flow (CBF). The image of the slice is acquired after a sufficient delay TI to allow the tagged blood to reach the slice and exchange with the tissue water altering the longitudinal magnetization of the local tissue (tag image). The experiment is then repeated without any labeling and the image of the slice is acquired again in such a way that the static tissue spins produces the same signal as in the tag image (control image). The two images are subtracted (control-tag) to produce the ASL difference image where the signal from static tissue spins subtracts out, leaving only the signal from arterial blood delivered to each tissue element during the time interval TI. Figure 1.1 illustrates the concept of ASL compared to PET methods.

From more physical point of view, in the control image the magnetization of arterial blood is fully relaxed and has an intrinsic magnetization of M_{0B}. In the tag image, the arterial blood carries a magnetization $-M_{0B}$ due to the inversion pulse in the ideal case
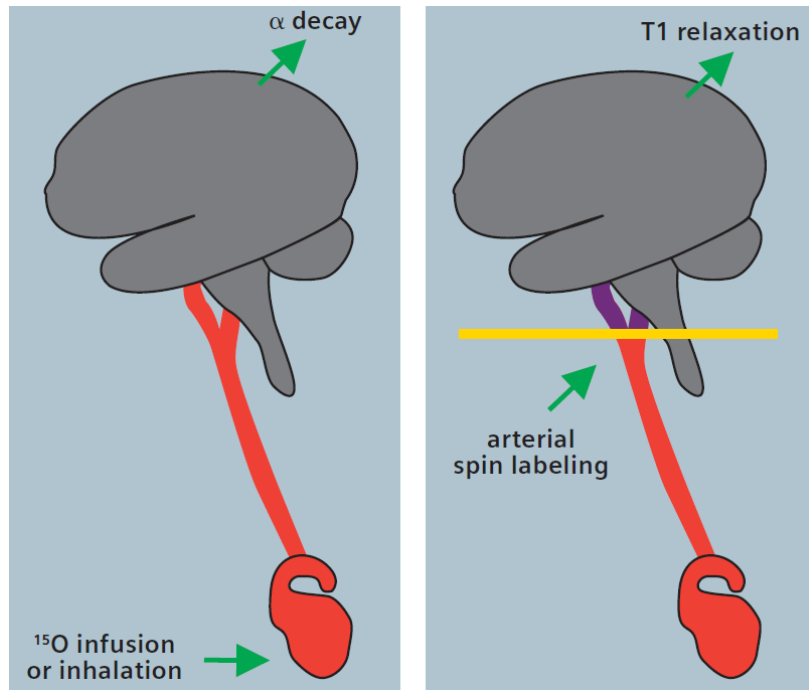
Figure 1.1 *Concept of Arterial Spin Labeling (ASL), comparing 15O-PET (a) and ASL (b) approaches. In ASL, endogenous arterial blood water is magnetically labeled instead of exogenously administered tracer, and the magnetic label decays with T1 instead of radioactive decay (α). (figure from Detre, J.A, Magnetom Flash, 2008).*

(ignoring the relaxation and other factors). The amount of delivered blood to the tissue during the interval TI is equal to $f.TI$ where f denotes the local CBF [9]. In this ideal case, the magnetization difference between the control and the tag image could be expressed as $\Delta M = 2.M_{0B}.f.TI$. The standard unit for CBF measurement is (milliliters of blood)/(100 grams of tissue)/minute and a typical value in human gray matter is about 60 mL/100 g/min. Assuming the average brain tissue density as 1 g/mL, the average CBF approximates to 0.01 s^{-1} implying that in 1 s period, around 1% of total tissue volume consists of freshly blood [8].

Although the fundamental principle behind ASL technique is simple, the implementation requires great care to optimize several parameters and experimental design and a number of confounding factors must be taken into account for an accurate CBF measurement. Since the original innovation of the basic ASL technique by Williams et al.(1992) [10], numerous ASL sequences have been developed mainly differ in how tagging is done, how the control image is acquired and how the potential systematic errors are handled. Generally speaking, the ASL sequences are mainly classified as pulsed ASL (PASL) [11-13] where short (millisecond) RF pulses are used for inversion

and continuous ASL (CASL) [6, 10] where long (seconds) RF pulses are used. Recently more sophisticated ASL sequences were developed including pseudo-continuous ASL (pCASL) [14-16] and velocity selective ASL (VS-ASL) [17] to handle a number of confounding such as magnetization transfer effects and transit delays more efficiently. We highlight the principles and the limitations of each of these ASL methods separately in the following parts of the thesis.

1.3 Continuous arterial spin labeling (CASL)

In continuous ASL, the magnetization of the arterial blood is 'continuously' inverted using a long (1-3s) RF pulse in conjunction with a constant gradient field to irradiate a narrow plane of spins with RF energy through a process called flow-driven adiabatic inversion [6, 10]. The essential idea of adiabatic inversion is that the orientation of the effective magnetic field, B_{eff} has to change at a sufficiently slow rate so that the angle between B_{eff} and net magnetization remains constant. In contrast to the general application of adiabatic inversion pulses where the RF is varied during the pulse to ensure the effective field to reach resonance, the motion of the blood itself produces a sweep of the effective field while the RF is constant in flow driven adiabatic inversion by applying a constant field gradient in the flow direction while the RF pulse is on. Then, the flow of the blood along the gradient axis changes the local resonant frequency causing the B_{eff} to sweep through resonance and invert the magnetization of blood [7]. Spins are inverted when the following condition is satisfied:

$$\frac{1}{T_1}, \frac{1}{T_2} \ll \frac{G_1.v}{B_1} \ll \gamma.B_1 \qquad [1.1]$$

where G_1 is the gradient field, B_1 is the RF field, v is the velocity of the blood, γ is the gyromagnetic ratio and T_1 and T_2 are the longitudinal and transverse relaxation times respectively [18]. Failure to satisfy the left inequality in the case of low velocities causes the T_2 relaxation to occur during the inversion while failure on the right inequality which occurs at high velocities results with a rotation of less than 180°.

It could be considered that the combination of the RF and the gradient field defines an inversion plane positioned in the carotids cutting through the major arteries proximal to the imaging slices where the average flow velocity satisfies the adiabatic conditions. This process of adiabatic inversion of flowing spins creates an arterial bolus of tagged blood

with a duration equal to the duration of RF. Figure 1.2 illustrates the physical background for CASL.
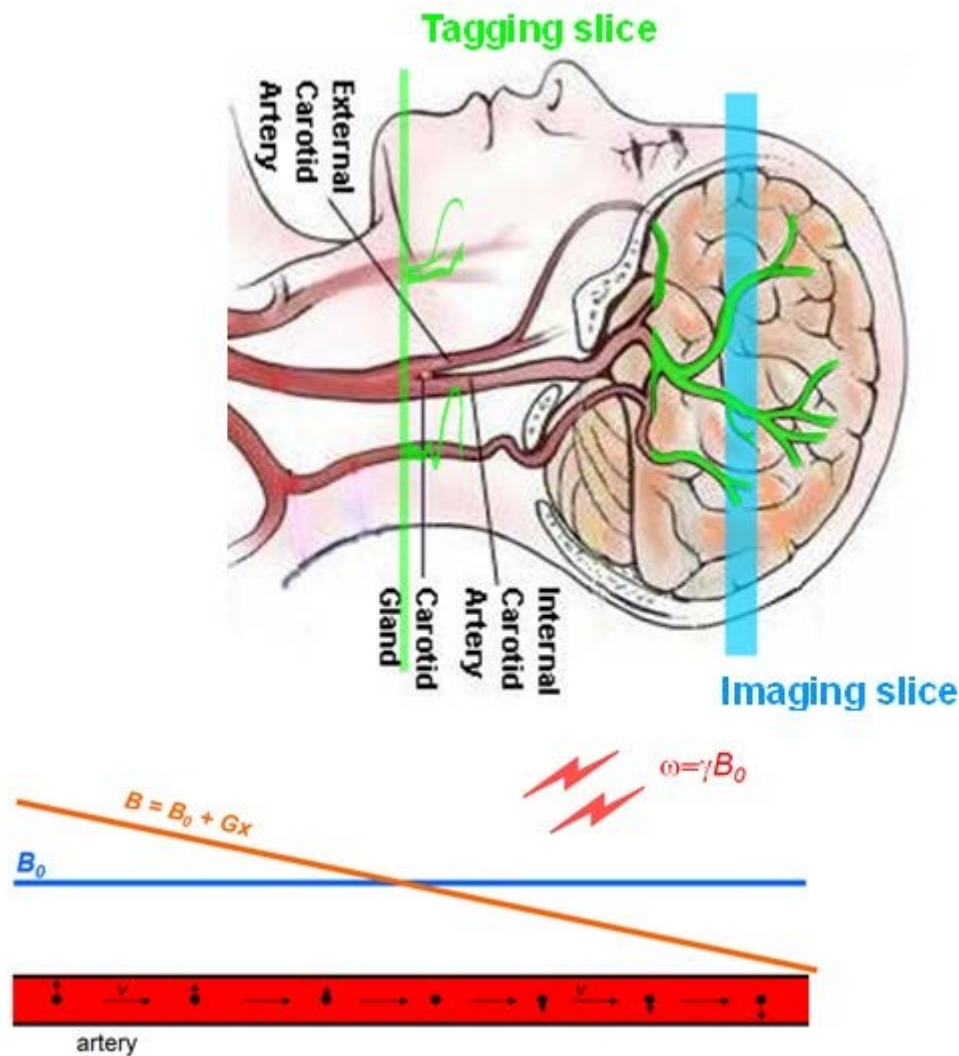
Figure 1.2 *Physical process of continuous arterial spin labeling. The effect of a B_1 field combined with a gradient is that flowing spins experience a frequency sweep to far below resonance to far above inducing adiabatic inversion.*

Arterial blood flowing toward the region of interest (ROI) is tagged by magnetic inversion and this tagged blood flows into the imaging slice or volume and relaxes with the longitudinal relaxation time constant of blood T_{1b}. After a delay of TI to allow for inflow of labeled spins the image is acquired. One important issue that has to be considered in ASL experiment is that the ASL signal difference (control-tag) where the CBF information is logged is only about 1% of the control image intensity. This means that a 1% of error in the control image would produce a 100% of error in the CBF image [7]. Thus, control image must satisfy two main conditions: 1) The arterial blood must

enter to tissue fully relaxed 2) the static tissue spins in the slice of interest must produce exactly the same signal as they did in the tag image [19, 20]. Figure 1.3 illustrates CASL scheme, control and tag images and their corresponding magnetization states and the calculated perfusion weighted image.
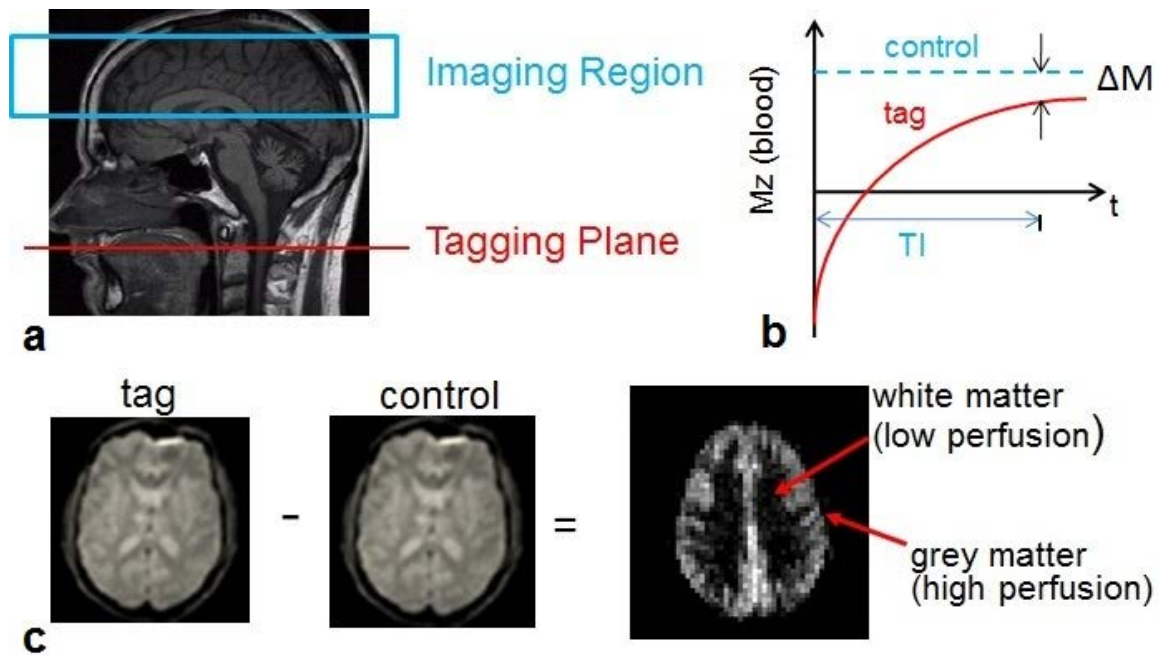
Figure 1.3 a) *Schematic illustration of CASL* ***b)*** *Magnetization of blood in control and tag experiments. In control image the blood is entering the tissue fully relaxed. In tag image, the magnetization is inverted with a 180° RF pulse and follows an inversion recovery curve with the longitudinal relaxation constant of blood T_{1b}.* ***c)*** *Control and tag images and their difference yielding the perfusion weighted image. The intensity of CBF image is around 1% of the control image. In the perfusion image, gray matter exhibits a higher CBF pattern relative to white matter.*

1.3.1 Limitations of CASL

A more practical problem that arises using long RF pulses required for the adiabatic, flow-driven inversion of the inflowing blood, which may last for several seconds is the continuous operation of RF amplifiers. Most commercially available MR scanners use pulsed RF amplifiers which are not able to supply continuous operation. Utting et al (2003) [21] showed that it is possible to approximate to a continuous RF by using multiple short pulses spaced closely together. This is a simple way of imitating a continuous RF but causes highly nonlinear dependence of the degree of inversion on the duty cycle of the RF pulse.

Another major drawback of CASL arises due to the requirement of long labeling pulse causing signal loss because of the presence of magnetization transfer effects (MT). The long labeling pulse applied before the acquisition of tag image is off-resonance with the spins in the slice of interest and ideally should have no effect on the imaging slice. However, despite the distance and the frequency offset between labeling and imaging slices, the long labeling pulse affects immobile, off-resonance spins and causes slight tipping of the magnetization in the region to be imaged [22]. These spins have very short T_2 values (<200 μs) and the NMR signal from the protons of bound water is not typically observed in MRI [23]. However, their saturation is transferred to the visible bulk water signal since the bound water may exchange magnetization with the free waterthrough and cross-relaxation exists. This causes a global decrease in the water signal, which ultimately alters the magnetization difference between tag and control scan and thus gravely affect the accuracy of the perfusion image [24]. In the initial implementation (Williams et al 1992) [10], control images were acquired by applying the same long RF pulse on the other side of the imaging slice at an equal distance, by the way designing a control scan that generates exactly the same degree of MT.

Locating the inversion planes of the two RF pulses symmetrically around the imaging slice balances the MT effects in the control and tag image however this constrains the implementation of CASL to a single slice since only one image plane is properly controlled with this approach. Alsop and Detre (1996) [25] proposed to apply an amplitude modulated (AM) RF pulse during the acquisition of the control image with the same duration as in the tag image. The underlying physics includes modulating a constant RF pulse at frequency f_0 with a sine wave oscillating at a frequency f_1 which produces an irradiation at frequencies f_0-f_1 and f_0+f_1. This results a double inversion with no net effect if the frequency spacing between the planes is large enough and creating the same MT effect minimizing the off-resonance signal alterations between control and tag experiments.

Inversion efficiency α, is also one of the critical factors in ASL which is defined as the fraction of the maximum achievable change in T_1 relaxation between control and tag experiments. Gach and Dai (2004) [26] defined an inversion efficiency parameter for CASL as a function of effective adiabaticity as follows:

$$\beta' = \frac{\gamma\, B_1^2}{G_1 v} \qquad\qquad [1.2]$$

Where β' is the effective adiabaticity and α approaches to 1(full inversion) in the case of $\beta' \ll 1$.

1.3.2 Dual coil continuous ASL (DC-CASL)

We discussed the MT effects in CASL as one of the limitations of the method and summarized the proposed solutions to minimize the signal loss due to this effect above. A promising alternative approach is to use separate labeling coils positioned at the subject's neck to directly label the blood flowing through the common carotid arteries into the brain [27, 28]. Since the labeling irradiation does not extend to the imaged slice, there will be minimum contamination of magnetization transfer effects leading to a higher SNR and the possibility of multi-slice imaging without MT-related problems. The control image than can be acquired exactly like the tag image except applying the labeling RF pulse. Depending on the geometry of the labeling coils, the labeling profile of this technique could cover either only the carotid arteries or also include the vertebral arteries supplying the cerebellum [29, 30].The main drawback of this method is the requirement of special hardware configuration, such as an additional transmit chain, which is not typically available on commercial MR scanners. Calibration and specific absorption rate (SAR) monitoring has to be manually handled for the second external transmit chain in DC-CASL experiments [31]. Although the safety of the method has been proven under normal conditions [27, 28], it is not protected against instrumentation malfunction or operating errors. A physical theory is described in detail by Zhang et al (2007) [32] to analyze the effects of cross-relaxation between tissue water and macromolecular spins on the measurement of perfusion when macromolecular spins are not saturated. One useful benefit of DC-CASL is that it allows obtaining territory maps of the left and right cerebral hemispheres by using an oblique labeling gradient which ensures that ASL occurs only for the selected artery as the endogenous water spins flowing in the contralateral arteries are out of resonance with in the longitudinal field of view of the labeling RF coil [33]. The angle ϴ, between the labeling plane and the plane perpendicular to the arteries to be labeled determines the perfusion territory profiles. Figure 1.4 shows a schematic representation of the DC-CASL and the obtained perfusion territories for different ϴ values [33].
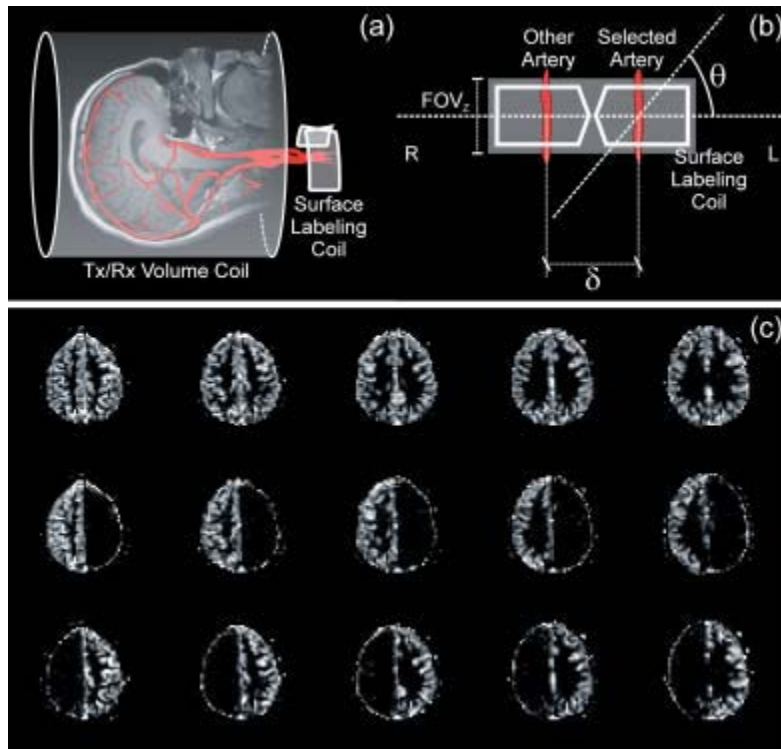
Figure 1.4 a) *Schematic representation of the separate labeling/imaging coil technique **b)** An oblique labeling plane, used at an angle Θ with respect to a plane perpendicular to blood flow allowing to label the selected arteries. angle Θ > 0 corresponds to the left circulation and angle Θ < 0 corresponds to the right circulation **C)** CBF images of a human brain angle Θ = 0 (top raw), angle Θ =+60 (middle raw), angle Θ=-60 (bottom raw). (Figure from Paiva et al, NMR in Biomedicin,2007).*

1.3.3 Absolute quantification of cerebral blood flow in CASL

A detailed model of the ASL process merging the tracer kinetics and relaxation is initially developed by Detre et al (1992) [6] to extract quantitative information from the ASL data. This model was based on single compartment kinetics and the Bloch equation for the Z magnetization is modified to include flow effects such as delivery and clearance proportional to the local cerebral blood flow f as described in Eq.[1.3]:

$$\frac{dM_b(t)}{dt} = \frac{M_b^0 - M_b(t)}{T_1} + fM_a(t) - \frac{f}{\lambda}M_b(t) \qquad [1.3]$$

where M_b and M_a is the time dependent concentration of the longitudinal magnetization of the tissue and arterial blood, M_b^0 is the equilibrium longitudinal magnetization of tissue, λ is the partition coefficient (or volume of distribution) for water defined as (ml water/g tissue)/(ml water/cc blood).

Assuming that $M_a = 0$ at $t = 0$ due to the saturation pulse, Eq.[1.3] can be solved to give:

$$M_b(t) = \frac{M_b^0}{1+fT_1/\lambda} \left\{ 1 + \frac{fT_1}{\lambda} \exp(-t(\frac{1}{T_1} + \frac{f}{\lambda})) \right\} \qquad [1.4]$$

The solution in eq.[1.4] implies that net relaxation curve including flow is again a simple exponential, but with an effective time constant T_{1app} given by:

$$\frac{1}{T_{1app}} = \frac{1}{T_1} + \frac{f}{\lambda} \qquad [1.5]$$

In the steady state, M_b decreases to M_b^{ss} calculated by solving the eq.[3] for $t = \infty$,

$$\frac{M_b^{ss}}{M_b^0} = \frac{1}{1+fT_1/\lambda} \qquad [1.6]$$

Solving eq.[1.5] and eq.[1.6] for f gives

$$f = \frac{\lambda}{T_{1app}} \left(1 - \frac{M_b^{ss}}{M_b^0} \right) \qquad [1.7]$$

Eq.[1.7] gives an estimate of local blood flow f by a measurement of the apparent T_1 of brain T_{1app} and the ratio of M_b^{ss} and M_b^0. However T_1 is a local tissue property and the difference between T_1 and T_{1app} is very small meaning that it is necessary to measure the true T_1 locally with high precision to estimate f/λ accurately [7].

From the point of MRI where the consecutive images are obtained with a time period of TR, eq.[1.3] can be solved in the presence of a proximal saturation as follows:

$$M_b^{tag}(TR) = \frac{M_b^0}{1+fT_1/\lambda} \left(\frac{1-\exp(-TR(1/T_1+f/\lambda))}{1-\cos\beta\exp(-TR(1/T_1+f/\lambda))} \right) \qquad [1.8]$$

where β is an arbitrary tip angle for slice selection. For the control experiment where there is no saturation for arterial blood, the M_a is replaced by M_b^0/λ to give:

$$M_b^{control}(TR) = M_b^0 \left(\frac{1-\exp(-TR(1/T_1+f/\lambda))}{1-\cos\beta\exp(-TR(1/T_1+f/\lambda))} \right) \qquad [1.9]$$

Then, the ratio of magnetization in the tag and the control experiments gives

$$\frac{M_b^{tag}(TR)}{M_b^{control}(TR)} = \frac{1}{1+fT_1/\lambda} \qquad [1.10]$$

which is identical with the solution in eq.[1.6] implying that the local flow in an imaging experiment could be estimated as

$$f = \frac{\lambda}{T_{1app}} \left(1 - \frac{M_b^{tag}(TR)}{M_b^{control}(TR)}\right)$$ [1.11]

Eq.[1.11] implies that determination of flow is independent of imaging parameters. Thus, a quantitative perfusion map can be calculated from images obtained with proximal and distal saturation, and a T_{1app} map. This model initially described by Detre et al (1992) [6] and Williams et al (1992) [10] was extended to cover a number of calibration parameters including transit delay times.

1.3.4 Transit delay time in CASL

The arterial transit time corresponding to the transit delay δt from the tagging region to the imaged voxel is also one of the main drawbacks in ASL experiments significantly affecting the perfusion estimates [25]. Since the transit delay time for each voxel is varying across the brain regions [34-36], the induced bias on the CBF images are not uniform making the δt a significant confounding factor for the interpretation of the ASL signal. The ASL difference signal equation accounting for δt is developed by Williams et al (1992) [10] giving:

$$M_b^{tag} - M_b^{control} = \frac{-2\alpha M_b^0 T_{1app} f}{\lambda} \exp\left(\frac{-\delta t}{T_{1a}}\right)$$ [1.12]

where M_b^{tag} and $M_b^{control}$ is the brain tissue magnetization in the labeling and control experiment respectively, α is the inversion efficiency, λ is the partition coefficient, T_{1a} is the longitudinal relaxation time of arterial blood and δt is the arterial transit time from labeling plane to the imaging volume. Eq.[1.12] shows the exponential decay of the ASL difference signal as a function of the transit delay time.

The solution the transit delay time problem was proposed by Alsop and Detre (1996) [25] by introducing a post-labeling delay time w to reduce the sensitivity of the CBF estimate to the arterial transit time variations. Instead of immediately acquiring the image right after the long labeling pulse, a delay w is inserted after the end of the tagging, before the image acquisition. If the inserted delay is greater than the longest

transit delay ($w > \delta t$), all the tagged arterial bolus will be delivered to all the image voxels. The expression for the signal evolution now becomes

$$M_b^{tag} - M_b^{control} = \frac{-2\alpha M_b^0 T_{1app} f}{\lambda} \exp\left(\frac{-w}{T_{1app}}\right) \exp\left[-\delta\left(\frac{1}{T_{1a}} - \frac{1}{T_{1app}}\right)\right] \qquad [1.13]$$

The CBF now depends on δt times the difference between the tissue and arterial blood relaxation rates. The tagged spins in the voxel with the longest transit delay spend more time in the blood and so relax somewhat less compared to spins that immediately exchange into tissue. Since the relaxation rates of tissue and blood water are close together, the sensitivity of the ASL signal to this residual difference signal is negligible and the trick of inserting a delay is effective in controlling the variability of δt [7].

1.4 Pulsed arterial spin labeling (PASL)

Instead of applying a continuous RF pulse as it flows through a plane using adiabatic inversion, a single 180° RF pulse is applied as a spatially selective pulse that tips over all spins in a thick band below the slice of interest [13, 37]. This labeled volume of blood then flows into tissue during the time TI. The distance between the labeling and imaging regions is minimized to achieve minimal loss of spin label. Similar to CASL, acquiring the control image properly is critical and even harder compared to CASL since the rectangular profile of the labeling slab nevertheless have small wings that can extend into the imaging slice [11].

The first technique for PASL was developed by Edelman et al (1994) [38] proposing an echo-planar imaging and signal targeting with alternating radio frequency (EPISTAR) combining labeling with echo-planar imaging (EPI). The labeling region is typically 10cm thick with a gap of 1 cm to the imaging slice. The control image is acquired similar to CASL by applying an identical inversion pulse on the other side of the imaging slice inverting the spins above the slice. Thus, the venous blood entering to the imaging slice above the slice will appear as focal dark spots in the ASL difference image [39].

Kim et al (1995) [40] proposed a different scheme for PASL called flow-sensitive alternating inversion recovery (FAIR) where the labeling experiment is a slice selective inversion while the control experiment is a non-selective inversion. The drawback of the FAIR scheme is to ensure that slice selective inversion produces a clean 180° inversion over the imaging slice that exactly matches the non-selective inversion.

Golay et al (1999) [41] improved the EPISTAR method called transfer insensitive labeling technique (TILT) which is insensitive to magnetization transfer effects. Labeling is performed by using two slices selective 90° pulses while in control experiment the second 90° pulse is applied with a phase difference of 180° resulting a labeled image in the prior and non-labeling in the later.

As we mentioned above, the EPISTAR suffers from slice profile imperfections and Wong et al (1997) [13] developed proximal inversion with control for off-resonance effects (PICORE) by replacing the inversion slab in the control acquisition with an RF pulse with the same frequency offset but without the gradient. Since there is no gradient is applied, the RF pulse is off-resonance for all spins, so nothing is inverted. PICORE has the advantage of not labeling the venous blood entering above the slice. Figure 1.5 demonstrates the tagging and control profile of the different PASL schemes.
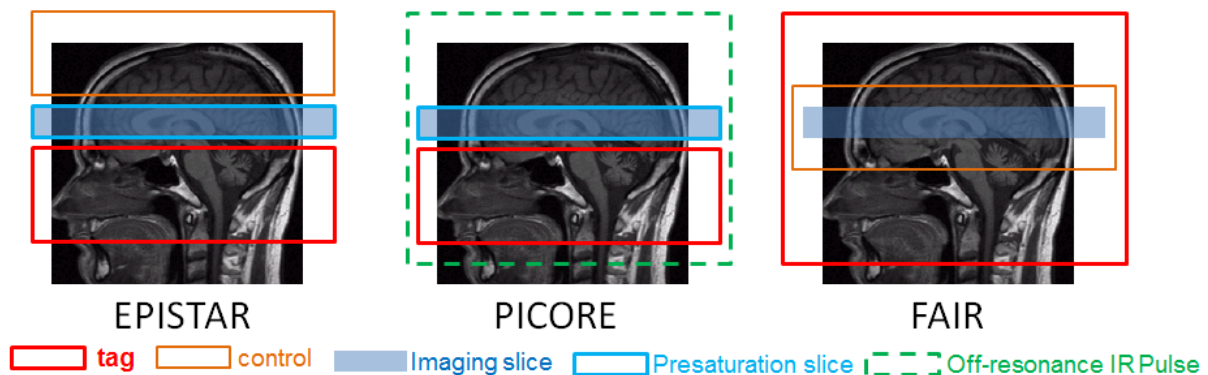
Figure 1.5 *Tagging and control profiles of EPISTAR, PICORE and FAIR pulsed arterial spin labeling sequences.*

In PASL, in order to improve the subtraction accuracy, a useful trick is application of the 90° pre-saturation pulses to the imaging slice by the way suppressing the intrinsic tissue signal which recovers from zero and so is weaker at the time of the measurement [11, 13]. A detailed comparison of PASL encoding schemes will be discussed further later of the thesis.

1.4.1 Quantitative imaging of perfusion using a single subtraction (QUIPSS II)

PASL suffer from a subtler problem related to the duration of the tagged bolus in the arterial blood [42]. The problem originates because in PASL the arterial tagging is done in space rather than in time. In other words, the duration of the arterial bolus is the average transit time of arterial blood out of the tagging band implying that the bolus

duration is determined by the physical extension of the tagging band. Wong et al (1998) [43] proposed the method quantitative imaging of perfusion using single subtraction (QUIPSS II) to obtain a well-defined bolus in PASL experiment mainly required to apply the idea of adding a delay to the pulse sequence to allow the tagged spins to arrive for reducing the transit delay time sensitivity. In QUIPSS II, a 90° saturation pulse is inserted between the inversion pulse and the imaging pulse that hits the same tagging band as the inversion pulse resulting a well-defined bolus by snipping-off the end of arterial bolus. For quantitative CBF estimation, QUIPSS II must be satisfied two conditions: 1) the 90° saturation pulse has to be applied before the bolus leaves the slice 2) the imaging time has to be long enough for all the labeled bolus reaches the slice [44]. Then the ASL difference signal can be expressed as:

$$M_b^{tag} - M_b^{control} = 2M_b^0 f \, TI_1 \exp(-TI_2/T_{1a}) \qquad [1.14]$$

where TI_1 is the time of applying the saturation pulse, TI_2 is the time of imaging, f is the CBF, M_b^0 is the equilibrium magnetization of blood and T_{1a} is the longitudinal relaxation time of arterial blood [9].

The quantification problem of the original PASL technique is corrected with QUIPSS II modification such that the number of tagged spins becomes proportional with the local blood flow similar to the CASL [43].

1.4.2 QUIPSS II with thin-slice TI_1 periodic saturation (Q2TIPS)

QUIPSS II modification improves the accuracy of quantitative perfusion estimation by minimizing the sensitivity to the variable transit delay time and reducing the intravascular signal contamination. In the initial implementation of QUIPSS II [42-44], two sources of residual errors occur: [45] 1) Incomplete saturation of spins over the tagging slab by the QUIPSS II saturation pulse. Through-plane $B1$ inhomogeneity is generally higher than in-plane $B1$ inhomogeneity using a typical head RF coil for a thick axial slice as used in QUIPSS II. 2) Spatial mismatch of the edges of the saturation and inversion slice profiles. The inversion pulse using a sech shaped pulse is highly selective creating a sharp edged inversion profile while the QUIPSS II saturation pulse is not spatially matching to this profile resulting an overestimation of perfusion. Luh et al (1999) [45] proposed to replace the single saturation pulse with a periodic train of thin-slice saturation pulses at the distal end of the tagging band to improve the quality of the

saturation (Q2TIPS). Figure 1.6 shows the Q2TIPS pulse sequence and positions of the in-plane pre-saturation slab, the inversion-tagged region, the periodic saturation slice, and the imaging slices [45].
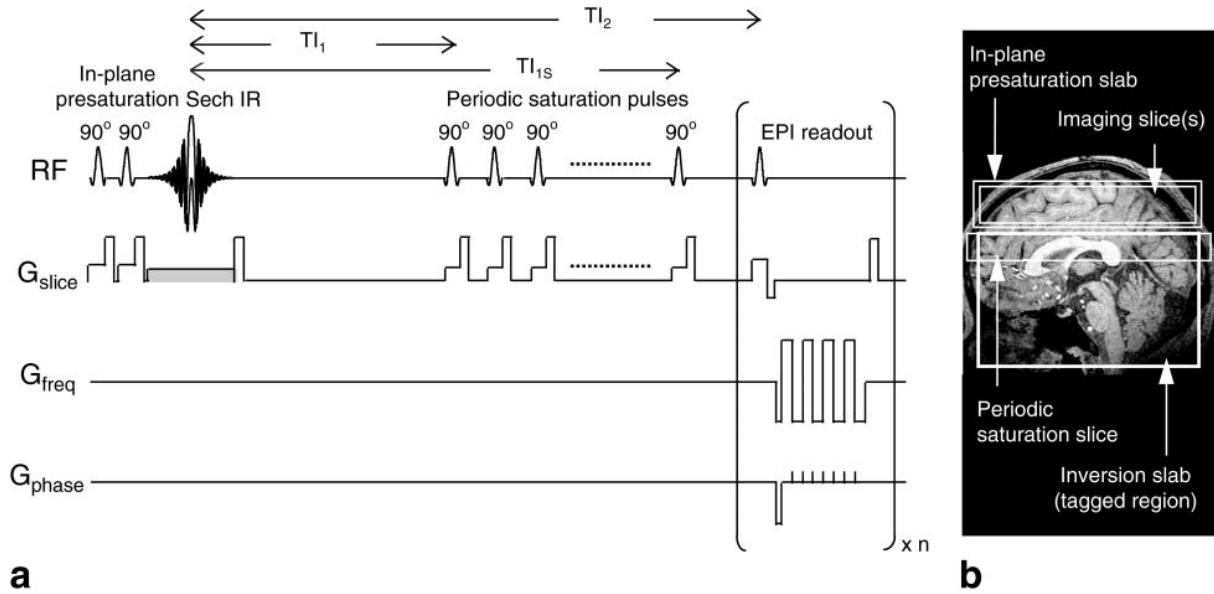
Figure.1.6 a) *Pulse sequence for Q2TIPS. Double in-plane presaturation pulses are applied followed by the sech inversion tagging pulse. For tag and the control images, the gradient lobe in gray is alternately applied. Periodic saturation pulses applied from TI1 to TI1S consist of a train of 90° excitation pulses each followed by a crusher gradient. Single or multislice EPI acquisition is applied at TI2.* ***b)*** *Locations of the in-plane presaturation slab, imaging slice(s), periodic saturation slice, and inversion slab used in the PICORE tagging scheme. (Figure from Luh et al 1999)*

1.4.3 Perfusion model in PASL with transit and trailing times

A perfusion model describing the blood/tissue water exchange kinetics and the magnetization characteristics is developed by Detre et al (1992) [6] by modifying the Bloch equations giving a similar equation described in eq.[1.3]. In PASL, the difference of arterial blood magnetization between the labeled and control experiments is:

$$\Delta M_a(t) = \begin{cases} 0, & 0 \leq t \leq \tau_a \\ \frac{2fM_o}{\lambda}\exp\left(-\frac{t}{T_{1a}}\right) & \tau_a \leq t \leq \tau_d \\ 0, & t \geq \tau_d \end{cases} \qquad [1.15]$$

where τ_a and τ_d are arterial transit and trailing times respectively, T_{1a} is the longitudinal relaxation time of arterial blood. Based on the perfusion model, the ASL difference signal in different tissue types such (i.e. gray matter and white matter), in different physiological states of the brain (i.e. activation and rest) and at different field strengths can be estimated. Modeling the ASL experiment for PASL will be discussed more in detail in chapter 2.

1.5 Pseudo-continuous ASL (pCASL)

The main drawback in CASL is the requirement of long RF labeling pulse which is not available in most of the commercially available MR scanners . Additionally, the long RF pulse creates MT effects biasing the absolute CBF quantification as we previously discussed. On the other hand, PASL is less susceptible to MT effects while suffering from lower SNR compared to CASL typically having on the order of 50% less SNR [37]. Dai et al (2008) [46] proposed an intermediate technique, pseudo-continuous ASL (pCASL) that takes the advantage of high SNR of CASL and high labeling efficiency of PASL without the requirement of long labeling RF pulse by using a train of short, shaped pulses in combination with rephased gradients to adiabatically invert the flowing blood. In the reference scan, every other one of these pulses is inverted in phase, resulting in an almost unchanged magnetization. Wu et al (2007) [14] compared pCASL with PASL and CASL at 3T and reported that pCASL provides 50% improvement in SNR compared to PASL and 18% increase in labeling efficiency compared to CASL. Gevers et al (2011) [47] reported lower inter-subject variability besides increased intra-subject SNR and reproducibility compared to standard ASL. Recently Dai et al (2008) [46] proposed a modified pCASL method to improve the labeling efficiency for the same RF power deposition by replacing the rectangular train of RF pulses with a more sophisticated Hanning pulse to achieve a more precise labeling profile without compromising the labeling efficiency of the previously implemented pCASL schemes. This method increased the labeling efficiency up to 81% for the same power as the standard CASL at 3T.

1.6 Velocity selective ASL (VS-ASL)

As we mentioned above, the magnitude and variability of the transit delay in relation to the T_1 decay of the tag is one of the major sources in perfusion estimation. In pathologies such as stroke where slow or collateral flow conditions may exist, conventional arterial

spin labeling (ASL) methods that apply spatially selective arterial tagging may not provide robust measures of cerebral blood flow (CBF) since δt is much larger than T_1. To obtain quantitative measures of CBF under slow and collateral flow conditions as well, Wong et al (2006) [17] proposed velocity selective (VS) ASL which applies a labeling based on the velocity of the arterial water rather than its position. This is accomplished with an RF and gradient pulse train that effectively dephases the MR signal from protons that are flowing faster than a specified cut-off velocity while rephrasing the signal from slower flowing protons. Using velocity selective pulses initially proposed by Norris and Schwartzbauer (1999) [48], a VS tag is applied that modulates the longitudinal magnetization of blood above a sharp cutoff velocity V_c. After a delay period of TI, the tag image is acquired by imposing the restriction to the image acquisition $V < V_c$ implying that resulting image includes tagged magnetization only from spins that decelerated during TI from above to below V_c. Assuming that the velocity of the blood in the arterial tree is monotonically decreasing, the amount of tagged blood that appears in the image is simply TI.CBF [49]. VS-ASL uses a pulse train that consists of nonselective 90°–180°–90° RF pulses and bipolar flow-sensitive gradients to generate a sinc modulation of the longitudinal magnetization. Figure 1.7 shows the schematic diagram of the VS-ASL sequence [50].
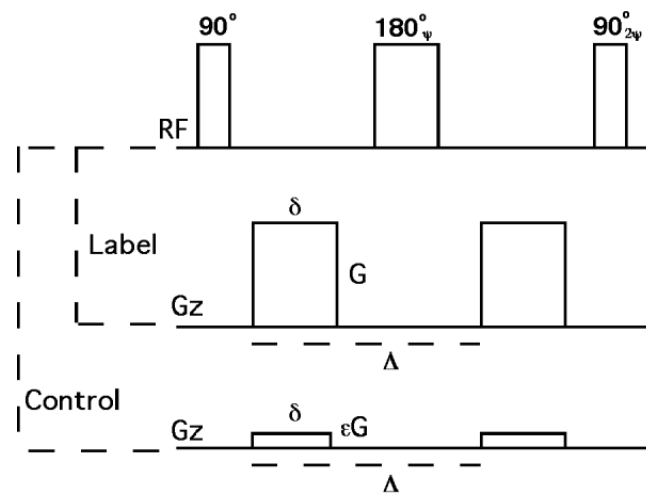
Figure 1.7 *Schematic of the VS pulse train. Identical sequences were used for both labeling and control, except that a small value of gradient was used for the control. The phase of the refocusing and second 90° pulses was cycled to reduce errors resulting from imperfect flip angles. (Figure from Duhamel et al 2003).*

This sequence produces a sinc modulated longitudinal magnetization given by [50]

$$M_z = M_{static} + M_v \cos(\beta) \qquad\qquad [1.16]$$

where M_z, M_{static} and M_v are the longitudinal magnetization, static tissue magnetization and flowing fluid magnetization respectively and β is expressed as:

$$\beta = \gamma G \delta \Delta v = \alpha v \qquad\qquad [1.17]$$

where γ is the gyromagnetic ratio, G is the gradient strength, δ is the gradient duration, v is the velocity and α is the velocity-encoding factor. Laminar flow is a physiologically plausible approach where the distribution of velocities is uniform from 0 to V_{max}. Averaging the velocities over this distribution gives

$$M_z^{total} = \frac{M_0}{V_{max}} \int_0^{V_{max}} dv \cos(\alpha v) = M_0 \frac{\sin(\alpha V_{max})}{\alpha V_{max}} \qquad\qquad [1.18]$$

Figure 1.8 plots the modulation of longitudinal magnetization versus the laminar flow velocity where the first zero-crossing is defined as the cut-off velocity expressed as [17, 49, 50]:

$$v_c = \frac{\pi}{\gamma \delta \Delta G} \qquad\qquad [1.19]$$
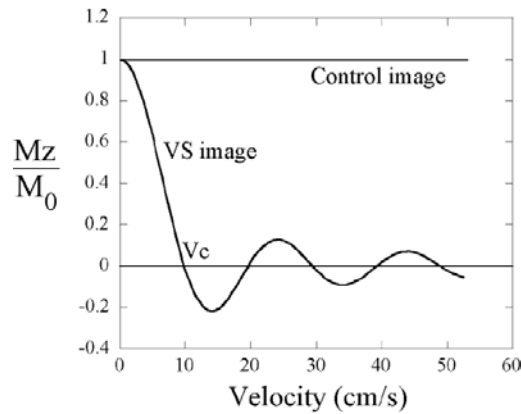
Figure 1.8 *VS selectivity profile. The VS pulse train modulates the longitudinal magnetization to a sinc function of flow velocity. The sinc function is used to approximate the ideal rectangular selectivity.(Figure from Duhannel et al 2003).*

We described in this chapter the physical principles of ASL and we gave a brief introduction of basic ASL sequences. The choice of the ASL sequence depends on the application, availability of hardware and power limitations. Application specific optimization of the sequence parameters is also crucial for an accurate CBF quantification.

References

1.   Baron, J.C., et al., *Use of PET methods for measurement of cerebral energy metabolism and hemodynamics in cerebrovascular disease.* J Cereb Blood Flow Metab, 1989. **9**(6): p. 723-42.
2.   Yonas, H., et al., *Mapping cerebral blood flow by xenon-enhanced computed tomography: clinical experience.* Radiology, 1984. **152**(2): p. 435-42.
3.   Detre, J.A., et al., *Measurement of regional cerebral blood flow in cat brain using intracarotid 2H2O and 2H NMR imaging.* Magn Reson Med, 1990. **14**(2): p. 389-95.
4.   Rosen, B.R., et al., *Perfusion imaging with NMR contrast agents.* Magn. Reson. Med., 1990. **14**: p. 249-265.
5.   Lassen, N.A. and W. Perl, *Tracer Kinetic Methods in Medical Physiology*1979, New York: Raven Press.
6.   Detre, J.A., et al., *Perfusion imaging.* Magn. Reson. Med., 1992. **23**: p. 37-45.
7.   Buxton, R.B., *Introduction to Functional Magnetic Resonance Imaging: Principles and Techniques*2002, Cambridge: Cambridge University Press.
8.   Liu, T.T. and G.G. Brown, *Measurement of cerebral perfusion with arterial spin labeling: Part 1. Methods.* Journal of the International Neuropsychological Society, 2007. **13**(3): p. 517-525.
9.   Buxton, R.B., et al., *A general kinetic model for quantitative perfusion imaging with arterial spin labeling.* Magn. Reson. Med., 1998. **40**: p. 383-396.
10.   Williams, D.S., et al., *Magnetic resonance imaging of perfusion using spin-inversion of arterial water.* Proc. Natl. Acad. Sci. USA, 1992. **89**: p. 212-216.
11.   Wong, E.C., R.B. Buxton, and L.R. Frank, *Pulsed Arterial Spin Labelling: A Comparison of Techniques for Quantitative Perfusion Imaging.* Magn. Reson. Med., Submitted.
12.   Cavusoglu, M., et al., *Comparison of pulsed arterial spin labeling encoding schemes and absolute perfusion quantification.* Magn Reson Imaging, 2009. **27**(8): p. 1039-45.
13.   Wong, E.C., R.B. Buxton, and L.R. Frank, *Implementation of quantitative perfusion imaging techniques for functional brain mapping using pulsed arterial spin labeling.* NMR in Biomed, 1997. **10**: p. 237-249.
14.   Wu, W.C., et al., *A theoretical and experimental investigation of the tagging efficiency of pseudocontinuous arterial spin labeling.* Magn Reson Med, 2007. **58**(5): p. 1020-7.
15.   Wong, E.C., *Vessel-encoded arterial spin-labeling using pseudocontinuous tagging.* Magn Reson Med, 2007. **58**(6): p. 1086-91.
16.   Dai, W., et al., *Continuous flow-driven inversion for arterial spin labeling using pulsed radio frequency and gradient fields.* Magn Reson Med, 2008. **60**(6): p. 1488-97.
17.   Wong, E.C., et al., *Velocity-selective arterial spin labeling.* Magnetic Resonance in Medicine, 2006. **55**(6): p. 1334-1341.
18.   A., A., *The Principles of Nuclear Magnetism*1961: Oxford University Press.
19.   Wong, E.C., R.B. Buxton, and L.R. Frank. *A theoretical and experimental comparison of continuous and pulsed arterial spin labeling techniques for quantitative perfusion imaging*. in *Sixth Meeting, International Society for Magnetic Resonance in Medicine*. 1998. Sydney, Australia.
20.   Yang, Y., et al., *Multislice imaging of quantitative cerebral perfusion with pulsed arterial spin labeling.* Magn. Reson. Med., 1998. **39**: p. 825-832.
21.   Utting, J.F., et al., *Velocity-driven adiabatic fast passage for arterial spin labeling: results from a computer model.* Magnetic Resonance in Medicine, 2003. **49**(2): p. 398-401.
22.   Wolff, S.D. and R.S. Balaban, *Magnetization transfer contrast (MTC) and tissue water proton relaxation in vivo.* Magnetic Resonance in Medicine, 1989. **10**(1): p. 135-44.
23.   Mehta, R.C., G.B. Pike, and D.R. Enzmann, *Magnetization transfer magnetic resonance imaging: a clinical review.* Top Magn Reson Imaging, 1996. **8**(4): p. 214-30.
24.   Balaban, R.S. and T.L. Ceckler, *Magnetization transfer contrast imaging.* Magn. Reson. Quart., 1992(8): p. 116-137.

25. Alsop, D.C. and J.A. Detre, *Reduced transit-time sensitivity in noninvasive magnetic resonance imaging of human cerebral blood flow.* J Cereb Blood Flow and Metab, 1996. **16**: p. 1236-1249.

26. Gach, H.M. and W. Dai, *Simple model of double adiabatic inversion (DAI) efficiency.* Magnetic Resonance in Medicine, 2004. **52**(4): p. 941-6.

27. Zaharchuk, G., et al., *Multislice perfusion and perfusion territory imaging in humans with separate label and image coils.* Magn Reson Med, 1999. **41**(6): p. 1093-8.

28. Mildner, T., et al., *Functional perfusion imaging using continuous arterial spin labeling with separate labeling and imaging coils at 3 T.* Magn Reson Med, 2003. **49**(5): p. 791-5.

29. Talagala, S.L., et al., *Whole-brain 3D perfusion MRI at 3.0 T using CASL with a separate labeling coil.* Magnetic Resonance in Medicine, 2004. **52**(1): p. 131-40.

30. Hetzer, S., et al., *Shielded dual-loop resonator for arterial spin labeling at the neck.* J Magn Reson Imaging, 2009. **29**(6): p. 1414-24.

31. Pohmann, R., et al., *Theoretical and experimental evaluation of continuous arterial spin labeling techniques.* Magn Reson Med, 2010. **63**(2): p. 438-46.

32. Zhang, X., et al., *Quantitative basal CBF and CBF fMRI of rhesus monkeys using three-coil continuous arterial spin labeling.* Neuroimage, 2007. **34**(3): p. 1074-83.

33. Paiva, F.F., A. Tannus, and A.C. Silva, *Measurement of cerebral perfusion territories using arterial spin labelling.* NMR Biomed, 2007. **20**(7): p. 633-42.

34. Lee, G.R., L. Hernandez-Garcia, and D.C. Noll, *Functional imaging with Turbo-CASL: transit time and multislice imaging considerations.* Magn Reson Med, 2007. **57**(4): p. 661-9.

35. Gonzalez-At, J.B., D.C. Alsop, and J.A. Detre, *Cerebral perfusion and arterial transit time changes during task activation determined with continuous arterial spin labeling.* Magn Reson Med, 2000. **43**(5): p. 739-46.

36. Yang, Y., et al., *Transit time, trailing time, and cerebral blood flow during brain activation: measurement using multislice, pulsed spin-labeling perfusion imaging.* Magn Reson Med, 2000. **44**(5): p. 680-5.

37. Wong, E.C., R.B. Buxton, and L.R. Frank, *A theoretical and experimental comparison of continuous and pulsed arterial spin labeling techniques for quantitative perfusion imaging.* Magn. Reson. Med., 1998. **40**: p. 348-355.

38. Edelman, R.R., et al., *Signal targeting with alternating radiofrequency (STAR) sequences: application to MR angiography.* Magn. Reson. Med., 1994. **31**: p. 233-238.

39. Edelman, R.R. and Q. Chen, *EPISTAR MRI: multislice mapping of cerebral blood flow.* Magn. Reson. Med., 1998. **40**: p. 800-805.

40. Kim, S.-G., *Quantification of regional cerebral blood flow change by flow-sensitive alternating inversion recovery (FAIR) technique: application to functional mapping.* Magn. Reson. Med., 1995. **34**: p. 293-301.

41. Golay, X., et al., *Transfer insensitive labeling technique (TILT): application to multislice functional perfusion imaging.* J Magn Reson Imaging, 1999. **9**(3): p. 454-61.

42. Wong, E.C., R.B. Buxton, and L.R. Frank. *Quantitative imaging of perfusion using a single subtraction (QUIPSS).* in *Neuroimage.* 1996.

43. Wong, E.C., R.B. Buxton, and L.R. Frank, *Quantitative imaging of perfusion using a single subtraction (QUIPSS and QUIPSS II).* Magn. Reson. Med., 1998. **39**: p. 702-708.

44. Wong, E.C., L.R. Frank, and R.B. Buxton. *Quantitative multislice perfusion imaging using QUIPSS II, EPISTAR, FAIR, and PICORE.* in *Fifth Meeting, International Society for Magnetic Resonance in Medicine.* 1997. Vancouver.

45. Luh, W.M., et al., *QUIPSS II with thin-slice TI1 periodic saturation: a method for improving accuracy of quantitative perfusion imaging using pulsed arterial spin labeling.* Magn Reson Med, 1999. **41**(6): p. 1246-54.

46. Dai, W., et al., *Continuous flow-driven inversion for arterial spin labeling using pulsed radio frequency and gradient fields.* Magnetic Resonance in Medicine, 2008. **60**(6): p. 1488-97.

47. Gevers, S., et al., *Intra- and multicenter reproducibility of pulsed, continuous and pseudo-continuous arterial spin labeling methods for measuring cerebral perfusion.* J Cereb Blood Flow Metab, 2011. **31**(8): p. 1706-15.

48.   Norris, D.G. and C. Schwarzbauer, *Velocity selective radiofrequency pulse trains.* J Magn Reson, 1999. **137**(1): p. 231-6.
49.   Wu, W.C. and E.C. Wong, *Feasibility of velocity selective arterial spin labeling in functional MRI.* J Cereb Blood Flow Metab, 2007. **27**(4): p. 831-8.
50.   Duhamel, G., C. de Bazelaire, and D.C. Alsop, *Evaluation of systematic quantification errors in velocity-selective arterial spin labeling of the brain.* Magnetic Resonance in Medicine, 2003. **50**(1): p. 145-53.

Chapter 2

Magnetization dispersion effects on quantitative perfusion imaging

Overview

The transit delay time is a key local variable in arterial spin labeling (ASL) magnetic resonance imaging. Most experiments assume a global transit delay time with blood flowing from the tagging region to the imaging slice in plug flow, without any dispersion of the magnetization. However, due to cardiac pulsation, nonuniform cross-sectional flow profile and complex vessel networks, the distribution of the transit delay times has a statistical nature instead of a single value. In this study, we explored the regional effects of magnetization dispersion for varying transit times on pulsed, pseudo-continuous and dual-coil continuous arterial spin labeling encoding schemes. The kinetic curves of cerebral blood flow (CBF) were measured for five healthy subjects in five regions of interest (ROIs) based on different perfusion territories. Transit delay time maps were calculated for each subject and the regional effects of magnetization dispersion on the perfusion estimates were characterized for each of the ASL variants. Longer distances between tagging and imaging region typically used for continuous tagging schemes were found to cause larger magnetization dispersion effects and, when plug flow is assumed, to enhance the regional bias on the quantitative CBF estimation up to 37%.

2.1 Introduction

Arterial Spin Labeling (ASL) is a magnetic resonance imaging method to map the cerebral blood flow (CBF) by tracking the inflow of magnetically labeled arterial water spins into an imaging slice [1-3]. The arterial blood water flowing into the imaging slice exchanges with tissue water, altering the tissue magnetization. A perfusion-weighted image can be generated by the subtraction of a tag image in which inflowing spins have been labeled

33

from a control image in which spin labeling has not been performed. Then, the magnetization difference $\Delta M(t)$ (control-tag) in the tissue at a time t can be considered to be proportional to the CBF. To obtain quantitative perfusion maps in absolute units (ml/gr-min), kinetic models were developed that consider the dynamics of the in- and outflowing magnetically labeled spins by modifying the Bloch equations [4]. Early models assumed a sudden and uniform (simultaneous) arrival of the tagged blood in the imaging slice [5-9]. However, many studies experimentally showed that the quantitative CBF values measured using ASL is highly dependent on the transit delay time (δt) varying even within an imaging slice [10-13]. The standard general kinetic model proposed by Buxton et el. [4] took this into account , incorporating δt in an arterial input function. In addition, usually plug-flow is assumed, which implies that the magnetically labeled spins enter the imaging slice without dispersion. In contrast to the plug flow approximation, a number of factors have been reported which could cause dispersion of the tagged spins as the blood flows from the tagging to the imaging region, such as viscosity, flow pulsation, turbulence and the non-uniform feeding characteristics of the voxels due to the complex structure of the vascular tree (i.e. multiple arteries feeding the same voxel) [14, 15]. Recently, Hrabe and Lewis extended the standard model by presenting an analytical solution for two more realistic arterial input functions taking into account the dispersion of the tagged spins [16]. They assumed a Gaussian distribution of δt and proposed to add the standard deviation of this distribution (σ) as a fitting parameter into the kinetic model to characterize the dispersive effects. This approach applies a Gaussian smoothing of the sharp-edged step waveform of the arterial input function which is physiologically more plausible.

Gallichan and Jezzard recently investigated the effect of tag dispersion on the CBF estimation by comparing the standard vs. the Hrabe model for pulsed ASL (PASL) [17]. In continuous ASL (CASL), the distance between the tagging and the imaging region is often larger than that of PASL, resulting in longer δt which ultimately leads to larger dispersion since there will be more time for dispersive effects to build up. In this study, we present a more general framework to characterize the magnitude of these dispersive effects for varying distances by using PASL, pseudo-continuous ASL (PCASL) and dual-coil continuous

ASL (DC-CASL) tagging schemes. Regional variations of CBF and δt are discussed based on the findings.

2.2 Methods

2.2.1 Theory

The kinetic model proposed by Buxton et al [4] defines three functions to quantify the CBF from the measured magnetization difference $\Delta M(t)$: the delivery function $c(t)$, the residue function $r(t)$ and the magnetization relaxation function $m(t)$:

$$\Delta M(t) = 2M_{0B}f \int_0^t c(t')r(t-t')m(t-t')dt'$$

$$= 2M_{0B}fc(t) \otimes [r(t)m(t)] \tag{2.1}$$

where $\otimes$ denotes convolution, M_{0B} is the equilibrium magnetization of arterial blood and f is the CBF in units of ml/g-s. The delivery function $c(t)$ usually is assumed to be a boxcar function multiplied with an exponential decay and represents the normalized arterial concentration of magnetization arriving at the voxel at time t. This corresponds to a plug-flow which is steady, uniform and non-dispersive. The residue function $r(t)$ is the fraction of tagged water molecules that remain in the voxel after a time t, thus taking the clearance of the labeled spins with venous flow into account. The magnetization relaxation function $m(t)$ is an exponential decay term accounting for the longitudinal relaxation of the magnetization. For PASL and CASL, these terms are expressed as

$$c(t) = \begin{cases} 0 & 0 < t < \delta t \\ \alpha e^{-t/T_{1B}} \quad (PASL) & \delta t < t < \tau + \delta t \\ \alpha e^{-\delta t/T_{1B}} \quad (CASL) & \\ 0 & \tau + \delta t < t \end{cases} \tag{2.2}$$

$$r(t) = e^{-ft/\lambda} \tag{2.3}$$

$$m(t) = e^{-t/T_1} \tag{2.4}$$

where α is the tagging efficiency, τ is the temporal width of the tag, λ is the equilibrium tissue-blood partition coefficient of water equivalent to the relative proton densities of tissue and blood and T_1 is the longitudinal relaxation time of the tissue.

Substituting the assumptions in eq. [2.2],[2.3],[2.4] into eq.[1] yields the solutions for $\Delta M(t)$ for PASL as follows [4]:

$$\Delta M(t) = \begin{cases} 0 & 0 < t < \delta t \\ 2M_{0B}f(t - \delta t)\alpha e^{-t/T_{1B}}q_p(t) & \delta t < t < \tau + \delta t \\ 2M_{0B}f\tau\alpha e^{-t/T_{1B}}q_p(t) & \tau + \delta t < t \end{cases} \qquad [2.5]$$

with

$$q_p(t) = \begin{cases} \dfrac{e^{kt}(e^{-k\delta t}-e^{-kt})}{k(t-\delta t)} & \delta t < t < \tau + \delta t \\ \dfrac{e^{kt}(e^{-k\delta t}-e^{-k(\tau+\delta t)})}{k\tau} & \tau + \delta t < t \end{cases} ,$$

$$k = \frac{1}{T_{1B}} - \frac{1}{T_{1'}}$$

$$\frac{1}{T_1'} = \frac{1}{T_1} + \frac{f}{\lambda}$$

Similarly for CASL, $\Delta M(t)$ was found to be [4]

$$\Delta M(t) = \begin{cases} 0 & 0 < t < \delta t \\ 2M_{0B}fT_1'\alpha e^{-\delta t/T_{1B}}q_{ss}(t) & \delta t < t < \tau + \delta t \\ 2M_{0B}fT_1'\alpha e^{-\delta t/T_{1B}}e^{-(t-\tau-\delta t)/T_1'}q_{ss}(t) & \tau + \delta t < t \end{cases} \qquad [2.6]$$

with

$$q_{ss}(t) = \begin{cases} 1 - e^{-(t-\delta t)/T_1'} & \delta t < t < \tau + \delta t \\ 1 - e^{-\tau/T_1'} & \tau + \delta t < t \end{cases}$$

As estimate for the tagging efficiency α, we used simulation results of the magnetization after the tag and control pulses as a function of gradient strength, gradient moment and blood flow velocity, yielding 0.955 for DC-CASL, 0.94 for PCASL and 0.98 for PASL (α is

defined as $(M_{control} - M_{tag})/(2M_0))$(for the simulation details, see [18]). The equilibrium magnetization of the blood,M_{0B}, is another direct scaling factor of CBF and could bias the CBF estimate up to 35% depending on the calculation methods [19]. To calculate the equilibrium magnetization of the blood, we used the method proposed in [19] which uses local M_{0B} instead of global values (M_{0B}map instead of a single global value) since this corrects for the artifacts caused by the spatial sensitivity profile of the RF coil. Relaxation times at 3T were assumed to be T_1= 1330 ms for gray matter and T_{1b}=1670 for arterial blood [6, 20]. The dimensionless terms $q_p(t)$ and $q_{ss}(t)$ represent factors related to changes in relaxation times and to venous clearance have typically values close to one and are ignored in many studies. However, Gallichan et al [17] reported a bias of up to 20% on the overall CBF estimation due to $q_p(t)$ in a PASL study, which cannot be considered negligible. Hence, we included them the original model as direct scaling factors of the CBF estimation, using the reported values for f=0.01 s^{-1} (corresponding to 60 ml/100 g-min) and λ=0.9 [4, 6].

Hrabe and Lewis [16] extended the standard model of Buxton to take the tag dispersion into account by constructing an alternative expression for $c(t)$, assuming a Gaussian dissipation of the input function and formulated the magnetization difference for PASL as

$$\Delta M(t) = \frac{F}{2R}\left\{[\text{erf}(u_1) - \text{erf}(u_2)]e^{Rt} - \left[1 + \text{erf}\left(u_1 - \frac{R\sigma_1}{\sqrt{2}}\right)\right]e^{R\left(\tau_1 + \frac{R\sigma_1^2}{2}\right)}\right.$$

$$\left. + \left[1 + \text{erf}\left(u_2 - \frac{R\sigma_2}{\sqrt{2}}\right)\right]e^{R\left(\tau_2 + \frac{R\sigma_2^2}{2}\right)}\right\}$$

[2.7]

where $F = 2\alpha M_0 \frac{f}{\lambda}e^{-t/T_1'}$, $u_1 = \frac{t-\tau_1}{\sqrt{2}\sigma_1}$, $u_2 = \frac{t-\tau_2}{\sqrt{2}\sigma_2}$ and $erf(x)$ represents the error function.

Similarly, the solution for the $\Delta M(t)$ is expressed for CASL as

$$\Delta M = T_1' 2\alpha M_0 \frac{f}{\lambda}e^{-\delta t/T_{1b}}e^{\sigma^2/2T_{1b}^2}$$

[2.8]

Here the leading and the trailing wavefront of the tagged region is considered to arrive with an average delay of τ_1 and τ_2, respectively. We slightly modified these equations for PASL by assuming $\tau_1 = \tau_2 = \delta t$ with an identical standard deviation of the distribution of $\sigma_1 = \sigma_2 = \sigma$ [16, 17]. This implies a Gaussian distribution of the tag arrival times δt with a standard deviation of σ.

2.2.2 Data Acquisition

MR images were acquired on a 3T Siemens MAGNETOM Trio scanner (Siemens Medical Solutions, Erlangen, Germany). Experiments were performed with three different ASL sequences, namely PASL [21], PCASL [22-24] and DC-CASL [25, 26]. For PASL, a 12 channel receive head coil (Siemens, Erlangen, Germany) was used in combination with the body coil for transmit. For DC-CASL, we used separate coils positioned at the neck of the subject to label the blood flowing through the carotid arteries. These were rectangular surface coils with a size of 5 x 7 cm and were actively detuned whenever they were not used for transmit. An additional custombuilt transmit channel was used to power the labeling coils and a single channel transmit-receive birdcage coil was used for imaging. The RF pulses were generated by a signal generator (Hameg Instruments, Mainhausen, Germany) and amplified by an RF amplifier (AR Modular RF, Bothell, WA) both triggered by the scanner. A power meter (Bird Electronic Corporation, Solon, OH) served to monitor the transmitted RF power and to control the SAR (specific absorption rate). A total RF power of 8W corresponding to a flip angle of 55°/ms at the position of the carotid arteries was used with an optimum gradient strength of 1.8 mT/m. To reduce the RF noise inside the scanner room, additional gating was applied for the signal generator and RF amplifier. The flip angle at the position of the carotid arteries was estimated from measurements on a phantom with a similar loading as the human neck (for a detailed description, see [18]). The single-channel birdcage coil was also used for PCASL experiments using a train of 24° Gaussian pulses with a duration of 600 μs to adiabatically invert the flowing blood separated by a 600 μs gradient rephasing delay (50% RF duty cycle). The slice gradient strength was 6 mT/m and the maximum amplitude of the rephrasing gradient was -15.4 mT/m. For PASL experiments, the PICORE tagging scheme was used with QUIPSS-II modification [27, 28] using a spatial tag width of 10 cm. A C-shaped FOCI [29] pulse was used for inversion and

two pre-saturation pulses were applied in the imaging plane immediately before the inversion pulse to minimize the impact of the static tissue.

Five male subjects with ages between 23 and 35 participated in the experiments. Written consent from the participants was obtained before the experiments and the experimental protocol was approved by the ethics committee of the University of Tübingen. All sequences used the same GE-EPI sequence for read out. Four axial slices were acquired, encompassing the corpus callosum and above with a slice thickness of 8 mm and 20% gap between the slices. Other relevant sequence parameters were: matrix size = 64 x 64, FOV=256 mm, TR= 3 s, TE=19 ms.

To span the kinetic curves for each of the ASL schemes, we used nine inversion times (TI)/post labeling delay (PLD) times ranging in [100, 250, 500, 750, 1000, 1250, 1500, 1750, 2000] ms. For PASL, the tagging slab was 3cm inferior to the proximal end of the image slices and TI_1 = 700 ms. For the runs with $TI < TI_1$, we disabled the saturation pulses since the 700 ms bolus would be still in the tagging region at the time of TI. For PCASL, the inversion plane was positioned 8cm proximal to the magnet isocenter and the tag duration was set to 500ms. For DC-CASL the distance between the labeling coils and the isocenter was measured and the labeling slice was positioned 15-17 cm proximal to the isocenter. The image slices were acquired in ascending order with each run alternating between tag and control scans in 30 repetitions. The same slices were imaged with all three ASL sequences with varying inversion times resulting in a total scan time of approximately 41 min for each subject. To define vascular territory based ROIs, we additionally acquired from each subject time-of-flight (TOF) angiography images and a high-resolution T1 weighted structural image using a 3D MP-RAGE (magnetization prepared - rapid acquisition gradient echo) sequence (TR = 2000 ms, TE = 3.25 ms, FOV = 256 mm, 176 sagittal slices, voxel size = 1 x 1 x 1 mm^3, flip angle = 9°).

2.2.3 Data Processing

MR data were analyzed using FSL software [30] with additional custom-made MATLAB and Linux shell script routines. The images obtained from all ASL sequences were coregistered and motion corrected utilizing the MCFLIRT module of FSL [31], using the central volume of the corresponding run as reference. Average perfusion weighted images were created by

calculating control-tag difference images using surround subtraction (i.e., computing the difference between each image and the average of its two nearest neighbors), thereby reducing BOLD signal contamination of the CBF time course [19, 32]. Gray matter voxels were selected to create a mask by thresholding the average perfusion weighted image acquired with TI=1500ms in a PASL experiment [15, 19]. Five regions of interest (ROIs) were defined on the gray matter masked CBF images for each subject based on the territorial characteristics of the major brain feeding arteries reported in previous studies [33-35]. Particularly, each ROI was placed in a way that it was linked to a single arterial territory and had a similar distance from the respective major artery [17, 33, 35]. Depending on the slice locations, the vascular territories included middle cerebral artery (MCA), posterior cerebral artery (PCA) and anterior cerebral arteries (ACA). Voxel-wise kinetic curves were calculated from the set of the averaged ΔM images (average of 30 volumes for each inversion time). Voxels with outlying perfusion values (i.e. due to the partial volume artifacts) were excluded by removing those voxels from the ROIs with less than 70% correlation between their kinetic curve and the average kinetic curve of the corresponding ROI from further analysis. Each data set was fit to the standard and the Hrabe-Lewis model, using a least-square fit. The parameters f, Δt and σ (for Hrabe-Lewis model) were estimated for each kinetic curve and their maps were calculated for each subject and for different ASL encoding schemes.

2.3 Results

Figure 2.1 shows the slice locations on the anatomical image, the arterial distribution on the TOF angiography image, the perfusion weighted image (average of control-tag obtained from PASL) and the five defined ROIs overlaid on the perfusion image, for a representative subject.
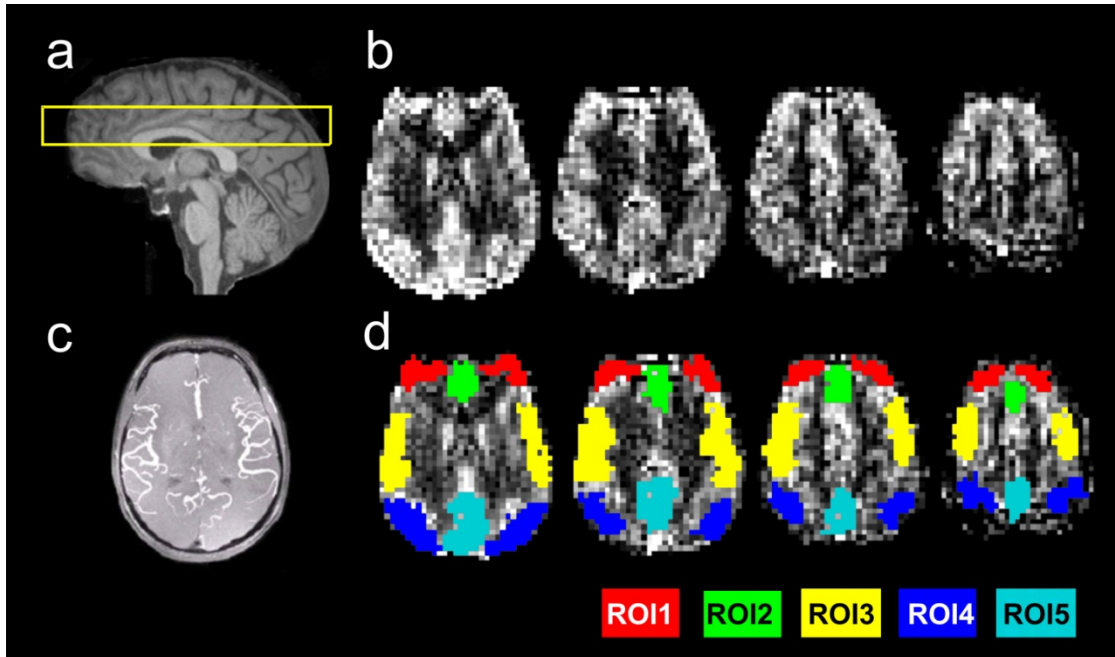
Figure 2.1.a) *Imaging slice locations* ***b)*** *CBF weighted images obtained with PASL* ***c)*** *TOF angiography image* ***d)*** *Defined ROIs of a representative subject.*

Figure 2.2 shows the δt maps calculated by fitting the Hrabe-Lewis model to the measured kinetic curves for PASL, PCASL and DC-CASL sequences. The δt values exhibit regional variations across the brain and get higher for ascending slice positions in all sequences. The increase in distance between the tagging and the imaging region for different ASL encoding schemes (PASL: 3cm, PCASL: 8cm, DC-CASL: 15-17cm) leads to higher δt values as is clearly observable in Figure 2.2 where red colors signify shorter and yellow colors longer transit times (i.e. δt is always lower for PASL and higher for DC-CASL for the same slice). Note that the transit delay time for CASL is the sum of tag duration and post labeling delay time. As a consequence of the longer transit times, the expected increase in the magnetization dispersion characterized by the standard deviation σ is intuitively observable in Figure 2.2, where the δt maps for PASL seems less variable (lower σ) than those for DC-CASL (higher σ).
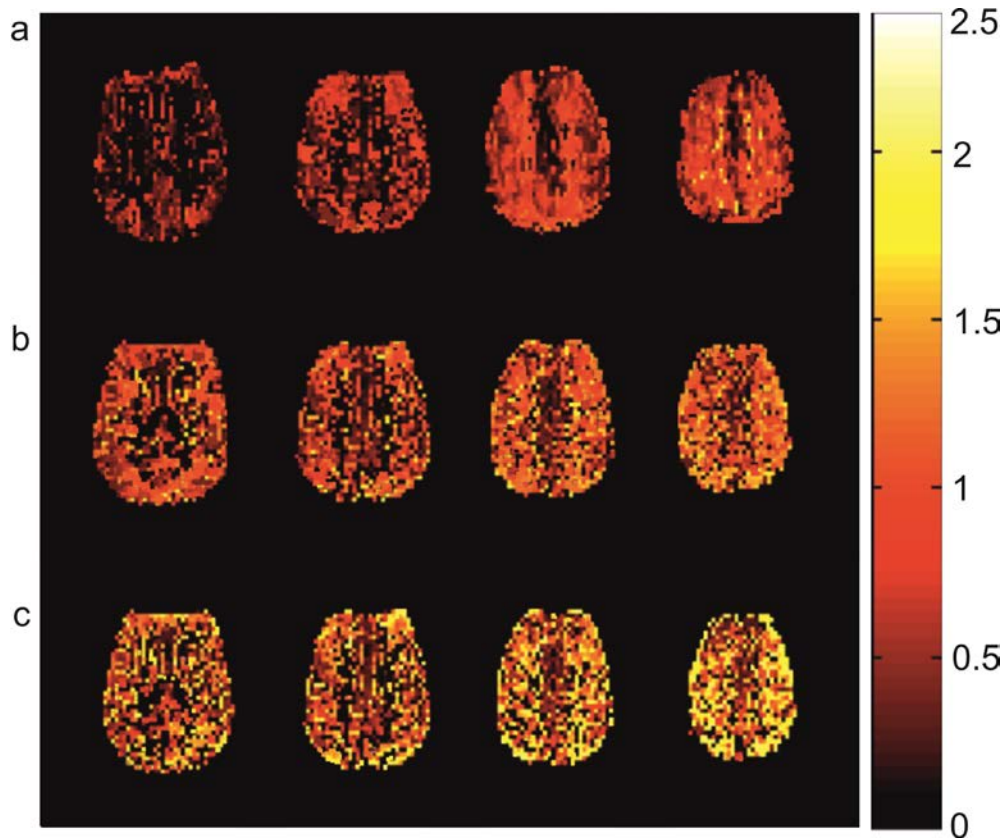
Figure 2.2. *Transit delay time maps of a representative subject calculated with the Hrabe model for **a)** PASL **b)** PCASL **c)** DC-CASL sequences. Slices were obtained in ascending order.*

A quantitative comparison of the effects of longer transit times on the magnetization dispersion is shown in Figure 2.3 (top row), where the fitted δt values from the Hrabe-Lewis model were plotted against the fitted σ values. There is a strong correlation between δt and σ with r=0.8 for PASL, r=0.94 for PCASL and r=0.93 for DC-CASL (r: Pearson correlation coefficient). The bottom row of Figure 2.3 compares the effect of increased σ on the ratio of CBF estimates from the Hrabe-Lewis and standard models for different ASL sequences. It is obvious that with increasing σ, the relative difference in CBF estimation between the Hrabe-Lewis and the standard model becomes higher.
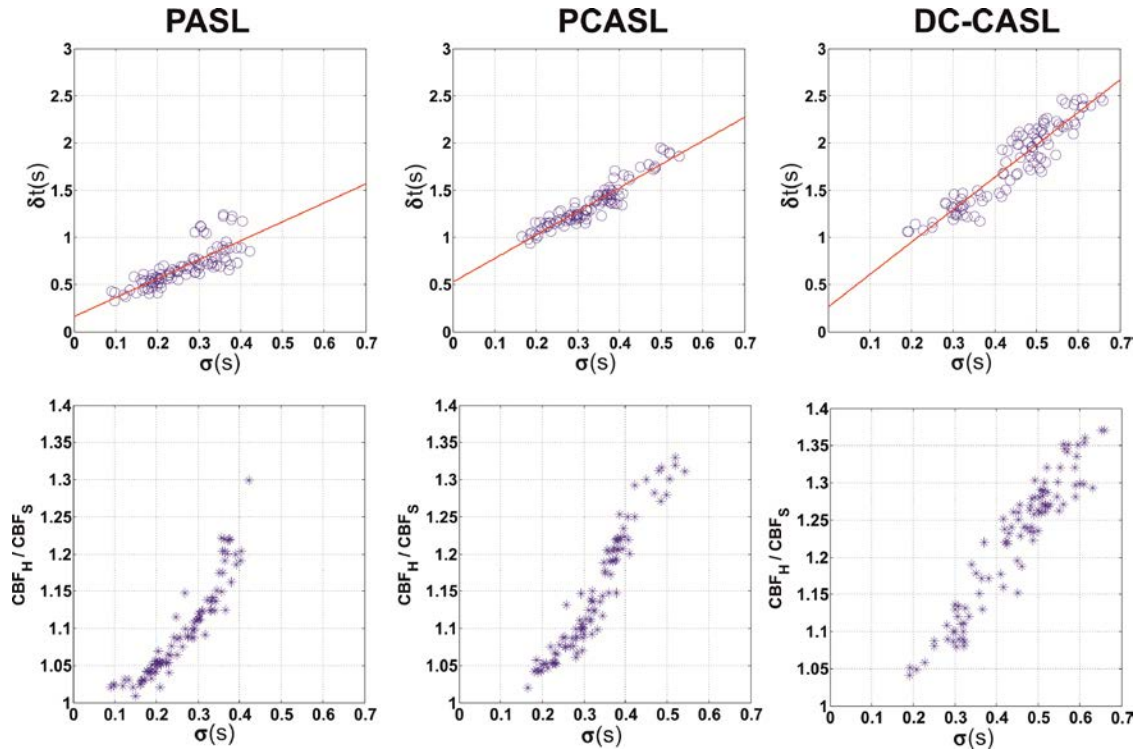
Figure 2.3. *Fitted δt versus σ values from the Hrabe model for all subjects, ROIs and slices for PASL, PCASL and DC-CASL. Solid lines show the linear regression fit (above). Relative differences between CBF estimates from Hrabe and standard model for all subjects, ROIs and slices for PASL, PCASL and DC-CASL (below).*

Figure 2.4 shows the effects of increased dispersion as a result of longer transit times on the accuracy of dynamic curve fits using the two different models. For PASL, σ is relatively small compared to the continuous ASL sequences as a result of the shorterδt, resulting in a close agreement of the two curves since both models converge. As σ increases for DC-CASL with longer transit time, the Hrabe-Lewis model exhibits a better fit to the data with a smoother dynamic curve resulting a higher CBF estimation. We found differences between the CBF estimates of the two models of up to 30% for PASL, 33% for PCASL and 37% for DC-CASL, depending on σ.
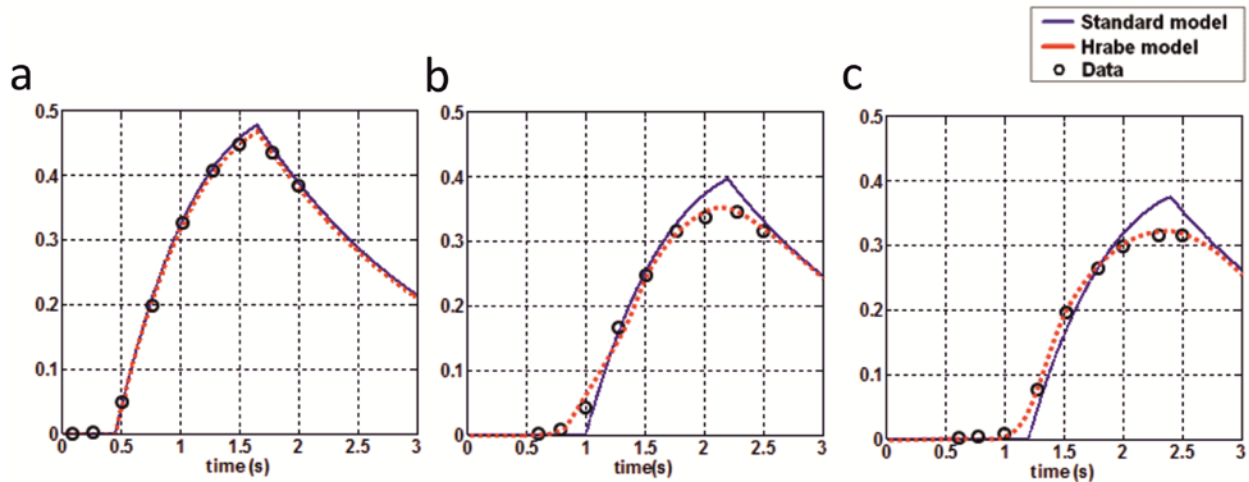
Figure 2.4. *Kinetic curves of a representative subject averaged in ROI2 (first slice) for a) PASL, b) PCASL, c)DC-CASL sequences from Hrabe model (dashed lines) and standard model (solid lines)*

Figure 2.5.a shows the regional variations of the fitted δt values obtained with different sequences for all subjects. It is obvious that transit delay times decrease from DC-CASL to PCASL and PASL. In addition, δt depends strongly on the ROI, with ROI4 and ROI5 showing highest and ROI2 lowest values. Those regional variations of δt are consistent for all sequences in all subjects. Figure 2.5.b shows the ROI-based comparison of the estimated CBF values obtained with different sequences for all subjects. ROI5, close to the PCA, has the highest CBF values, closely followed by ROI4 and ROI3, which are located near the MCA. ROI2, positioned close to the ACA, has the lowest CBF estimation. While the values found with DC-CASL seem to be slightly higher than those determined with PCASL and PASL for all ROIs, there is no significant difference between the CBF estimates of different sequences. The intra-subject variation of CBF (up to 80% for different subjects and sequences) is much higher than the inter-subject variation (8%-17% for different ROIs and sequences).
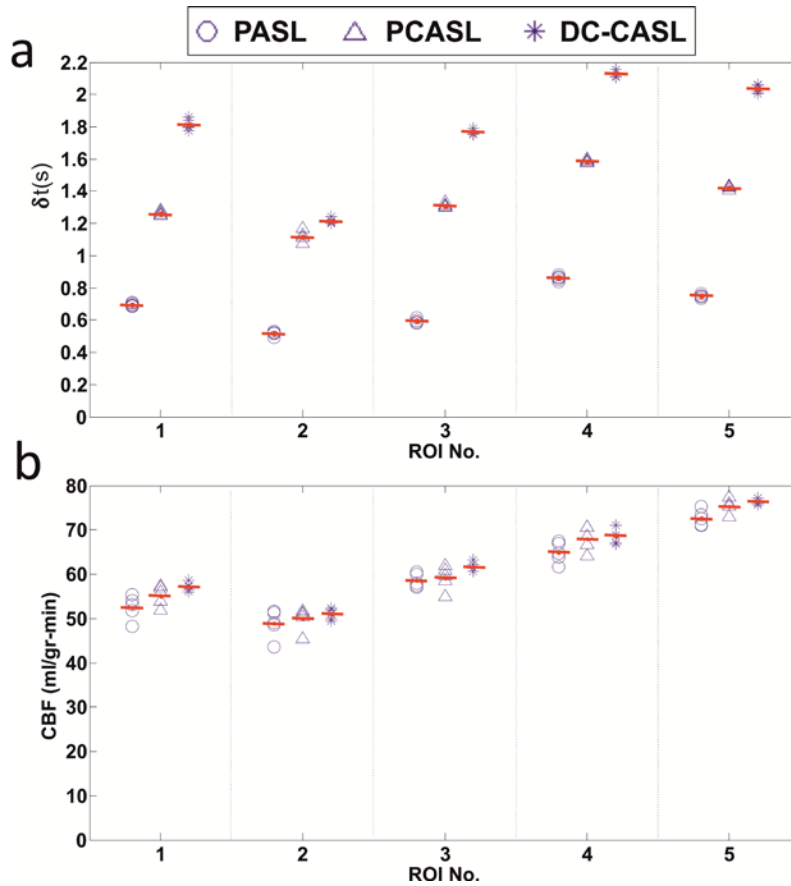
Figure 2.5. *ROI based comparison of **a)** δt values **b)** CBF values values estimated using the Hrabe model for PASL, PCASL and DCASL sequences for all subjects. Red bars shows the mean values across the five subjects.*

2.4 Discussion

The quantitative estimation of CBF from measured magnetization differences using ASL is highly dependent on the transit delay time (δt) [10-13]. Gallichan and Jezzard [17] previously examined its influence on the shape of the kinetic curve and perfusion estimate using pulsed ASL data and reported significant underestimation of CBF by the standard general kinetic model [4]. For continuous tagging schemes, the longer distance between the tagging and imaging planes is expected to lead to larger dispersion effects potentially amplifying the regional bias on the CBF estimation. Therefore, similar to multiple inversion time PASL experiments, a multiple PLD study is required to characterize the magnitude of these effects for continuous ASL for accurate perfusion estimation. In this study, we have investigated the regional effects of magnetization dispersion on quantitative perfusion

imaging for pulsed, pseudo-continuous and dual-coil arterial spin labeling encoding schemes. All of the implemented sequences generated excellent perfusion images with clear gray and white matter contrast (Figure 2.1.b). We put great effort in optimizing each of the implemented sequences to achieve the best possible SNR for a robust kinetic curves fit and perfusion estimation, although only relatively short tag durations were possible since we wanted to sample the beginning of the kinetic curve where the transit delay time information is logged. Hence, the specified tag durations that we used in this study are optimized for each sequence to obtain best possible SNR while still being able to sample early enough for ultimately yielding reliable transit delay time information. The experimental gray matter SNR of the perfusion images varies between DC-CASL ($\sim$10.5), PCASL ($\sim$9.5) and PASL ($\sim$5.7).

The transit delay time maps in Figure 2.2 show that δt varies across the brain and has higher values with increasing distance between tagging and imaging regions (distance increases either for ascending slices of the same sequence or for the same slice of different sequences). The expected effect of increased δt on the magnetization dispersion, characterized by σ, is confirmed by Figure 2.3 (top row). There is a strong correlation between δt and σ, which is in very good agreement with the results recently reported for PASL [17] and implies that the effect of magnetization dispersion is more pronounced for longer transit times simply because there is more time for dispersion to accrue. As a consequence of increasing σ, relative differences in CBF estimation between Hrabe-Lewis and standard model become higher (Figure 2.3, bottom row). The reason for the higher CBF estimates of the Hrabe-Lewis model and the increase in the ratio is explained in Figure 2.4. For PASL, where σ is relatively small, the kinetic curves obtained from the standard and the Hrabe-Lewis model converge, yielding almost equal CBF estimates, while for PCASL and DC-CASL the Hrabe-Lewis model fits better to the data, resulting in an increased difference in CBF estimates as a consequence of higher dispersion. Gallichan et al [17] previously explained the reason for the underestimation of CBF with the standard model based on the structure of the dynamic curve fit as an increase in σ reduces the peak of the curve in the Hrabe-Lewis model causing a smoother curve and a higher CBF estimate to fit the same data. Our findings for PCASL and DC-CASL (illustrated for a representative subject in Figure

2.4) are consistent with those previous reports and provide an extended view for longer transit times (larger dispersions).

In many studies, it has been reported that the statistical nature of the transit delay times changes with the varying path lengths and the velocities of the blood between the tagging and imaging regions [4, 10-12, 16]. Although absolute transit delay time is a function of the parameter set in ASL signal acquisition, the regional variation of δt across the brain should be consistent and independent from the sequence parameters [36]. Hence, the utility of investigating the ROI based variation of δt lies in comparing the estimated values across brain regions. Figure 2.5.a confirms what we expect from the arterial anatomy and is in agreement with previously reported δt distributions for PASL as shorter arrival times were found for the major branches of ACA [17, 33, 35, 36]. The higher values of δt with increased distance between the tagging and imaging region is clearer as DC-CASL has the highest δt in all ROIs. The order of the δt distribution among the ROIs is also almost same for all sequences where ROI2 has shortest δt and ROI4 has longest which is clear evidence that the structural pattern of transit time distribution is independent of signal acquisition parameters (i.e. tag duration, distance between the tagging and imaging region, encoding scheme). The regional variation of the CBF estimate using the Hrabe-Lewis model is interpreted in Figure 2.5.b. There is a significant (p < 0.01, two tailed t test) discrepancy between the perfusion of ROI5 close to the PCA and ROI2 close to ACA and the variation of CBF across the ROIs is consistent for different sequences. Similar to δt, the regional variation of CBF is also not affected by the differences in measurement methods. It is also clear that the inter-subject CBF variation is much lower compared to the intra-subject variation. We found 8%-17% inter-subject variability and up to 88% intra-subject variability. These are close to the previous values as 12%-22% for inter-subject and up to 100% intra-subject variability reported by Hetzer et al [37] in a CASL study using a shielded dual-loop resonator for labeling. In a recent study by Wang et al [38], who explored the regional reproducibility of CBF, reported 9.9%-16.8% inter-subject variation in CBF estimate based on different ROIs and more than 100% change in regional CBF values. The small discrepancy between those results and our findings could be explained by the different positions of ROIs and slices. There is also slight difference in the CBF estimates found with the different sequences, which may be due to the SNR differences of the

implemented sequences. Additional effects, like the reduced magnetization transfer in DC-CASL, the instabilities or eddy currents caused by the rapidly switched gradients in PCASL [18] as well as partial volume effects may cause these significant variations in the CBF estimates. To reduce the partial volume effects, scaling each voxel's CBF value with its corresponding gray matter weight could be a solution but this requires a very accurate registration of T1 weighted structural image with CBF weighted data which generally fails due to the voxel size difference and the inadequate contrast in CBF weighted image. Implementation of ASL sequences at ultra-high fields (above 7T) could provide high resolution perfusion maps (0.9x0.9x1.5 mm^3 voxel size at 7T [39]) thereby reducing the partial volume artifacts. Another factor likely to affect the regional CBF variation is T_1 for tissue which is assumed to have a single value in this study while it in fact varies across the brain.

Here, we performed a multi slice ASL study with EPI read-out with multiple inversion times imaging lasting in 41 min. Implementation of 3D read-out schemes and spiral trajectories could accelerate the data acquisition and shorten the echo time providing more robust protocols for clinical applications. Vessel-selective ASL implementations could improve the definition of ROIs by segmenting vascular territories and similarly velocity-selective ASL protocols could provide exploring the regional transit time distribution with respect to blood velocities.

In summary, we have investigated the regional effects of magnetization dispersion on quantitative perfusion imaging for varying distances between tagging and imaging regions by implementing pulsed, pseudo-continuous and dual-coil arterial spin labeling encoding schemes. The transit delay time variation across the brain regions is relatively independent of the measurement protocol and the dispersive effects become more pronounced for longer transit times. Using the standard model for perfusion quantification could cause a significant underestimation of CBF particularly for continuous tagging schemes, for which transit delay times are typically longer.

REFERENCES

1.   Williams, D.S., et al., *Magnetic resonance imaging of perfusion using spin-inversion of arterial water.* Proc. Natl. Acad. Sci. USA, 1992. **89**: p. 212-216.
2.   Detre, J.A., et al., *Perfusion imaging.* Magn. Reson. Med., 1992. **23**: p. 37-45.
3.   Roberts, D.A., et al., *Quantitative magnetic resonance imaging of human brain perfusion at 1.5T using steady-state inversion of arterial water.* Proc Nat Acad USA, 1994. **91**: p. 33-37.
4.   Buxton, R.B., et al., *A general kinetic model for quantitative perfusion imaging with arterial spin labeling.* Magn. Reson. Med., 1998. **40**: p. 383-396.
5.   Kim, S.-G., *Quantification of regional cerebral blood flow change by flow-sensitive alternating inversion recovery (FAIR) technique: application to functional mapping.* Magn. Reson. Med., 1995. **34**: p. 293-301.
6.   Wong, E.C., R.B. Buxton, and L.R. Frank, *Implementation of quantitative perfusion imaging techniques for functional brain mapping using pulsed arterial spin labeling.* NMR in Biomed, 1997. **10**: p. 237-249.
7.   Golay, X., et al., *Transfer insensitive labeling technique (TILT): application to multislice functional perfusion imaging.* J Magn Reson Imaging, 1999. **9**(3): p. 454-61.
8.   Wong, E.C., R.B. Buxton, and L.R. Frank, *Quantitative imaging of perfusion using a single subtraction (QUIPSS and QUIPSS II).* Magn. Reson. Med., 1998. **39**: p. 702-708.
9.   Helpern, J.A., et al., *Perfusion imaging by un-inverted flow-sensitive alternating inversion recovery (UNFAIR).* Magn Reson Imaging, 1997. **15**(2): p. 135-9.
10.   Lee, G.R., L. Hernandez-Garcia, and D.C. Noll, *Functional imaging with Turbo-CASL: transit time and multislice imaging considerations.* Magn Reson Med, 2007. **57**(4): p. 661-9.
11.   Gonzalez-At, J.B., D.C. Alsop, and J.A. Detre, *Cerebral perfusion and arterial transit time changes during task activation determined with continuous arterial spin labeling.* Magn Reson Med, 2000. **43**(5): p. 739-46.
12.   Yang, Y., et al., *Transit time, trailing time, and cerebral blood flow during brain activation: measurement using multislice, pulsed spin-labeling perfusion imaging.* Magn Reson Med, 2000. **44**(5): p. 680-5.
13.   Yang, Y., et al., *Multislice imaging of quantitative cerebral perfusion with pulsed arterial spin labeling.* Magn. Reson. Med., 1998. **39**: p. 825-832.
14.   Tortoli, P., et al., *Interaction between secondary velocities, flow pulsation and vessel morphology in the common carotid artery.* Ultrasound Med Biol, 2003. **29**(3): p. 407-15.
15.   Wu, W.C., Y. Mazaheri, and E.C. Wong, *The effects of flow dispersion and cardiac pulsation in arterial spin labeling.* IEEE Trans Med Imaging, 2007. **26**(1): p. 84-92.
16.   Hrabe, J. and D.P. Lewis, *Two analytical solutions for a model of pulsed arterial spin labeling with randomized blood arrival times.* J Magn Reson, 2004. **167**(1): p. 49-55.
17.   Gallichan, D. and P. Jezzard, *Variation in the shape of pulsed arterial spin labeling kinetic curves across the healthy human brain and its implications for CBF quantification.* Magn Reson Med, 2009. **61**(3): p. 686-95.
18.   Pohmann, R., et al., *Theoretical and experimental evaluation of continuous arterial spin labeling techniques.* Magn Reson Med, 2010. **63**(2): p. 438-46.
19.   Cavusoglu, M., et al., *Comparison of pulsed arterial spin labeling encoding schemes and absolute perfusion quantification.* Magn Reson Imaging, 2009. **27**(8): p. 1039-45.
20.   Lu, H., et al., *Determining the longitudinal relaxation time (T1) of blood at 3.0 Tesla.* Magn Reson Med, 2004. **52**(3): p. 679-82.
21.   Luh, W.M., et al., *QUIPSS II with thin-slice TI1 periodic saturation: a method for improving accuracy of quantitative perfusion imaging using pulsed arterial spin labeling.* Magn Reson Med, 1999. **41**(6): p. 1246-54.

22.   Wong, E.C., *Vessel-encoded arterial spin-labeling using pseudocontinuous tagging.* Magn Reson Med, 2007. **58**(6): p. 1086-91.
23.   Wu, W.C., et al., *A theoretical and experimental investigation of the tagging efficiency of pseudocontinuous arterial spin labeling.* Magn Reson Med, 2007. **58**(5): p. 1020-7.
24.   Dai, W., et al., *Continuous flow-driven inversion for arterial spin labeling using pulsed radio frequency and gradient fields.* Magn Reson Med, 2008. **60**(6): p. 1488-97.
25.   Zaharchuk, G., et al., *Multislice perfusion and perfusion territory imaging in humans with separate label and image coils.* Magn Reson Med, 1999. **41**(6): p. 1093-8.
26.   Mildner, T., et al., *Functional perfusion imaging using continuous arterial spin labeling with separate labeling and imaging coils at 3 T.* Magn Reson Med, 2003. **49**(5): p. 791-5.
27.   Wong, E.C., L.R. Frank, and R.B. Buxton. *QUIPSS II: a method for improved quantitation of perfusion using pulsed arterial spin labeling*. in *Fifth Meeting, International Society for Magnetic Resonance in Medicine*. 1997. Vancouver.
28.   Wong, E.C., L.R. Frank, and R.B. Buxton. *Quantitative multislice perfusion imaging using QUIPSS II, EPISTAR, FAIR, and PICORE*. in *Fifth Meeting, International Society for Magnetic Resonance in Medicine*. 1997. Vancouver.
29.   Yongbi, M.N., C.A. Branch, and J.A. Helpern, *Perfusion imaging using FOCI RF pulses.* Magn. Reson. Med., 1998. **40**: p. 938-943.
30.   Smith, S.M., et al., *Advances in functional and structural MR image analysis and implementation as FSL.* Neuroimage, 2004. **23 Suppl 1**: p. S208-19.
31.   Jenkinson, M., et al., *Improved optimization for the robust and accurate linear registration and motion correction of brain images.* Neuroimage, 2002. **17**(2): p. 825-41.
32.   Liu, T.T. and E.C. Wong, *A signal processing model for arterial spin labeling functional MRI.* Neuroimage, 2005. **24**(1): p. 207-15.
33.   van Laar, P.J., et al., *In vivo flow territory mapping of major brain feeding arteries.* Neuroimage, 2006. **29**(1): p. 136-44.
34.   Tatu, L., et al., *Arterial territories of the human brain: cerebral hemispheres.* Neurology, 1998. **50**(6): p. 1699-708.
35.   Duvernoy, H.M., *The human brain: surface, three-dimensional sectional anatomy with MRI and blood supply*1999, Wien NewYork: Springer-Verlag
36.   MacIntosh, B.J., et al., *Assessment of arterial arrival times derived from multiple inversion time pulsed arterial spin labeling MRI.* Magn Reson Med. **63**(3): p. 641-7.
37.   Hetzer, S., et al., *Shielded dual-loop resonator for arterial spin labeling at the neck.* J Magn Reson Imaging, 2009. **29**(6): p. 1414-24.
38.   Wang, Y., et al., *Regional reproducibility of pulsed arterial spin labeling perfusion imaging at 3T.* Neuroimage. **54**(2): p. 1188-95.
39.   Pfeuffer, J., et al., *Perfusion-based high-resolution functional imaging in the human brain at 7 Tesla.* Magn Reson Med, 2002. **47**(5): p. 903-11.

Chapter 3

Comparison of PASL encoding schemes and absolute perfusion quantification

Overview

Arterial spin labeling (ASL) using MRI is a powerful non-invasive technique to investigate the physiological status of brain tissue by measuring cerebral blood flow (CBF). ASL assesses the inflow of magnetically labeled arterial blood into an imaging voxel. In the last two decades, various ASL sequences have been proposed which differ in their ease of implementation and their sensitivity to artifacts. In addition, several quantification methods have been developed to determine the absolute value of CBF from ASL magnetization difference images. In this study, we evaluated three pulsed ASL sequences and three absolute quantification schemes. It was found that FAIR-QUIPSSII implementation of ASL yields 10-20% higher SNR and 15% higher CBF as compared with PICORE-Q2TIPS (with FOCI pulses) and PICORE-QUIPSSII (with BASSI pulses). In addition, quantification schemes employed can give rise to up to a 35% difference in CBF values. We conclude that, although all quantitative ASL sequences and CBF calibration methods should in principle result in the similar CBF values and image quality, substantial differences in CBF values and SNR were found. Thus, comparing studies using different ASL sequences and analysis algorithms is likely to result in erroneous intra- and inter-group differences. Therefore, i) the same quantification schemes should consistently be used and ii) quantification using local tissue proton density should yield the most accurate CBF values because, although still requiring definitive demonstration in future studies, the proton density of blood is assumed to be very similar to the value of gray matter.

3.1 Introduction

Arterial Spin Labeling (ASL) is a non-invasive magnetic resonance imaging (MRI) technique that provides quantitative information about local tissue perfusion by assessing the inflow of magnetically tagged arterial water into an imaging slice. Cerebral blood flow (CBF) is determined from the signal intensity differences of the MR images with and without tagging, thereby subtracting out the static magnetization of the imaging slice [1, 2]. ASL has the potential to be very useful for clinical applications and has been used, for example, in vascular and neuronal diseases such as stroke, arteriostenosis, schizophrenia, Alzheimer´s, epilepsy etc. [3, 4]. Moreover, ASL is a powerful tool to study the baseline physiological state of brain tissue and the basis of blood oxygenation level-dependent (BOLD) signals [5].

A number of ASL techniques have been developed, which can be broadly divided into continuous and pulsed tagging techniques. In the latter, inversion is done with a slice-selective or non-slice-selective 180° pulse, and with continuous labeling the inversion is done adiabatically as the blood moves through a gradient field during a continuous RF pulse [1, 2]. Ideally, CBF is proportional to the ASL difference signal (control–tag image). However, several confounding factors have been reported that complicate the calculation of a quantitative CBF map. The major systematic error is caused by transit delay artifacts from the intravascular tagged blood [6-12]. Large amplitude blood vessel artifacts may appear due to the presence of tagged blood flowing through the imaging slice decicated to perfuse other slices. These systematic errors can be minimized if a delay is introduced between the tagging and image acquisition longer than the longest transit time of blood from the arteries to the capillaries.

In addition, artifacts stemming from how blood water is magnetically labeled and the control images acquired, such as magnetization transfer (MT) effects, yield false estimates of absolute CBF [11, 13]. To control for these effects, different pulsed ASL (PASL) sequences have been proposed. These methods vary in their tagging schemes, their sensitivity to the blood entering from the distal side of the slice and the type of applied inversion pulses. Here, we evaluated SNR and magnetization difference of three widely used PASL sequences.

a) "Q2TIPS": PICORE labeling scheme (proximal inversion with a control for off-resonance effects) using a FOCI pulse with Q2TIPS (QUIPSS-II with thin-slice TI1 periodic saturation) [14].

b) "FAIR-QII": FAIR (Flow alternated inversion recovery) combined with QUIPSS-II saturation using a hyperbolic secant (HS) pulse for inversion [15].

c) "BASSI-QII": PICORE labeling scheme (using asymmetric BASSI pulses) with QUIPSS-II saturation [16].

Furthermore, to quantify absolute CBF, it is necessary to determine the equilibrium magnetization of blood: M_{0B}. Since M_{0B} cannot easily be determined in vivo, its value is usually computed using magnetization M_0 either of local tissue, white matter or CSF. In principle, all ASL sequences and quantification schemes should yield the same absolute CBF values. In the present study, the absolute CBF values for gray matter obtained using the methods described above are within the physiologically plausible range: 54-80 ml/g-min. However, the PASL sequences used resulted in ~18% different absolute CBF values. In addition, a higher SNR for FAIR-QII compared to the two other ASL schemes (10-20% higher SNR) was found. Furthermore, substituting M_{0B} of blood with M_0 values from white matter, local tissue and CSF can give rise to up to ~35% different absolute CBF values. That is, the different ASL and quantification schemes tested do not result in the same image quality and absolute CBF although the values for CBF and SNR are comparable in magnitude.

3.2 Methods

3.2.1 PASL sequences and tagging profiles

Three different PASL sequences were investigated: a) "Q2TIPS": PICORE-Q2TIPS using a FOCI pulse [10] for inversion, b) "FAIR-QII": FAIR-QUIPSS II using a hyperbolic secant (HS) pulse for inversion and c) "BASSI-QII": PICORE-QUIPSSII using asymmetric BASSI pulses for inversion and saturation. Although these PASL sequences differ regarding how they acquire tagged and control images, the difference image for all of them should simply be proportional to CBF.

In the PICORE method ('proximal inversion with a control for off-resonance effects'), a slab selective inversion is applied just beneath the imaging slice. In the control condition, an off-resonance inversion pulse without any spatial encoding gradient is utilized. Hereby, to create the same magnetization transfer effect in the imaging slice as during the tag condition, the frequency offset of the pulse has to be matched to the frequency that the slice experienced during the tag condition. In the FAIR method ('Flow sensitive Alternating Inversion Recovery'), an inversion pulse without (or with a very small) slab selective gradient is used, labeling all protons in the whole volume [17]. In contrast, under the control condition, an inversion pulse is directed only to the imaging slice.

The QUIPSS II saturation module for a PASL sequence was introduced by Wong et al. and stands for 'Quantitative Imaging of Perfusion Using a Single Subtraction' [18]. It uses saturation RF pulses at the end of the tagging period to control the bolus duration. Q2TIPS is the modified version of the QUIPSS II to eliminate the residual errors remaining due to incomplete saturation of the spins using QUIPSS II and to minimize the spatial mismatch of the saturation and inversion slabs [14]. In the present study, the PICORE-QUIPSS II implementation additionally applies asymmetric BASSI ('Bandwidth-modulated selective saturation and inversion') pulses recently introduced by Warnking et al. [16]. BASSI utilizes frequency- and gradient-modulated radiofrequency (RF) pulses by changing the bandwidth parameter temporally, thereby increasing the selectivity of the tagged region in addition to minimizing the RF energy.

3.2.2 Absolute quantification of CBF

In these PASL sequence implementations, bolus width TI_1 is well defined and can be set by the user. The ASL difference signal (control-tag) can be made independent from the transit delay δt (time required for the tag to reach the imaging slice) by setting the image acquisition time $TI_2 \geq TI_1 + \delta t$ [10]. Then, the signal is given by

$$\Delta M = 2 \cdot M_{0B} \cdot f \cdot TI_1 \cdot e^{-TI_2/T_{1B}} \qquad\qquad [3.1]$$

where M_{0B} is fully relaxed longitudinal magnetization of arterial blood, f the CBF (ml/g-min), and T_{1B} the T_1 of blood [11]. T_{1B} is a global parameter depending only on the properties of blood; for 3T, it has been determined to be 1684 ms [19].

3.2.3 Blood equilibrium magnetization

The ASL subtraction image (control-tag) is a map of the relative perfusion. In order to determine the absolute value of local CBF, the value of M_{0B} has to be known [10, 12]. Voxels only filled with blood are typically not measured since the standard spatial resolution of 3-4 mm³ is not enough to image an artery without any partial volume effect. Thus, different methods have been proposed to substitute the global parameter M_{0B} with M_0 values of 1) white matter, 2) CSF and 3) local tissue.

The magnitude of the fully relaxed MRI signal M_0 can be obtained from a single shot EPI image with an infinite pulse repetition time $(TR = \infty)$. This value has to be corrected for the different proton density and relaxation rate of the blood compared to the values of white matter, CSF or local tissue:

$$M_{0B} = R_i \cdot M_{0i} \cdot e^{(1/T_{2i}^* - 1/T_2^*) \cdot TE}$$ [3.2]

The index i specifies the tissue type used for calculating M_{0B} (i.e., i = white matter (method 1), CSF (method 2) or local tissue (method 3)) (see Figure 3.2.a). *R* is the signal ratio of the tissue type used to blood from a proton density-weighted image. T_2^* is the transverse relaxation time with which the tagged protons relax during image acquisition. That is, T_2^* of blood and/or gray matter has to be inserted depending on how much the tagged protons have exchanged into the gray matter. In the following calculations, we use the relaxation time of blood T_{2B}^* value. T_{2B}^* is difficult to measure *in vivo*. Thus, analytical expression for T_{2B}^* as a function of oxygenation given by Zhao et al. was utilized, yielding a value of 43.6 ms for 77.5% of blood oxygenation which corresponds approximately to the oxygenation level in the capillaries [20].

Method 1: Wong et al. used the white matter (WM) signal M_{0WM} to estimate M_{0B} [10]. R_{WM} has been determined to be 1.06 in the sagittal sinus [14, 18]. However, recent data indicate a higher value of 1.19 which we employed in the following calculations [21]. We measured the transverse relaxation time T_{2WM}^* value as 44.7 ms for WM (Figure 3.1).
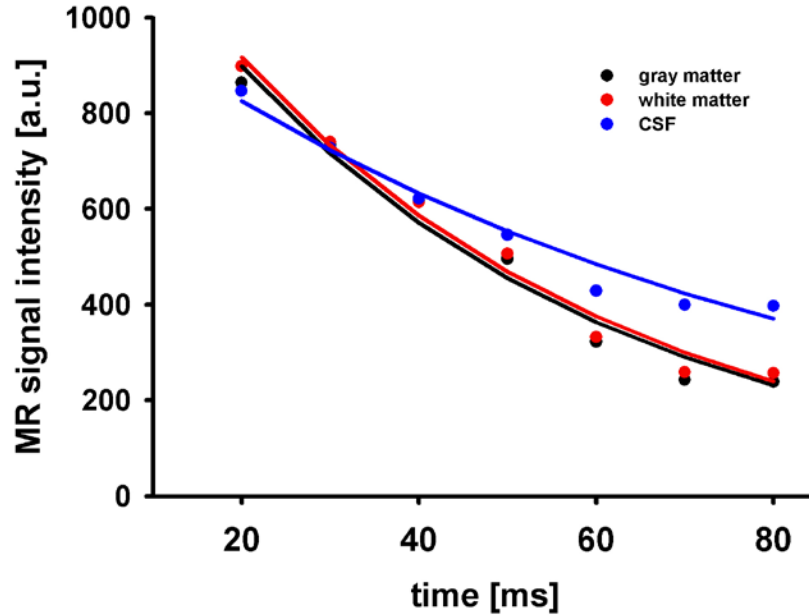
Figure 3.1 *Experimental transversal relaxation curves for gray matter, white matter and CSF. They can all be fitted by a mono-exponential decay function resulting in: $T_{2GM}^* = 44.2$ ms, $T_{2WM}^* = 44.7$ ms and $T_{2CSF}^* = 74.9$ ms. (Root mean square error (RMSE) values of the fits for GM=39.34, WM=32.68 and CSF=36.11)*

Method 2: Because CSF consists mostly of water, it is usually believed that the proton density resembles M_{0B} of the blood. However, again as reported by Donahue and colleagues, the blood proton density is in fact not equal to that of CSF, possibly because blood includes many different molecules not present in the CSF. We took the value for R from Donahue et al. and measured T_{2CSF}^* (Figure 3.1) obtaining 0.87 and 74.90 ms, respectively.

Method 3: The most widely used approach to estimate the M_{0B} is scaling the local tissue equilibrium magnetization with the blood brain partition coefficient λ' that is $\lambda' = M_{0T} / M_{0B}$ [12, 22]. This is equivalent to the equation where the transversal relaxation rate for blood is equal to the value for gray matter, which is true for 1.5T and 3T. In the current study, the values for gray matter proton density and relaxation rate are taken from the studies of Donahue et al. and Uludag et al., namely, $R = 0.98$ and $T_{2GM}^* = 44.2$ ms, respectively [21, 23]. Note that in contrast to Methods 1 and 2, this method uses voxel-specific local values of M_{0T} instead of the global scaling value of M_{0B}. This error, however, corrects automatically for the spatial sensitivity profile of the imaging coil.

Note that the parameters R and T_2* for the three quantification methods are different than typically used in ASL studies. In addition, in many studies, the relaxation rate of either arterial blood or tissue is utilized instead of that of capillary blood used in the current study.

3.2.4 Data Acquisition

MR images were acquired on a 3T Siemens Tim Trio scanner using a 12-channel head coil (Siemens, Erlangen, Germany). 12 healthy human subjects were scanned using identical sequence parameters: TE = 13 ms; TR = 2500 ms; tagging duration TI1 = 700 ms; time for periodic saturation pulses to define bolus duration TI1s = 900 ms (see [14] for details); starting time of EPI read-out TI2 = 1400 ms; voxel size 3.5x3.5x3 mm^3; FOV = 224 mm; FA=90º, EPI module for read-out. A total of 4 slices with slice thickness of 3 mm were obtained in ascending slice order. The tag was 10 cm in width positioned at a 1 cm gap to the imaging slices. Two presaturation pulses were applied in the imaging planes immediately before the inversion tag to minimize the impact of the static tissue. In the PICORE sequences (Q2TIPS and BASSI-QII) a 20 mm thick saturation slab was repeatedly applied for the bolus cut-off. In the FAIR sequence an inferior as well as a superior saturation slab outside the slices was applied. Each PASL run consisted of 156 frames resulting in total time of a run of 390 s. The same sequences are used to determine the equilibrium magnetization. The same sequence parameters as above were used except that

TR and TI2 were chosen to be 10 s and 4 s, respectively, in order to allow for T1 recovery and avoid saturation effects.

3.2.5 Correcting for Spatial Sensitivity of the RF Coil

Because the sensitivity of the RF head coil is subject to spatial variation, coil inhomogeneity also has to be taken into account for an accurate quantification of CBF. According to eq.[3.1], f is proportional to the $\Delta M / M_{0B}$ and in general this ratio can be expressed by considering the coil homogeneity as

$$\frac{\Delta M_{ap}}{M_{0B,ap}} = \frac{\Delta M \cdot C}{M_{0B} \cdot C_{method}}$$

[3.3]

where C represents the coil sensitivity and the index ap is the apparent measured value of the magnetizations. Provided that the head is in the same location, the coil sensitivities in method 3 (local tissue) are the same for ΔM and M_{0B} measurements and cancel out. In other words, since M_{0B} in method 3 intrinsically carries the spatial sensitivity of the coil, there is no need for an extra correction for coil inhomogeneity.

In methods 1 and 2, M_{0B} is a global value computed in a specific ROI of WM or CSF. Because the coil sensitivity of this specific ROI does not match with all of the other regions of the brain, the C values in equation 3 are different and do not cancel out. Hence, the ΔM and M_{0B} images have to be separately corrected with the corresponding coil sensitivity maps. We first obtained the coil sensitivity image using a standard field map MRI sequence and normalized this image such that the maximum value is set to one. The range of the resulting coil sensitivity values for the head coil used is 0.91-1.08. Then the apparent ΔM image was divided with the corresponding normalized coil sensitivity values and the M_{0B} value was divided by the average coil sensitivity within the ROI. In the following, the results will be given after normalization with the coil sensitivity maps.

3.2.6 Data Analysis

FSL software (http://www.fmrib.ox.ac.uk/fsl), self-written MATLAB (The Mathworks, Natick, MA, USA) and Linux shell script routines were used for data analysis [24]. Time

courses of all voxels were motion-corrected utilizing the MCFLIRT module [25] of FSL using the mean volume of the corresponding run as reference. The images obtained of all PASL sequences were co-registered. CBF time series were created by calculating control-tag difference images using surround subtraction (i.e. computing the difference between each image and the average of its two nearest neighbors) thereby reducing BOLD signal contamination of the CBF time course [10].

The difference images were thresholded to obtain the gray matter voxels (see Figure 3.2.b). Only the voxels passing the threshold in the images acquired with all 3 different ASL sequences were included in the subsequent analysis. The middle two slices were used for all experiments. For each PASL sequence, SNR (mean/standard deviation over time) was computed for the CBF time series of all gray matter voxels. In addition, temporal SNR was also calculated for control and tag time series separately.

a   b   c
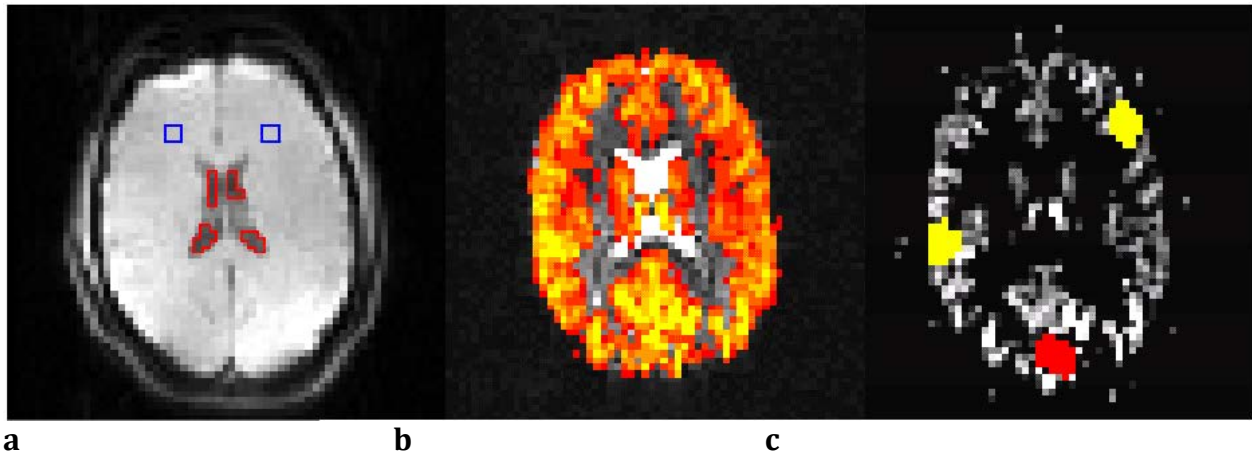
Figure 3.2. a) *WM (blue) and CSF (red) ROIs* *b)* *ASL difference image superimposed on a single shot EPI image (TR = 3800 ms, TE = 102 ms) to identify the CSF, GM and WM regions for creating the corresponding ROIs accurately (i.e. CSF is bright without any perfusion and GM has higher perfusion than WM)* *c)* *GM (yellow) and visual cortex (VC) ROIs drawn on a thresholded ASL difference image.*

The average absolute CBF (mL/g-min) values were calculated for three ROIs (see Figure 3.2c). Because functional runs of all experiments were co-registered, selecting an ROI ensures that same voxels were chosen in all functional runs both in the calculation of M_{0B} and the absolute CBF.

3.3 Results

Figure 3.3 shows the control, tag and averaged perfusion images of a representative subject for the three PASL sequences. Although generally very similar in appearance, well-known residual artifacts that are different between the sequences are present. As an example, a large vein located along the midline in the posterior occipital lobe (indicated by a red circle in Figure 3.3) appears bright (positive signal) in the second image while it is dark (no signal) in the first and third images. This is because the FAIR tagging also labels venous blood flowing in a superior-to-inferior direction.
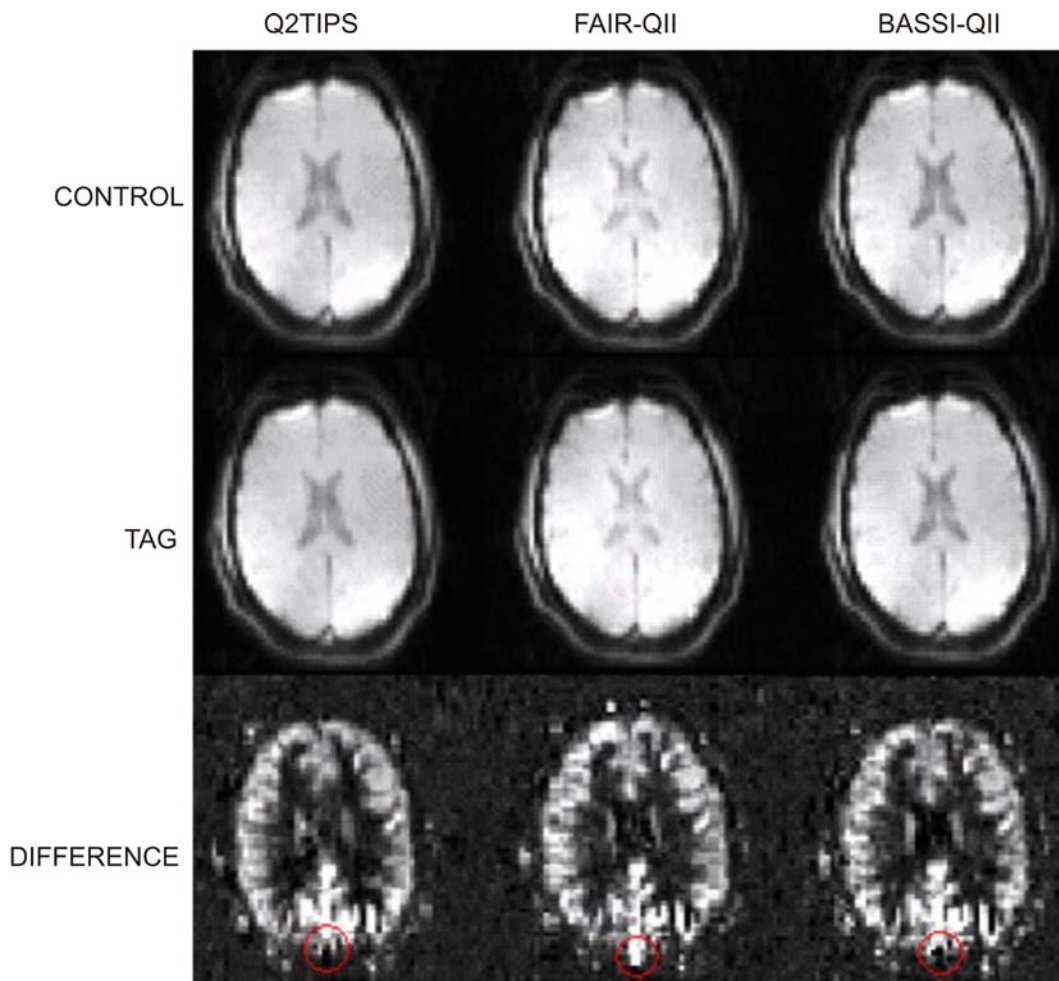
Figure 3.3. *Control (top), tag (middle) and subtraction (bottom) images of a representative subject acquired using Q2TIPS (first column), FAIR-QII (second column) or BASSI-QII (third column).*

The average SNR of the ASL difference signals of all 12 subjects are shown in Table 3.1.a. FAIR-QII has the highest average SNR and Q2TIPS the lowest, being ~20% lower than FAIR-QII. To investigate the cause underlying the different noise levels, temporal SNR for control and tag images were also determined separately, as shown in Table 3.1.b. The average noise (N=12) is lower in FAIR-QII both in tag and control experiments. In addition, control images have lower SNR levels than tag images.

Table 3.1.a Average SNR of the ASL difference signals for different PASL sequences.

Subject	Q2TIPS	FAIR-QII	BASSI-QII
1	1.54	2.08	1.95
2	1.82	2.33	2.03
3	1.69	2.31	2.14
4	1.64	1.81	1.64
5	1.53	1.69	1.4
6	1.6	1.94	1.81
7	1.37	1.87	1.65
8	1.64	1.74	1.68
9	1.6	2.13	1.93
10	1.63	2.15	1.9
11	2.22	2.07	1.96
12	1.93	1.73	1.57
Mean ± std	1.68±0.22	1.99±0.22	1.81±0.22

Table 3.1.b Average temporal noise levels (standard-deviation of the time series) (N=12) for control and tag

Experiment	Q2TIPS	FAIR-QII	BASSI-QII
Control	0.93	0.8	0.88
Tag	1.03	0.9	1.01

The average M_{0B} values (N=12) calculated using the three different methods described above are given in Table 3.2 for all sequences. The equilibrium magnetization obtained using local tissue (LT) values is higher than the values calculated with the other two

methods. As expected, there are no significant differences between the M_{0B} values obtained by the different PASL sequences.

Table 3.2 Average M_{0B} values calculated with different methods [a.u.].

Sequence	Method1 (WM)	Method2 (CSF)	Method3 (LT)
Q2TIPS	1599±89	1377±74	1872±152
FAIR-QII	1595±85	1378±73	1854±133
QII-BASSI	1588±78	1369±64	1864±147

The average absolute CBF values (ml/g-min) of all subjects computed for 3 ROIs are shown in Table 3.3. For this, method 3 was used to compute the equilibrium magnetization for absolute quantification. FAIR-QII can yield up to 18% higher absolute CBF values compared to the two other PASL sequences. Both in the gray matter and visual cortex, the difference between FAIR-QII and Q2TIPS is statistically significant (p=[0.005-0.011], one way repeated measurement ANOVA test) while the difference between FAIR-QII and BASSI-QII is not (p=[0.062-0.074]). As has been shown in other studies, the visual cortex has ~25% higher CBF than the other gray matter ROIs examined.

Table 3.3 Average (n=12) absolute CBF in ml/g-min values computed for 3 different ROIs (see Figure 3.1). Method 3 (Local tissue) is used to calculate the M_{0B}.

Sequence	ROI1	ROI2	ROI3
Q2TIPS	51.84±10.33	53.45±11.93	67.14±12.38
FAIR-QII	59.72±8.72	62.99±10.30	76.07±11.95
BASSI	56.73±12.15	59.10±11.38	70.11±12.69

3.4 Discussion

Arterial spin labeling (ASL) MRI is a non-invasive alternative to contrast-agent administration to assess cerebral blood flow (CBF) [26]. CBF is determined by measuring magnetization differences occurring in an imaging slice after labeling inflowing arterial blood. Over the last two decades, various ASL sequences have been developed which differ

in their ease of hard- and software implementation, sensitivity to physiological noise and sequence imperfections and artifacts. In principle, all quantitative ASL sequences should yield the same absolute CBF values. In this study, we examined the characteristics of three widely used pulsed ASL sequences: a) PICORE-Q2TIPS (FOCI), b) FAIR-QUIPSS II (HS), and c) PICORE-QUIPSS II (asymmetric BASSI).

It was found that FAIR-QII yields ~18% higher absolute CBF values than the two other ASL schemes (Table 3.3). There are several possible reasons for this observation: The sequences differ in their tagging profiles and how control images are acquired. In the FAIR tagging scheme, venous blood superior to the imaging slice is also tagged, although there is no venous blood contamination for whole brain coverage. For the typical parameters used in human functional ASL studies, part of the venous blood might not have been carried out of the imaged volume as shown in the venous artifacts in Figure 3.3. This causes an erroneous overestimation of perfusion [14]. This effect might also be the cause of the higher SNR of FAIR-QII compared to the other ASL schemes. For whole brain ASL imaging, however, this FAIR sequence artifact might be reduced.

In addition, to elaborate on the cause of the SNR values of the PASL sequences, SNR has been separately determined for control and tagged images. It was found that FAIR-QII also had lower noise levels both for tag and control images (Table 3.1.b). Due to the fact that the timing parameters of all sequences are identical, the sensitivity to physiological noise (e.g. cardiac pulsation and respiration) should also be identical. Thus, the likely reason for the lower noise is the remaining magnetization transfer effects in the PICORE tagging scheme. Clearly, more work is required to determine why PASL sequences with identical parameters vary in noise and CBF levels.

In addition, substituting M_{0B} of blood with other values that can be measured more easily gives rise to different absolute CBF values. The M_{0B} value calculated from magnetization of local tissue resulted in the highest CBF values; when calculated from magnetization of CSF, it resulted in the lowest CBF values (~35% lower than the local tissue-method). This result is quite surprising as in all methods the values for proton density, relaxation rate and coil inhomogeneity were corrected and, thus, should result in the same CBF values. As the

relaxation rates were measured in the ASL experiments presented in this study, this discrepancy can only be resolved by assuming other proton density values. As a recommendation, i) the same quantification schemes should consistently be used in order to avoid erroneous intra- and inter-subject CBF differences and ii) due to the fact that the proton density of blood is thought to be very similar to the value of gray matter, quantification method 3 should yield the most accurate CBF values. However, this has to be proven in future studies.

Note that the parameters *R* and *T2** in the three quantification methods are different from those typically employed in ASL studies. We have derived these parameters from the latest results on the proton density of the various tissue types as reported by Donahue et al. and from the integrative model of Uludag et al. summarizing the transverse relaxation rates found experimentally [21, 23]. In addition, in many studies, the relaxation rate of either arterial blood or tissue instead of capillary blood is utilized. The correct choice depends, however, on where the tagged blood is located when a particular slice is imaged. For the ASL parameters used in this study, most of the tagged arterial blood is delivered to the capillaries and only part of it exchanged to the tissue. That is, most of the blood relaxes with the transversal relaxation time of the capillary and part of it with that of tissue. As shown by Buxton, for typical parameters of human ASL studies, the error introduced by using only one single relaxation rate is small [27]. For example, if half of the blood has already exchanged to tissue and given the relaxation rates above, the error is only 5% at 3T. Using the relaxation rate of arterial or capillary blood also results in a small error of ~13% at 3T. However, at higher field strengths, for which the relaxation rate of blood differs substantially from the value of the tissue, the error might be considerably larger and thus knowledge of the tissue exchange time more important. Many of these potential errors originating from the *T2** uncertainties can be minimized with spiral trajectory k-space coverage and other short TE methods.

In summary, methods to quantify absolute CBF values and different PASL sequences in terms of their SNR have been evaluated. We showed that CBF values vary up to ~18% for the PASL sequences and up to ~35% for the quantification methods examined. The FAIR-QII sequence yielded the highest calculated CBF values and SNR possibly due to residual

tagged venous blood in the imaged volume. Thus, care has to be taken to ensure that the same sequence parameters and quantification schemes are used to determine inter- and intra-subject differences using ASL. This is of special importance if the physiological status of brain tissue is assessed with CBF in patients compared to healthy subjects.

REFERENCES

1.   Williams, D.S., et al., *Magnetic resonance imaging of perfusion using spin-inversion of arterial water.* Proc. Natl. Acad. Sci. USA, 1992. **89**: p. 212-216.
2.   Detre, J.A., et al., *Perfusion imaging.* Magn. Reson. Med., 1992. **23**: p. 37-45.
3.   Detre, J.A., et al., *Noninvasive MRI evaluation of cerebral blood flow in cerebrovascular disease.* Neurology, 1998. **50**(3): p. 633-41.
4.   Chalela, J.A., et al., *Magnetic resonance perfusion imaging in acute ischemic stroke using continuous arterial spin labeling.* Stroke, 2000. **31**(3): p. 680-7.
5.   Behzadi, Y., et al., *A component based noise correction method (CompCor) for BOLD and perfusion based fMRI.* Neuroimage, 2007. **37**(1): p. 90-101.
6.   Alsop, D.C. and J.A. Detre, *Reduced transit-time sensitivity in noninvasive magnetic resonance imaging of human cerebral blood flow.* J Cereb Blood Flow and Metab, 1996. **16**: p. 1236-1249.
7.   Kim, S.-G. and N.V. Tsekos, *Perfusion imaging by a flow-sensitive alternating inversion recovery (FAIR) technique: application to functional brain imaging.* Magn. Reson. Med., 1997. **37**: p. 425-435.
8.   Kim, S.-G., *Quantification of regional cerebral blood flow change by flow-sensitive alternating inversion recovery (FAIR) technique: application to functional mapping.* Magn. Reson. Med., 1995. **34**: p. 293-301.
9.   Edelman, R.R., et al., *Noninvasive mapping of cerebral perfusion by using EPISTAR MR angiography.* JMRI, 1994. **4(P), [Abstr.]**: p. 68.
10.   Wong, E.C., R.B. Buxton, and L.R. Frank, *Implementation of quantitative perfusion imaging techniques for functional brain mapping using pulsed arterial spin labeling.* NMR in Biomed, 1997. **10**: p. 237-249.
11.   Wong, E.C., R.B. Buxton, and L.R. Frank, *A theoretical and experimental comparison of continuous and pulsed arterial spin labeling techniques for quantitative perfusion imaging.* Magn. Reson. Med., 1998. **40**: p. 348-355.
12.   Buxton, R.B., et al., *A general kinetic model for quantitative perfusion imaging with arterial spin labeling.* Magn. Reson. Med., 1998. **40**: p. 383-396.
13.   Wong, E.C., *Quantifying CBF with pulsed ASL: technical and pulse sequence factors.* J Magn Reson Imaging, 2005. **22**(6): p. 727-31.
14.   Luh, W.M., et al., *QUIPSS II with thin-slice TI1 periodic saturation: a method for improving accuracy of quantitative perfusion imaging using pulsed arterial spin labeling.* Magn Reson Med, 1999. **41**(6): p. 1246-54.
15.   Wang, J., et al., *Pediatric perfusion imaging using pulsed arterial spin labeling.* J Magn Reson Imaging, 2003. **18**(4): p. 404-13.
16.   Warnking, J.M. and G.B. Pike, *Reducing contamination while closing the gap: BASSI RF pulses in PASL.* Magn Reson Med, 2006. **55**(4): p. 865-73.
17.   Kwong, K.K., et al. *Perfusion MR imaging*. in *Proc., SMR, 2nd Meeting*. 1994. San Francisco.
18.   Wong, E.C., R.B. Buxton, and L.R. Frank, *Quantitative imaging of perfusion using a single subtraction (QUIPSS and QUIPSS II).* Magn. Reson. Med., 1998. **39**: p. 702-708.
19.   Lu, H., et al., *Determining the longitudinal relaxation time (T1) of blood at 3.0 Tesla.* Magn Reson Med, 2004. **52**(3): p. 679-82.
20.   Zhao, J.M., et al., *Oxygenation and hematocrit dependence of transverse relaxation rates of blood at 3T.* Magn Reson Med, 2007. **58**(3): p. 592-7.
21.   Donahue, M.J., et al., *Theoretical and experimental investigation of the VASO contrast mechanism.* Magn Reson Med, 2006. **56**(6): p. 1261-73.
22.   Frank, L.R., et al., *Dynamic imaging of perfusion in human skeletal muscle during exercise with arterial spin labeling.* Magn Reson Med, 1999. **42**(2): p. 258-67.

23.   Uludag, K. and K. Ugurbil, *A general model for neuronal activity-induced signal changes for gradient and spin echo functional imaging.* (submitted), 2008.
24.   Smith, S.M., et al., *Advances in functional and structural MR image analysis and implementation as FSL.* Neuroimage, 2004. **23 Suppl 1**: p. S208-19.
25.   Jenkinson, M., et al., *Improved optimization for the robust and accurate linear registration and motion correction of brain images.* Neuroimage, 2002. **17**(2): p. 825-41.
26.   Calamante, F., et al., *Measuring cerebral blood flow using magnetic resonance imaging techniques.* J Cereb Blood Flow Metab, 1999. **19**(7): p. 701-35.
27.   Buxton, R.B., *Introduction to Functional Magnetic Resonance Imaging: Principles and Techniques*2002, Cambridge: Cambridge University Press.

Chapter 4

Perfusion-based functional magnetic resonance imaging

Overview

The strong and the weak features of arterial spin labeling (ASL) and blood oxygenation level dependent (BOLD) functional magnetic resonance imaging (fMRI) is discussed. The subtraction methods to create perfusion time series from ASL data are described and compared in the context of ASL signal processing. An analytical model developed for describing the ASL signal processing path is explained. Signal to noise ratio (SNR) in ASL experiment is described and compared with BOLD fMRI. The methods for simultaneously acquiring the perfusion and BOLD weighted images are summarized. Finally the modified version of general linear model for ASL data analysis is briefly described.

4.1 Functional brain imaging: ASL vs. BOLD

Positron emission tomography (PET) which is applied to measure the cerebral blood flow (CBF) in 1980s by Raichle et al (1983) [1] was a revolution in functional brain imaging by injecting radioactive [^{15}O] water and using tracer kinetic theory to create images measuring the perfusion of brain tissue over time in physiologic units (cc of blood per 100 g of tissue per minute). Although its high impact in cognition and neural activity studies, PET has consistent drawbacks mainly including low temporal resolution (on the order of a minute) limiting its repeatable application [2]. Since its discovery in the early 1990s blood oxygenation level-dependent (BOLD) MRI is the most pervasively used method for mapping the task-specific activations in the brain [3]. BOLD is basically a T_2^*-weighted imaging by exploiting local susceptibilities in the main magnetic field induced by the changes in the relative concentrations of oxygenated and deoxygenated hemoglobin (dHb) accompanying brain activation. Currently BOLD is the standard and most widely used non-invasive method to study the brain function because of its relatively higher signal to noise ratio (SNR) and higher temporal resolution (on the order of seconds) and easier implementation without requiring any additional RF and gradient system [4]. After a series of technical improvements and methodological developments, perfusion fMRI using ASL is poised for widespread application in functional neuroimaging and provides several advantages over standard BOLD fMRI [5].

Because the BOLD signal reflects a combined measure of changes associated with cerebral blood flow (CBF), cerebral blood volume (CBV) and the cerebral metabolic rate of oxygen ($CMRO_2$), the complex interactions of these underlying mechanisms complicate the interpretation of the BOLD signal changes in fMRI activation studies and unable to pin down to a single correlate of neural activity. It has been experimentally and theoretically shown that at 1.5 and 3T magnetic field strength, using the gradient-echo and spin-echo MRI acquisition schemes, most of the BOLD signal originates from veins [6]. As a result, the spatial location of the BOLD signal change at 3T fails to define exactly where the neuronal activity occurs. Hence, the BOLD signal might show a spatial displacement from the actual site of neuronal activation, thereby reducing the specificity of the functional localization [7]. In contrast to BOLD signal which is primarily a change in venous oxygenation, ASL activation is a change in arterial flow to a region and more tightly linked to the site of neural activity. In other words, ASL signal is not affected from draining veins which can produce an apparent BOLD activation in a brain region downstream from the actual activation region. Consequently, using ASL for mapping the task-specific patterns yields more accurate spatial correlations with actual site of regional involvement than BOLD [8]. Furthermore, gradient echo-echo planar imaging (GE-EPI) which is commonly employed to achieve the maximum sensitivity causes BOLD signal prone to artefacts in the areas with high susceptibility such as tissue-bone and tissue-air boundaries where ASL signal is not affected [9]. However, the feasibility of implementing spin-echo BOLD fMRI reduces those susceptibility artefacts particularly at high magnetic fields [10].

A powerful feature of ASL is that it provides physiologically quantitative measure of CBF in absolute units of (mL/100g-min) thus allowing baseline measurements [11]. However, BOLD is primarily a task-associated signal typically expressed in percent change [12]. Cohen et al (2004) [13] and Brown et al (2003) [14] experimentally investigated the baseline variability in BOLD fMRI data and reported a mismatch between the change in baseline CBF and the corresponding BOLD response for the same subject and stimulus.

Another important drawback of BOLD signal is originated due to 1/f noise which induces high power at low frequencies in the BOLD spectrum [15]. These slow "drifts" in fMRI signal confound comparisons of activity spaced much more than a minute apart and shown to be a property of the scanning system itself, rather than a physiologic property of the brain [15, 16]. This temporal autocorrelation precludes the application of BOLD signal in experimental designs with fundamental frequency below 0.01 Hz including experiments for emotional response, procedural learning, mood changes, diseases and drug therapy [15, 17]. On the other hand, due to the pairwise subtraction of adjacent images and the subsequent calibration process, the slow drifts present in BOLD contrast images are eliminated in ASL [18].

Besides those aforementioned superiorities of ASL, there are few significant challenges in ASL imaging that hamper its routine usage in functional brain imaging including relatively low SNR and low temporal resolution. It is reported that the SNR of ASL is 3-5 times lower compared to BOLD SNR [19]. Temporal resolution of ASL is inherently low as a direct consequence of pairwise acquisition which is doubling the effective TR typically varying between 3-8 s. This poor temporal resolution of ASL precludes detecting fast changes in brain function due to activation. The signal and noise characteristics and temporal resolution of ASL will be discussed further later.

4.2 ASL signal processing

In an ASL fMRI, a number of control and tag images in which arterial blood is either fully relaxed or magnetically inverted, respectively, are acquired. Typically, the control and tag images are acquired in an interleaved fashion and a perfusion time series can be formed from the running subtraction of the control and tag images as illustrated in Figure 4.1 [5].
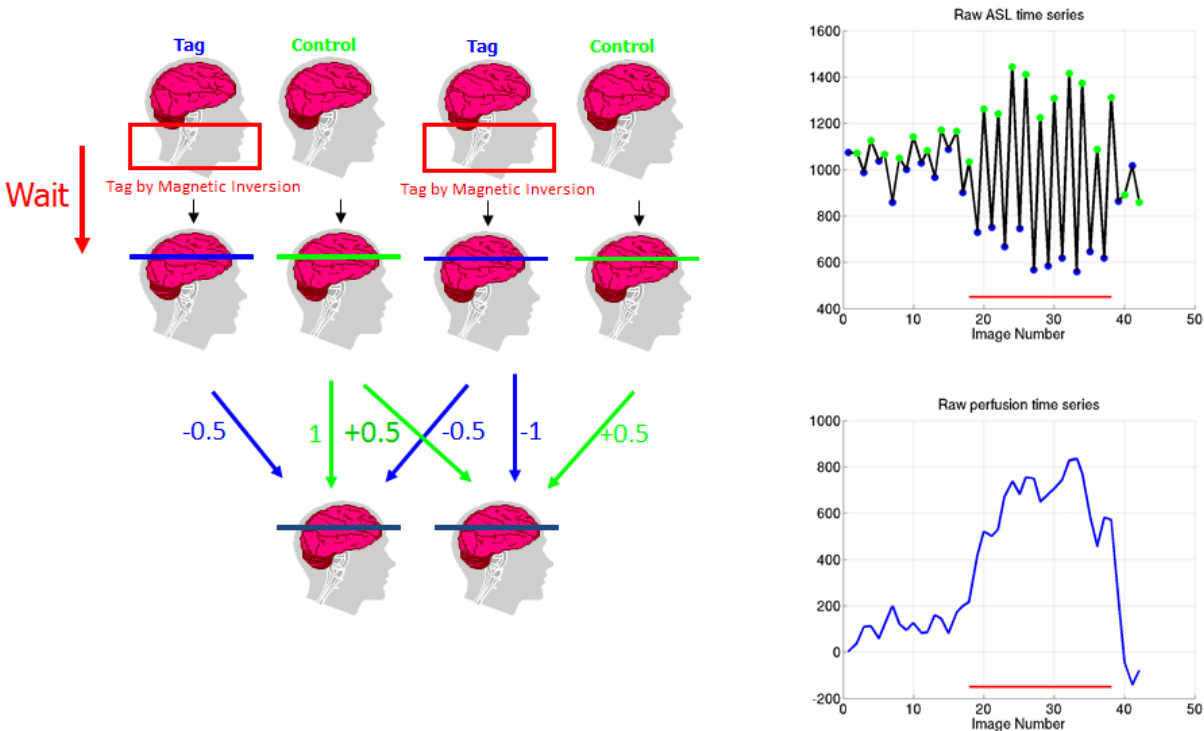
Figure 4.1 *Formation of a perfusion time series from the "surround subtraction" of control and tag images. An example time series of control (green) and tag (blue) signals is shown in the upper right panel. The perfusion time series created by surround subtraction is shown in the lower right panel where the solid red line corresponds the time of stimulus on. (Figure from Liu and Brown et al (2007)).*

There are mainly three subtraction methods are being used in practice including "pairwise subtraction", "surround subtraction" and "sinc-interpolated subtraction". "Pairwise

subtraction" is a simple subtraction of consecutive control and tag images. "Surround subtraction" corresponds to difference between each image and the average of its two nearest neighbors. "Sinc-interpolated subtraction" interpolates the control and tag series with a sinc function and calculated the difference of the time aligned control and tag images [20]. Wong et al (1997) [21] is reported that "surround subtraction" reduces transient artifacts due to blood oxygenation level dependent (BOLD) weighting of the acquired images therefore most accurately recovers the true shape of the perfusion hemodynamic response. Aguirre et al (2002) [15] reported that "sinc-interpolated subtraction" offers better results compared to the other two subtractions and significantly reduces the BOLD weighting of ASL time series. Wang et al (2003) [22] reported that "sinc-interpolated subtraction" and "pairwise subtraction" offers relatively flat power spectra in the frequency range below 0.10 Hz whitening the low frequency 1/f noise whereas surround subtraction exhibited a slightly increased power at lower frequencies.

4.2.1 Analytical model of ASL signal processing chain

Liu and Wong (2005) [20] developed a model of the signal path in arterial spin labeling based functional magnetic resonance imaging that allows deriving expressions for the BOLD contamination of the perfusion estimate and for the perfusion weighting of the BOLD estimate. Figure 4.2 illustrates block diagram of the signal processing model that captures the essential features of a pulsed ASL experiment.
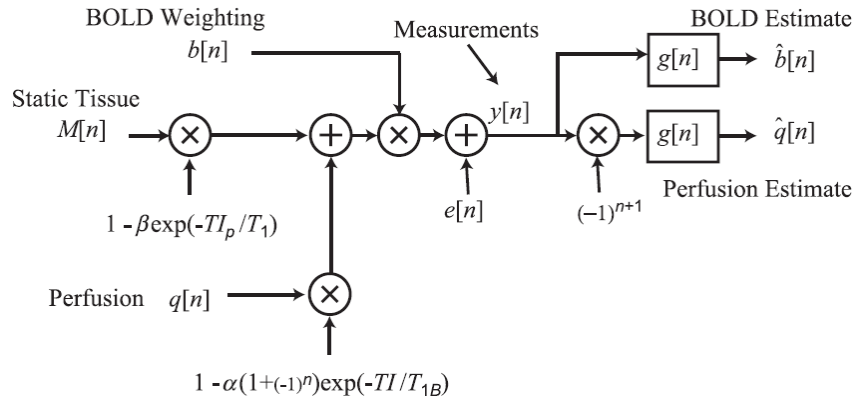
Figure 4.2 *Block diagram of the signal processing model in ASL. (Figure from Liu and Wong (2005)).*

The measured time series (ASL time series) $y[n]$, is the sum of the interleaved BOLD-weighted tag and control images plus an additive noise term e[n] with autocorrelation function $\rho[n]$. Because of the non-zero echo time (TE) which ideally should be zero for the maximum ASL signal, the perfusion measurements included BOLD signal contamination $b[n]$ given by:

$$b[n] = e^{-TE(R_{2,0}^* - \Delta R_2^*[n])} \qquad \qquad [4.1]$$

where $R_{2,0}^*$ is the apparent transverse relaxation rate at rest and $\Delta R_2^*[n]$ is the time varying change in relaxation rate with functional activation. By considering that the total bold weighting is the superimposition of the weighting at rest and the time varying signal change during the activation, the bold weighting can be expressed in two parts:

$$b[n] \approx b_0 + \Delta b[n] \qquad [4.2]$$

with

$$b_0 = e^{-TE.R_{2,0}^*} , \ \Delta b[n] = -b_0 \Delta R_2^*[n]TE \qquad [4.3]$$

Magnetization of static tissue spins in the imaging slice is represented by $M[n]$ which is multiplied by a saturation recovery term $(1 - \beta e^{-TI_p/T_1})$ with $\beta = 1$ and tissue longitudinal time constant T_1 in the case of application of a pre-saturation pulse to suppress the intrinsic tissue signal. If there is no pre-saturation pulse is applied then $\beta = 0$. $q[n]$ represents the amount of CBF that perfuse the tissue multiplied by $1 - \alpha(1 + (-1)^n)\exp(-TI/T_{1B})$. The odd values of n corresponds to the control states and even values of n corresponds to the tag states with the labeling efficiency α and exponential inversion recovery term. The measured time series than could be expressed as $y[n] = y_b[n] + y_q[n] + e[n]$ where $y_b[n]$ correspond to the sum of BOLD weighted static tissue and perfusion components given as:

$$y_b[n] = b[n]\left((1 - \beta e^{-TI_p/T_1})M[n] + (1 - \alpha e^{(-\frac{TI}{T_{1B}})}q[n])\right) \qquad [4.4]$$

and $y_q[n]$ is the BOLD weighted perfusion signal expressed as:

$$y_q[n] = (-1)^{n+1}b[n]q[n]\alpha e^{(-\frac{TI}{T_{1B}})} \qquad [4.5]$$

The surround subtraction over the image acquisition time series produces the perfusion weighted time series: $(\{y[1] - (y[0] + y[2])/2\}, \ \{(y[1] + y[3])/2 - y[2]\},...)$. These estimates can be expressed as a convolution given by:

$$\hat{q}[n] = \sum_{k=-\infty}^{\infty}((-1)^{n+1}y[k]g[n - k]) = ((-1)^{n+1}y[k]) * g[n] \qquad [4.6]$$

where $g[n]$ is a low pass interpolation filter determining the type of subtraction which is equal to [1 1] for "pairwise subtraction" and [1 2 1]/2 for "surround subtraction".

4.2.2 Signal and noise characteristics in perfusion fMRI

As we previously mentioned, the SNR of ASL method is intrinsically low because the inflowing blood signal is on the order of 1% of the tissue signal. Background suppression method that reduces the intrinsic tissue signal is an efficient way of reducing the noise [9]. Similar to the BOLD fMRI, cardiac and respiratory fluctuations are the major noise sources in ASL experiments. Due to the low SNR, physiological noise reduction is particularly

pronounced in ASL signal processing. Restom et al (2006) [23] proposed retrospective image based correction method which is an extension within the framework of a general linear model (GLM) for ASL experiments that significantly reduce physiological noise. We will discuss the GLM for ASL more in further in this chapter.

The temporal autocorrelation of ASL perfusion data exhibits a different patter compared to BOLD since the subtraction of adjacent and temporally interleaved images dampens the long-time-scale autocorrelation present in the source noise [24]. Aguirre et al (2002) [15] theoretically and experimentally showed that the power spectrum of the perfusion data is flat whereas BOLD signal has high power at low frequencies originated due to 1/f noise as illustrated in Figure 4.3.
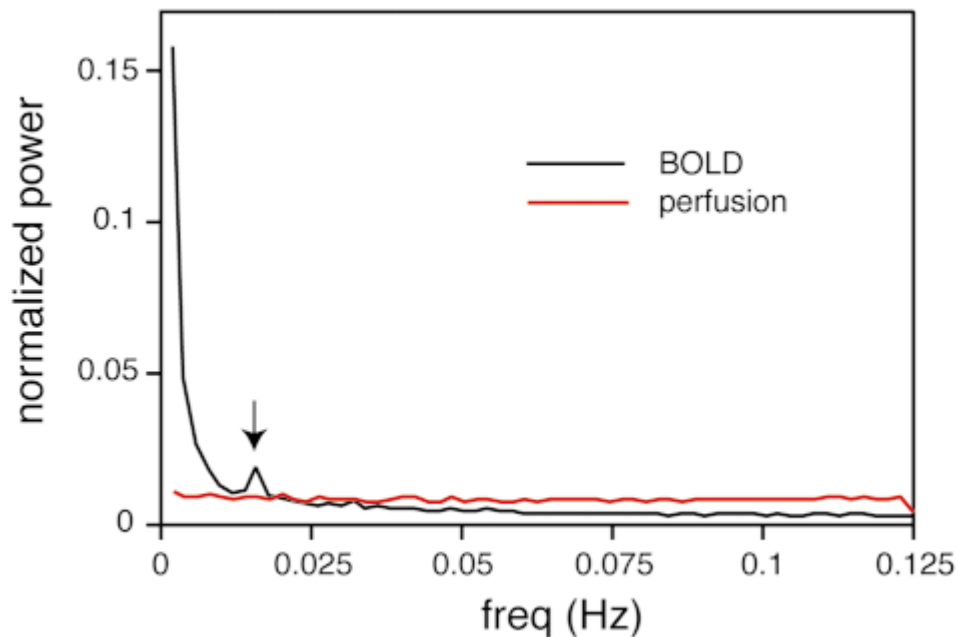
Figure 4.3 *The power spectrum typically observed in BOLD fMRI data (black line) has ever‐increasing power at lower frequencies. In contrast, the power spectrum of perfusion data (red line) is flat, indicating that the observations are independent in time under the null hypothesis. (Figure from Aguirre et al (2002)).*

The temporal resolution of ASL signal is poorer relative to BOLD since each perfusion image is derived from two time points corresponding to control and tag images. Typically TR=2s is used in ASL yielding one control and tag image pair in 4s which seems to preclude the use of ASL to accurately measure the shape of the perfusion hemodynamic response evoked by neural activity. Wong et al (2000) [25] proposed turbo-ASL that shortens the imaging time by utilizing the image acquisition at a short delay (~100ms) following the control to acquire the preceding tag signal and *vice versa*. The combined effect of low SNR and poor temporal resolution of ASL signal results in a low contrast-to-noise ratio relative to BOLD.

4.3 Simultaneous acquisition of BOLD and CBF signals

An appropriate modification of ASL sequence allows simultaneous estimate of CBF and BOLD time series independently [26, 27]. In ASL experiment using gradient echo readouts with sufficiently long echo times, each individual image is BOLD weighted. A BOLD time series can be formed from the control and tag images through running average process and a perfusion time series can be formed through running difference process. Simultaneous measures of CBF and BOLD has made ASL a primary tool for investigating the underlying mechanisms of the BOLD effect such as the transients of BOLD signal [28] and post-stimulus undershoot [27]. In a recent study, Cavusoglu et al (2011) [29] explored the retinotopic maps and hemodynamics delays using simultaneous acquisition of CBF and BOLD data. This study will be presented in the next chapter of the thesis. Figure 4.4 shows the simultaneous estimates of BOLD and CBF time series during an experimental design of eyes are closed and open.
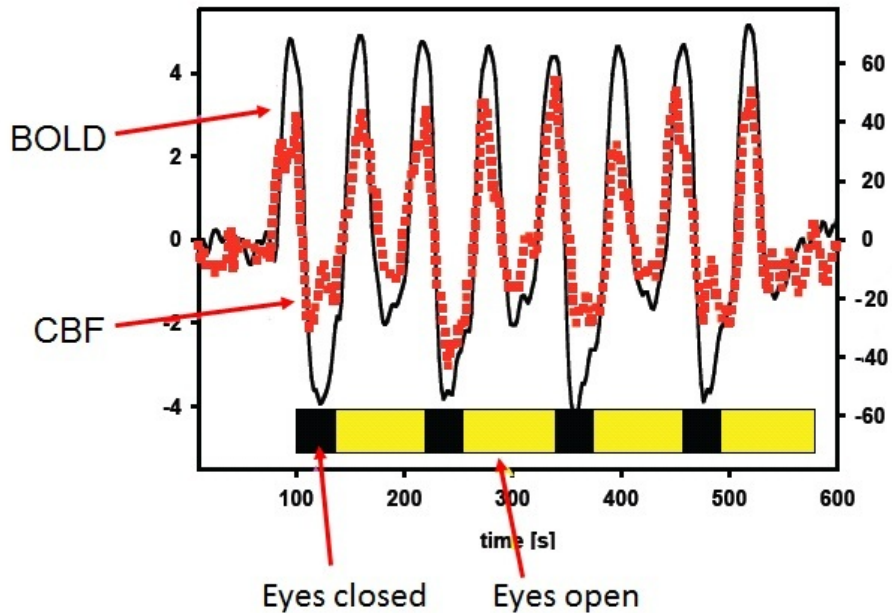
Figure 4.4 *Simultaneous estimates of BOLD and CBF time series during an experimental design of eyes are closed and open. Left axis scales the BOLD signal change (%) and right axis scales the CBF signal change (%) during the activation. (Figure from courtesy of Uludag, K.).*

Another promising modification of ASL sequence for simultaneous estimation of CBF and BOLD time series is the use of dual-echo acquisition that allows to form perfusion time series from the images obtained at short echo time (TE=3ms) and BOLD time series obtained at a later echo time (TE=30ms) [9]. Figure 4.5 shows the BOLD and CBF

weightings of the acquired echoes depending on the TE as the relative power in their Fourier spectrum. A detailed comparison of BOLD and ASL fMRI is presented by Liu and Brown et al (2006) [5] and Aguirre et al (2005) [24].
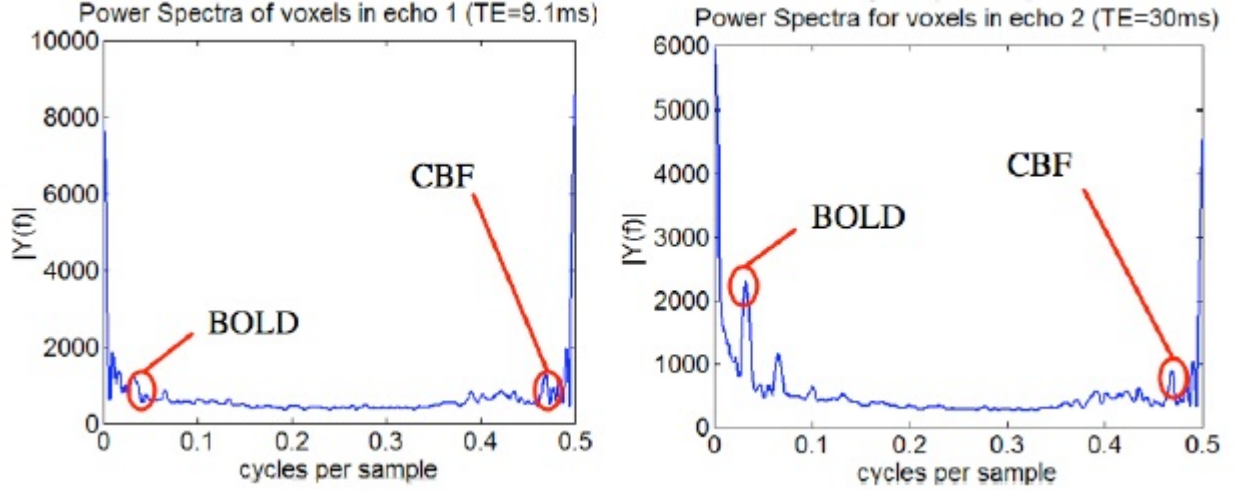
Figure 4.5 *BOLD and CBF weightings of the acquired echoes depending on the TE as the relative power in their Fourier spectrum. For short echo times (left) CBF weighting dominates BOLD weighting whereas at long echo times (right) BOLD weighting is more pronounced (Figure from courtesy of Wong E.C.).*

4.4 General linear model (GLM) for ASL

Based on the work of Liu and Wong (2005) [20] where they modeled the ASL time series as:

$$y[n] = b[n]\left(s_M M_0 + s_q q[n]\right) + (-1)^{n+1} b[n] q[n] \alpha e^{\left(-\frac{TI}{T_{1B}}\right)} + e[n] \qquad [4.7]$$

where $s_M = (1 - \beta e^{-TIp/T_1})$ and $s_q = 1 - \alpha \exp(-TI/T_{1B})$ as described in eq.[4.4], Restom et al (2006) [23] expressed eq.[4.7] in the matrix form as:

$$\mathbf{y} = s_m M_0 \mathbf{b} + s_q \mathbf{q} \circ \mathbf{b} + \alpha \exp\left(-\frac{TI}{T_{1B}}\right) \mathbf{Mq} \circ \mathbf{b} + \mathbf{U_c D_c Pc_c} + \mathbf{U_t D_t Pc_t} + \mathbf{e} \qquad [4.8]$$

where **y, b, q** and **e** are the vector version of $y[n], b[n], q[n]$ and $e[n]$ respectively, **M** is a N dimensional square diagonal matrix made up alternating -1 and 1s along the diagonal corresponding to tag and control images and **q** o **b** represents the Hadamard product of two vectors. $\mathbf{U_c D_c Pc_c} + \mathbf{U_t D_t Pc_t}$ corresponds to the physiological noise contaminations in the control and tag images respectively where **P** is a Nxm matrix including m regressors and $\mathbf{c_c}$ and $\mathbf{c_t}$ corresponds to regressor weights for the control and tag images. The detailed description of **U** and **D** matrices is given by Liu et al (2002) [30] representing the up-sampling and down-sampling matrices. Then, a general linear model for ASL was described as

$$\hat{q} = GXh + Sd + GU_cD_cPc_c - GU_tD_tPc_t + n \qquad [4.9]$$

where **X** corresponds to a vector including the smoothed stimulus pattern, **h** corresponds to a scalar representing the unknown amplitude, **S** is a *Nxl* matrix comprised of *l* nuisance model functions and **d** is an *l*x1 vector of nuisance parameters and **n** is an additive noise term. Within the framework of the GLM developed for ASL by Liu et al (2002) [30] and Restom et al (2006) [23] and summarized above, physiological noise is reduced by removing an estimate of the physiological noise terms $GU_cD_cPc_c - GU_tD_tPc_t$ from the perfusion time series. Figure 4.6 illustrates the effect of noise removing on CBF time series [23].
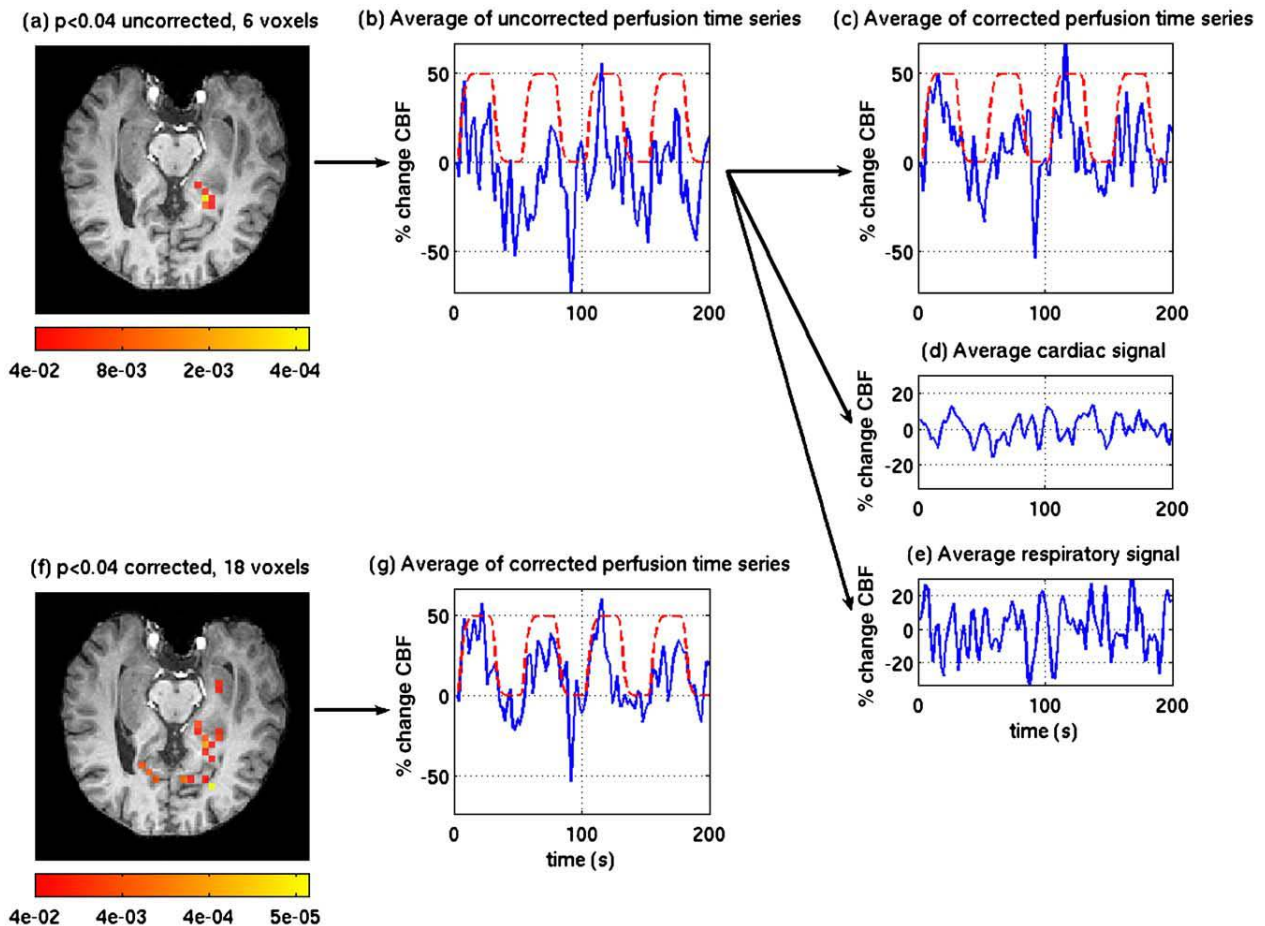
Figure 4.6 *Example single subject data from hippocampus data. Statistical significance maps These maps are overlaid on high resolution anatomical images. Uncorrected and corrected average CBF time courses corresponding to the activated region in panel **(a)** are shown in panels **(b)** and **(c)**, respectively, with the cardiac and respiratory components shown in panels **(d)** and **(e)**, respectively. (Figure from Restom et al (2006)).*

References

1.   *Raichle, M.E., Brain blood flow measured with intravenous H2-O-15: implementation and validation. J. Nucl. Med., 1983. **24**: p. 790-798.*

2.   *Raichle, M.E., Behind the scenes of functional brain imaging: A historical and physiological perspective. Proc. Natl. Acad. Sci., USA, 1998. **95**: p. 765-772.*

3.   *Ogawa, S., et al., Intrinsic signal changes accompanying sensory stimulation: functional brain mapping with magnetic resonance imaging. Proc Natl Acad Sci U S A, 1992. **89**(13): p. 5951-5.*

4.   *Logothetis, N.K., What we can do and what we cannot do with fMRI. Nature, 2008. **453**(7197): p. 869-78.*

5.   *Liu, T.T. and G.G. Brown, Measurement of cerebral perfusion with arterial spin labeling: Part 1. Methods. Journal of the International Neuropsychological Society, 2007. **13**(3): p. 517-525.*

6.   *Uludag, K., B. Muller-Bierl, and K. Ugurbil, An integrative model for neuronal activity-induced signal changes for gradient and spin echo functional imaging. Neuroimage, 2009. **48**(1): p. 150-65.*

7.   *Ugurbil, K., L. Toth, and D.S. Kim, How accurate is magnetic resonance imaging of brain function? Trends Neurosci, 2003. **26**(2): p. 108-14.*

8.   *Diekhoff, S., et al., Functional localization in the human brain: Gradient-Echo, Spin-Echo, and arterial spin-labeling fMRI compared with neuronavigated TMS. Hum Brain Mapp, 2011. **32**(3): p. 341-57.*

9.   *Buxton, R.B., Introduction to Functional Magnetic Resonance Imaging: Principles and Techniques2002, Cambridge: Cambridge University Press.*

10.   *Wang, J., et al., Reduced susceptibility effects in perfusion fMRI with single-shot spin-echo EPI acquisitions at 1.5 Tesla. Magnetic Resonance Imaging, 2004. **22**(1): p. 1-7.*

11.   *Wong, E.C., Quantifying CBF with pulsed ASL: technical and pulse sequence factors. J Magn Reson Imaging, 2005. **22**(6): p. 727-31.*

12.   *Shulman, R.G., D.L. Rothman, and F. Hyder, A BOLD search for baseline. Neuroimage, 2007. **36**(2): p. 277-81.*

13.   *Cohen, E.R., et al., Hypercapnic normalization of BOLD fMRI: comparison across field strengths and pulse sequences. Neuroimage, 2004. **23**(2): p. 613-24.*

14.   *Brown, G.G., et al., BOLD and Perfusion Response to Finger-Thumb Apposition After Acetazolamide Administration: Differential Relationship to Global Perfusion. J Cereb Blood Flow Metab, 2003. **23**(7): p. 829-837.*

15.   *Aguirre, G.K., et al., Experimental design and the relative sensitivity of BOLD and perfusion fMRI. Neuroimage, 2002. **15**(3): p. 488-500.*

16.   *Zarahn, E., G. Aguirre, and M. D'Esposito, A trial based experimental design for fMRI. NeuroImage, 1997. **5**: p. 179-197.*

17.   *Liu, T.T. and A.C. Fraser-Smith, Detection of transients in 1/f noise with the undecimated discrete wavelet transform. Ieee Transactions on Signal Processing, 2000. **48**(5): p. 1458-1462.*

18.   *Wang, J., et al., Empirical analyses of null-hypothesis perfusion FMRI data at 1.5 and 4 T. Neuroimage, 2003. **19**(4): p. 1449-62.*

19.   *Perthen, J.E., et al., SNR and functional sensitivity of BOLD and perfusion-based fMRI using arterial spin labeling with spiral SENSE at 3 T. Magnetic Resonance Imaging, 2008. **26**(4): p. 513-22.*

20.   *Liu, T.T. and E.C. Wong, A signal processing model for arterial spin labeling functional MRI. Neuroimage, 2005. **24**(1): p. 207-15.*

21.   *Wong, E.C., R.B. Buxton, and L.R. Frank, Implementation of quantitative perfusion imaging techniques for functional brain mapping using pulsed arterial spin labeling. NMR in Biomed, 1997. **10**: p. 237-249.*

22. *Wang, J., et al., Arterial spin labeling perfusion fMRI with very low task frequency. Magn Reson Med, 2003.* **49**(5): p. 796-802.

23. *Restom, K., Y. Behzadi, and T.T. Liu, Physiological noise reduction for arterial spin labeling functional MRI. Neuroimage, 2006.* **31**(3): p. 1104-15.

24. *Aguirre, G.K., J.A. Detre, and J. Wang, Perfusion fMRI for functional neuroimaging. Int Rev Neurobiol, 2005.* **66**: p. 213-36.

25. *Wong, E.C., W.M. Luh, and T.T. Liu, Turbo ASL: arterial spin labeling with higher SNR and temporal resolution. Magnetic Resonance in Medicine, 2000.* **44**(4): p. 511-5.

26. *Yang, Y., et al., Simultaneous perfusion and BOLD imaging using reverse spiral scanning at 3T: characterization of functional contrast and susceptibility artifacts. Magn Reson Med, 2002.* **48**(2): p. 278-89.

27. *Buxton, R.B., E.C. Wong, and L.R. Frank, Dynamics of blood flow and oxygenation changes during brain activation: the balloon model. Magn. Reson. Med., 1998.* **39**: p. 855-864.

28. *Obata, T., et al., Discrepancies between BOLD and flow dynamics in primary and supplementary motor areas: application of the balloon model to the interpretation of BOLD transients. Neuroimage, 2004.* **21**(1): p. 144-53.

29. *Cavusoglu, M., Bartels, A., Yesilyurt, B., Uludag, K., Retinotopic maps and hemodynamic delays in human visual cortex measured using arterial spin labeling. Neuroimage, 2011.*

30. *Liu, T.T., et al., Analysis and Design of Perfusion-Based Event-Related fMRI Experiments. Neuroimage, 2002.* **16**(1): p. 269-82.

Chapter 5

Retinotopic maps and hemodynamic delays in the human brain measured using arterial spin labeling

Overview

Cortical representations of the visual field are organized retinotopically, such that nearby neurons have receptive fields at nearby locations in the image. Many studies have used blood oxygenation level-dependent (BOLD) fMRI to non-invasively construct retinotopic maps in humans. Several studies using gradient-echo MRI at 1.5T and 3T showed that most of the BOLD signal originates from veins, which might lead to a spatial displacement from the actual site of neuronal activation, thus reducing the specificity of the functional localization. In contrast to BOLD signal, cerebral blood flow (CBF) as measured using arterial spin labeling (ASL) is less or not at all affected by remote draining veins, and therefore spatially and temporally more closely linked to the underlying neural activity. In the present study, we determined retinotopic maps in the human brain using CBF as well as using BOLD signal in order to compare their spatial relationship as well as the temporal delays of each imaging modality for visual areas V1, V2, V3, hV4 and V3AB. We tested the robustness and reproducibility of the maps across different sessions, calculated the overlap as well as signal delay times across visual areas. While area boundaries were relatively well preserved, we found systematic differences of response latencies between CBF and the BOLD signal between areas. In summary, CBF data obtained using ASL allows reliable retinotopic maps to be constructed; this approach is, therefore, suitable for studying visual areas especially in close proximity to large veins where the BOLD signal is spatially inaccurate.

5.1 Introduction

The human visual cortex is partitioned into a number of functional areas with specific local neuronal properties [1-6]. That is, adjacent neurons have receptive fields covering adjacent points in the visual field [2, 7]. This spatial organization of the neuronal properties is called retinotopy. Functional magnetic resonance imaging (fMRI) has been used for over a decade to identify the visual field maps in the human cortex [4-6, 8-16]. Many studies have used BOLD-fMRI to non-invasively visualize retinotopic maps, e.g. for inter-subject comparisons of the human visual system [17, 18], for measuring the position, surface area and visual field representations of the visual cortex [6, 19, 20], for quantitative estimation of cortical magnification factor [4] and receptive field size [21] and in numerous cognitive experiments [22-26].

Although measuring the BOLD signal is the main fMRI tool for mapping studies and has been widely used to create visual field maps and delineate visual areas, it has potential limitations due to the underlying physiological and physical processes giving rise to the BOLD signal. BOLD contrast relies on changes of local magnetic susceptibility induced by the changes in paramagnetic deoxyhemoglobin, reflecting the increased metabolic demands of enhanced neural activity [27]. In addition, the fMRI signal also directly depends on cerebral blood volume changes altering the balance of intra- and extra-vascular MRI signal contributions ([28], and references therein). Many studies have shown that such changes not only occur in brain parenchyma (e.g., grey matter) but also in the draining veins on the surface of the parenchyma. It has been experimentally and theoretically shown that at 1.5 and 3T magnetic field strength, using the gradient-echo and spin-echo MRI acquisition schemes, most of the BOLD signal originates from veins [28-32]. As a result, the spatial location of the BOLD signal change at 3T fails to define exactly where the neuronal activity occurs. Hence, the BOLD signal might show a spatial displacement from the actual site of neuronal activation, thereby reducing the specificity of the functional localization [33]. In addition, the BOLD signal delays can vary considerably depending on the local vasculature. Signals originating near large draining veins have been shown to have delays of several seconds longer compared to those originating from the capillary bed [34-36]. This is substantial for retinotopic mapping studies even if the rotation direction of phase-encoding

stimuli is systematically reversed, as the noise in their averaged signal can increase the more the assumed global BOLD signal delay differs from the actual BOLD signal delay.

Several alternative fMRI methods to BOLD contrast were proposed in the last decade. These assess different physiological processes and have different sensitivities such as contrast agent methods, vascular space occupancy (VASO) and nuclear medicine. Direct measurement of CBF using arterial spin labeling (ASL) MRI is a promising alternative for functional activation and baseline studies. Perfusion imaging using ASL allows noninvasive measurement of CBF by assessing the inflow of magnetically tagged arterial water into an imaging slice [37, 38]. The CBF signal arises from labelled water spins that have passed through the capillary walls into the tissue or are still within the capillaries [39], as the amount of tagged water in humans at 3T reaching the veins is negligible [40]. Therefore, CBF signal is more tightly linked to the capillary bed whose vascular properties are directly modulated by the surrounding nervous tissue. In accordance with this, a number of fMRI studies that compared BOLD and CBF signals reported that CBF measurements provide better functional localization than the BOLD signal [41-45]. In addition, several authors have reported that CBF changes have lower inter-subject variability and are more reproducible compared to BOLD signals [43-45]. On the other hand, ASL has relatively lower SNR than BOLD signal and has a number of systematic confounding factors such as transit delay, magnetization transfer and relaxation artefacts as we previously discussed in chapter 4.

The current study was therefore driven by two main motivations: firstly, to demonstrate, for the first time, delineation of visual areas using CBF weighted retinotopic maps and secondly the systematic characterization of BOLD signal delays relative to those of CBF across human visual areas. To this end, we exposed five human volunteers to visual displays of rotating wedge and expanding ring stimuli utilizing an ASL sequence that enabled simultaneous acquisition of BOLD- and perfusion-weighted images. We calculated the phase maps for the polar angle and eccentricity across their occipital cortices for each of the two fMRI imaging modalities. The visual areas were then determined for each of the fMRI imaging modalities and the overlap of the resulting visual areas V1, V2, V3, hV4, V3A/B was compared. Furthermore, the general approach in retinotopic mapping is

assuming that the hemodynamic delay of the response remains fixed at each cortical position. Here, we calculated the hemodynamic delays for each voxel separately and used the corresponding values for phase calculations. We assessed the potential sources for the discrepancies between the BOLD signal and perfusion-based retinotopic maps from the aspect of both calculation methods and underlying physiology. Finally, we assessed the reproducibility of the retinotopic maps created from BOLD signal and perfusion-weighted images. A preliminary version of this work has been previously presented in abstract form [46].

5.2 Methods

5.2.1 Subjects

Five healthy subjects participated in the experiments (mean age 26±6 years). They were familiarized with the stimuli outside the scanner, and practiced each task for 4-6 min in the scanner. Written consent from the participants was obtained before the experiments began and the experimental protocol was approved by the ethics committee of the University of Tübingen.

5.2.2 Stimulus Paradigm

Phase-encoded retinotopic maps were calculated from measurements obtained using standard rotating wedge and expanding ring stimuli that induce travelling waves of neural activity in the visual cortex [4-6, 16, 47, 48]. To measure the polar angle representation, a single wedge was rotated either clockwise or counterclockwise around a central fixation point. The wedge spanned 30° of angle completing a full rotation every 45s. Eccentricity was mapped by using an expanding or contracting ring completing a full expansion every 45s. After reaching maximal expansion, the ring-stimulus re-started with the minimum size after each expansion (and vice versa for the contracting ring stimulus). The movement of both stimuli was non-continuous and occurred in 12 discrete steps. The temporal frequency of 45 s for both polar angle and eccentricity stimulation allowed the signal to return to baseline before subsequent activations. For each subject, the rotation direction was set to

clockwise/contraction in half of the scans and counterclockwise/expansion in the other half in order to cancel out phase errors caused by hemodynamic delays [4, 48].

The stimuli were generated using MATLAB software (MathWorks) and Cogent toolbox (http://www.vislab.ucl.ac.uk/cogent.php). The stimulus patterns were achromatic checkerboards flickering at 6 Hz with 90% contrast and 360 cd/m² full white luminance. Stimuli were projected onto a translucent screen located at the head end of the scanner bore using a projector located outside the scanning room. Subjects viewed the screen through a mirror attached to the head coil with a viewing distance (eyes to projection screen) of 82 cm and a visual angle of 24° x 18°. The onset of the change in the stimulus position was synchronized with a trigger pulse from the scanner at every repetition time (TR). All subjects were instructed to fix their gaze on a central crosshair during the experiments.

5.2.3 Data Acquisition

MR data were acquired on a 3T Siemens MAGNETOM Trio TIM scanner (Erlangen, Germany) using a 12-channel head coil. ASL images were obtained with a FAIR-QUIPSS II (flow sensitive alternated inversion recovery - quantitative imaging of perfusion using a single subtraction) sequence using a hyperbolic secant (HS) pulse for inversion and echo planar imaging (EPI) readout for acquisition (for the pulse sequence diagram, see appendix and [40]). Each PASL run consisted of 180 alternating tag and control images resulting in a total scan time of 7.5 min with the following sequence parameters: TI1=700ms, TI2=1400ms, TE=20ms, TR=2500ms, voxel size=3.5x3.5x3.5mm³, FOV=224mm, FA=90°. 16 axial slices oriented approximately parallel to the corpus callosum were scanned covering the occipital cortex. The tag was 10 cm in width positioned at a 1 cm gap to the imaging slices. Two pre-saturation pulses were applied in the imaging planes immediately before the inversion tag to minimize the impact of the static magnetization of the tissue. Inferior as well as superior saturation slabs outside the slices were applied. To suppress the intravascular signal contribution, a flow crusher (25cm/s) was applied in the direction of slice selection gradient. Each functional run was repeated 6 times for both eccentricity and polar angle stimulations for all subjects to increase the SNR. For cortical surface

reconstruction, two high-resolution T1 weighted structural scans were acquired from each subject using a 3D MP-RAGE (magnetization prepared - rapid acquisition gradient echo) sequence (TR = 2000 ms, TE = 3.25 ms, FOV = 256 mm, 176 sagittal slices, voxel size = 1 x 1 x 1 mm^3, flip angle = 9°).

5.2.4 Processing of Anatomical Data

The cortical surface of each subject was reconstructed from two high-resolution T1-weighted structural scans which were registered with FLIRT (www.fmrib.ox.ac.uk/fsl) and averaged. The data were analysed using cortical surface-based methods with FreeSurfer [49-51]. Each subject's cortical hemispheres were segmented into white and grey matter, inflated and, for better visualization of the data, the occipital lobe area was computationally flattened by cutting the inflated brain along the calcarine fissure. The accuracy of white matter identification is crucial in surface-based analysis because small segmentation errors may cause significant reconstruction artifacts. We therefore took great care to optimize this process. To improve the brain extraction, the skull stripping was visually checked and the voxels still containing small pieces of skull were manually removed. Also, determining an accurate pial surface boundary is affected by the white matter segmentation because the pial surface is created by expanding the white matter surface so that it follows the gray matter-CSF intensity gradient. Due to the curly and thin structure of white matter fibers in the occipital lobe, the result of the automatic segmentation algorithms generally contains false-positive and -negative white matter voxels. We also corrected these inaccuracies of the initial automatic segmentation algorithm by manual editing [19].

5.2.5 Processing of Functional Data

Functional data were analyzed using FreeSurfer [50] & FS-FAST, FSL software [52], and with additional custom-made MATLAB and Linux shell script routines. Pre-processing were performed on the functional data including brain-extraction, slice scan time correction and motion-correction utilizing the MCFLIRT module of FSL using the mean volume of the corresponding run as reference. Time series of all functional runs were high-pass filtered (cut-off 45s) to remove low frequency baseline drifts potentially caused by scanner

instability, subject motion and physiological noise. For each subject, all the repeated runs for polar angle and eccentricity stimulus were co-registered. Because of the non-zero echo time (TE), ASL sequence enables simultaneous acquisition of BOLD- and perfusion-weighted images. The BOLD signal is constructed as the running average of the control and tag images [38]. To create the CBF time series, we calculated control-tag difference images using surround subtraction (i.e., computing the difference between each image and the average of its two nearest neighbors), thereby reducing BOLD signal contamination of the CBF time course (for details, see [40, 53]).

Because the local functional organization of the cortex follows the cortical surface, application of a smoothing kernel to the volume data causes averaging of functionally unconnected areas and different tissue types (i.e. GM, WM, and CSF) which increases partial volume effects and reduces functional specificity. Surface-based smoothing is less prone to these errors because averaging is performed on the nearby vertices instead of nearby voxels and provides a more accurate view of the spatial extent of the activation sites according to their locations relative to sulcal/gyral landmarks [54]. Thus, we smoothed the flattened functional data with a number of nearest neighbor smoothing iterations corresponding to 7mm FWHM Gaussian kernel before the subsequent analyses [50, 55].

5.2.6 Fourier Analysis and Delineation of Visual Areas

Analysis methods were similar to previous studies [4], but it differed in some important aspects that allowed us to estimate absolute signal delays for each of the imaging modalities. The voxel-wise phase and amplitude of the hemodynamic responses was separately estimated for each of the polar stimulus rotation directions (clockwise and counterclockwise). The time course of each voxel from the phase-encoded data (10 cycles/run) was Fourier transformed and the signal amplitude and phase were calculated from the complex valued Fourier transform at the stimulation frequency (0.022Hz=1/45s). Because the measured phase of the hemodynamic response is linked to the position of the stimulus, the sign of the phase depends on the direction of the stimulus movement. We chose a positive sign for counterclockwise rotating and expanding stimuli with the initial stimulus position corresponding to zero phase.

5.2.7 Estimation of voxel-specific hemodynamic delays t_H

The phase of each voxel obtained from the Fourier transform in retinotopic mapping corresponds to the delay the stimulus takes to reach the voxel's receptive field, plus the additional delay of the hemodynamic response due to the neurovascular response time. Thus, the relation between the observed response phase and the position of the stimulation in the visual field is biased by the hemodynamic delay t_H. Since the hemodynamic delay varies in a spatially dependent manner across the brain [56] with delays ranging between 4 s (micro-vessels) to 12 s (large draining veins) [34-36], the magnitude of the bias is not uniform. Hence, the hemodynamic delay of each voxel needs to be measured and a local correction is necessary for an accurate calculation of the retinotopic phase maps. The general approach to overcome this problem is by averaging the phases of the counter propagating stimuli (after inverting one of the time-series) to average out local hemodynamic response function (HRF) delay differences, thus allowing for a reasonable estimate of the stimulus-induced delay. To optimize the averaging process, a fixed mean hemodynamic delay is assumed and subtracted from each time-series prior to averaging, henceforth referred to as global correction [4, 48, 57, 58]. This process is explained step by step in the following and in Figure 5.1.

To find the stimulus-related phase for a given voxel, the phase for clockwise/contracting data is reversed, an estimate of t_H is subtracted from both of reversed and non-reversed data, and the resulting hemodynamic responses are averaged. The peak of the average should in principle correspond to the neural activation time, as the voxel's individual t_H is averaged out. The idea behind this correction is that the receptive field positions estimated from the delayed hemodynamic responses t_H of reversed and non-reversed data are biased by the same amount but in opposite directions relative to the true neural activation time. Note that the outcome of the estimated phase is not entirely affected by the magnitude of the subtracted t_H since averaging reduces the bias. Nevertheless, a bad estimate of t_H would lead to a broadened or double-peaked average that would introduce noise to the phase estimates. In contrast to the general approach of assuming a fixed t_H for every voxel and subtracting this global value for correction prior to averaging, we calculated the t_H of the BOLD and CBF time courses for each voxel individually.
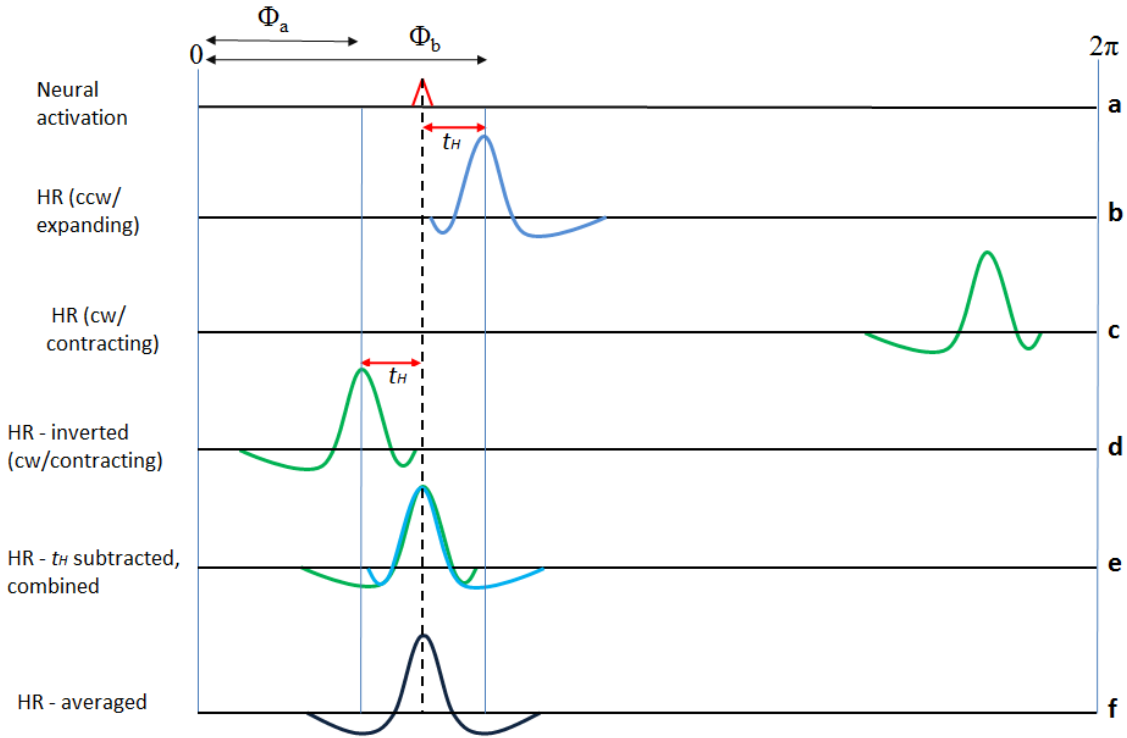
Figure 5.1 *Correction for the variable hemodynamic delay of the responses in phase calculation by assuming the time lag remains fixed at each cortical position. The response is delayed (tH) relative to neural activation time **(a)** biasing the true phase value for a given voxel **(b)**. To correct for this, the response from the counter propagating stimuli **(c)** is reversed since the reversed and non-reversed data are biased by the same amount but in opposite directions **(d)** relative to the true neural activation time. Then the assumed delay is subtracted from both of the data **(e)** and the responses are averaged to estimate a mean hemodynamic delay **(f)**.*

This allowed us firstly to obtain hemodynamic delay maps of each imaging modality separately, and secondly it allowed us to calculate the BOLD and CBF retinotopy phase maps by applying a local correction using each voxel's individual t_H. To calculate the voxel specific t_H we calculated the raw phase for the reversed (clockwise/contracting) and non-reversed (counterclockwise/ expanding) data obtained from the stimuli moving in opposite directions. Then, we inverted the phase found for clockwise/contracting stimuli by adding π. If the phase in the retinotopic map for the counterclockwise/expanding stimuli direction is Φ_a and for the clockwise/contracting direction with inversion Φ_b, then the phase induced by the hemodynamic delay t_H is equal to $(\Phi_b - \Phi_a)/2$ for that voxel (Figure 5.1). Therefore,

we subtracted this voxel-wise determined t_H to create both BOLD and CBF retinotopy phase maps accurately.

5.2.8 Phase and power maps

For each subject, the repeated functional runs were averaged in the Fourier domain to increase the SNR. The phase maps corresponding to polar angle and eccentricity stimuli were separately calculated for the BOLD signal and for perfusion-weighted data, and further analysis were performed based on these phase maps. Many studies use pseudocolors to represent the combined effect of phase and significance (i.e. -log10(significance)*phase) of each voxel (or vertex), a method that would preclude the direct comparison of raw phase values obtained using different measures, such as in our case between BOLD and perfusion maps [11, 58]. Because the precision and reliability of the locations of visual areas between BOLD and CBF contrasts was to be investigated in the present study, the retinotopic maps are represented in the color scale between 0 and 2π labeling the raw phase values.

For each voxel, we calculated an F ratio and corresponding p values by dividing the squared amplitude of the response at the stimulus frequency with the average squared amplitudes at all other frequencies (excluding higher harmonics and low frequency signals) and with degrees of freedom equal to the number of time points [4, 57, 59]. For each subject, the statistical map of the BOLD signal retinotopy was thresholded and an ROI was created including significantly activated voxels (p<0.01) separately for polar angle and eccentricity maps. The same ROI created from the BOLD signal was used to mask the retinotopic maps of perfusion-weighted signals due to the lower SNR of perfusion-weighted images, and all further analyses were performed in these defined ROIs. At each voxel j, SNR is defined as the ratio of the amplitude of the Fourier transform A_j at the stimulation frequency f_0 to the standard deviation of the noise σ_j. For the frequencies above the higher harmonics, noise component of raw data is assumed to be white and can be measured assuming to contain no signal, $SNR_j = \frac{A_j}{\sigma_j})$[48].

The travelling-wave fMRI measurements for both BOLD- and CBF-weighted signals reveal human hemifield maps in the occipital cortex. Consistent with numerous previous studies [4-6, 16, 60], the boundaries of retinotopic cortical areas (V1, V2, V3, hV4, V3A/B) were identified for each subject from phase-encoded retinotopic maps by calculating the visual field signs [48, 61]. This method is based on the fact that the orientation of visual field representation on the cortical surface changes between adjacent areas. Delineation of the visual areas based on the visual field signs provides more objectivity than manual determination in drawing borders between areas without requiring prior assumptions about the visual field map layout; this approach also supports quantitative analyses.

5.2.9 Comparison of locally and globally corrected phase maps

The absolute phase of each voxel in the retinotopic map is affected by the hemodynamic delay of the response that has a non-uniform distribution across the brain. In principle, if we take into account the voxel specific hemodynamic delay time in the calculations (local correction), we do not expect any difference between the BOLD and perfusion weighted phase maps since we are applying correction which ultimately results the same phase value regardless of the magnitude of the delay. We compared the phase maps that were globally corrected by assuming a fixed delay of t_H =5 s across all visual areas [48, 57, 62] with locally corrected phase maps to test the improvement of phase estimation. . For this calculation, we expressed the phase maps as vectors $\vec{B}$ (BOLD signal) and $\vec{P}$ (perfusion) with each entry in the vector corresponding to the phase of a single voxel in the ROI. The cross-correlation coefficients between $\vec{B}$ and $\vec{P}$ vectors were calculated as follows: $\vec{r_i} = xcorr(\vec{B}, mod_{\pm\pi}(\vec{P} \pm i.\frac{\pi}{1000}))$ where *xcorr(x,y)* estimates the cross-correlation sequence of a random process by $R_{xy}(m) = E\{x_{n+m}y_n^*\}$, x_n and y_n are jointly stationary random processes with $-\infty < n < \infty$, and $E\{\cdot\}$ is the expected value operator. This way, we calculated the correlation coefficients between $\vec{B}$ and $\vec{P}$ by very slightly shifting the $\vec{P}$ vector ($\pi/1000$ at each step) and by keeping the phase interval fixed in [-π +π] range. When we plot the distribution of the correlation coefficients vs. phase shifts, in the case of 100% overlap of the vectors (i.e. when same vectors are used), we expect maximum correlation at the origin ($r_0 = 1$) where there is no shift. The observed phase where the maximum correlation occurs yields the shift between

$\vec{B}$ and $\vec{P}$ vectors that in turn corresponds to the differential time lags of the BOLD and perfusion signals. In other words, the observed phase shift corresponding to the best correlation point is the measure of discrepancy between the BOLD and CBF weighted retinotopic maps. For each subject, we calculated the amount of shift between the phase maps and compared for globally and locally corrected phase maps.

5.2.10 Reproducibility

Finally, in order to assess the reproducibility of BOLD- and CBF-weighted retinotopic mapping, we independently acquired a second functional data set for 3 of the subjects. The same data acquisition and analysis procedure was applied. The two experimental runs were co-registered and the borders and the contour lines obtained from the second experimental run were projected onto that of the first run by resampling onto the surface of the first run and applying corresponding transformation matrixes. The projected borders determined from both runs were displayed on the polar and eccentricity maps to evaluate the similarity of their patterns. To quantitatively assess the reproducibility, the correlation between the two runs for BOLD and perfusion retinotopy, respectively, was calculated.

5.3 Results

5.3.1 Retinotopic mapping with perfusion contrast

Figure 5.2 shows a color plot of the CBF responses to the rotating wedge and expanding ring stimuli on the inflated and flattened cortical surface representations from the right hemisphere of a representative subject. The color scale indicates the raw phase values between 0 and 2π for polar angle and eccentricity. Similar to the well-established BOLD signal retinotopy, CBF activation led to reliable maps throughout the early visual areas.

In the eccentricity map (Figure 5.2.A, 5.2.B), where the fovea is denoted in red and the periphery in blue, there is a systematic increase in phase (red → yellow → green → blue) originating from the occipital pole towards more anterior locations. For the polar angle map, the phase is proportional to the polar angle of the local visual field representation. The upper visual field (UVF) is denoted in blue and the lower visual field (LVF) in red-yellow, each exhibiting alternations between vertical and horizontal (green) meridians.
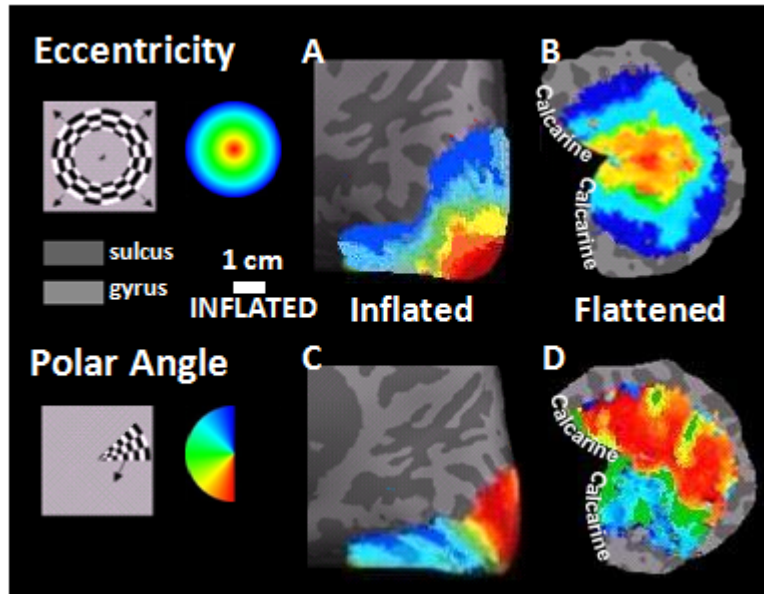
Figure 5.2 *Retinotopic maps created by using CBF signal presented on the inflated and flattened brain surface for polar and eccentricity stimuli from the right hemisphere of a representative subject. In the eccentricity map the fovea is denoted in red and the periphery in blue. For the polar angle map, the upper visual field (UVF) is denoted in blue, the lower visual field (LVF) in red-yellow and horizontal meridian in green.*

5.3.2 Time series of BOLD and CBF signals

Figure 5.3 shows examples of BOLD signal and CBF time series for the same ROIs defined on the eccentricity maps and the corresponding spectral responses (average spectral responses of all 3 ROIs). In concordance with the phase of the vertex in the defined ROIs, the increase in the temporal delay (i.e. phase) of the BOLD and CBF signals from fovea to periphery is clearly observable. The BOLD and CBF signal changes are in physiologically plausible ranges and around 3.5% and 65%, respectively. The peaks at the stimulus frequency and their higher harmonics are clearly observable in the spectrum of both BOLD and CBF time series. The CBF signal has lower SNR, apparent in the lower peak in the power spectrum of figure 5.3.F compared to figure 5.3.C, and in the noisier time-series curves in figure 5.3.E compared to figure 5.3.B. The magnitude of the peak in the BOLD spectrum is around 3 times higher than that of CBF due to the difference in SNR levels. The average SNR

(n=5) is calculated for BOLD maps as 32.7 and for CBF as 11.3 ($SNR_j = \frac{A_j}{\sigma_j}$ see 'Phase and power maps' part).   We also compared the average response curves in the defined ROIs and we did not see any considerable variation in the shapes of the hemodynamic responses.
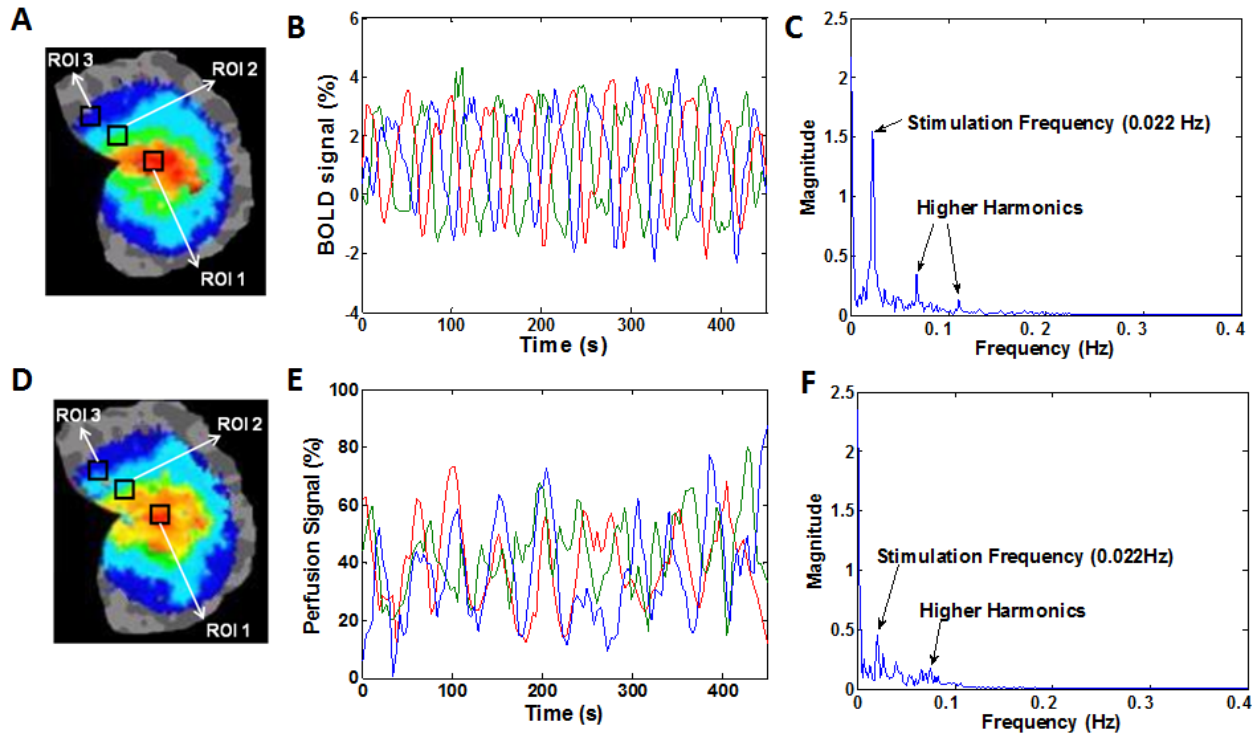
Figure 5.3 *Examples of BOLD signal and CBF time series obtained in the eccentricity data. **(A-C):** ROI locations, time-courses, and Fourier power spectra obtained from BOLD signal. **(D-F):** ROI locations, time-courses, and Fourier power spectra obtained from CBF signal. Identical ROIs are used for both BOLD and CBF signals representing different eccentricities, as shown in **(A and D)**, ROI1: red time course, ROI2: green time course, ROI3: blue time course. Note that while the temporal delay (i.e. phase) of both, BOLD and CBF signals increase from the fovea (centre of map) to the periphery (edge of map), there appear to be also phase-differences between BOLD signal and CBF maps, which are also apparent in the time-courses. The peaks at the stimulus frequency in both Fourier spectra in **C** and **F** are clear although the CBF signal exhibits lower SNR.*

5.3.3 Delineation of visual areas

We consistently identified the dorsal and ventral parts of areas V1-V3 and additionally delineated the hemifield maps of V3A/B and hV4 (V1d, V1v, V2d, V2v, V3d, V3v, V3A/B,

hV4) for each of the 5 subjects. The validity of the delineated areas was visually assessed by comparing the visual field signs [4, 48]. Figure 5.4-A,B,C,D shows the borders between delineated visual areas on the flattened surface for BOLD and perfusion contrasts for a representative subject. V1v-V3v represent the contralateral upper visual quadrants, and V1d-V3d represent the contralateral lower visual quadrants.

In Figure 5.4-A,B the borders of these visual areas are superimposed on the eccentricity map showing that the eccentricity representations of early visual areas run in register by sharing a foveal confluence and extending toward anterior positions with increasing eccentricity [47]. hV4 represents a full hemifield consistent with hV4 models previously proposed [2, 7, 18, 63]. V3A/B also represent a full hemifield, yet in our thresholding the upper visual quadrant and part of the separate foveal representation were cut off [5, 8, 23, 64]. In this study, we limited ourselves to areas V1-V3, V3A/B and hV4, and refrained from attempting to localize areas more dorsal or lateral to V3A/B, or more anterior than hV4 due to the lower SNR available in CBF.
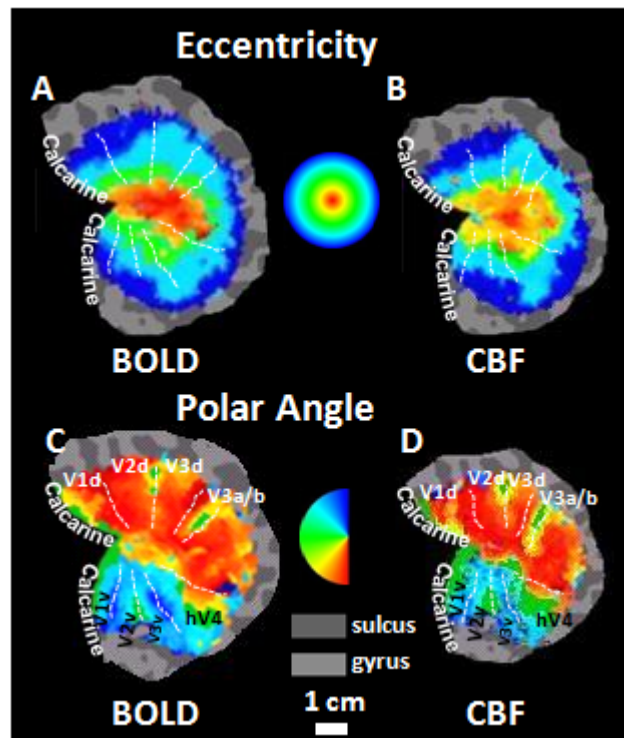
Figure 5.4 *The borders between delineated visual areas (V1, V2, V3, hV4, V3A/B) on the flattened surface for BOLD and perfusion contrasts respectively for the RH of a representative subject.* ***(A,B)*** *eccentricity maps.* ***(C,D)*** *polar angle maps.*

5.3.4 Hemodynamic Delays in BOLD and CBF signals

In order to assess the bias on the retinotopic phase maps induced by the hemodynamic delay time (t_H) that may be spatially non-uniform across the brain, we calculated the t_H for every voxel and averaged it for each of the visual areas, separately for BOLD and CBF signals. Figure 5.5 shows the comparison of hemodynamic delay times (t_H) of BOLD and CBF signals for distinct visual areas. The corresponding average t_H values are listed in table 5.1. The calculated t_H values for BOLD signal were larger than those for CBF signal, implying an earlier perfusion response across the brain. We found that hV4 had the longest delay for both BOLD (5.34 ± 0.62 s (mean ± SD)) and CBF (3.16 ± 0.17 s) signals (Figure 5.5.A). The difference between BOLD and CBF hemodynamic delay times was also calculated for each visual area, with hV4 having the largest difference (2.18 ± 0.32 s) and V2v having the smallest difference (0.98 ± 0.14 s) (Figure 5.5.B) (See Table 5.2 for statistical comparisons). Because there is a relatively high density of larger vessels near the occipital pole containing the foveal visual field representation (see e.g. [35]), we examined the hemodynamic delays of the foveal region compared to the peripheral representation (the foveal ROI was defined as the region surrounded by the inner circle of dashed white lines in Figure 5.7.A and the peripheral ROI was defined as the region between the inner and outer dashed white lines). For both BOLD and CBF signals, t_H at foveal regions was slightly higher than for peripheral sites and the difference was 1.62±0.14 s for the foveal region and 1.36±0.21 s for the peripheral region. Table 5.2 shows the statistical significance of the calculated differences across the visual areas (one-way ANOVA with post-hoc bonferroni correction, p=0.05).

5.3.5 Comparison of locally and globally corrected phase maps

Figure 5.6 shows the voxel-wise comparison of globally and locally corrected retinotopic phase maps, i.e. phase-maps obtained assuming a fixed t_H across all voxels vs. individually estimated t_H for every voxel. The blue line shows the ideal curve that would appear if the vectors overlapped 100% (i.e. when same vectors are used). For this ideal case, the curve has the shape of a monotonically-decreasing exponential function in the interval of [-π +π] with a mirror symmetry along the y axis and the maximum correlation occurring at the origin ($r_0 = 1$). The green and red curves correspond to the correlation coefficient between CBF and BOLD signals as a function of phase-shift between the two, i.e. the distribution of
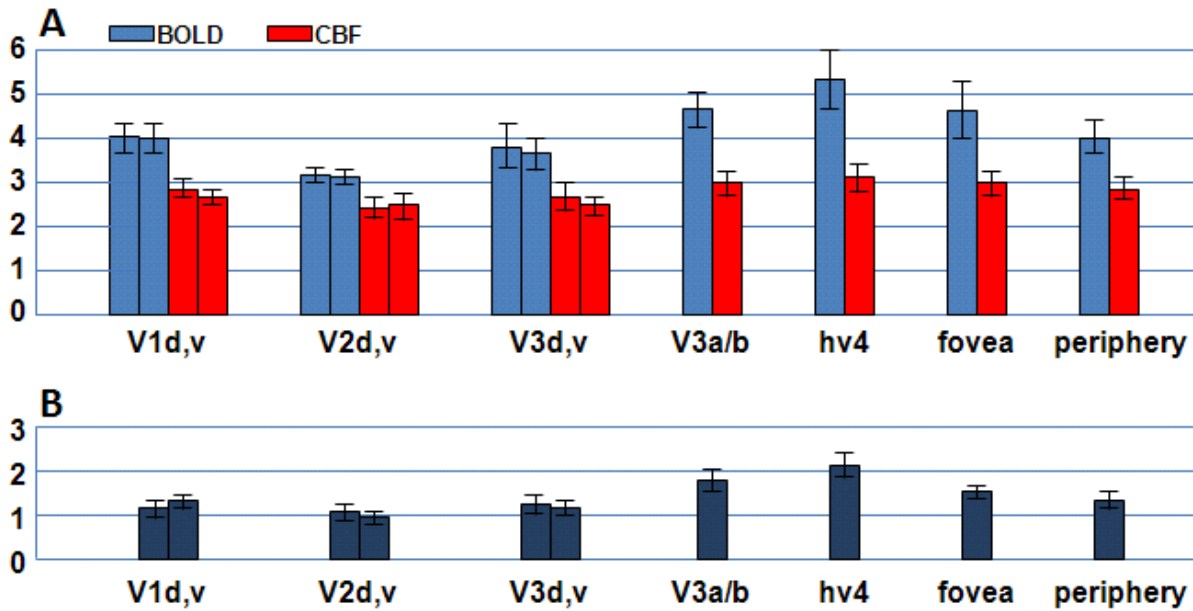
Figure 5.5.A) *Comparison of hemodynamic delay times (t_H) [seconds] of BOLD and CBF signals for distinct visual areas and fovea vs. peripheral sites (averaged across all hemispheres). The first bars represent the dorsal areas and the second bars represent the ventral regions of the visual areas. **B)** The difference of the hemodynamic delay times between BOLD and CBF signals for distinct visual areas and fovea vs. peripheral sites (averaged across all hemispheres).*

Table 5.1 Average (n=5) t_H values (s).

	V1d	V1v	V2d	V2v	V3d	V3v	V3a/b	hV4
BOLD	4.04±0.4	4.01±0.4	3.16±0.21	3.12±0.20	3.84±0.54	3.71±0.39	4.85±0.41	5.34±0.62
CBF	2.88±0.23	2.7±0.22	2.09±0.28	2.14±0.32	2.62±0.3	2.59±0.17	3±0.16	3.16±0.17
difference	1.16±0.21	1.31±0.15	1.07±0.18	0.98±0.14	1.22±0.26	1.12±0.16	1.85±0.28	2.18±0.32

	fovea	periphery
BOLD	4.62±0.61	4.02±0.38
CBF	3±0.21	2.66±0.19
difference	1.62±0.14	1.36±0.21

Table 5.2 Statistical significance of the calculated differences across the visual areas (multiple comparison of one-way anova, alpha=0.05 with bonferroni correction,"*" : statistically significant, p=0.05, "ns": statistically insignificant).

	V1	V2	V3	V3a/b	hV4	fovea	periphery
V1	ns	ns	ns	*	*	ns	ns
V2		ns	ns	*	*	*	ns
V3			ns	*	*	ns	ns
V3a/b				ns	ns	ns	*
hV4					ns	*	*
fovea						ns	ns
periphery							ns

the cross-correlation coefficients between the vectors $\vec{B}$ and $\vec{P}$ vs phase shift. For global correction (t_H =5 s) the maximum correlation between the BOLD and CBF weighted retinotopic maps occurs at a phase shift of 22.96±4.61 degrees (~2.87 s, averaged across maps and subjects). For local correction the best correlation was closer to the origin occurring at the phase shift of 7.21± 0.59 degrees (~0.9 s, averaged across maps and subjects), and had a higher peak compared to the global correlation. Since we kept the $\vec{B}$ vector unchanged and shifted the $\vec{P}$ vector at each step for calculating the $\vec{r_i}$ vector, phase shifts on the negative direction indicate that $\vec{B}$ and $\vec{P}$ vectors align better when the voxel-wise phase values of the perfusion-based maps are slightly reduced. The observed phase shift, therefore, indicates an earlier perfusion signal compared to the BOLD signal. In the case of local correction, the maximum correlation coefficient (r= 0.5±0.07) is slightly higher relative to the global correction (r= 0.44±0.08) case.

Note that a mismatch in phases between perfusion and BOLD signal alone would not be expected to lead to a shift in the boundaries between visual areas, because areal boundaries were defined by the field-signs, and not the absolute phase-shift. For example, the border between V1v and V2v represents the upper vertical meridian of the visual field (see e.g. figure 4C). When the stimulus-wedge rotates from the horizontal towards the upper meridian, the evoked activity stripes in V1v and V2v will move in opposite directions to converge (and 'collide') at their boundary. Their anatomical boundary is defined as this
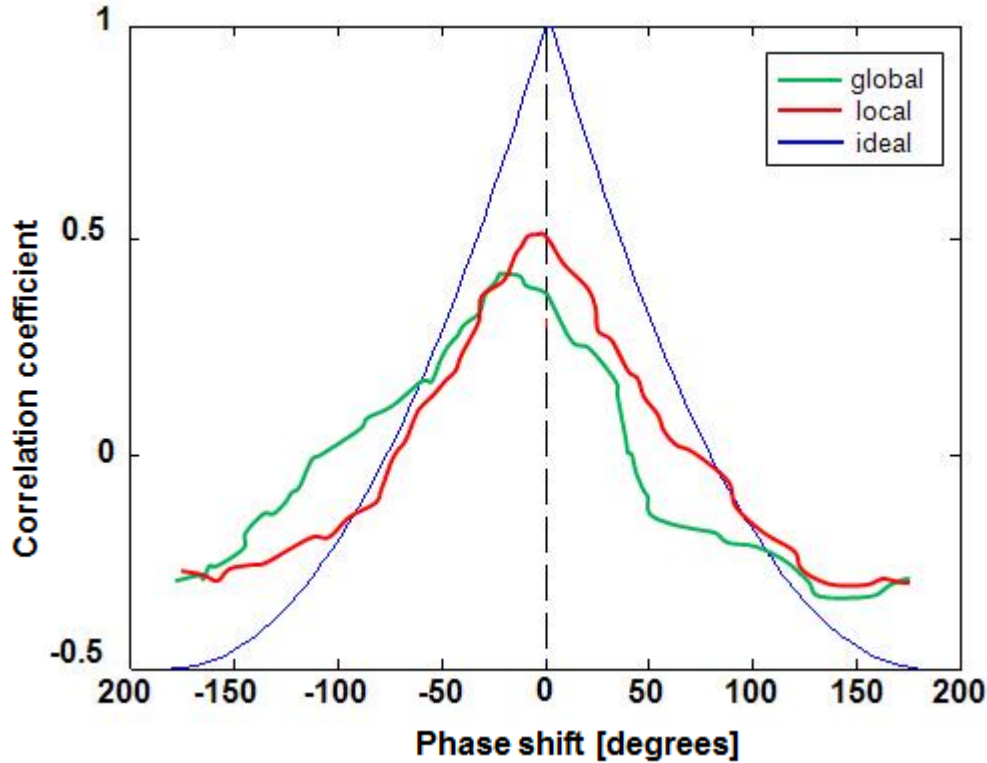
Figure 5.6 *Voxel-wise comparison of globally and locally corrected retinotopic phase maps. Green and red curves corresponds to the distribution of the cross-correlation coefficients between the vectors B and P vs phase shift. The observed phase shift corresponding to the best correlation point is the measure of phase difference between the BOLD and CBF weighted retinotopic maps.*

collision point, i.e. the symmetry axis dividing the two mirror-symmetric activity patterns evoked by the rotating wedge, which stays the same regardless of the signal delay. Therefore, differences in area boundaries between BOLD and perfusion maps are either due to noise, or due to small shifts in field-sign boundaries caused by the different signal types, such as the more precise location of perfusion signals relative to the more draining vein-driven BOLD signals. Table 5.3 lists the average number of voxels and the percentage of overlap at each of the eight distinct topographically organized visual areas obtained from BOLD- and CBF-weighted fMRI signals, separately for right and left hemispheres. The sizes of the identified areas agree quantitatively with previously reported surface area measurements [19, 65]. The percentage of overlap between maps obtained from BOLD- and CBF-weighted signals was good, but nevertheless showing some discrepancy (the overlap was between 72.8% and 89.9%, see Table 5.3).

Table 5.3 Average (n=5) number of voxels and the amount of overlap (%) for each visual area.

	V1d	V1v	V2d	V2v	V3d	V3v	V3a/b	hV4
BOLD (RH)	80.0±8.8	62.2±6.3	81.6±5.9	55.6±4.0	74.4±6.1	57.2±7.0	56.6±6.0	135.0±13.5
BOLD (LH)	84.0±10.6	66.2±10.9	86.0±13.7	55.4±5.6	81.0±6.3	61.0±8.4	52.8±9.6	138.2±11.5
Perf. (RH)	81.4±9.5	64.8±7.5	81.2±5.9	56.8±5.3	75.0±9.9	60.0±3.5	59.8±6.1	139.8±14.1
Perf. (LH)	79.6±11.6	69.2±9.5	87.0±10.7	48.2±4.2	74.8±5.7	55.2±10.2	54.4±7.5	136.4±14.2
Overlap (RH)	89.9±3.8	84.3±8.1	86.6±2.2	84.4±2.2	86.4±2.5	83.8±5.9	87.4±5.9	84.52±5.7
Overlap (LH)	82.03±4.8	88.6±4.7	89.6±4.6	72.8±6.9	78.8±3.1	75.4±8.4	83.9±5.7	73.6±8.7

5.3.6 Reproducibility

In order to illustrate the within-modality reproducibility of both the BOLD and perfusion-weighted retinotopic maps in the same subjects, we obtained two datasets of each (for three of the subjects). Figure 5.7 shows the borders of visual regions obtained from the first and second experiments superimposed, for both BOLD and perfusion-weighted data, to assess the reproducibility of the retinotopic maps. For eccentricity and polar maps (Figure 5.4.A-D), we found that the visual area borders closely matched each other for both BOLD- and CBF-weighted maps with high correlation coefficient values (for bold r=0.79, for CBF r=0.68).

5.4 Discussion

In this study, we used arterial spin labeling (ASL) fMRI that enables the simultaneous acquisition of BOLD- and perfusion-weighted images [66] to i) determine the delineations of early visual areas for retinotopic mapping of the human brain using perfusion data, ii) investigate the variations in hemodynamic delay times across the visual areas, iii) explore the uncertainties in retinotopic maps caused by the measurement artifacts particularly due to the underlying vascular anatomy.

Retinotopy of early visual areas (V1-hV4) using CBF activation was similar to that derived from the BOLD signal but not identical (Figure 5.4). We found considerable variation of signal delays across regions, but also across imaging modalities. There are several potential

explanations for the observed discrepancy in signal latencies, including the differences in the underlying physiology, the physics giving rise to the BOLD and CBF signals, and the
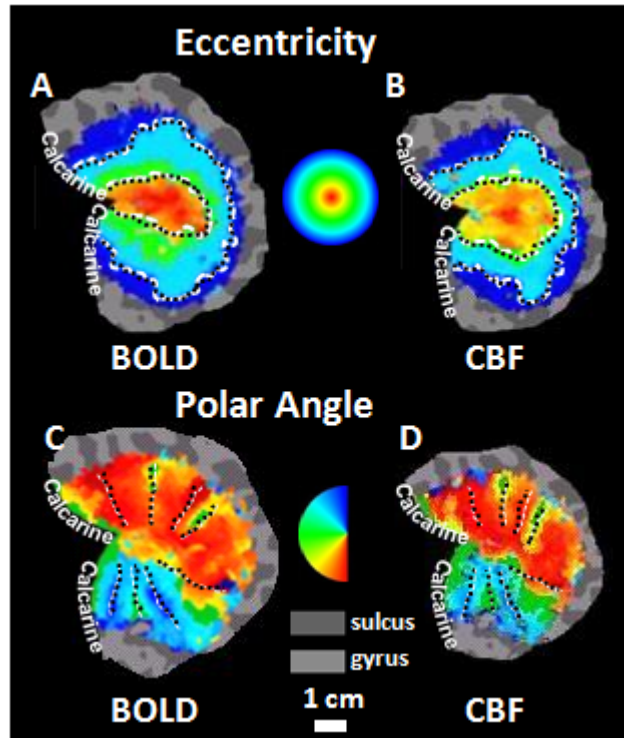
Figure 5.7 *Reproducability of visual area borders obtained in two separate experiments within the same subject, presented on the flattened patch of a representative subject for the RH. For eccentricity maps (A-B), the contour lines of the phase transitions estimated on the basis of two separate experiments exhibit a highly matched pattern. For polar maps (C-D), the visual area borders (white-dashed lines and black-solid lines) closely match each other for both BOLD and CBF weighted maps.*

calculation methods for retinotopic mapping. The BOLD signal at 3T is primarily caused by oxygenation and volume changes in veins ([28], and references therein) whereas ASL is more closely associated with the capillary bed. This difference in the vascular sites contributing to the BOLD and CBF signals might directly correlate with different hemodynamic time-lags relative to each other and with different spatial locations contributing to the observed discrepancy between CBF and BOLD retinotopic maps. It has been suggested that the hemodynamic response is later the more downstream and the

larger the vasculature is, with delays ranging between 4 s (micro-vessels) to 12 s (large draining veins) [66]. Figure 5.5 clearly demonstrates the non-uniform distribution of the hemodynamic delay times (t_H) across the visual areas that is likely due to the macro- or microvascular differences. For example, the results reveal a consistent delay difference between V1 and V2, in that both ventral as well as dorsal V2 show the shortest delays (shorter than V1 located right between them), suggesting area-specific signal delays. These can in principle be due to neural or to anatomical delays, which neuroimaging alone can hardly distinguish [67]. Anatomically, it is known that V1 differs in its micro-vascular density compared to other regions [68], but effects of eccentricity have not been studied so far. From the comparison of the response latencies of BOLD and CBF signals for distinct visual areas and fovea vs. peripheral sites, we saw that the difference in latencies between BOLD and CBF responses were significantly different especially in hV4 relative to the other areas (Figure 5.5, Table 5.1&2). We found corresponding sites of large signal delay differences between the eccentricity and polar angle difference maps, suggesting anatomical rather than stimulus-driven reasons for the observed delay differences. Our results are in good agreement with those of a recent study by Winawer et al (2010) [69] exploring the uncertainties concerning the spatial organization of hV4. They noticed a variance in the visual field maps across subjects, which was particularly strong in the ventral occipital cortex near hV4. By combining the venogram images with retinotopic maps, they reported one likely source of this variance as the dural, transverse and straight sinuses that carry venous blood and converge near the occipital pole. They depicted the relative orientation of the visual maps and dorsal sinuses that introduce significant B_0 inhomogeneities in the nearby ventral cortex. In particular, they reported that the transverse sinus is positioned approximately orthogonal to the B_0 direction, creating a relatively higher change in the B_0 field in the ventral occipital cortex. This makes hV4 especially vulnerable to these artefacts. Therefore, it is conceivable that hV4 and other brain areas closely located due large draining veins may be more accurately explored by using the CBF signal.

One typical approach for retinotopic mapping is average out small differences in HRF delays by combining responses to counter-propagating stimuli following a global lag correction that assumes a fixed delay across the cortex. Warnking et al (2002) [48] assumed a mean

hemodynamic delay of 5 s and [62] observed 5.7 s delay and used 6 s for a global correction. We found that t_H varies in the range of 3.12 s to 5.34 s for BOLD signal even after averaging across areas and subjects, with a smaller range of CBF between 2.09 s to 3.16 s. Due to the considerable differences in t_H we suggested using a local correction of the phases at each voxel with its individually estimated t_H value. We used the correlation of BOLD and CBF weighted maps to figure out the reduced discrepancy between each other. The highest correlations that were also most precise in terms of phase-shift were achieved when using local correction compared to those achieved using global correction, indicating an advantage for using local correction (see figure 5.6). In principle, for locally corrected phase maps, we do not expect any difference between the BOLD and perfusion weighted maps because the correction results the same phase value regardless of the magnitude of the delay. The slight shift around 7.21 degree observed for the local correction is probably due to the SNR differences of the BOLD and perfusion signals and the remaining residual noise. Differences between the BOLD signal and perfusion retinotopy maps might additionally arise from differential susceptibility to image artifacts (i.e. motion), the acquisition parameters of the ASL sequence and the residual errors in the data-analyzing process. However, manual correction of the segmentation errors and motion artifacts do not seem to have played a large role as the retinotopic maps were highly reproducible (see Figure 5.7). ASL sequence parameters were also optimized to reduce contamination of the ASL signal by imaging artifacts, such as transit delay time, magnetization transfer effect, blood-tissue water exchange time and imperfect slice profiles [40]. Functional mapping with ASL data tends to be sensitive to high-frequency noise components and therefore relatively stronger smoothing can be applied without significantly deteriorating the retinotopic mapping. Since we applied 7 mm FWHM surface based smoothing, it was not a goal of the study to allow for a direct and detailed comparison of the spatial specificity of the BOLD and CBF weighted maps. However, using ASL for retinotopic mapping at higher magnetic fields using higher resolution images would allow to study the specificity of both MRI modalities in humans, combined with careful analyses (see e.g. [70]).

Additionally, because of the non-zero echo time (TE), the perfusion measurements included BOLD signal contamination. Ideally TE should be zero for the maximum ASL signal and typically 30-40 ms for a good level of BOLD contrast. We observed that the best trade-

off for a simultaneous acquisition was satisfied around TE=20ms (data not shown). Also, we used surround subtraction to calculate the control-tag difference images. This approach interpolates the ASL data by computing the difference between each image and the average of its two nearest neighbors and therefore does not induce any shift in the calculated BOLD- and CBF-weighted time series. Liu and Wong et al (2005) developed a model to derive analytical expressions for the BOLD contamination on the amplitude of the perfusion estimate [71]. Based on our acquisition parameters and surround subtraction method, the BOLD contribution to the perfusion signal was estimated to be less than 10%, implying that CBF activation signals were dominated by the true CBF change. Simultaneous BOLD and perfusion acquisition scheme shortens the scanning time by half and eliminates the errors of mis-registration between time series acquired separately and can be improved using reverse spiral scanning, with better BOLD and CBF contrast and reduced susceptibility artifacts [72]. Our findings of ~3.5% change in BOLD signal and ~65% change in CBF signal (see Figure 5.3) are in agreement with many previously reported values and are in a physiologically plausible range. Despite the lower sensitivity of the ASL sequence compared to BOLD signal optimized acquisition, it allowed for a clear observation of the retinotopic organization of the early visual cortex. Low frequency noise caused mainly by subject movement and scanner instability also appeared in both spectra. In summary, the biggest source for the discrepancy of the BOLD signal and CBF retinotopic maps seems to stem from the vascular structures involved. A better SNR level could be reached by using continuous type tagging schemes such as pseudo-continuous ASL with a cost of longer transit delay times and higher magnetization transfer effect. Also more optimization for a better trade-off between BOLD and CBF weighting in the simultaneous acquisition by considering the longer transit delay times in the occipital regions could yield better retinotopic mapping, however, with even less SNR for CBF. The perfusion information in the tag images represents only a small change in the image intensity. Typically, at 3T in humans with standard acquisition parameters, the signal-to-noise is lower by a factor of 3-5 in CBF images compared to the BOLD signal. The peaks at the stimulus design frequency (0.022 Hz) were clearly observable in the spectrum of both BOLD and CBF time series (Figure 5.3). The peak for the CBF exhibited relatively lower SNR by a factor of 3 but the SNR levels of both BOLD and CBF were sufficient to yield clear retinotopic maps (see Figure 5.2). A

previous study has also used ASL to explore the resolution and reproducibility of perfusion MRI including visual stimulation with two spatially non-overlapping visual stimuli [73], but it did not directly compare these quantitatively with visual areas obtained using the BOLD signal. In that study, two alternating stimuli were used to excite different patches of V1 in order to evaluate the localization accuracy in the visual system. A similarity coefficient based on the center of gravity of the activation was defined and a substantial overlap between the activation patterns for both stimuli with a large similarity coefficient was reported (on average 0.79-0.84 for perfusion and BOLD respectively and reduced overlap in V1 for perfusion signal). The same study evaluated the reproducibility of the BOLD and perfusion signals using a finger-tapping paradigm to activate the primary sensory and motor cortices and reported no significant difference in the variability of the locus of activity between the BOLD and perfusion data, which is similar to our findings for visual areas.

In summary, we performed perfusion contrast-based retinotopic mapping of the human brain at 3T using ASL and compared the results with those obtained from the BOLD-weighted signal. Although the overlap of both maps was high, we observed significant temporal shifts between the BOLD signal and perfusion maps that most likely reflect differential time-lags and spatial sensitivity of the two imaging signals. We explored the variation of hemodynamic delay times across the visual areas and assessed the differences between the BOLD and CBF signals from the aspects of underlying anatomy and discussed the potential sources of the discrepancy between the BOLD signal and perfusion-based retinotopic maps. We suggest using local correction of the phases to minimize the varying hemodynamic delay time artifacts for improved retinotopic mapping. We assessed the reproducibility of the retinotopy for BOLD and CBF signal. The considerable and systematic differences across visual areas in their mean hemodynamic delays that were identified here emphasize the importance of analysis techniques that remain unbiased by such delays, e.g. those using derivatives of the HRF for event-related studies, or local HRF-delay estimates for retinotopic mapping. Furthermore, the use of ASL to determine retinotopic maps, but also its use for other functional units in other brain systems (i.e. tonotopy in the auditory cortex), are likely to yield most benefit when macroscopic surface veins mask the fine-structure of these units.

References

1. Zeki, S., et al., *A direct demonstration of functional specialization in human visual cortex.* J Neurosci, 1991. **11**(3): p. 641-649.
2. Wandell, B.A., S.O. Dumoulin, and A.A. Brewer, *Visual field maps in human cortex.* Neuron, 2007. **56**(2): p. 366-83.
3. Watson, J.D., et al., *Area V5 of the human brain: evidence from a combined study using positron emission tomography and magnetic resonance imaging.* Cereb Cortex, 1993. **3**(2): p. 79-94.
4. Sereno, M.I., et al., *Functional MRI reveals borders of multiple visual areas in humans.* Science, 1995. **268**: p. 889 - 893.
5. DeYoe, E.A., et al., *Mapping striate and extrastriate visual areas in human cerebral cortex.* Proc. Natl. Acad. Sci., 1996. **93**: p. 2382 - 2386.
6. Engel, S.A., G.H. Glover, and B.A. Wandell, *Retinotopic organization in human visual cortex and the spatial precision of functional MRI.* Cerebral Cortex, 1997. **7**: p. 181-192.
7. Brewer, A.A., et al., *Visual field maps and stimulus selectivity in human ventral occipital cortex.* Nat Neurosci, 2005. **8**(8): p. 1102-9.
8. Sereno, M.I., S. Pitzalis, and A. Martinez, *Mapping of contralateral space in retinotopic coordinates by a parietal cortical area in humans.* Science, 2001. **294**(5545): p. 1350-4.
9. Sereno, M.I., *Brain mapping in animals and humans.* Curr Opin Neurobiol, 1998. **8**(2): p. 188-194.
10. Tootell, R.B. and J.B. Taylor, *Anatomical evidence for MT and additional cortical visual areas in humans.* Cereb Cortex, 1995. **5**(1): p. 39-55.
11. Tootell, R.B., et al., *Functional analysis of V3A and related areas in human visual cortex.* J Neurosci, 1997. **17**(18): p. 7060-78.
12. Huk, A.C., R.F. Dougherty, and D.J. Heeger, *Retinotopy and functional subdivision of human areas MT and MST.* J Neurosci, 2002. **22**(16): p. 7195-205.
13. Hasson, U., et al., *Large-scale mirror-symmetry organization of human occipito-temporal object areas.* Neuron, 2003. **37**(6): p. 1027-41.
14. Silver, M.A., D. Ress, and D.J. Heeger, *Topographic maps of visual spatial attention in human parietal cortex.* J Neurophysiol, 2005. **94**(2): p. 1358-71.
15. Swisher, J.D., et al., *Visual topography of human intraparietal sulcus.* J Neurosci, 2007. **27**(20): p. 5326-37.
16. Engel, S.A., et al., *fMRI of human visual cortex.* Nature, 1994. **369, 370 [erratum]**(6481): p. 525, 106 [erratum].
17. Tootell, R.B. and N. Hadjikhani, *Where is 'dorsal V4' in human visual cortex? Retinotopic, topographic and functional evidence.* Cereb Cortex, 2001. **11**(4): p. 298-311.
18. Wade, A.R., et al., *Functional measurements of human ventral occipital cortex: retinotopy and colour.* Philos Trans R Soc Lond B Biol Sci, 2002. **357**(1424): p. 963-73.
19. Dougherty, R.F., et al., *Visual field representations and locations of visual areas V1/2/3 in human visual cortex.* J Vis, 2003. **3**(10): p. 586-98.
20. Endo, S., et al., *Mapping visual field with positron emission tomography by mathematical modeling of the retinotopic organization in the calcarine cortex.* IEEE Trans Med Imaging, 1997. **16**(3): p. 252-60.
21. Smith, A.T., et al., *Estimating receptive field size from fMRI data in human striate and extrastriate visual cortex.* Cereb Cortex, 2001. **11**(12): p. 1182-90.
22. Wandell, B.A., *Computational neuroimaging of human visual cortex.* Annu Rev Neurosci, 1999. **22**: p. 145-73.
23. Tootell, R.B., et al., *The retinotopy of visual spatial attention.* Neuron, 1998. **21**(6): p. 1409-22.
24. Saygin, A.P. and M.I. Sereno, *Retinotopy and attention in human occipital, temporal, parietal, and frontal cortex.* Cereb Cortex, 2008. **18**(9): p. 2158-68.

25.   Brefczynski, J.A. and E.A. DeYoe, *A physiological correlate of the 'spotlight' of visual attention.* Nat Neurosci, 1999. **2**(4): p. 370-4.

26.   Boynton, G.M., *Attention and visual perception.* Curr Opin Neurobiol, 2005. **15**(4): p. 465-9.

27.   Logothetis, N.K., *What we can do and what we cannot do with fMRI.* Nature, 2008. **453**(7197): p. 869-78.

28.   Uludag, K., B. Muller-Bierl, and K. Ugurbil, *An integrative model for neuronal activity-induced signal changes for gradient and spin echo functional imaging.* Neuroimage, 2009. **48**(1): p. 150-65.

29.   Song, A.W., et al., *Diffusion weighted fMRI at 1.5T.* Magn. Reson. Med., 1996. **35**(2): p. 155-158.

30.   Lai, S., et al., *Identification of vascular structures as a major source of signal contrast in high resolution 2D and 3D functional activation imaging of the motor cortex at 1.5T: preliminary results.* Magn. Reson. Med, 1993. **30**: p. 387-392.

31.   Boxerman, J.L., et al., *The intravascular contribution to fMRI signal change: Monte Carlo modeling and diffusion-weighted studies in vivo.* Magn. Reson. Med., 1995. **34**: p. 4-10.

32.   Buxton, R.B., E.C. Wong, and L.R. Frank, *Dynamics of blood flow and oxygenation changes during brain activation: the balloon model.* Magn. Reson. Med., 1998. **39**: p. 855-864.

33.   Ugurbil, K., L. Toth, and D.S. Kim, *How accurate is magnetic resonance imaging of brain function?* Trends Neurosci, 2003. **26**(2): p. 108-14.

34.   Lee, A.T., G.H. Glover, and C.H. Meyer, *Discrimination of large venous vessels in time-course spiral blood-oxygen-level-dependent magntic-resonance functional neuroimaging.* Magn. Reson. Med., 1995. **33**: p. 745 -754.

35.   Saad, Z.S., et al., *Analysis and use of FMRI response delays.* Hum Brain Mapp, 2001. **13**(2): p. 74-93.

36.   Birn, R.M., Z.S. Saad, and P.A. Bandettini, *Spatial heterogeneity of the nonlinear dynamics in the FMRI BOLD response.* Neuroimage, 2001. **14**(4): p. 817-26.

37.   Detre, J.A., et al., *Perfusion imaging.* Magn. Reson. Med., 1992. **23**: p. 37-45.

38.   Wong, E.C., R.B. Buxton, and L.R. Frank, *Quantitative imaging of perfusion using a single subtraction (QUIPSS and QUIPSS II).* Magn. Reson. Med., 1998. **39**: p. 702-708.

39.   Silva, A.C., D.S. Williams, and A.P. Koretsky, *Evidence for the exchange of arterial spin -labeled water with tissue water in rat brain from diffusion-sensitized measurements of perfusion.* Magn. Reson. Med., 1997. **38**: p. 232-237.

40.   Wong, E.C., R.B. Buxton, and L.R. Frank, *Implementation of quantitative perfusion imaging techniques for functional brain mapping using pulsed arterial spin labeling.* NMR in Biomed, 1997. **10**: p. 237-249.

41.   Duong, T.Q., et al., *Localized cerebral blood flow response at submillimeter columnar resolution.* Proc Natl Acad Sci U S A, 2001. **98**(19): p. 10904-9.

42.   Luh, W.M., et al., *Comparison of simultaneously measured perfusion and BOLD signal increases during brain activation with T(1)-based tissue identification.* Magn Reson Med, 2000. **44**(1): p. 137-43.

43.   Tjandra, T., et al., *Quantitative assessment of the reproducibility of functional activation measured with BOLD and MR perfusion imaging: implications for clinical trial design.* Neuroimage, 2005. **27**(2): p. 393-401.

44.   Aguirre, G.K., et al., *Experimental design and the relative sensitivity of BOLD and perfusion fMRI.* Neuroimage, 2002. **15**(3): p. 488-500.

45.   Wang, J., et al., *Arterial spin labeling perfusion fMRI with very low task frequency.* Magn Reson Med, 2003. **49**(5): p. 796-802.

46.   Cavusoglu, M., Yesilyurt, B., Bartels, A., Uludag, K. , *Retinotopy of the human visual cortex with perfusion contrast using arterial spin labeling*, in *Human Brain Mapping Conference*2010: Barcelona.

47. Wandell, B.A., A.A. Brewer, and R.F. Dougherty, *Visual field map clusters in human cortex.* Philos Trans R Soc Lond B Biol Sci, 2005. **360**(1456): p. 693-707.

48. Warnking, J., et al., *fMRI retinotopic mapping--step by step.* Neuroimage, 2002. **17**(4): p. 1665-83.

49. Dale, A.M., B. Fischl, and M.I. Sereno, *Cortical surface-based analysis. I. Segmentation and surface reconstruction.* Neuroimage, 1999. **9**(2): p. 179-94.

50. Fischl, B., M.I. Sereno, and A.M. Dale, *Cortical surface-based analysis. II: Inflation, flattening, and a surface-based coordinate system.* Neuroimage, 1999. **9**(2): p. 195-207.

51. Fischl, B., et al., *High-resolution intersubject averaging and a coordinate system for the cortical surface.* Hum Brain Mapp, 1999. **8**(4): p. 272-84.

52. Smith, S.M., et al., *Advances in functional and structural MR image analysis and implementation as FSL.* Neuroimage, 2004. **23 Suppl 1**: p. S208-19.

53. Cavusoglu, M., et al., *Comparison of pulsed arterial spin labeling encoding schemes and absolute perfusion quantification.* Magn Reson Imaging, 2009. **27**(8): p. 1039-45.

54. Dale, A.M. and M.I. Sereno, *Improved localization of cortical activity by combining EEG and MEG with MRI cortical surface reconsteruction: A linear approach.* Journal of Cognitive Neuroscience, 1993. **5**: p. 162-177.

55. Chung, M.K., et al., *Cortical thickness analysis in autism with heat kernel smoothing.* Neuroimage, 2005. **25**(4): p. 1256-65.

56. Kastrup, A., et al., *Regional variability of cerebral blood oxygenation response to hypercapnia.* Neuroimage, 1999. **10**(6): p. 675-81.

57. Hagler, D.J., Jr. and M.I. Sereno, *Spatial maps in frontal and prefrontal cortex.* Neuroimage, 2006. **29**(2): p. 567-77.

58. Pitzalis, S., et al., *Human v6: the medial motion area.* Cereb Cortex, 2006. **20**(2): p. 411-24.

59. Sereno, M.I. and R.B. Tootell, *From monkeys to humans: what do we now know about brain homologies?* Curr Opin Neurobiol, 2005. **15**(2): p. 135-44.

60. DeYoe, E.A., et al., *Functional magnetic resonance imaging (FMRI) of the human brain.* J. Neuroscience Methods, 1994. **54**: p. 171-187.

61. Dumoulin, S.O., et al., *Automatic volumetric segmentation of human visual retinotopic cortex.* Neuroimage, 2003. **18**(3): p. 576-87.

62. White, B.R. and J.P. Culver, *Phase-encoded retinotopy as an evaluation of diffuse optical neuroimaging.* Neuroimage, 2010. **49**(1): p. 568-77.

63. Bartels, A. and S. Zeki, *The architecture of the colour centre in the human visual brain: new results and a review.* Eur J Neurosci, 2000. **12**(1): p. 172-93.

64. Press, W.A., et al., *Visual areas and spatial summation in human visual cortex.* Vision Res, 2001. **41**(10-11): p. 1321-32.

65. Amunts, K., et al., *Brodmann's areas 17 and 18 brought into stereotaxic space-where and how variable?* Neuroimage, 2000. **11**(1): p. 66-84.

66. !!! INVALID CITATION !!!

67. Bartels, A., N.K. Logothetis, and K. Moutoussis, *fMRI and its interpretations: an illustration on directional selectivity in area V5/MT.* Trends Neurosci, 2008.

68. Weber, B., et al., *The Microvascular System of the Striate and Extrastriate Visual Cortex of the Macaque.* Cereb Cortex, 2008.

69. Winawer, J., et al., *Mapping hV4 and ventral occipital cortex: the venous eclipse.* J Vis, 2010. **10**(5): p. 1-22.

70. Schira, M.M., et al., *The foveal confluence in human visual cortex.* J Neurosci, 2009. **29**(28): p. 9050-8.

71. Liu, T.T. and E.C. Wong, *A signal processing model for arterial spin labeling functional MRI.* Neuroimage, 2005. **24**(1): p. 207-15.

72.   Yang, Y., et al., *Simultaneous perfusion and BOLD imaging using reverse spiral scanning at 3T: characterization of functional contrast and susceptibility artifacts.* Magn Reson Med, 2002. **48**(2): p. 278-89.

73.   van Gelderen, P., et al., *Resolution and reproducibility of BOLD and perfusion functional MRI at 3.0 Tesla.* Magn Reson Med, 2005. **54**(3): p. 569-76.

Chapter 6

Applications of ASL in Neuroscience

Overview

Arterial spin labeling (ASL) techniques currently became a widely used tool to address questions in neuroscience. In this part, we present three studies performed in collaboration with neuroscientist as examples of ASL applications. The peer-reviewed papers published as being co-author compose this chapter.

In the first study entitled "Quantifying the Link between Anatomical Connectivity, Gray Matter Volume and Regional Cerebral Blood Flow: An Integrative MRI Study", we quantified the covariation of local anatomical connectivity, gray matter volume and perfusion by conducting an integrative MRI study on 23 subjects, utilizing a combination of diffusion tensor imaging, arterial spin labeling and anatomical imaging. Based on our hypothesis that local connectivity, gray matter volume and perfusion are linked, we correlated these measures and particularly isolated the covariation of connectivity and perfusion by statistically controlling for gray matter volume. We found significant levels of covariation on the group- and region-wise level, particularly in regions of the default brain mode network.

In the second study, we explored the differential effects of intranasal insulin and caffeine on cerebral blood flow (CBF). To test whether insulin has a specific effect on CBF and BOLD response under euglycaemic conditions, we used an intranasal insulin application and simultaneously measured the corresponding BOLD and CBF responses by using ASL-fMRI. Furthermore, we compared the insulin effect with caffeine. We hypothesized that intranasal insulin will not change CBF, both during the basal and task-induced state, in comparison with the pre-dose measurement. Caffeine, however, as a vasoconstrictive agent should lead to a pronounced decrease in CBF in relation to the pre-dose measurement. We found that insulin had no effect on basal CBF and task-induced CBF in comparison with drug-free baseline measurement in the visual cortex and control regions. After caffeine application, however, there was a significant decrease of CBF during stimulation in the visual cortex. The BOLD response was not altered by insulin or caffeine between pre- and post-dose measurements. In summary, we found no evidence for a direct vasodilatory effect of intranasal insulin on the cerebral vascular system.

In the third study, we aimed to investigate whether displacements between transcranial magnetic stimulation (TMS) and fMRI might rely on the fMRI sequence used. We

hypothesized that at 3 T, spin echo (SE) BOLD and ASL-CBF may provide more accurate information in terms of functional localization of the motor hand area than gradient echo (GRE) BOLD. In particular, we aimed to test the hypothesis that spatial differences are functionally relevant by stimulating brain tissue at fMRI peak voxel coordinates with single-pulse neuronavigated TMS. Finally, we aimed to answer the question whether the spatially more accurate fMRI sequences better match with optimal TMS sites for evoking highest motor responses. Our findings imply that spatial differences between fMRI and TMS are unlikely to be caused by spatial mismatch of GRE-BOLD fMRI but might be attributed to other factors, e.g., interactions between TMS-induced electric field and neural tissue. Differences between techniques should be kept in mind when using fMRI coordinates as TMS (intervention) targets.

6.1 Quantifying the Link between Anatomical Connectivity, Gray Matter Volume and Regional Cerebral Blood Flow: An Integrative MRI Study

PLoS one

Quantifying the Link between Anatomical Connectivity, Gray Matter Volume and Regional Cerebral Blood Flow: An Integrative MRI Study

Bálint Várkuti[1,3]*, **Mustafa Cavusoglu[2]**, **Alexander Kullik[4]**, **Björn Schiffler[5]**, **Ralf Veit[1]**, **Özge Yilmaz[1]**, **Wolfgang Rosenstiel[4]**, **Christoph Braun[1,6]**, **Kamil Uludag[2]**, **Niels Birbaumer[1,7]**, **Ranganatha Sitaram[1]**

1 Institute of Medical Psychology and Behavioral Neurobiology, University of Tübingen, Tübingen, Baden-Württemberg, Germany, 2 Max Planck Institute for Biological Cybernetics, Tübingen, Baden-Württemberg, Germany, 3 Graduate Training Centre of Neuroscience, International Max Planck Research School, Tübingen, Baden-Württemberg, Germany, 4 Wilhelm-Schickard Institute for Computer Engineering, University of Tübingen, Tübingen, Baden-Württemberg, Germany, 5 Institute of Psychology, Albert-Ludwigs-University, Freiburg im Breisgau, Baden-Württemberg, Germany, 6 CIMeC - Centro interdipartimentale Mente/Cervello, Rovereto, Trento, Italy, 7 Ospedale San Camillo, Istituto di Ricovero e Cura a Carattere Scientifico, Venezia, Veneto, Italy

Abstract

Background: In the graph theoretical analysis of anatomical brain connectivity, the white matter connections between regions of the brain are identified and serve as basis for the assessment of regional connectivity profiles, for example, to locate the hubs of the brain. But regions of the brain can be characterised further with respect to their gray matter volume or resting state perfusion. Local anatomical connectivity, gray matter volume and perfusion are traits of each brain region that are likely to be interdependent, however, particular patterns of systematic covariation have not yet been identified.

Methodology/Principal Findings: We quantified the covariation of these traits by conducting an integrative MRI study on 23 subjects, utilising a combination of Diffusion Tensor Imaging, Arterial Spin Labeling and anatomical imaging. Based on our hypothesis that local connectivity, gray matter volume and perfusion are linked, we correlated these measures and particularly isolated the covariation of connectivity and perfusion by statistically controlling for gray matter volume. We found significant levels of covariation on the group- and regionwise level, particularly in regions of the Default Brain Mode Network.

Conclusions/Significance: Connectivity and perfusion are systematically linked throughout a number of brain regions, thus we discuss these results as a starting point for further research on the role of homology in the formation of functional connectivity networks and on how structure/function relationships can manifest in the form of such trait interdependency.

Introduction

Recent findings are beginning to shed light on the organisational principles behind the structure of the brain [1]. Instead of studying the brain merely as an agglomeration of individual regions with their very specific functions and structural idiosyncrasies, this research, with its new and more systemic perspective, is trying to understand the fundamental lines along which structure/function relationships form [2–5].

Such principles are identified by studying the parts (e.g. brain regions) and analysing the global properties of the entire system that emerge from links between the parts (e.g. white matter connections). The network of white matter connections in the brain seems to adhere to a small-world organisation principle, defined by short path lengths for reaching any part from any other part, while providing high clustering and highly efficient wiring.

Once such a property is established, relations to properties of other systems can be analysed.

The shared small-world properties of interregional gray matter structural similarity [6–7] and white matter connectivity, and the small-world properties of functional brain networks as assessed with electroencephalography [8], are recent examples that certain common principles of organisation can be found in a multitude of brain systems and on a number of scales [9].

As some of these traits, such as number of synapses, cell body population, perfusion and type and quantity of neural fiber bundles have proven to be examinable using advanced imaging methods of spectroscopy, perfusion, structural or diffusion MRI, brain regions can now be characterised regarding multiple traits at once. In certain cases the relationship between different structural properties is formed in a systematic way, e.g. larger brain regions tend to have more connections than smaller brain regions. In other

cases, structural and functional traits are also systematically coupled, e.g. the neural computations that take place in a particular brain region are partially shaped by the quantity, quality and usage of the in- and outgoing connections of that region. In turn the principle of functional (computational) segregation - as reflected in the typology of unimodal motor and sensory or heteromodal association areas of the cortex - is known to be mirrored both in the macroscopic white matter network topology [10] and in functional connectivity networks [11]. The afferent and efferent white matter connections of the motor system, the ascending pathways of the primary sensory cortices and the rich interconnectivity of the association areas are not uncoupled from the function of these areas, but rather allow us to formulate hypotheses on their functional roles.

Mounting evidence suggests [12–15] that certain functional traits - such as the activity profile of a brain region arising from its function and its metabolic demand as reflected e.g. by local capillary density - are closely coupled [16,17]. Local metabolic demand and perfusion are directly linked in the healthy brain, thus allowing the indirect assessment of metabolism through means of perfusion weighted imaging.

If local white matter connectivity shapes neurocomputational processes, and these processes influence local function and therefore metabolic demand, one could hypothesise that local white matter connectivity and local perfusion might be coupled throughout the brain as well. If this were the case, such coupling would constitute the manifestation of a supply-and-demand-principle - the metabolic demand being shaped by connectivity - in the formation of a previously undocumented structure/function relationship.

In order to quantify the outlined traits of perfusion and white matter connectivity we conducted an integrative MRI study on 23 healthy subjects (divided into two groups of 11 and 12 participants), utilising a combination of Diffusion Tensor Imaging (DTI), Arterial Spin Labeling (ASL) and anatomical imaging.

DTI and ASL are methods to non-invasively characterise white matter structure and gray matter function of the brain, respectively [18–19]. While DTI allows for the estimation of anatomical connectivity between regions of the brain, ASL represents a MRI method for the quantification of global and regional Cerebral Blood Flow (rCBF).

DTI based tractography can be used to characterise the amount and integrity of white matter tracks between two regions and allows for an estimation of connection probability. For this purpose, probability density maps can be formed from the repeated propagation of curves through the DTI-based tensor field, which is representing local white matter orientation. Currently, DTI data are integrated into graph representations [20,21] of the white matter network in order to analyse the relation of network topology to function [22] and its impairment [23]. This type of network modelling has originated from the broader discipline of graph theory [24], which is dedicated to the understanding of the emergence of certain global and local properties of a given system from the distribution of pairwise relations of parts of that system (e.g. if many nodes have one connection to another single node, the sum of these connections or edges make that node the hub of the system).

This approach allows for the quantification of node specific traits (e.g. the number of edges connecting one node to others nodes, termed degree), edge specific traits (e.g. how severely a network is affected by the removal of an edge) and general graph properties (e.g. how efficient is the information transfer from any point A to any point B in general).

ASL [25,26] on the other hand has proven to be a sensitive and reliable method for the quantification of gray matter perfusion,

defined as the volume of arterial blood delivered to the capillary bed per unit volume of brain tissue per unit time. It has been utilised to study brain function following neuronal activation, as well as for the detection of changes of perfusion occurring during brain pathology, maturation and aging [27,28]. This is done by assessing the inflow of magnetically labelled arterial water spins into an imaging slice. For quantitative measurement of rCBF, ASL constructs images following a tagging of inflowing arterial blood by a 180° radiofrequency inversion pulse and, in an interleaved fashion, acquiring control images without prior tagging, so that the subtraction of these two images (control-tag) only leaves magnetisation proportional to the blood flow.

So far, only limited attention has been paid to possible synergies from the combined use of these two imaging modalities. As a result, the link between white matter network connectivity and rCBF has not yet been systematically addressed. Currently, there are a few studies focusing on rCBF alterations and changes in white matter integrity (e.g. level of myelinisation, orientation of fibers) as markers of Alzheimer's disease (AD) and mild cognitive impairment [29], but the number of systematic studies using state of the art imaging of both modalities in the same sample is low. White matter lesions in the frontal lobe were found [30] to be correlated with a lower CBF in the elderly. [31] reported that rCBF reductions in the parietal cortex are correlated with white matter integrity reductions in the Posterior Cingulum in a healthy sample. However, evidence for a systematic relationship between white matter network topology and rCBF has yet to be established.

Following our hypothesis that local metabolic demands are largely determined by the connectivity profile of a brain region, we assumed that local perfusion and local connectivity measures of gray matter regions are to be correlated. In order to take into account the properties of the gray matter regions themselves (e.g. a region with larger volume might show higher perfusion and higher degree), we integrated a Voxel-based Morphometry (VBM) analysis into our design. VBM is an established method [32,33] for the quantification of volumetric differences for the entire brain and its subparts based on anatomical MRI images.

Our approach allows for the analysis of the entire trait triplet of gray matter volume (GMV), white matter connectivity and perfusion at once.

Using this multi-facetted data we analysed the connectivity/ perfusion-covariation profiles for regions of the Automated Anatomical Labeling (AAL) atlas, while controlling for GMV (see Figure 1).

For the further analysis we divided the regions into the region classes cortical, subcortical and regions of the Default Brain Mode Network (DMN). The rationale for this division are manifold, on the one hand the graph theoretical and perfusion specific characterisation of subcortical regions is a novelty of this study, on the other hand it stands to reason that vasculature and connectivity systematically differ between cortical and subcortical regions and thus should be considered separately. Because we were particularly interested in the covariation profiles of regions with documented high resting state activity, we subdivided the class of cortical regions further into a DMN regions class. These region classes were comprehensively analysed on the individual-, group- and regionwise levels while controlling for local GMV. Furthermore we report on the correlation between perfusion with GMV, as well as GMV and perfusion with graph theoretical properties of white matter connectivity, respectively.

We employed a probabilistic tractography approach for the estimation of our white matter connectivity graphs and provide results from not one, but many plausible white matter networks (connectomes). Whereas the state of the art does currently not serve with unambiguous properties of a commonly accepted
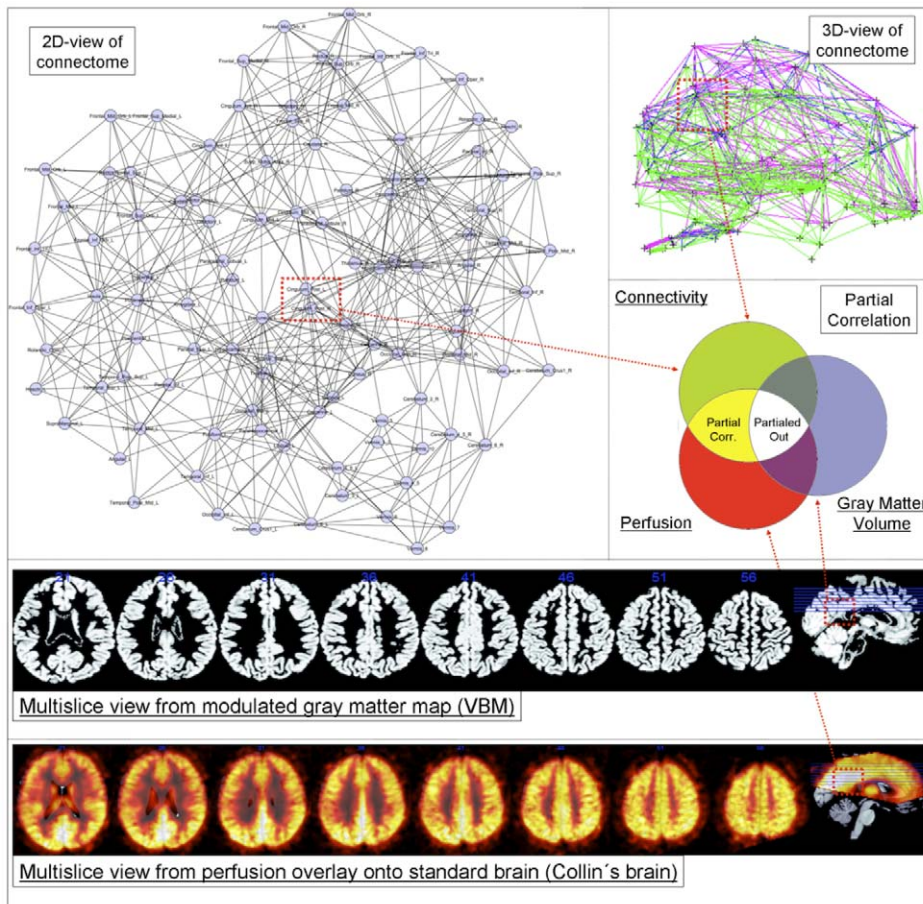
Figure 1. General principle. Graph theoretical properties of the nodes (in this example Posterior Cingulate) are correlated with their relative perfusion (multi-slice example in low row) while controlling for GMV (multi-slice example in upper row) - left-upper 2D graph in background formed by using the Spring Embedder Algorithm on a group averaged connectome for cortico-cortical sparsity 11%. In our PC approach we partial out the statistical influence of GMV in order to assess the covariation of perfusion and connectivity directly.
doi:10.1371/journal.pone.0014801.g001

connectome standard, we provide results from a sweep over plausible edge probability thresholds and resulting cortico-cortical sparsity values in Figure 2.

Results

2.1 White matter network topology

Adjacency graphs such as connectomes can be described regarding their small-world properties using path length, clustering and the ratio of both. Relative path length is calculated as the current path length in a given adjacency graph relative to the path length in an equal random graph and expressed in the coefficient Lambda. The coefficient Gamma is calculated analogously for clustering and the coefficient Sigma is defined as Gamma/Lambda ratio, respectively.

The estimated connectomes of all subjects showed small-world characteristics (Group 1, Lambda $M = 1.3413$ $SD = 0.0121$; Gamma $M = 5.1155$ $SD = 0.5179$; Sigma $M = 3.6525$ $SD = 0.3181$; Group 2, Lambda $M = 1.3283$ $SD = 0.0218$; Gamma $M = 4.6459$ $SD = 0.54341$; Sigma $M = 4.2216$ $SD = 0.3260$) as described by [10] for the plausible cortico-cortical sparsity sweep range of 11–17%.

The different DTI scanning parameters (higher number of diffusion directions and better spatial resolution for Group 2) for both groups resulted in Group 2 showing higher Sigma values for

the sweep range than Group 1 for comparable sparsity values. Further it is to note that thresholding with equal edge probability values in both groups consistently lead to a higher number of accepted edges for the connectomes of Group 2.

Small-world property analyses for interregional GMV and perfusion correlations are provided in Text S1.

2.2 General sample characteristics

To address relation between the total rCBF in non-cerebellar regions of the brain and whole-brain graph theoretical metrics, we tested for such correlations in each group. For this analysis, whole-brain connection density, Lambda, Gamma, average degree, clustering coefficient and global efficiency values for the brain of each subject were paired with the same individual's average rCBF values (ASL measured in resting state), derived from of all non-cerebellar brain regions. These variables were tested for potential correlations (Spearman's rho) with graph metrics resulting from each step of the sweep over plausible edge probability thresholds. For each group p-values for all thresholding steps were False Discovery Rate (FDR, $p < 0.05$) corrected. No significant results were obtained.

With respect to regional properties, as expected relative perfusion (after within-subject normalisation) was found to be higher in DMN regions than in other regions of the cortex (two-
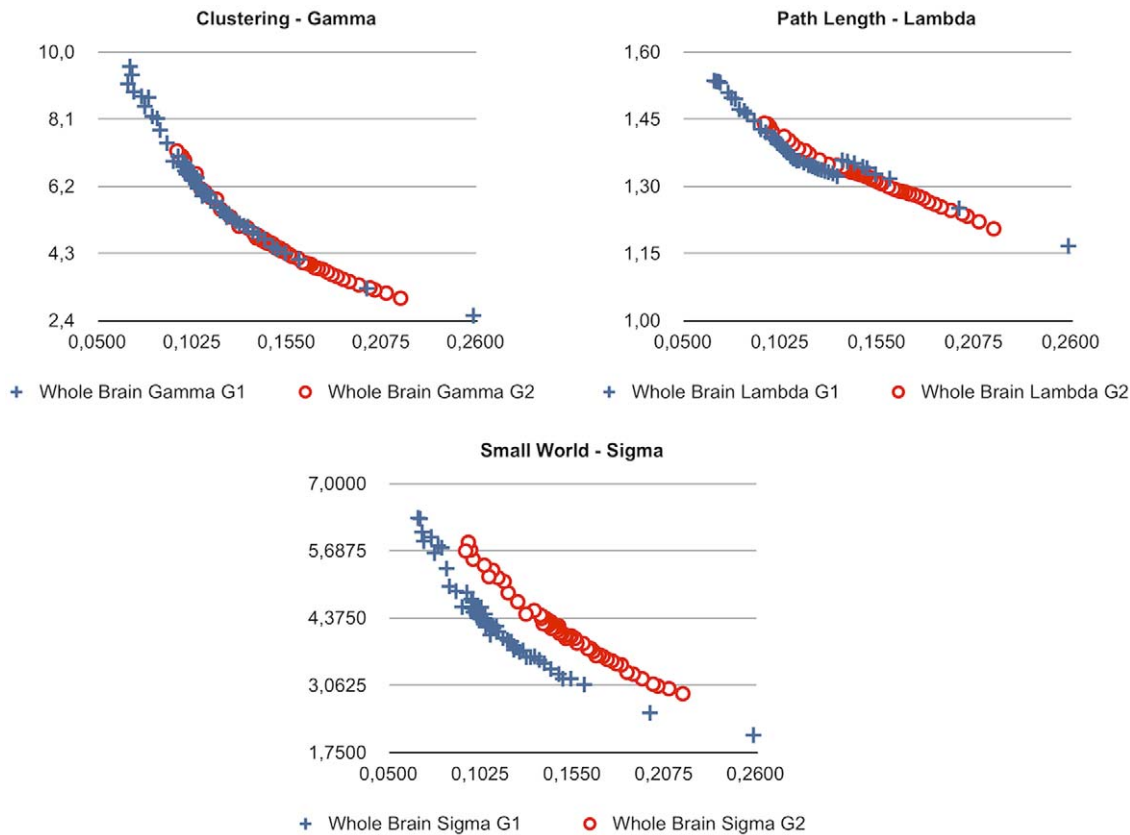
Figure 2. Changes in white matter topology for the whole-connectome values of Gamma, Lambda and Sigma (y-axis) and cortico-cortical sparsity (x-axis, 1 = 100%) for Group 1 and Group 2.
doi:10.1371/journal.pone.0014801.g002

sample t-test, p = 0.0019), in accordance with our hypothesis. The difference between total perfusion (unnormalised rCBF) in regions of the DMN and the rest of the cortex showed a tendency towards significance (two-sample t-test, p = 0.0723). Regions of the DMN had significantly higher relative GMV than other regions of the cortex (two-sample t-test, p = 7.6283*10^{-8}).

2.3 Correlation between perfusion, connectivity and GMV

The correlation between perfusion and graph metrics for cortical, subcortical and DMN regions for connectomes from the plausible cortico-cortical sparsity range of 11–17% [20] with their respective minima and maxima magnitudes (Spearman's rho correlation, all FDR, p<0.05 corrected) are reported for both groups in Figures 3, 4, 5 and Table 1.

The correlation between GMV and graph metrics for cortical, subcortical and DMN regions for connectomes from the plausible cortico-cortical sparsity range of 11–17% [20] with their respective minima and maxima magnitudes (Spearman's rho correlation, all FDR, p<0.05 corrected) are reported for both groups in Figures 6, 7, 8 and Table 2.

The correlation between GMV and perfusion for cortical, subcortical, all non-cerebellar and DMN regions (Pearson's correlation, all FDR, p<0.05 corrected) are reported for a whole-sample analysis (perfusion and anatomical image acquisition were similar in both groups, therefore a whole-sample analysis can be conducted exclusively for this trait pair) in Figure 9 and Table 3.

Both GMV and perfusion are systematically correlated with graph metrics, hence we repeated our analysis using GMV as a control variable.

2.4 Partial correlation between perfusion and connectivity controlling for GMV

2.4.1 Group Level - Cortical Nodes. For the 78 cortical nodes the partial correlations (PCs) of perfusion and the graph theoretical metrics local clustering coefficient, local efficiency, local vulnerability, degree and betweenness (control variable: local GMV) fail to reach significance (FDR correction applied for each metric and group separately, p<0.05) in both groups for all connectome estimations from the cortico-cortical sparsity range 11–17%. Significant PCs are found for Group 1 in the form of a negative covariation of the clustering coefficient (in range 13–16%, rho between -0.095 and −0.077) and a positive covariation of vulnerability (in range 10–16%, rho between 0.144 and 0.23), degree (in range 13.5–16%, rho between 0.093 and 0.148) and betweenness (in range 11.5–16%, rho between 0.074 and 0.11) with perfusion, but are minor in magnitude. Group 2 only shows a minor covariation of perfusion and degree (in range 11.5–13.5%, rho between −0.129 and −0.09).

2.4.2 Group Level - Subcortical Nodes. For the 10 subcortical nodes the PCs of perfusion and the graph theoretical metrics namely local clustering coefficient and betweenness (control variable: local GMV) fail to reach significance (FDR correction applied for each metric and group separately, p<0.05) in both groups for all connectome estimations from the cortico-cortical sparsity range 11–17%.

Significant PCs are found for both groups in the sparsity range of 13–16% in the form of a negative covariation of local efficiency with perfusion (Group 1, rho between −0.351 and −0.249, Group 2 rho between −0.3940 and −0.2979), and a positive covariation
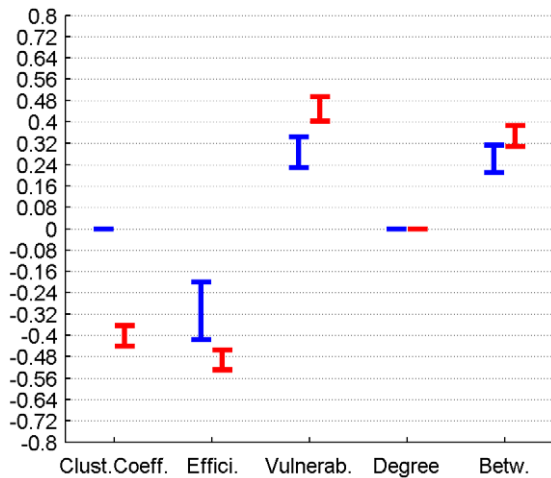
Figure 3. Correlation between graph theoretical metrics and perfusion for Group 1 (in blue) and Group 2 (in red), for the subcortical region class. The minima and maxima of correlation magnitudes are provided for FDR (p<0.05) corrected significant correlations (Spearman's rho), calculated with graph metrics from connectomes resulting from the sweep over plausible cortico-cortical sparsity levels (11–17% range).
doi:10.1371/journal.pone.0014801.g003

of vulnerability and perfusion (in range 12–13%, Group 1 rho between 0.2276 and 0.257, Group 2 rho between 0.1858 and 0.3012).

When groups are analysed separately, significant PCs are found for Group 2 in the form of a negative covariation of degree (in range 11.8–17%, rho between −0.2523 and −0.1932) with perfusion, but are not supported by results from Group 1.

2.4.3 Group Level - DMN Nodes. In order to specifically characterise regions (such as Medial Prefrontal Gyrus, Medial Temporal Lobe and Pole, Posterior Cingulate Cortex, Precuneus,
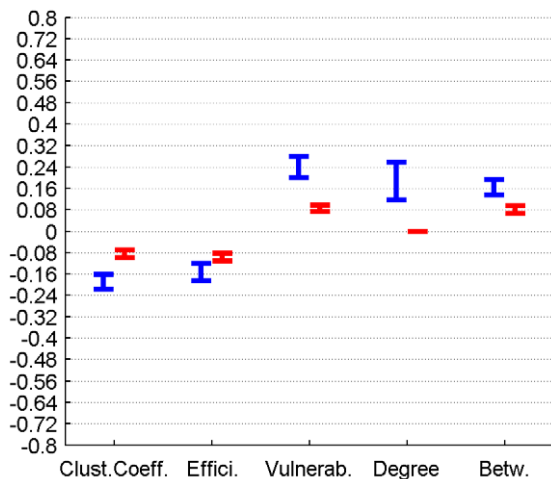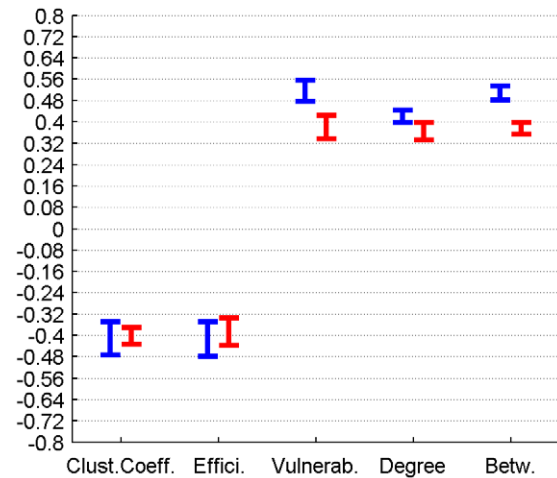

Figure 4. Correlation between graph theoretical metrics and perfusion for Group 1 (in blue) and Group 2 (in red), for the cortical region class. The minima and maxima of correlation magnitudes are provided for FDR (p<0.05) corrected significant correlations (Spearman's rho), calculated with graph metrics from connectomes resulting from the sweep over plausible cortico-cortical sparsity levels (11–17% range).
doi:10.1371/journal.pone.0014801.g004

Figure 5. Correlation between graph theoretical metrics and perfusion for Group 1 (in blue) and Group 2 (in red), for the DMN region class. The minima and maxima of correlation magnitudes are provided for FDR (p<0.05) corrected significant correlations (Spearman's rho), calculated with graph metrics from connectomes resulting from the sweep over plausible cortico-cortical sparsity levels (11–17% range).
doi:10.1371/journal.pone.0014801.g005

Inferior Parietal Lobe) which are associated with the Default Brain Mode [34] we singled these cortical nodes out and repeated the groupwise analysis.

For these 12 cortical nodes the PCs of perfusion and the graph theoretical metrics local clustering coefficient, local efficiency, vulnerability, degree and betweenness (control variable: local GMV) reached significance (FDR correction applied for each metric and group separately, p<0.05) in both groups for all connectome estimations from the cortico-cortical sparsity range 11–17%. The results are summarised in Figure 10 and Table 4.

2.4.4 Individual Level. For each group, double FDR correction (p<0.05) was applied separately for the PC analyses carried out for each single subject and each single edge threshold (for the plausible sparsity range). On the individual level only five subjects showed any significant covariation (four from Group 1).

The significant correlations on the individual level were all positive and minor to medium in magnitude, found only for the graph metrics degree, betweenness and vulnerability and only for nodes from the DMN and cortical regions.

2.4.5 Regionwise Level. The perfusion, GMV and five graph theoretical metric trait measures of each non-cerebellar brain region of the AAL atlas were collected from each subject into two groupwise tables, one seven-value vector per person for each edge probability threshold. As a result each region can be characterised with respect to the covariation profile of perfusion and graph theoretical anatomical connectivity metrics while controlling for local GMV. For each group, double FDR correction (p<0.05) was applied separately for the PC analyses carried out for each single region and each single edge threshold. Only covariation profiles of regions are reported that passed the double FDR correction in both groups for more than half of the edge thresholds in the plausible cortico-cortical sparsity range. The statistically significant regional covariation profiles of the five graph theoretical metrics with local perfusion are provided in the supporting information files (Table S1) with a visualisation in Figure 11.

Table 1. Correlation between graph theoretical metrics and perfusion for Group 1 and Group 2, for the region classes subcortical, cortical and DMN.

Correlation of graph theoretical metrics and perfusion	Group		Clustering Coefficient	Efficiency	Vulnerability	Degree	Betweenness
Subcortical Regions	1	min Value	n.s.	-0,42	0,23	n.s.	0,21
Subcortical Regions	1	max Value	n.s.	-0,20	0,34	n.s.	0,31
Subcortical Regions	2	min Value	-0,44	-0,53	0,40	n.s.	0,31
Subcortical Regions	2	max Value	-0,36	-0,46	0,49	n.s.	0,39
Cortical Regions	1	min Value	-0,22	-0,19	0,20	0,12	0,14
Cortical Regions	1	max Value	-0,16	-0,12	0,28	0,26	0,19
Cortical Regions	2	min Value	-0,10	-0,11	0,07	n.s.	0,07
Cortical Regions	2	max Value	-0,07	-0,08	0,10	n.s.	0,09
DMN Regions	1	min Value	-0,48	-0,48	0,48	0,40	0,48
DMN Regions	1	max Value	-0,35	-0,35	0,56	0,44	0,53
DMN Regions	2	min Value	-0,43	-0,44	0,34	0,33	0,35
DMN Regions	2	max Value	-0,37	-0,33	0,42	0,40	0,40

The minima and maxima of correlation magnitudes are provided for FDR (p<0.05) corrected significant correlations (Spearman's rho), calculated with graph metrics from connectomes resulting from the sweep over plausible cortico-cortical sparsity levels (11–17% range).
doi:10.1371/journal.pone.0014801.t001

Discussion

To the best of our knowledge, this study represents the first attempt to quantify the relation of local perfusion and local anatomical connectivity, using the described MR sequences in combination with a probabilistic estimation of the connectivity graph. Our results on the robust small-world properties of the white matter connectomes are in accordance with previous findings.

3.1 Connectome topology

When conducting a sweep over the range of plausible edge probability thresholds, the properties of the white matter networks from both groups of participants show marked differences. For identical edge probability thresholds the sparsity of the resulting connectomes from Group 2 (DTI measured with a higher number of diffusion directions and a higher spatial resolution) is higher than the sparsity of connectomes in Group 1. On the other hand small-world property (Sigma) values are numerically higher for the same sparsity levels in Group 2.

It can be assumed that more edges of the white matter network are reliably identified with the superior DTI measurement parameters used in Group 2, and that the entirety of these reliably identifiable edges tend to display small-world properties. The numerically higher path length ratio values (Lambda) in Group 1 might indicate that long-distance white matter connections are measured more reliably with the superior DTI
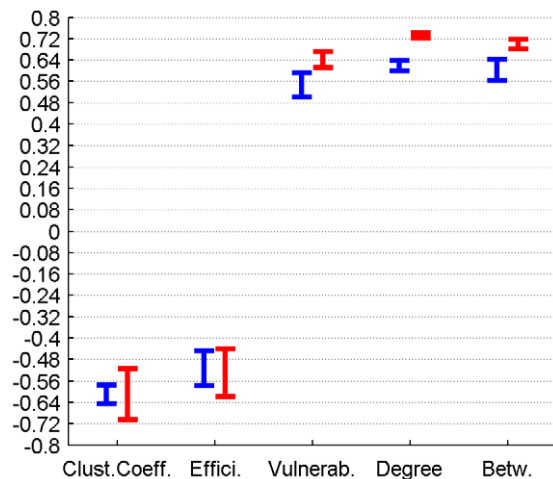
Figure 6. Correlation between graph theoretical metrics and GMV for Group 1 (in blue) and Group 2 (in red), for the subcortical region class. The minima and maxima of correlation magnitudes are provided for FDR (p<0.05) corrected significant correlations (Spearman's rho), calculated with graph metrics from connectomes resulting from the sweep over plausible cortico-cortical sparsity levels (11–17% range).
doi:10.1371/journal.pone.0014801.g006
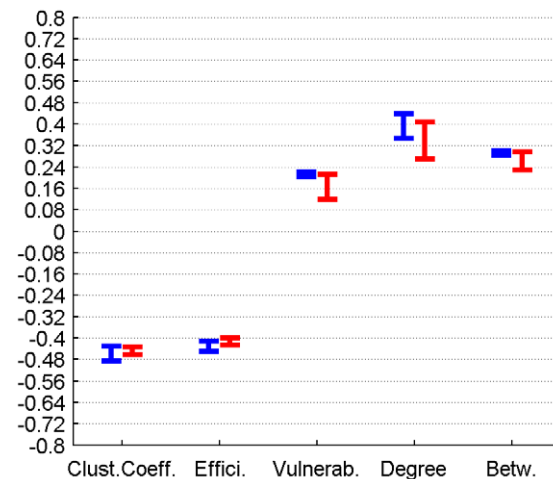
Figure 7. Correlation between graph theoretical metrics and GMV for Group 1 (in blue) and Group 2 (in red), for the cortical region class. The minima and maxima of correlation magnitudes are provided for FDR (p<0.05) corrected significant correlations (Spearman's rho), calculated with graph metrics from connectomes resulting from the sweep over plausible cortico-cortical sparsity levels (11–17% range).
doi:10.1371/journal.pone.0014801.g007
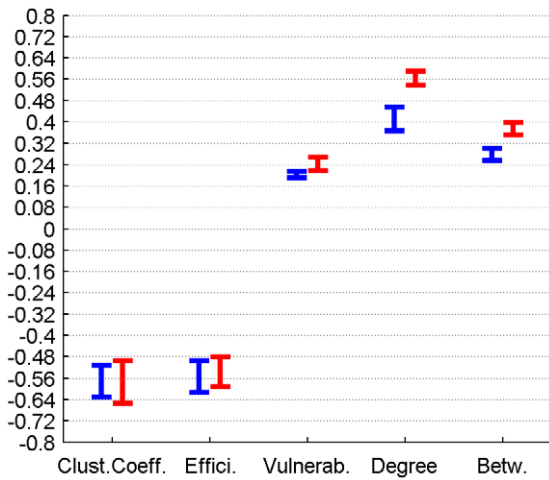
Figure 8. Correlation between graph theoretical metrics and GMV for Group 1 (in blue) and Group 2 (in red), for the DMN region class. The minima and maxima of correlation magnitudes are provided for FDR (p<0.05) corrected significant correlations (Spearman's rho), calculated with graph metrics from connectomes resulting from the sweep over plausible cortico-cortical sparsity levels (11–17% range).
doi:10.1371/journal.pone.0014801.g008

measurement parameters, thus facilitating their probabilistic tracking and acceptance as edge in the subsequent edge probability thresholding process. The acceptance of only a few more long-distance edges can decrease path length drastically, while influencing the sparsity value only minimally.

The deviating Sigma values for equal cortico-cortical sparsity in the two groups might indicate that two qualitatively different white matter networks are compared with one another. But as we presently provide whole-connectome Sigma over cortico-cortical sparsity the deviation in small-world properties may as well be attributable to superior reliability in measuring non-cortico-cortical edges for the DTI sequences applied to Group 2.

As can be seen in Figure 2 a sudden rise in path length Lambda can be observed in Group 1 between 13.3 and 13.6% cortico-cortical sparsity. A rise in path length occurring when more edges are added is unusual and indicates that a new cluster of nodes was connected to the rest of the connectome with the additional edges passing a decreasing threshold (leading to higher sparsity level). As clusters unconnected to the rest of the connectome are unlikely, this might be an indication that the true level of cortico-cortical sparsity might be in a range above 13.6%.

3.2 General sample characteristics

The lack of any significant relation of whole-brain graph metrics and average perfusion values indicates that there is no relation of overall absolute perfusion and overall connectivity in our healthy sample.

3.3 Correlation between perfusion, connectivity and GMV

Both local GMV and local perfusion show a pattern of significant covariation with local graph theoretical metrics in both groups and for all three described region classes. This pattern of covariation indicates that higher perfusion and higher GMV are more likely to be found in hub-like regions of the brain, with high degree, betweenness and vulnerability, thus with low clustering coefficient and local efficiency.

GMV and perfusion show a marked covariation profile on the whole-sample level, with the strongest correlation for subcortical regions, followed by regions of the DMN and finally non-cerebellar regions in general and cortical regions. The marked correlations of perfusion and GMV could theoretically be a confound due the fact that relatively larger regions contain more large vessels and have a superior ASL Signal-to-Noise ratio (SNR) when compared with smaller regions. Alternatively the correlations could indicate a genuine association of average perfusion and relative GMV.

3.4 Covariation of perfusion and connectivity

Cortical and subcortical nodes were characterised with respect to their graph theoretical properties, which were further correlated with measures of perfusion, while controlling for local GMV.

Table 2. Correlation between graph theoretical metrics and GMV for Group 1 and Group 2, for the region classes subcortical, cortical and DMN.

Correlation of graph theoretical metrics and GMV	Group		Clustering Coefficient	Efficiency	Vulnerability	Degree	Betweenness
Subcortical Regions	1	min Value	-0,64	-0,58	0,50	0,60	0,56
Subcortical Regions	1	max Value	-0,57	-0,45	0,59	0,64	0,64
Subcortical Regions	2	min Value	-0,70	-0,62	0,61	0,72	0,68
Subcortical Regions	2	max Value	-0,52	-0,44	0,67	0,74	0,72
Cortical Regions	1	min Value	-0,49	-0,45	0,20	0,35	0,29
Cortical Regions	1	max Value	-0,43	-0,41	0,22	0,44	0,30
Cortical Regions	2	min Value	-0,46	-0,43	0,12	0,27	0,23
Cortical Regions	2	max Value	-0,43	-0,40	0,21	0,41	0,30
DMN Regions	1	min Value	-0,63	-0,61	0,19	0,37	0,26
DMN Regions	1	max Value	-0,51	-0,50	0,22	0,46	0,30
DMN Regions	2	min Value	-0,65	-0,59	0,22	0,54	0,35
DMN Regions	2	max Value	-0,50	-0,48	0,27	0,59	0,40

The minima and maxima of correlation magnitudes are provided for FDR (p<0.05) corrected significant correlations (Spearman's rho), calculated with graph metrics from connectomes resulting from the sweep over plausible cortico-cortical sparsity levels (11–17% range).
doi:10.1371/journal.pone.0014801.t002
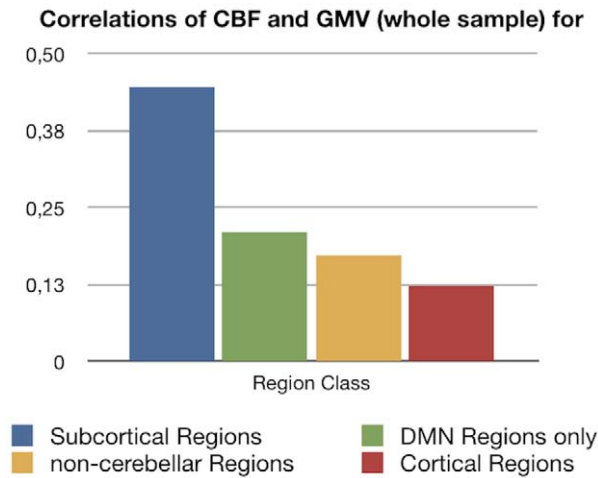
Figure 9. Correlation between GMV and perfusion for the whole-sample level are provided for the region classes cortical, subcortical, all non-cerebellar and DMN, all results FDR (p<0.05) corrected.
doi:10.1371/journal.pone.0014801.g009

3.4.1 Group Level. The covariations found on a group level, analysing the trait correlations of all cortical nodes, were only minor (<0.25) in magnitude and inconclusive in terms of cross-group stability. The covariation profile of traits from subcortical nodes on the other hand shows a negative covariation of local efficiency and a positive covariation of vulnerability with perfusion in a minor to medium (<0.6) range of magnitude.

For regions associated with the DMN we observe similar patterns of covariation, but complemented by a positive covariation of degree and betweenness and a negative covariation of the clustering coefficient with perfusion, in a range of minor to medium magnitude.

For all three classes of nodes, the magnitude of covariation observed in Group 1 exceeds the magnitude of covariations in Group 2.

3.4.2 Individual Level. On the individual level correlations for all cortical, subcortical and DMN regions largely fail to reach significance in a stable pattern.

3.4.3 Regionwise Level. On a regionwise level, frontal, cingular and hippocampal regions show a negative covariation of perfusion with the clustering coefficient and local efficiency, while mainly posterior portions of the brain show a positive covariation particularly with vulnerability. All covariations remain minor to medium in magnitude and have the same sign in both groups, except for the Frontal Inferior Cortex (pars triangularis and

Table 3. Correlation between GMV and perfusion for the whole-sample level are provided for the region classes cortical, subcortical, all non-cerebellar and DMN, all results FDR (p<0.05) corrected.

Correlations of CBF and Gray Matter Volume (whole sample) for	p-value	r
Subcortical	1E-12	0,45
DBM	0,00042	0,21
non-cerebellar	5E-15	0,17
Cortical	2E-07	0,12

doi:10.1371/journal.pone.0014801.t003
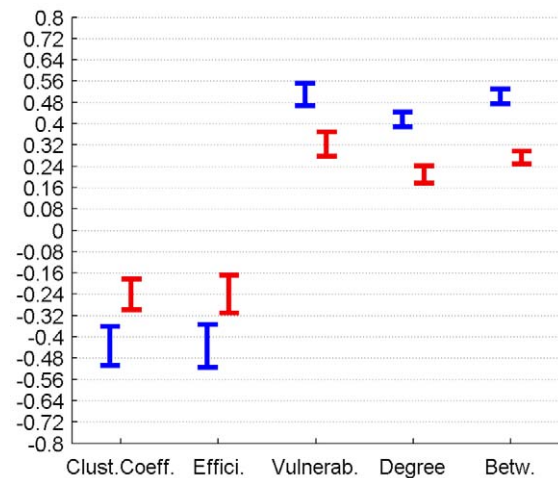
Figure 10. PC of graph theoretical metrics and perfusion for Group 1 (in blue) and Group 2 (in red) for the region class DMN are provided with the minima and maxima of correlation magnitudes for FDR (p<0.05) corrected significant correlations (Spearman's rho), calculated with graph metrics from connectomes resulting from the sweep over plausible cortico-cortical sparsity levels (11–17% range).
doi:10.1371/journal.pone.0014801.g010

orbitalis), the Frontal Superior Medial Gyrus, the Supplementary Motor Area, the Olfactory Cortex and the Rolandic Operculum, where the signs of covariation are contradictory.

3.5 General covariation pattern

The present results do not allow for a clear and global falsification of a perfusion/connectivity-covariation in the brain. Rather the results on group- and regionwise levels point towards a positive covariation of rCBF with degree, betweenness and vulnerability and a negative covariation of rCBF with the clustering coefficient and efficiency for some particular regions of the brain.

The correlation results for the covariation of GMV, perfusion and connectivity (no statistical control of GMV) point into the same direction, thus could be influenced by the issues indicated in the methods section.

This might indicate that for some areas of the brain an increased rCBF is more likely to be found in regions, which have a central position in the white matter network and possess hub-like properties, but have poor local clustering and number of parallel pathways to any other node (local efficiency). This might be the manifestation of a structural organisation principle, which strives to minimise the potential of metabolic deficiencies in central nodes, which are part of a rather sequential connection architecture.

The failure of the correlations to reach significance on the individual level could be attributed to the low statistical power, since for the DMN twelve and for the subcortical regions merely ten pairs of values are correlated for each participant, further decreasing the degrees of freedom by using PC and using conservative multiple comparison correction. The same holds for results on the regionwise level (the number of value pairs correlated for each region is equal to the number of subjects in that group, which are eleven and twelve, respectively), which might offer one explanation for the contradictory findings in some regions.

The most stable results are obtained for regions of the DMN on a group- and regionwise level. Regions of the DMN are known to

Table 4. PC of graph theoretical metrics and perfusion for Group 1 and Group 2 for the region class DMN are provided with the minima and maxima of correlation magnitudes for FDR (p<0.05) corrected significant correlations (Spearman's rho), calculated with graph metrics from connectomes resulting from the sweep over plausible cortico-cortical sparsity levels (11–17% range).

Partial Correlation (Spearman's Rho) with Perfusion in		Clustering Coefficient	Efficiency	Vulnerability	Degree	Betweenness
Group 1	min Value	-0,51	-0,52	0,47	0,39	0,47
Group 1	max Value	-0,36	-0,35	0,55	0,44	0,53
Group 2	min Value	-0,30	-0,31	0,28	0,18	0,25
Group 2	max Value	-0,18	-0,17	0,37	0,24	0,30

doi:10.1371/journal.pone.0014801.t004

possess hub-like properties in terms of both anatomical and functional connectivity [4]. Possibly the present results point towards an exclusive realisation of an observable linear supply-and-demand-principle of perfusion and connectivity in these regions, although it can not be excluded that regions show possibly non-linear relations, which we did not test for in this present study.

3.6 Implications

These results might have implications on our understanding of resting state networks in general, not only those exclusively involving nodes of the DMN network [34–39].

The finding that DMN regions (e.g. Posterior Cingulate) might play a role as bottlenecks in a potentially task-negative default mode of macroscopic neural traffic might be underlined by past [34] [40] and present results on the coincidence of heightened resting state perfusion and hub characteristics (marked by high degree and vulnerability) in DMN regions. Just like the hubs of any traffic network can form bottlenecks where traffic might dam up,

some nodes with a central position within the white matter network might show heightened activity during distinct global states, such as rest. But whether the apparent functional connectivity of these hubs can be attributed to genuine joint information processing in a functionally relevant network or merely to similar activity arising from e.g. coincidentally relaying traversing neural signals, or parts of both, can currently not be conclusively answered.

It is possible that the common traits (high perfusion, hub-like connectivity, large relative GMV) and the strong covariation of these traits contribute either causally to the formation, or confoundingly to our awareness of resting state networks. Similar Blood Oxygen Level Dependent (BOLD) activity profiles might in principle be caused by node interactivity in a functionally relevant information processing network or alternatively by mere similarity of isolated neural processes in individual nodes [3]. It is unclear, to what extent the coincidence of high resting state perfusion and hub-like connectivity can distort estimations of functional connectivity between such nodes, by influencing the BOLD signal
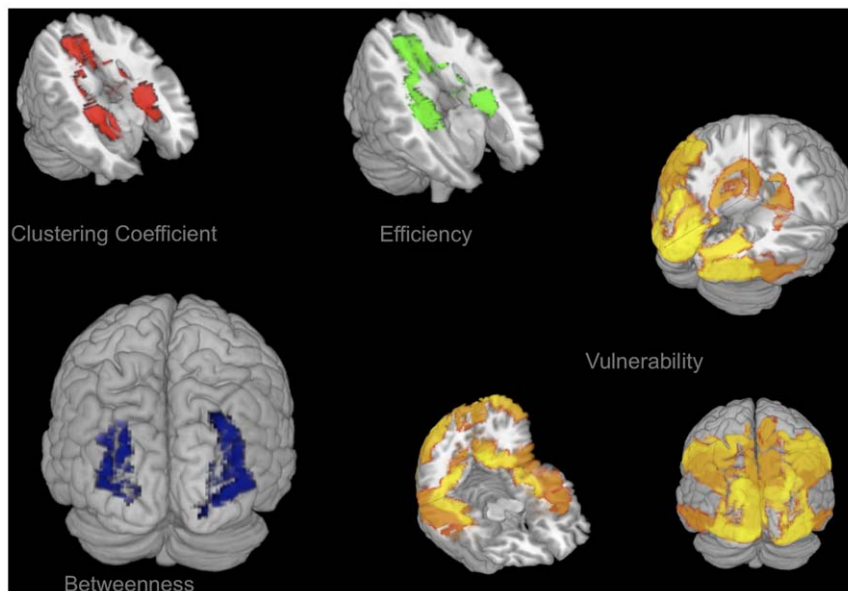
Figure 11. PC of graph theoretical metrics and perfusion for Group 1 and Group 2 for regionwise FDR (p<0.05). Corrected significant non-contradictory correlations (Spearman's rho) are visualised with colour intensity based on the absolute maxima of correlation magnitudes; PCs calculated with graph metrics from connectomes resulting from the sweep over plausible cortico-cortical sparsity levels (11–17% range). PC of local clustering coefficient and perfusion is negative (red, upper left), PC of local efficiency and perfusion is negative (green, upper middle), PC of local betweenness and perfusion is positive (blue, lower left), PC of local vulnerability and perfusion is positive (yellow, lower right).
doi:10.1371/journal.pone.0014801.g011

from these nodes generally with their mutually high perfusion and the underlying activity in these nodes with their common hub-like connectivity.

Understanding the link between local function and local connectivity better, might help understand the apparent link between functional and anatomical connectivity networks [4–5] and resolve the role of mere homology in our perception of resting state networks.

It is a further open question of interest, whether there is any causal neurobiological link between a regional perfusion profile and the emergence of hub characteristics or vice versa.

3.7 Conclusion

The method described might hold potential for the diagnosis of various diseases, as the identified dependency of perfusion and connectivity might reflect the balance resulting from organisational principles inherent to the structural architecture of the healthy brain. Although the identified coefficients from the present healthy sample are only minor to medium in magnitude, it is to note that two traits might be only rudimentarily related in the healthy brain, but might show stronger links in the pathologically altered brain (e.g. hypoperfusion preceding gray matter atrophy).

However, to better understand the relevance of the identified relationships and to explore changes of the derived coefficients due to ageing or disease future studies have to be performed on the respective populations.

3.8 Potential confounds

It can be assumed that during our resting state ASL measurement, the regions of the DMN showed their - by definition - heightened resting state activity and metabolic demand and it is possible that our measurements were therefore systematically biased. If the metabolic profile of a region is best assessed when this region shows a stable amount of activity over time, the metabolic demand of the resting state active brain regions (the DMN) was eventually captured more clearly by our resting state experiment, than the metabolic demand profile of a less resting state involved region such as e.g. the Fusiform Gyrus. This issue touches on the general question whether stimulus-free measurements constitute a reliable baseline measurement for the whole brain, or only for regions active under stimulus-free conditions.

Thus it can not be excluded that covariations of the present form could be identified more conclusively for others regions of the brain as well. For such experiments, these regions would need to be consistently activated for a prolonged amount of time (e.g. by presentation of a series of faces for characterisation of the Fusiform Gyrus), what might allow us to assess their metabolic demand during activity better.

It might be argued that the prospect of such studies might be limited, as brain regions do not merely show a straightforward type of homogeneous functional specialisation, but are rather able to perform heterogenous functions that depend on the task-specific network(s) they are integrated in at a point of time. Nevertheless it should be possible to capture the range of metabolic demand spanned by the conditions of activity and rest for each region of the brain, as any computational process is likely to influence metabolic demand in a specific way.

Studies on the relation of functional and anatomical connectivity networks in general might be influenced by a similar aspect. The definition of functional connectivity is always limited to the state of the brain the connectivity is observed in, therefore the definition of network nodes is not state-independent (the stable association of the nodes with a network is one but not the only

defining trait of the nodes) and thus probably not one-by-one mappable onto other data, e.g. to adequately assess the underlying anatomical connectivity network.

It stands to reason that both the range of metabolic demand states, local connectivity and GMV, and the probability ranking of affiliations to functional connectivity networks of a brain region might be related in some manner to the shape of the Hemodynamic Response Function in that region.

Alternatively to a direct causal interpretation, the co-variation of perfusion and connectivity could as well be caused by a confounding third, presently unregarded variable other than GMV. Our initial hypothesis on the link between local connectivity and local neural computations, neural computations and neural activity, and neural activity and metabolic demand involves a series of dependencies, making the influence of intermediary variables highly likely.

A more comprehensive model, including more potentially intermediate variables beyond merely GMV, could be used in future studies to investigate the relations of local computational processes (e.g. using electroencephalographic methods), neural circuitry (e.g. by utilising information on local cell body types), neurotransmitter concentrations (e.g. by using Magnetic Resonance Spectroscopy), metabolism and connectivity at once. With such a larger and more comprehensive dataset it is likely that the particular perfusion/connectivity balance profile of each region could be resolved further.

3.9 Methodological issues

Several methodological issues need to be addressed. Although we employed a probabilistic tracking approach with a high number of random walks and conservative thresholding, presently it is not possible to ensure the validity of one singular estimated connectome with complete certainty due to the methodological difficulty of proper edge falsification and the strong dependency of the results upon the chosen brain parcellation scheme (the AAL atlas in this case). For a more precise estimation, the methodology has to be refined by extending it to more sophisticated graph estimation methods e.g. based on Q-ball imaging data [41] or diffusion tensor studies utilising multi b-value imaging - and by combining these advanced measurements with advanced brain function atlases, derived from large databases of functional connectivity data, since the optimal anatomical connectivity network nodes stem from the parcellation of the brain into those regions, which eventually form a multitude of functional cooperations with others but always do this as a whole [4].

The combination of multiple methods (DTI based connectivity estimation, VBM, ASL) allows for quantifying and describing brain regions with a high number of measures, both on a global as well as on a regional scale. The proper interpretation of this multifaceted data, with respect to the multiple comparisons problem and open questions on the combination of non-gaussian measures with classical statistical approaches, needs to be advanced in an integrative manner.

Further as the present findings are based on cross-sectional data from small samples, the results could be influenced by potential cohort or small sample size effects. A longitudinal study design with a higher number of subjects is necessary to broaden our understanding of the link of these structural and functional brain properties.

It is to note that many different methods with their individual assumptions and errors are combined in an integrative study, and that any of the modules (probabilistic tractography, graph theoretical analysis, anatomical image segmentation, perfusion measurement, artefact control, normalisation etc.) could clearly be

improved on their own. Our approach is merely intended as a starting point for the combination of the provided measures.

Therefore the present findings are of a preliminary nature, as for the integration of information about local perfusion, connectivity and gray matter properties, the issues of natural variability versus the distribution of measurement error have to be further resolved. Other quantification approaches for measuring integrity or impairment of gray matter such as spectroscopy of synaptic density or recently introduced Positron Emission Tomography methods [42] focussing on the quantification of plaques and tangles in AD might complement the present approach in the future [4].

Methods

4.1 Subjects and data acquisition

Eleven participants (5 females) were recruited for Group 1 from a student sample (average age = 25.4 years, SD = 3.4 years, Range: 21–32). After an update of scanner software twelve further participants (7 females) were recruited, referred to as Group 2 (average age = 36.7 years, SD = 10.7 years, Range: 23–57). Participants of both groups gave written informed consent. All participants were right handed (as confirmed by the Edinburgh Handedness Questionnaire) and both physically (confirmed by extensive health questionnaire) and mentally healthy (confirmed by the german ICD-10-Symptomrating questionnaire). The experiments were approved by the local ethics committee. All MR data were acquired on a 3T Siemens MAGNETOM Trio TIM (Erlangen, Germany) scanner using a 12-channel head coil. The head of each subject was bedded in a deflatable pillow so as to minimise head motion artefacts.

4.2 Anatomical data acquisition and processing

Anatomical images were acquired using a T1 weighted sequence using a 3D MP-RAGE (magnetisation prepared - rapid acquisition gradient echo) sequence ($1 \times 1 \times 1$ mm voxels, TR = 7.92, TE = 2.48, Flip Angle = $16°$, FoV = 256*256, 192 transversal slices, Group 1 - $1 \times 1 \times 1.1$ mm voxels, TR = 2.3, TE = 2.98, Flip Angle = $9°$, FoV = 230*256, 160 sagittal slices, Group 2). The brain was extracted from the raw image using the robust iterative estimation function (Fractional intensity threshold = 0.5) of the Brain Extraction Tool and subsequently segmented into gray and white matter ([43], distributed within the FMRIB's Software Toolbox - FSL 4.0; http://www.fmrib.ox.ac.uk/fsl).

4.3 DTI data acquisition

Each subject in Group 1 participated in a DTI measurement ($1.3 \times 2.4 \times 2.4$ mm voxels, no gap, TR = 8.83 sec, TE = 98 ms, FoV = 1360*1360, Flip Angle = $90°$, 50 transversal slices, 12 diffusion directions, two averages, b-value = 1000 s/mm^2) with the field of view (FoV) comprising the full cerebrum and parts of the rostral cerebellum like the Uvula and Tuber of Vermis, Flocculus and Crus Cerebelli (dependent on individual overall brain size).

Each subject in Group 2 participated in a DTI measurement ($1.8 \times 1.8 \times 2.2$ mm voxels, no gap, TR = 6.8 sec, TE = 93 ms, FoV = 1782*1840, Flip Angle = $90°$, 50 transversal slices, 64 diffusion directions, two averages, b-value = 1000 s/mm^2) with the FoV comprising the full cerebrum and parts of the rostral cerebellum. The DTI data were processed using the DTI and Fibertools Software Package [44] as described in the section Network Edge Definition.

4.4 Connectome construction and edge calculation

For an overview on data flow for each participant and employed analysis schemes please see Figure S1 and Figure S2.

4.4.1 Network node definition. In order to define the network nodes, gray matter areas were labelled for each subject individually based on the AAL atlas [45], resulting in 116 nodes (80 cortical, 10 subcortical, 26 cerebellar) by using the procedure of normalisation and parameter inversion analogous to the method described in [20].

In order to transfer the images into DTI native space, T1 weighted structural images were coregistered with the B0 (non-diffusion) image and then normalised to the Montreal Neurological Institute (MNI) space. The resulting transformation was inverted to warp the AAL template from MNI space to the DTI space. The discrete labeling values were preserved by using a nearest neighbour interpolation method. Normalisation and inverse transformation were implemented using the SPM8 package.

All available subcortical (Caudate, Putamen, Pallidum, Hippocampus and Thalamus) and cerebellar areas, which were within the individual DTI FoV were included as nodes in order to round out the validity of the individual connectivity graph estimation.

4.4.2 Network edge tracking. Using in-house code, the white matter voxels, which were neighbouring the gray matter of each network node, were defined as seed voxels of that area.

Only voxels with a Fractional Anisotropy (FA) value above 0.3 (gray matter FA can reach values up to ~0.2, [46]) were admitted to this procedure. In addition, these voxels also had to be labelled as white matter by the segmentation step and reside within the brain outline mask resulting from the iterative Brain Extraction Step.

Probabilistic tracking from the seed points was realised by using the PiCo [47] approach. The number of random walks was adjusted to the number of voxels within the white matter tracking area for each single seed point.

The algorithms implemented in the DTI and Fibertools Software Package [44] allow for creating extended visitation maps for the tracking from each seed set (all seed voxels of an AAL area) separately, based on the curves originating from the seed points and being propagated through the tensor field (number of curves equalling the number of random walks) and combine this information with statistical estimates on the plausibility of confluence of two white matter tracts anywhere in the brain. Please see [44] for more precise information, as our definition of edge probability is based on the Probability Index of forming a part of the Bundle of Interest (PIBI) value concept developed by [44].

Although theoretically one single edge probability value can be chosen for edge-thresholding based on estimates of the cortico-cortical white matter network sparsity (the percentage of accepted edges, relative to the amount of possible edges) derived from the literature, we provide our results in the form of a sweep over a range of plausible thresholds - in order to avoid false conclusions originating in the limitations of only one threshold-specific white matter network (see [48]).

In order to substantiate this sweep, to ensure the validity of the present findings and to avoid false conclusions due to erroneous selection of the edge probability threshold, we performed a number of connectome estimations based on a large range of thresholds (step width $2.5*10^{-9}$). The applied thresholds ranged from implausibly low thresholds (average edge probability in non-zero voxels min. 10^{-10}) allowing for a very high number of accepted edges to overly conservative high thresholds (average non-zero edge probability min. $8*10^{-7}$) making the adjacency

matrix very sparse respectively. The selection of the threshold for calculation of the graph metrics employed in the present work was based on both empirical and theoretical considerations and reproduces values for cortico-cortical sparsity, clustering, average path length and resulting small-world coefficients, which are comparable with the results described by [20]. For better comparison the figures are provided with our measure of sparsity of cortico-cortical edges only, resulting from the applied thresholds. Changes of overall graph metrics over various thresholds (decreasing small-world coefficient Sigma with decreasing threshold, resulting from higher Gamma values and constant Lambda) are as well in concordance with the literature.

It is to be noted that a less conservative threshold, allowing for a higher number of edges within each individuals' connectome seems to result in increasing PCs of vulnerability (and other metrics) with perfusion for both cortical and subcortical network nodes. This might indicate that the real relation is even stronger than depicted in this context, since there is no other overt reason why the consideration of implausible edges with lower connection probability (which appear only when the threshold is decreased) should systematically increase the PCs. Instead the presented results of our sweep over possible thresholds show that reforming the white matter network topology by adding more edges systematically strengthens statistical relations of perfusion and connectivity.

Further, as for the same threshold more edges are identified for the superior DTI measurement scheme (please see Figure S3), this could mean that equal sparsity for both groups can only be attained by using a more conservative threshold for Group 2. The deviating Sigma for identical cortico-cortical sparsity in Group 2 indicates that either other cortico-cortical or additional non-cortico-cortical edges can be found with higher statistical plausibility, when data from advanced DTI measurements is utilised. The fact that with a higher statistical plausibility higher Sigma can be observed for identical sparsity further validates the small-world property as an inherently stable feature of the white matter connectome.

Particularly interesting is the fact that edge probability shows a power-law style distribution (as well for far lower thresholds, data not shown), indicating that for a low number of edges probability values are very high, while for a very large number of possible edges probability values are very low. How this is related to the observed power-law distribution of hubs for certain edge probability thresholds could be subject of further numerical simulations.

4.4.3 Definition of Graph metrics. For each node, edge and resulting overall graph the available metrics were calculated using the scripts provided within the Brain Connectivity Toolbox [49]. The vulnerability metric was calculated as described by [20]. Please see Figure 12 for illustration of the different graph metrics.

It is to be noted, that graph analysis of white matter connectivity has the advantage that connectivity is not restricted to concepts of direct links only, which is often the case in classical Region-of-Interest to Region-of-Interest deterministic tractography, but incorporates notions of indirect (path length >1) connectivity in all utilised graph metrics but degree.

Degree is the number of edges connecting one node by a path length of one with other nodes (e.g. a hub has a high degree vs. an isolated node with only one connection to the rest of the network has a low degree). In order to normalise local degree values to make them comparable across graphs, the values are divided by the sum of all node degree values.

A node with high **betweenness** is at a central position of the network, meaning that many of the paths connecting any node A
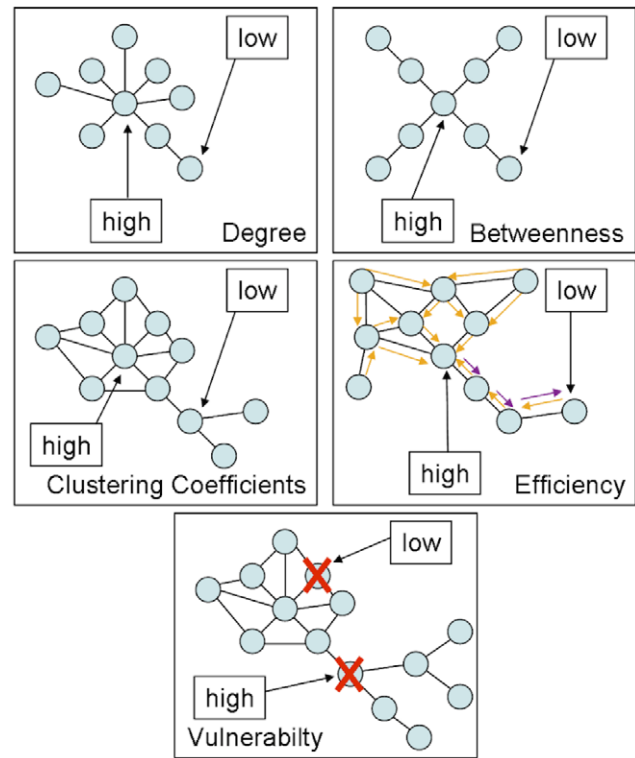
Figure 12. Illustration of utilised node-level graph metrics.
doi:10.1371/journal.pone.0014801.g012

and any node B traverse that node (e.g. while a central hub has high betweenness, a node forming a cul-de-sac has the lowest betweenness). Betweenness is calculated as the fraction of all shortest paths in the network, which traverse a given edge/node. In order to normalise local betweenness values to make them comparable across graphs, the values are divided by the sum of all node betweenness values within the graph.

If the nearest neighbours (path length = 1) of a node are also directly connected to each other they form a cluster (e.g. when an individual's friends are also friends with one another). The **clustering coefficient** quantifies the number of connections that exist between the nearest neighbours of a node as a proportion of the maximum number of possible connections amongst them. This normalisation allows comparing the clustering coefficient of two nodes directly, irrespective of their individual degree.

Efficiency is inversely related to minimum path length (shortest) and quantifies how easily one node can be reached from any other node. Nodes with a high efficiency have many interconnected neighbours and are thus more easily reachable via a number of (parallel) direct paths from any other node. Local efficiency of a node is therefore calculated as the harmonic mean for neighbour-neighbour distances.

The **vulnerability** metric describes how strongly the average shortest path lengths (the mean distance to get from any node A to any node B) in a network grow if a node is removed. If a node with high betweenness, high degree, low efficiency and low clustering coefficient is removed, a central hub is eliminated leading to insufficient cost-effective (short) detours for reconnecting severed nodes and high node vulnerability. If a network is fully connected (all nodes are connected to all other nodes) degree, efficiency and clustering coefficient might be high for all nodes, but vulnerability

might be low, as the removal of one node would not affect the average distance of any pair of nodes significantly, due to the high number of parallel connecting paths/cost-effective detours.

4.5 ASL data acquisition

ASL data were acquired with a FAIR-QUIPSSII PASL encoding scheme with echo-planar imaging (EPI) readout. A total of 201 alternating tag and control images were obtained in each run (total scan time 10 min, TI1 = 700 ms, TI2 = 1100 ms, TE = 20 ms, TR = 3000 ms, voxel size = $3.5 \times 3.5 \times 10$ mm). For ASL measurements of Group 2 the number of slices was increased from ten to eleven (TI2 was changed to 1400 respectively). In order to determine the equilibrium magnetisation for absolute CBF quantification, the same parameters as above were used except that the TR and TI2 were 10000 ms and 4000 ms, respectively [50]. For analysing the ASL data, FSL software (http://www.fmrib.ox.ac.uk/fsl), self-written MATLAB (The Mathworks, Natick, MA, USA) and Linux shell script routines were used. Time courses of all voxels were motion-corrected utilising the MCFLIRT module of FSL using the mean volume of the corresponding run as reference. CBF time series were created by calculating control-tag difference images using surround subtraction (i.e., computing the difference between each image and the average of its two nearest neighbors), thereby reducing BOLD signal contamination of the CBF time course [50].

For the ASL resting state data acquisition subjects were instructed to relax with closed eyes while staying awake. The ASL values for the nodes were extracted by averaging the absolute CBF (in ml/100 g-min) from the voxels within each network node Volume of interest (VOI) for each subject.

Regional absolute and within-subject normalised rCBF values are provided for all non-cerebellar regions of the AAL atlas in the Figure S4.

4.6 Gray matter characterisation through Voxel-Based Morphometry

In order to address the relation between gray matter characteristics, graph theoretical measures and resting state perfusion, we performed a VBM Analysis of the T1 weighted anatomical scans so as to derive descriptives regarding the relative volume of each AAL region. As described in the section Network Node Definition, each anatomical image was skull stripped and the Voxel-based Morphometry Toolbox (VBM5.1, v.1.15, by Christian Gaser) was used subsequently for estimation of the individual modulated and unmodulated segmentation outputs. As the modulated outputs can be corrected for non-linear warping only and therefore make any further correction for different brain size redundant, these images can be used directly for volume estimations.

For the unified segmentation approach (repeated segmentation, bias correction and warping iterations as described in [51]) used in this study the tissue probability maps provided within the SPM5 template set were used since the subjects were drawn from the appropriate population. We applied the thorough clean-up option of the VBM toolbox and made use of a medium Hidden Markov Random Field model for an optimal denoising of the T1 image.

A check of sample homogeneity of the modulated images (using the standard deviation approach within VBM5.1) revealed that the VBM results of the images were all within a tolerable range.

So as to optimise the validity of our GMV estimation, we performed a voxel-wise multiplication of each modulated gray matter image with the coregistered corresponding perfusion image (containing absolute CBF information). Although perfusion imaging of white matter regions of the brain is possible in principle [52], with many sequences estimation accuracy is limited due to the longer transit delay time (the travelling time of blood from labelling region to reach the tissue) of white matter. As perfusion in gray matter is higher, such a multiplication significantly sharpens the gray matter image histogram, thus facilitating the valid estimation of GMV. In order to smooth the image histogram we applied a three dimensional Gaussian smoothing kernel (FWHM = 3 mm, being significantly below the rounded down cubic root of the volume of the smallest AAL-region in equal voxel-space). For each AAL region (network node) the number of gray matter voxels within the atlas derived volumes of interest was counted - equalling the regional volume as relative to the entire individual brain. Naturally these volume values are strongly correlated across our healthy sample as they all measure brain part volumes for identical regions.

Regional GMV values are provided for all non-cerebellar regions of the AAL atlas in Figure S5.

4.7 Employed data level and artefact control

As a univariate factor analysis revealed significant interindividual variability of rCBF values and an effect of gender, the analysis was performed using within-subject z-scored rCBF values. Following this approach, graph metrics and the GMV of nodes were all normalised (z-scored) on a within-subject level. The normalisation was performed separately for cortical and subcortical nodes.

Cortical or subcortical regions for which no connections could be found (due to a tracking failure) or for which no perfusion data could be obtained (due to localisation outside of the ASL imaging FoV) were excluded pairwise from the analysis (in Group 1 seven missing values in different regions, in Group 2 four missing values in two different regions). Cerebellar regions were not considered for correlation analysis, as for 30.94% of cerebellar regions rCBF could not be measured.

VOI specific artefacts in the estimation of rCBF can not be fully eliminated, due to the generally increased SNR ratio of the ASL signal and the higher chance of intravascular artefacts in larger VOIs, which naturally contain more large arteries and veins that distort rCBF estimations. Also imperfect slice profiles, remaining magnetisation transfer effects and blood tissue water exchange time are factors, which cause artefacts on rCBF estimation. In order to decrease the impact of VOI size on the estimation of relations, we included GMV estimations from VBM as a control variable into our analysis and restricted the presented results to the significant PCs calculated with Spearman's rho.

The data derived from the entirety of these measures constitute for each member of the sample a subjectwise region-by-trait table, with the columns representing local perfusion, local GMV and five graph theoretical metrics of local white matter connectivity, and with 116 rows - one for each region of the AAL atlas.

In order to interpret such multifaceted data one can take various perspectives. The data can be sorted and the trait measurements can be correlated on an individual subjectwise level, to answer the question, whether there is a significant PC - controlling for local GMV - between local perfusion and local connectivity for all the 116 regions of the AAL atlas in the brain of a given subject. Alternatively the data can be normalised on a within-subject level and integrated with data from all other subjects into a group table, to answer the question whether the previously outlined PC is significant in an analysis of pooled data as well. As a second alternative approach, the data can be sorted by region, so as to answer the question whether in pooled group data local perfusion and local connectivity of some regions shows stronger correlation than others (e.g. the left Precentral Gyrus displays a stronger PC, than the same two traits of the right Precentral Gyrus). Figures of

dataflow and analaysis schemes are depicted in Figure S1 and Figure S2.

Results are presented for white matter connectomes that show plausible cortico-cortical sparsity (between 11 and 17%).

Supporting Information

Figure S1 Dataflow of each participant is illustrated; please see Methods section for details. For each participant one table like in the lower left corner of the image results from the combination of all the measures, the node-specific graph metrics part of that table changes for each edge probability thresholding step while the rCBF and GMV parts stay constant.
Found at: doi:10.1371/journal.pone.0014801.s001 (10.24 MB TIF)

Figure S2 Illustration for the group, individual and regionwise analysis schemes. C indicates the control variable GMV in the PC approach.
Found at: doi:10.1371/journal.pone.0014801.s002 (10.24 MB TIF)

Figure S3 Upper: Distribution of cortico-cortical sparsity over identical edge probability thresholds for both groups. Lower: Distribution of whole-brain sparsity over identical edge probability thresholds for both groups; edge probability thresholds (x-axis) become more conservative towards the right end of the x-axis (higher threshold) leading to lower resulting sparsity due to less accepted edges.
Found at: doi:10.1371/journal.pone.0014801.s003 (1.82 MB TIF)

Figure S4 Upper: Regional total perfusion in all 23 subjects (y-axis in ml/100g-min, x-axis AAL region code). Lower: Regional within-subject normalised perfusion in all 23 subjects for cortical regions (y-axis z-score, x-axis AAL region code).
Found at: doi:10.1371/journal.pone.0014801.s004 (12.04 MB TIF)

Figure S5 Relative GMV of non-cerebellar Regions for all 23 subjects (y-axis number of voxels from non-linear warping only corrected modulated output image-space, x-axis AAL region code).
Found at: doi:10.1371/journal.pone.0014801.s005 (10.24 MB TIF)

Table S1 Results of the regionwise PC analysis (graph theoretical metrics with perfusion, controlling for local GMV), presented for statistically significant (FDR corrected, $p<0.05$) regions only provided with minima and maxima of correlation magnitudes for Group 1 and Group 2.
Found at: doi:10.1371/journal.pone.0014801.s006 (0.04 MB XLS)

Text S1 Notes on the small-world characteristics of binary adjacency graphs defined by the significant correlations of cortical perfusion and GMV values.
Found at: doi:10.1371/journal.pone.0014801.s007 (0.04 MB PDF)

Author Contributions

Conceived and designed the experiments: BV MC RS. Performed the experiments: BV BS ÖY. Analyzed the data: BV MC AK. Contributed reagents/materials/analysis tools: BV MC AK BS RV ÖY KU. Wrote the paper: BV MC AK BS ÖY WR CB KU NB RS.

References

1. Bassett DS, Bullmore E (2006) Small-world brain networks. The neuroscientist 12: 512.
2. Greicius MD, Supekar K, Menon V, Dougherty RF (2008) Resting-state functional connectivity reflects structural connectivity in the default mode network. Cerebral Cortex.
3. van den Heuvel M, Mandl R, Luigjes J, Hulshoff Pol H (2008) Microstructural organization of the cingulum tract and the level of default mode functional connectivity. Journal of Neuroscience 28: 10844.
4. Buckner RL, Sepulcre J, Talukdar T, Krienen FM, Liu H, et al. (2009) Cortical hubs revealed by intrinsic functional connectivity: mapping, assessment of stability, and relation to Alzheimer's disease. Journal of Neuroscience 29: 1860.
5. Honey CJ, Sporns O, Cammoun L, Gigandet X, Thiran JP, et al. (2009) Predicting human resting-state functional connectivity from structural connectivity. Proceedings of the National Academy of Sciences 106: 2035.
6. He Y, Chen ZJ, Evans AC (2007) Small-world anatomical networks in the human brain revealed by cortical thickness from MRI. Cerebral Cortex 17: 2407.
7. Chen ZJ, He Y, Rosa-Neto P, Germann J, Evans AC (2008) Revealing modular architecture of human brain structural networks by using cortical thickness from MRI. Cerebral cortex 18: 2374.
8. Stam C, Jones B, Nolte G, Breakspear M, Scheltens P (2007) Small-World Networks and Functional Connectivity in Alzheimer's Disease. Cerebral Cortex 17(1): 92–99.
9. Sporns O (2006) Small-world connectivity, motif composition, and complexity of fractal neuronal connections. Biosystems 85: 55–64.
10. Sporns O, Zwi JD (2004) The small world of the cerebral cortex. Neuroinformatics 2: 145–162.
11. Achard S, Salvador R, Whitcher B, Suckling J, Bullmore E (2006) A resilient, low-frequency, small-world human brain functional network with highly connected association cortical hubs. Journal of Neuroscience 26: 63.
12. Kuschinsky W (1991) Coupling of function, metabolism, and blood flow in the brain. Neurosurgical review 14: 163–168.
13. Farkas E, Luiten PG (2001) Cerebral microvascular pathology in aging and Alzheimer's disease. Progress in Neurobiology 64: 575–611.
14. Arthurs OJ, Boniface S (2002) How well do we understand the neural origins of the fMRI BOLD signal? TRENDS in Neurosciences 25: 27–31.
15. Magistretti PJ (2006) Neuron-glia metabolic coupling and plasticity. Journal of Experimental Biology 209: 2304.
16. Gjedde A, Diemer NH (1985) Double-tracer study of the fine regional blood-brain glucose transfer in the rat by computer-assisted autoradiography. Journal of cerebral blood flow and metabolism: official journal of the International Society of Cerebral Blood Flow and Metabolism 5: 282.
17. Klein B, Kuschinsky W, Schrock H, Vetterlein F (1986) Interdependency of local capillary density, blood flow, and metabolism in rat brains. American Journal of Physiology- Heart and Circulatory Physiology 251: H1333.
18. Detre JA, Wang J, Wang Z, Rao H (2009) Arterial spin-labeled perfusion MRI in basic and clinical neuroscience. Current opinion in neurology 22: 348.
19. Jellison BJ, Field AS, Medow J, Lazar M, Salamat MS, et al. (2004) Diffusion tensor imaging of cerebral white matter: a pictorial review of physics, fiber tract anatomy, and tumor imaging patterns. American Journal of Neuroradiology 25: 356.
20. Gong G, He Y, Concha L, Lebel C, Gross DW, et al. (2009) Mapping anatomical connectivity patterns of human cerebral cortex using in vivo diffusion tensor imaging tractography. Cerebral Cortex 19: 524.
21. Bullmore E, Sporns O (2009) Complex brain networks: graph theoretical analysis of structural and functional systems. Nature Reviews Neuroscience 10: 186–198.
22. Li Y, Liu Y, Li J, Qin W, Li K, et al. (2009) Brain anatomical network and intelligence. PLoS Comput Biol 5: e1000395.
23. Cammoun L, Gigandet X, Sporns O, Thiran JP, Maeder P, et al. (2009) Connectome alterations in schizophrenia. NeuroImage 47: S157.
24. Barabási AL, Crandall RE (2003) Linked: The new science of networks. American journal of Physics 71: 409.
25. Williams DS, Detre JA, Leigh JS, Koretsky AP (1992) Magnetic resonance imaging of perfusion using spin inversion of arterial water. Proceedings of the National Academy of Sciences of the United States of America 89: 212.
26. Wong EC, Buxton RB, Frank LR (1997) Implementation of quantitative perfusion imaging techniques for functional brain mapping using pulsed arterial spin labeling. NMR in Biomedicine 10: 237–249.

27. Parkes LM, Rashid W, Chard DT, Tofts PS (2004) Normal cerebral perfusion measurements using arterial spin labeling: reproducibility, stability, and age and gender effects. Magnetic Resonance in Medicine 51: 736–743.

28. Biagi L, Abbruzzese A, Bianchi MC, Alsop DC, Del Guerra A, et al. (2007) Age dependence of cerebral perfusion assessed by magnetic resonance continuous arterial spin labeling. Journal of Magnetic Resonance Imaging 25: 696–702.

29. Schuff N, Zhu XP (2007) Imaging of mild cognitive impairment and early dementia. British Journal of Radiology 80: S109.

30. Kawamura J, Meyer JS, Ichijo M, Kobari M, Terayama Y, et al. (1993) Correlations of leuko-araiosis with cerebral atrophy and perfusion in elderly normal subjects and demented patients. British Medical Journal 56: 182.

31. Jahng G, Schuff N, Du A, Zhang Y, Mueller S, et al. (2007) Age-related Reductions of Cerebral Blood Flow and White Matter Integrity by High-Field Perfusion and Diffusion MRI. World Congress on Medical Physics and Biomedical Engineering 2006. S. pp 1380–1383.

32. Ashburner J, Friston KJ (2001) Why voxel-based morphometry should be used. Neuroimage 14: 1238–1243.

33. Mechelli A, Price CJ, Friston KJ, Ashburner J (2005) Voxel-based morphometry of the human brain: methods and applications. Current Medical Imaging Reviews 1: 105–113.

34. Raichle ME, MacLeod AM, Snyder AZ, Powers WJ, Gusnard DA, et al. (2001) A default mode of brain function. Proceedings of the National Academy of Sciences of the United States of America 98: 676.

35. Gusnard DA, Raichle ME (2001) Searching for a baseline: functional imaging and the resting human brain. Nature Reviews Neuroscience 2: 685–694.

36. Calhoun VD, Adali T, Hansen LK, Larsen J, Pekar JJ (2003) ICA of functional MRI data: an overview. in Proceedings of the International Workshop on Independent Component and Blind Signal Separation.

37. Jafri MJ, Pearlson GD, Stevens M, Calhoun VD (2008) A method for functional network connectivity among spatially independent resting-state components in schizophrenia. Neuroimage 39: 1666–1681.

38. Fair DA, Cohen AL, Dosenbach NU, Church JA, Miezin FM, et al. (2008) The maturing architecture of the brain's default network. Proceedings of the National Academy of Sciences 105: 4028.

39. Buckner RL, Vincent JL (2007) Unrest at rest: default activity and spontaneous network correlations. Neuroimage 37: 1091–1096.

40. van den Heuvel MP, Mandl RC, Kahn RS, Hulshoff Pol HE (2009) Functionally linked resting-state networks reflect the underlying structural connectivity architecture of the human brain. Human brain mapping 30: 3127–3141.

41. Sotiropoulos SN, Bai L, Morgan PS, Constantinescu CS, Tench CR (2010) Brain tractography using Q-ball imaging and graph theory: Improved connectivities through fibre crossings via a model-based approach. NeuroImage 49: 2444–2456.

42. Nordberg A (2010) Amyloid Imaging in Early Detection of Alzheimer's Disease. Neurodegenerative Diseases 7: 136–138.

43. Smith SM (2002) Fast robust automated brain extraction. Human Brain Mapping 17: 143–155.

44. Kreher BW, Schnell S, Mader I, Il'yasov KA, Hennig J, et al. (2008) Connecting and merging fibres: Pathway extraction by combining probability maps. NeuroImage 43: 81–89.

45. Tzourio-Mazoyer N, Landeau B, Papathanassiou D, Crivello F, Etard O, et al. (2002) Automated anatomical labeling of activations in SPM using a macroscopic anatomical parcellation of the MNI MRI single-subject brain. Neuroimage 15: 273–289.

46. Le Bihan D, Mangin JF, Poupon C, Clark CA, Pappata S, et al. (2001) Diffusion tensor imaging: concepts and applications. Journal of magnetic resonance imaging 13: 534–546.

47. Parker GJ, Haroon HA, Wheeler-Kingshott CA (2003) A framework for a streamline-based probabilistic index of connectivity (PICo) using a structural interpretation of MRI diffusion measurements. Journal of Magnetic Resonance Imaging 18: 242–254.

48. Sporns O, Tononi G, Kotter R (2005) The human connectome: a structural description of the human brain. PLoS Comput Biol 1: e42.

49. Rubinov M, Sporns O (2009) Complex network measures of brain connectivity: uses and interpretations. Neuroimage.

50. Cavusoglu M, Pfeuffer J, Ugurbil K, Uludag K (2009) Comparison of pulsed arterial spin labeling encoding schemes and absolute perfusion quantification. Magnetic resonance imaging 27: 1039–1045.

51. Ashburner J, Friston KJ (2005) Unified segmentation. Neuroimage 26: 839–851.

52. van Osch MJ, Teeuwisse WM, van Walderveen MA, Hendrikse J, Kies DA, et al. (2009) Can arterial spin labeling detect white matter perfusion signal? Magnetic Resonance in Medicine 62: 165–173.

6.2 Differential Effects of Intranasal Insulin and Caffeine on Cerebral Blood Flow

Differential Effects of Intranasal Insulin and Caffeine on Cerebral Blood Flow

Y. Grichisch,[1] M. Çavuşoğlu,[2,3] H. Preissl,[4,5] K. Uludağ,[2] M. Hallschmid,[6]
N. Birbaumer,[7,8] H.-U. Häring,[1] A. Fritsche,[1] and R. Veit[4,7]*

[1]Department of Internal Medicine IV, University Hospital, Tübingen, Germany
[2]Max Planck Institute for Biological Cybernetics, High-Field Magnetic
Resonance Center, Tübingen, Germany
[3]Faculty of Mathematics and Physics, University of Tübingen, Germany
[4]MEG Center, University of Tübingen, Germany
[5]Department of Obstetrics and Gynecology, University of Arkansas for Medical
Sciences, Little Rock, AR, USA
[6]Institute of Neuroendocrinology, University of Lübeck, Germany
[7]Institute of Medical Psychology and Behavioral Neurobiology, University of Tübingen, Germany
[8]Ospedale San Camillo, Istituto di Ricovero e Cura a Carattere Scientifico, Venezia, Italy

◆———————◆

Abstract: Insulin is an important modulator of brain functions such as memory and appetite regulation. Besides the effect on neuronal activity, it is also possible that insulin has a direct vasodilatory effect on cerebral blood flow (CBF). We investigated the impact of increased insulin levels in the central nervous system on basal and task-induced CBF as well as blood oxygenation level-dependent (BOLD) response in the visual cortex using pulsed arterial spin-labeling MRI. An intranasal insulin application was used to avoid peripheral hyperinsulinaemia, which would lead to a cascade of hormonal changes. In a control experiment, caffeine was applied due to its well-known impact on the vasculature of the brain leading to a reliable reduction of CBF. Eight lean subjects were included in the study. On 2 separate days, intranasal human insulin or caffeine tablets were given to the subjects after fasting over night. On each day, basal CBF and task-induced CBF were measured before and 30 min after application of insulin or caffeine in each subject. During the task condition, a flickering checkerboard was presented. Insulin had no effect on basal CBF and task-induced CBF in comparison with drug-free baseline measurement in the visual cortex and control regions. After caffeine application, however, there was a significant decrease of CBF during stimulation in the visual cortex. The BOLD response was not altered by insulin or caffeine between pre- and postdose measurements. In conclusion, we found no evidence for a direct vasodilatory effect of intranasal insulin on the cerebral vascular system in this study. Hum Brain Mapp 00:000–000, 2011.   © 2011 Wiley-Liss, Inc.

Key words: glucose metabolism; central nervous system; insulin resistance; functional magnetic resonance imaging; pulsed arterial spin labeling; intranasal insulin; cerebral blood flow

◆———————◆

INTRODUCTION

Insulin is an important regulator of neuronal function on single cell and network level in the central nervous system (CNS). Animal studies have shown that brain-specific deletion of the insulin receptor in mice results in diet-induced obesity and insulin resistance [Brüning et al., 2000]. Insulin is a hormone released in response to food intake and increasing glucose levels and is involved in the regulation of energy homeostasis [Schwartz et al., 2000; Woods et al., 1998]. In humans, it is hypothesized that reduced CNS insulin signaling contributes to the pathogenesis of common metabolic disorders, including diabetes and obesity [Porte et al., 2005]. Indeed, insulin resistance of the brain is associated with obesity and related metabolic diseases as well as cognitive impairments [Hallschmid and Schultes, 2009; Tschritter et al., 2006].

To study the effect of insulin on the brain, insulin has been administered intravenously or intranasally (review in Hallschmid and Schultes [2009]). Intranasal insulin application, compared to intravenous systemic insulin administration, has the major advantage that insulin levels are specifically increased in the CNS. Thus, the unwanted side effects of systemic hyperinsulinaemia (e.g., hypoglycaemia, increased counterregulatory hormones, increased systemic blood flow) can be avoided.

Intranasal insulin reduces body weight and body fat mass in lean male subjects [Hallschmid et al., 2004] and improves memory function in humans [Benedict et al., 2007]. Furthermore, a reduced level of insulin action in the brain can play a role in neurodegenerative diseases [Craft and Watson, 2004]. Reger et al. [2008] showed that intranasal insulin application improves memory function in Alzheimer's disease. In summary, insulin has various effects in the brain, an organ that has been considered to be insulin independent for a long time.

In addition, insulin may also affect cerebral blood flow (CBF) directly by masking insulin effects on neuronal activity. In the periphery, insulin acts as a vasoactive hormone and causes vasodilatation of peripheral tissues like skeletal muscle [Baron, 1996]. Several studies investigated changes in CBF or brain activity measured by blood oxygenation level-dependent (BOLD) signal during hyperinsulinaemic hypoglycaemic and euglycaemic conditions with positron emission tomography or functional magnetic resonance imaging (fMRI). During hypoglycaemia, it was consistently shown that basal CBF was increased [Kennan et al., 2005; Kerr et al., 1993; Powers et al., 1996]. However, it is unclear whether the increase in CBF during hypoglycaemic hyperinsulinaemia is caused by a systemic effect of peripheral vasodilatation, stress-induced counterregulation, or specifically increased local CBF. In contrast, only two studies using systemically induced euglycaemic hyperinsulinaemia [Rotte et al., 2005; Seaquist et al., 2006] and one study using intranasal insulin application [Guthoff et al., 2010] have been performed by means of fMRI. Although Seaquist et al. [2006] reported a decrease of the BOLD response in the visual cortex during hyperinsulinaemia, Rotte et al. [2005] and Guthoff et al. [2010] did not find insulin-induced changes in the visual cortex. However, these studies did not measure CBF.

To test whether insulin has a specific effect on CBF and BOLD response under euglycaemic conditions, we used an intranasal insulin application and simultaneously measured the corresponding BOLD and CBF responses by using arterial spin-labeling MRI. Furthermore, we compared the insulin effect with caffeine. Caffeine is an adenosine antagonist and a well-known vasoconstrictive agent reducing basal CBF [Liau et al., 2008; Perthen et al., 2008]. Therefore, caffeine ingestion is used as a standard approach to validate our experimental findings by measuring pharmacological-induced changes in CBF.

We used visual stimulation, in addition to basal measurements, to elaborate the influence of insulin on both basal and task-induced CBF, because these two measurements could be controlled via different neurochemical pathways. For example, Mintun et al. [2004] found that intravenously injected lactate does affect stimulus-evoked CBF, but not baseline CBF. For visual stimulation, we used a flickering checkerboard, which is a passive perceptual stimulation that is not confounded by cognitive or emotional demands and a standard experimental approach to detect functional activation in the primary visual cortex.

We hypothesized that intranasal insulin will not change CBF, both during the basal and task-induced state, in comparison with the predose measurement. Caffeine, however, as a vasoconstrictive agent should lead to a pronounced decrease in CBF in relation to the predose measurement.

MATERIALS AND METHODS

Participants

Eight healthy subjects participated in the study (five females and three males, age range, 18–34; body mass index, 20–25). The subjects had no history of psychiatric or neurologic problems. Written consent from the participants was obtained before the study, and the study protocol was approved by the local ethics committee.

For each subject, the study was conducted on two different days, starting approximately at the same time of day (see Table I). The subjects were asked to be abstinent from caffeine and food consumption for at least 12 h before the imaging sessions. Each day started with a predose CBF measurement for the two task conditions. Following the predose CBF measurement, the participants applied an intranasal insulin spray or ingested caffeine tablets outside of the scanner. About 30–40 min later, the subjects were placed again in the scanner, and the postdose CBF measurement was performed. This time interval was chosen to allow insulin as well as caffeine to reach the maximum effect in the brain [Born et al., 2002; Perthen et al., 2008]. The insulin was prepared in a nasal spray as described in Hallschmid et al. [2004]. Each puff consisted of 0.1 ml

TABLE I. fMRI protocol

Time of day	Insulin day	Caffeine day
fMRI protocol		
8:00	Predose measurement	Predose measurement
	Flickering checkerboard	Flickering checkerboard
8:30	Intranasal insulin application (160 IU insulin)	Oral caffeine application (200 mg)
9:00	Postdose measurement	Postdose measurement
	Flickering checkerboard	Flickering checkerboard

solution containing 40 IU insulin (400 IU/ml; Insulin Actrapid; Novo Nordisk, Mainz, Germany). Each subject received four doses of 0.1 ml insulin spray within 5 min. In the left and right nostril, two doses each were delivered resulting in a total insulin dose of 160 IU. Ingested caffeine tablets contained a 200 mg oral dose corresponding to a dose of two cups of coffee [Field et al., 2003; Laurienti et al., 2003]. The sequence of the insulin and caffeine application was randomized: four subjects applied insulin in the first day and ingested caffeine the second day and four subjects performed the experiments in the reversed order. Because of technical problems during scanning (artifacts during image acquisition), data of two subjects were disregarded for the analyses of the CBF data of the caffeine day, and the results for caffeine CBF measurements are presented for six subjects. After the experiments, the amount of daily/weekly caffeine intake was recorded. All participants reported a low-to-moderate (one to three cups of coffee, corresponding to 100–300 mg of caffeine) daily caffeine consumption.

Experimental Task

A flickering radial checkerboard with full contrast alternating black and white patterns (temporal frequency of 8 Hz, inner radius 20, outer radius 200, radial square size 10, and angular square size 18 degree) with a cross hair in the center of the checkerboard was presented via a mirror mounted on the scanner head coil. A gray background, isoluminant to the average luminance of the checkerboard, with a crosshair in the middle of the screen was shown during resting phases. The stimuli were presented in a block design with six stimulation trials and seven alternating resting periods each lasting for 30 s starting and ending with a resting period [Seaquist et al., 2006]. The task lasted 390 s. The subjects were instructed to fixate the cross hair throughout the session. Imaging data during the resting phase are regarded as basal measurements and during stimulation as task-induced measurements.

The stimulation was controlled by Cogent 2000 (http://www.vislab.ucl.ac.uk) interfaced with Matlab (MATLAB 6.5.1, The Mathworks, Natick, MA) and synchronized with the trigger from the scanner.

Data Acquisition

MR images were acquired on a 3T Siemens MAGNETOM TIM-Trio (Erlangen, Germany) scanner using a 12-channel trans-receiver head coil. To improve the co-registration between sessions, laser alignment was used to landmark the head position. For each session, the same slice positioning parameters were used.

Quantitative arterial spin labeling (ASL) images were obtained with a flow alternating inversion recovery—quantitative imaging of perfusion using a single subtraction (FAIR-QUIPSSII) pulsed arterial spin labeling (PASL) encoding scheme with echo-planar imaging readout. FAIR-QUIPSSII sequence has less physiological noise contamination in both control and tag images of the ASL time course and higher signal-to-noise ratio compared to PICORE-based tagging schemes [Cavusoglu et al., 2009]. A total of 24 oblique slices with slice thickness of 3.5 mm and 25% gap were acquired in a linear fashion from inferior to superior. Labeling was achieved using a hyperbolic secant inversion pulse with two presaturation pulses applied in the imaging planes immediately before the inversion tag to minimize the impact of the static tissue. Each PASL run consisted of 156 alternating tag and control images resulting in a total scan time of 390 s. Identical sequence parameters were used for all subjects (TI1 = 700 ms, TI2 = 1,400 ms, TE = 13 ms, TR = 2,500 ms, voxel size = $3.5 \times 3.5 \times 3.5$ mm, FOV = 224 mm; FA = 90°). To determine the equilibrium magnetization for absolute CBF quantification, the same sequence parameters as above were used except that the TR and TI2 were chosen to be 10,000 ms and 4,000 ms, respectively [Cavusoglu et al., 2009].

Image Processing

Preprocessing of the ASL data was performed using FSL (FMRIB's Software Library, http://www.fmrib.ox.ac.uk/fsl) [Smith et al., 2004] and self-written routines (MATLAB 7.4, The Mathworks, Natick, MA). Time courses of all voxels were motion-corrected using the MCFLIRT module of FSL. The mean functional image of each session was used as reference for co-registration. Registration of the respective mean volume images was carried out using a rigid body six parameter model and sinc interpolation. The estimated transformation parameters were then applied for all other images. Thereafter, the functional images were smoothed with a Gaussian kernel (FWHM 8 mm). CBF time series were generated by calculating control-tag
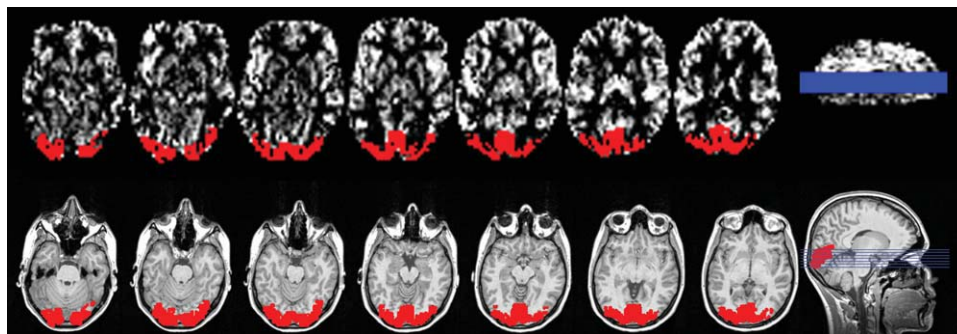
Figure 1.

Illustration of region-of-interest (ROI) generation for the checkerboard task (seven continuous slices) covering the visual cortex of a representative subject. On the top, the ROI (depicted in red) is overlaid on the thresholded average ASL image. On the bottom, the ROI is shown on the coregistered anatomical image. The actual slice position can be seen on the sagital slice on the right side. [Color figure can be viewed in the online issue, which is available at wileyonlinelibrary.com.]

difference images using surround subtraction (i.e., computing the difference between each image and the average of its two nearest neighbors) in order to reduce the BOLD signal weighting of CBF [Wong et al., 1997]. Absolute perfusion quantification was calculated according to the formula $\Delta M = 2M_{0B}f \cdot TI_1 \; e^{-TI_2/T_{1B}}$, where f denotes the CBF (ml/100 g-min) and T_{1B} and M_{0B} are the longitudinal relaxation time and equilibrium magnetization of the arterial blood, respectively (see details for absolute quantification of CBF in Cavusoglu et al. [2009]). The value of T_{1B} at 3T was estimated to be 1,684 ms [Lu et al., 2004]. For determining the equilibrium magnetization of blood, we used a M_{0B} map instead of a global value, estimated by scaling the local tissue equilibrium magnetization taking into account the proton density and relaxation rate differences of gray matter and blood [Cavusoglu et al., 2009].

To get rid of the poststimulus undershoot effect of the previous task period, only images belonging to the second half of the resting period were used for further analyses. The end slices (the first and the last two slices) of the volumes in each run were excluded from the analyses due to possible imperfect slice profiles.

Data Analyses

To ensure that only gray matter voxels in the region-of-interests (ROIs) were included for the CBF quantification, the computed-average ASL images of the basal and task-induced measurements for both insulin and caffeine treatment conditions were intensity thresholded, because gray matter perfusion is higher than white matter perfusion [Cavusoglu et al., 2009]. Then, for each subject, the intersection of the computed gray matter masks for the predose and postdose measurements of each insulin or caffeine treatment were calculated to ascertain that only overlapping gray matter voxels were included in the statistical analyses. We defined ROIs on the thresholded ASL differ-

ence image individually for each subject. The three-dimensional ROIs were hand drawn using the create mask option in FSLview. The mask for the checkerboard task includes the visual cortex (BA17, BA18, and BA19) encompassing seven slices (see Fig. 1). In addition to the visual cortex ROI, two control ROIs in the right anterior and left posterior part of the brain were created (Supporting Information Fig. 1) based on the study of Cavusoglu et al. [2009]. Thereafter, the average CBF of all voxels in the ROIs was computed. CBF-values above 200 ml/g-min were excluded from further analyses, because those high values are not in the physiologically plausible range implying artifacts due to motion or intra-arterial signal [Wong et al., 1997].

To quantify the activation maps of the BOLD signal in the ROIs, we performed a first level analysis on the preprocessed functional data using the full perfusion signal modeling in the FMRI Expert Analysis Tool implemented in FSL 4.1.1. (high-pass filter cut off: 65 s). The mean of the control and tag images obtained from the PASL sequence were calculated and corresponded to BOLD-weighted data. The resulting z-statistic of the BOLD activation was multiplied with the prior computed gray matter masks of the visual cortex separately for each task. Only voxels exceeding a z-value of three were used. The parameter estimates of each of those voxels were then converted into percent BOLD signal change, and the average signal changes during stimulation were calculated for the three ROIs.

Statistical Analyses of CBF and the BOLD Response

A two-way repeated-measure ANOVA was used to evaluate the effects of two within-subjects' factors including stimulation (resting or stimulation period) and treatment (predose compared to postdose) on the CBF and
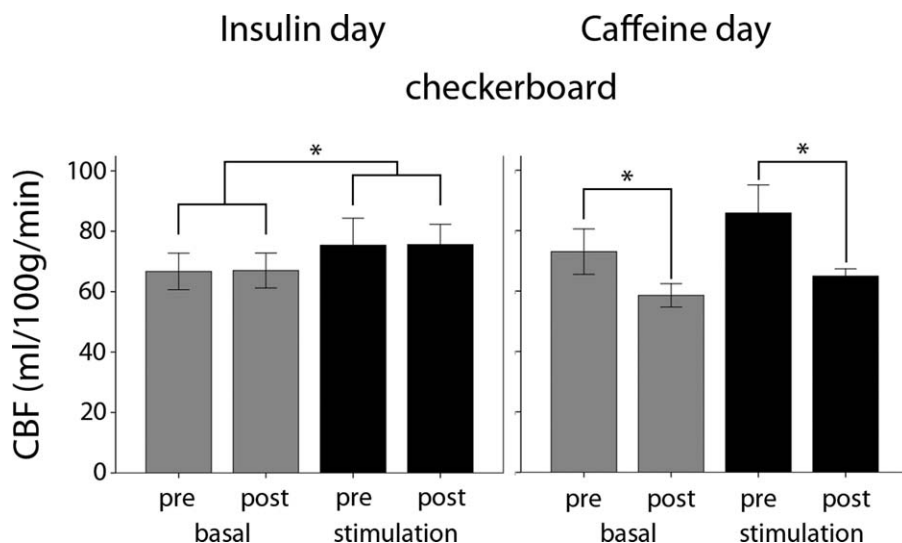
Figure 2.
Group-averaged basal and task-related CBF (±SD) in the visual cortex ROI in the basal (gray bars) and task-induced (black bars) measurements in the insulin day (left) and the caffeine day (right). Significant differences in the respective conditions are indicated with *(P < 0.05).

BOLD response separately for the insulin and the caffeine day in the predefined ROIs.

Regression coefficients were computed using an ordinary least square fit between the CBF-values in the same voxels before (predose measurement) and after treatment (postdose measurement) separately for condition and day. In addition, the r^2 values estimating the goodness of fit of the regression lines to the pre- and postdose conditions (separately for resting and stimulation periods) were computed.

The intraindividual comparison of the regression coefficients between insulin and caffeine day was performed on the six subjects participating in both treatment conditions using SPSS 13.0 statistical software (SPSS, Chicago, IL). For this analysis, a dummy variable coded with one for insulin day and 0 for caffeine day and the product of the dummy variable and the predose CBF-values (pv) were computed and entered into a multiple regression model as predictors. The variable pv is used to test the null hypothesis that the regression coefficients are not significantly different between pre- and postdose measurements [Bosch, 2005].

RESULTS

CBF Quantification Insulin Treatment

On the insulin day, we found a significant stimulation effect [$F(1,7) = 36.55$; $P < 0.001$] in the visual cortex with higher CBF-values during stimulation (CBF increase 12.94%) compared to the resting period for both visits (Fig. 2, left).

With respect to the treatment effect (predose compared to postdose measurement), no significant differences in baseline and task-induced CBF before and after insulin application were found [$F(1,7) = 0.018$; $P = 0.896$] (Fig. 2, left). The mean and individual CBF-values (±SD) for the visual cortex ROI are listed in Table II, for each condition and visit separately.

Regarding the control ROIs outside the visual cortex, we found no significant differences between treatment [anterior: $F(1,7) = 0.554$; $P = 0.481$; posterior: $F(1,7) = 0.295$; $P = 0.604$] and conditions [anterior: $F(1,7) = 0.020$; $P = 0.892$; posterior: $F(1,7) = 0.233$; $P = 0.644$]. A complete list of the individual and averaged CBF values, for the visual cortex treatment and visit separately, is provided in Supporting Information Table IIa,b.

CBF Quantification Caffeine Treatment

Caffeine, however, induced a treatment effect (predose compared to postdose measurement) with a significant reduction in baseline CBF in the visual cortex with an average decrease of 19.80% and in stimulation CBF with an average decrease of 24.8% [$F(1,5) = 46.29$, $P = 0.001$] (Fig. 2, right). This significant reduction was observed in each subject (Table II). As expected, there was also a significant main effect of stimulation compared to resting period [$F(1,5) = 31.68$; $P = 0.002$]. The individual CBF values (±SD) in the visual cortex ROI for each condition, and visit are listed in Table II.

The control ROIs showed highly significant CBF decreases in both areas after caffeine ingestion [anterior: $F(1,5) = 141,488$; $P = 0.000$; posterior: $F(1,5) = 19,719$; $P = 0.007$]. Like on the insulin day, there were no significant

TABLE II. Gray-matter CBF-values (ml/100 g/min) ± SD in the visual cortex on the insulin day and caffeine day

Subject	Basal CBF		Stimulation CBF	
	Pre	Post	Pre	Post
Insulin day				
1	61.38 ± 12.40	62.28 ± 12.66	62.24 ± 11.72	67.57 ± 13.45
2	73.89 ± 13.24	76.45 ± 14.75	84.46 ± 17.34	84.08 ± 15.42
3	62.20 ± 11.62	67.24 ± 16.81	64.24 ± 12.17	79.68 ± 13.67
4	71.97 ± 14.96	67.41 ± 13.44	79.75 ± 17.88	69.41 ± 15.17
5	56.94 ± 9.58	57.68 ± 12.10	69.75 ± 17.93	68.60 ± 17.72
6	67.35 ± 15.86	69.00 ± 15.77	85.93 ± 24.21	82.21 ± 22.51
7	72.22 ± 14.27	71.86 ± 15.68	77.71 ± 17.47	80.56 ± 16.25
8	67.61 ± 11.56	64.14 ± 11.49	79.09 ± 16.84	72.63 ± 18.21
Mean ± SD	66.69 ± 6.03	67.00 ± 5.78	75.40 ± 8.94	75.59 ± 6.73
Caffeine day				
2	82.77 ± 11.73	61.28 ± 11.79	92.37 ± 19.70	67.67 ± 12.97
4	76.72 ± 15.47	61.01 ± 12.79	79.22 ± 15.58	67.41 ± 12.48
5	70.77 ± 12.51	56.64 ± 11.82	90.86 ± 19.22	62.89 ± 11.98
6	75.03 ± 12.00	56.20 ± 9.35	96.63 ± 22.65	65.64 ± 14.76
7	72.73 ± 16.14	63.25 ± 15.52	84.22 ± 16.45	64.61 ± 14.09
8	60.21 ± 8.45	53.06 ± 8.33	71.59 ± 16.78	61.68 ± 12.24
Mean ± SD	73.04 ± 7.51	58.57 ± 3.87	85.81 ± 9.31	64.98 ± 2.40

differences between baseline and task-induced CBF [anterior: $F(1,5) = 0.000$; $P = 0.996$; posterior: $F(1,5)$ 1,29; $P = 0.308$].

Voxel-Wise CBF Regression Analyses

To investigate the voxel-wise treatment effect (predose vs. postdose measurement), we performed a regression analysis using the CBF values of each voxel of the predose measurement as independent variables, and the corresponding voxels of the postdose measurement as dependent variables separately for baseline and stimulation of both tasks. Figure 3 shows voxel-by-voxel scatter plots and regression lines during the checkerboard task in the visual cortex ROI for the insulin (depicted in red) and caffeine treatment (depicted in blue) in a representative subject. Note that regression slopes of the CBF values for insulin treatment have a significant steeper slope compared to the caffeine administration in the basal and task-induced state. During the insulin day, we found a strong linear relationship between the baseline CBF values of the pre- and postdose measurements for the checkerboard task (slope = 0.95; rank: 0.82–1.11). The regression slopes during checkerboard stimulation were slightly smaller: slope = 0.89; rank: 0.76–1.03. In comparison, the regression slopes during the caffeine day were consistently smaller (Supporting Information Table Ia). Intraindividual comparisons of the regression slopes between the insulin and caffeine day showed that all subjects exhibited a significant steeper slope after insulin compared to caffeine administration in the basal and task-induced state (Supporting Information Table Ia). Similarly, the goodness of

fit estimates (Supporting Information Table Ib) support our findings showing that significantly more variance can be explained after intranasal insulin (r^2 ranging from 0.74 to 0.83) compared to caffeine application (r^2 ranging from 0.48 to 0.65).

BOLD Response

The BOLD response in the visual cortex was not significantly different between pre- and postdose measurements on the insulin day [$F(1,7) = 0.018$; $P = 0.855$; $0.45 ± 0.08$ vs. $0.46 ± 0.08$% signal change]. No voxel exceeded the statistical threshold ($z > 3$) in the two control ROIs. Similarly, caffeine ingestion showed no significant effect on the amplitude of the BOLD signal [$F(1,5) = 5.892$, $P = 0.060$; $0.50 ± 0.18$ vs. $0.64 ± 0.13$% signal change] when contrasted with the predose measurement.

DISCUSSION

This is the first imaging study showing that intranasally administered insulin has no direct effects on baseline and stimulus-induced CBF measured with a noninvasive ASL MRI technique. Intranasal insulin has the advantage of showing no indirect or confounding systemic effects, which are triggered by intravenous insulin application (decrease of plasma glucose concentration and changes in peripheral hormone levels). We found similar CBF before and after intranasal insulin application for the basal and task-induced CBF.

However, we cannot rule out that insulin has no effect on CBF in all brain areas. Furthermore, it might be that we
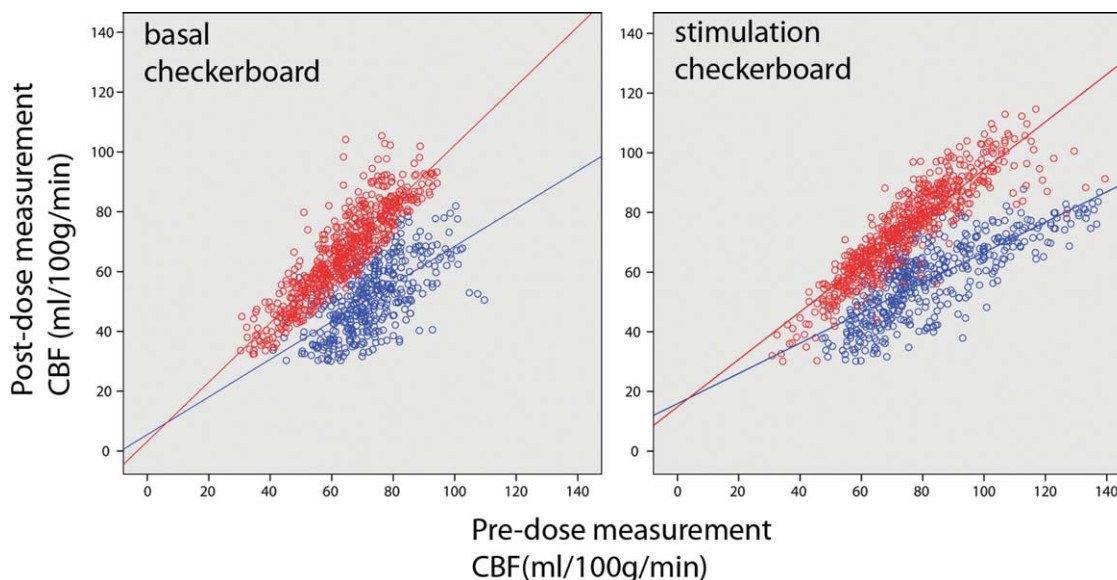
Figure 3.

Voxel-by-voxel scatter plots and regression line in the visual cortex ROI for the insulin (depicted in red) and caffeine day (depicted in blue) in a representative subject. On the left, the scatter plots of the basal CBF in the checkerboard in the pre (x-axes) and post-dose (y-axes) sessions are displayed. On the right, the scatter plots of the task-induced changes during checkerboard (upper right) are presented. Each dot represents the gray matter CBF value (ml/100 g/min) in the same voxel in the pre- and postdose session. In the case with identical CBF values in each voxel in the predose and postdose measurements, the slope of the regression line is one. The regression slopes of the CBF values for insulin treatment are significant steeper compared to the caffeine treatment in the basal and task-induced state.

missed a small effect of insulin on CBF because of the limited number of subjects. Another possible explanation for the negative finding in the present study may be that insulin concentration in the CNS is not increased sufficiently by the intranasal application. However, several previous studies (Born et al., 2002; Guthoff et al., 2010; Hallschmid and Schultes, 2009) showed that intranasal insulin, equivalent dose as used in the present study, increases intracerebral insulin concentration and affects brain function.

In the visual cortex, we did not find a task-induced change in the BOLD signal after intranasal insulin application compared to the predose measurement, which is in line with the studies by Guthoff et al. [2010] and Rotte et al. [2005]. In contrast, Seaquist et al. [2006] reported a profound reduction in the BOLD signal of around 16% in the visual cortex using a checkerboard task, but no changes in visual evoked potentials in the EEG (electroencephalography). However, based on the study design the authors could not rule out that this effect is mainly generated by fatigue.

The analyses of regression coefficients and the voxel-wise CBF changes after insulin or caffeine application confirm the results using average CBF-value. The comparison of the regression coefficients between the insulin and caffeine day revealed a significantly lower slope during caffeine administration compared to insulin. The lower slope

during the caffeine day shows that the effect is detectable on the average but also on a single voxel level. Furthermore, the goodness of fit estimates revealed that significantly less variance can be explained after caffeine intake compared to insulin in relation to the respective predose measurement. This indicates a higher voxel-to-voxel variability after caffeine intake. It has to be mentioned that the predose CBF-values cannot entirely predict the postdose CBF values after insulin application. Several methodological factors must be taken into account. Partial volume effects can lead to the miscalculation of the actual CBF [Chen et al., 2004] when the voxel covers not only arterial input (capillary beds) but also substantial intravascular signal as well as residual components of static magnetization from the blood. Beside these methodological issues, experimental as well as subject related factors can confound the stability of our measurements. Time-varying effects, like fatigue and increasing hunger due to prolonged fasting, can change the blood flow. It has been shown that fasting and therefore caffeine deprivation in high-caffeine users changes the BOLD signal and CBF differently compared to low-caffeine users [Laurienti et al., 2002]. Further studies are required to clarify this issue.

Caffeine administration, in contrast, revealed a significant reduction in basal blood flow as well as during visual stimulation both on the group and on the individual

level in all investigated cortical regions. The amount of decreases in CBF during caffeine were quite comparable with other studies [Field et al., 2003; Laurienti et al., 2003; Liau et al., 2008; Perthen et al., 2008]. Caffeine is a well-known vasoactive agent, which leads to the constriction of the vessels and a subsequent decrease of basal CBF.

In summary, we found no evidence for a direct effect of intranasal insulin on the basal CBF as well as on task-induced CBF changes in this study. Similarly, the BOLD signal seems to be not globally altered by insulin, although further studies are needed to resolve this issue. In contrast, caffeine as a control condition elicited pronounced decreases in CBF as a result of its vasoconstrictive effects. Although insulin seems to modify cerebral metabolism, it does not affect the vasculature in a notable manner. This is of particular relevance when using intranasal insulin as possible medication for food-related disorders or even neurodegenerative diseases.

REFERENCES

Baron AD (1996): Insulin and the vasculature—Old actors, new roles. J Investig Med 44:406–412.

Born J, Lange T, Kern W, McGregor GP, Bickel U, Fehm HL (2002): Sniffing neuropeptides: A transnasal approach to the human brain. Nat Neurosci 5:514–516.

Bosch K. 2005. Elementare Einführung in die angewandte Statistik, 8th ed. Wiesbaden: Germany, Vieweg.

Brüning JC, Gautam D, Burks DJ, Gillette J, Schubert M, Orban PC, Klein R, Krone W, Müller-Wieland D, Kahn CR (2000): Role of brain insulin receptor in control of body weight and reproduction. Science 289:2122.

Cavusoglu M, Pfeuffer J, Ugurbil K, Uludag K (2009): Comparison of pulsed arterial spin labeling encoding schemes and absolute perfusion quantification. Magn Reson Imaging 27:1039–1045.

Chen X-Q, Fawcett JR, Rahman Y-E, Ala TA, Frey WH II (1998): Delivery of nerve growth factor to the brain via the olfactory pathway. J Alzheimer's Dis 1:35–44.

Craft S, Watson GS (2004): Insulin and neurodegenerative disease: Shared and specific mechanisms. Lancet Neurol 3:169–178.

Guthoff M, Grichisch Y, Canova C, Tschritter O, Veit, R Hallschmid M, Häring H-U, Preissl H, Hennige AM, Fritsche A (2010): Insulin modulates food-related activity in the central nervous system. J Clin Endocrinol Metab 95:748–755.

Hallschmid M, Schultes B (2009): Central nervous insulin resistance: A promising target in the treatment of metabolic and cognitive disorders? Diabetologia 52:2264–2269.

Hallschmid M, Benedict C, Schultes B, Fehm H-L, Born J, Kern W (2004): Intranasal insulin reduces body fat in men but not in women. Diabetes 53:3024–3029.

Kennan RP, Takahashi K, Pan C, Shamoon H, Pan JW (2005): Human cerebral blood flow and metabolism in acute insulin-induced hypoglycaemia. J Cereb Blood Flow Metab 25:527–534.

Kerr D, Stanley JC, Barron M, Thomas R, Leatherdale BA, Pickard J (1993): Symmetry of cerebral blood flow and cognitive responses to hypoglycaemia in humans. Diabetologia 36:73–78.

Laurienti PJ, Field AS, Burdette JH, Maldjian JA, Yen YF, Moody DM (2003): Relationship between caffeine-induced changes in resting cerebral perfusion and blood oxygenation level-dependent signal. Am J Neuroradiol 24:1607–1611.

Liau J, Perthen JE, Liu TT (2008): Caffeine reduces the activation extent and contrast-to-noise ratio of the functional cerebral blood flow response but not the BOLD response. Neuroimage 42:296–305.

Lu H, Clingman C, Golay X, van Zijl PC (2004): Determining the longitidunal relaxation time (T1) of blood at 30 Tesla. Magn Reson Med 52:679–682.

Mintun MA, Vlassenko AG, Rundle MM, Raichle ME (2004): Increased lactate/pyruvate ratio augments blood flow in physiologically activated human brain. Proc Nat Acad Sci USA 101:659–664.

Perthen JE, Lansing AE, Liau J, Liu TT, Buxton RB (2008): Caffeine-induced uncoupling of cerebral blood flow and oxygen metabolism: A calibrated BOLD fMRI study. Neuroimage 40:237–247.

Porte D Jr, Baskin DG, Schwartz MW (2005): Insulin signaling in the central nervous system: A critical role in metabolic homeostasis and disease from C. elegans to humans. Diabetes 54:1264–1276.

Powers WJ, Hirsch IB, Cryer PE (1996): Effects of stepped hypoglycemia on regional cerebral blood flow response to physiological brain activation. Am Physiol Soc 0363–6135/96.

Reger MA, Watson GS, Green PS, Baker LD, Cholerton B, Fishel MA, Plymate SR, Cherrier MM, Schellenberg GD, Frey WH II, Craft S (2008): Intranasal insulin administration dose-dependently modulates verbal memory and plasma amyloid-β in memory-impaired older adults. J Alzheimers Dis 13:323–331.

Rotte M, Baerecke C, Pottag G, Klose S, Kanneberg E, Heinze H-J, Lehnert H (2005): Insulin affects the neuronal response in the medial temporal lobe in humans. Neuroendocronology 81:49–55.

Schwartz MW, Woods SC, Porte D Jr, Seeley RJ, Baskin DG (2000): Central nervous system control of food intake. Nature 404:661–671.

Seaquist ER, Chen W, Bendedict LE, Ugurbil K, Kwag JH, Zhu XH, Nelson CA (2006): Insulin reduces the BOLD response but is without effect on the VEP during presentation of a visual task in humans. J Cereb Blood Flow Metab 27:154–160.

Smith SM, Jenkinson M, Woolrich MW, Beckmann CF, Behrens TE, Johansen-Berg H, Bannister PR, De Luca M, Drobnjak I, Filtney DE, Niazy RK, Saunders J, Vickers J, Zhang Y, De Stefano N, Brady JM, Matthews PM (2004): Advances in functional and structural MR image analysis and implementation as FSL. Neuroimage 23(Suppl 1):208–219.

Tschritter O, Preissl H, Hennige AM, Stumvoll M, Porubska K, Frost R, Marx H, Klösel B, Lutzenberger W, Birbaumer N, Häring H-U, Fritsche A (2006): The cerebrocortical response to hyperinsulinemia is reduced in overweight humans: A magnetoencephalographic study. Proc Natl Acad Sci USA 103: 12103–12108.

Wong EC, Buxton RB, Frank LR (1997): Implementation of quantitative perfusion imaging techniques for functional brain mapping using pulsed arterial spin labeling. NMR Biomed 10:237–249.

Woods SC, Seeley RJ, Porte D Jr, Schwartz MW (1998): Signals that regulate food intake and energy homeostasis. Science 280:1378–1383.

6.3 Functional Localization in the Human Brain: Gradient-Echo, Spin-Echo, and Arterial Spin-Labeling fMRI Compared with Neuronavigated TMS

Functional Localization in the Human Brain: Gradient-Echo, Spin-Echo, and Arterial Spin-Labeling fMRI Compared with Neuronavigated TMS

Svenja Diekhoff,[1] Kamil Uludağ,[2] Roland Sparing,[3] Marc Tittgemeyer,[1] Mustafa Cavuşoğlu,[2] D. Yves von Cramon,[1] and Christian Grefkes[1,3]*

[1]*Max Planck Institute for Neurological Research, Cologne, Germany*
[2]*High-Field Magnetic Resonance Center, Max Planck Institute for Biological Cybernetics, Tübingen, Germany*
[3]*Department of Neurology, University of Cologne, Cologne, Germany*
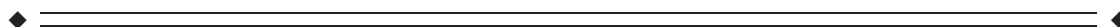
Abstract: A spatial mismatch of up to 14 mm between optimal transcranial magnetic stimulation (TMS) site and functional magnetic resonance imaging (fMRI) signal has consistently been reported for the primary motor cortex. The underlying cause might be the effect of magnetic susceptibility around large draining veins in Gradient-Echo blood oxygenation level-dependent (GRE-BOLD) fMRI. We tested whether alternative fMRI sequences such as Spin-Echo (SE-BOLD) or Arterial Spin-Labeling (ASL) assessing cerebral blood flow (ASL-CBF) may localize neural activity closer to optimal TMS positions and primary motor cortex than GRE-BOLD. GRE-BOLD, SE-BOLD, and ASL-CBF signal changes during right thumb abductions were obtained from 15 healthy subjects at 3 Tesla. In 12 subjects, tissue at fMRI maxima was stimulated with neuronavigated TMS to compare motor-evoked potentials (MEPs). Euclidean distances between the fMRI center-of-gravity (CoG) and the TMS motor mapping CoG were calculated. Highest SE-BOLD and ASL-CBF signal changes were located in the anterior wall of the central sulcus [Brodmann Area 4 (BA4)], whereas highest GRE-BOLD signal changes were significantly closer to the gyral surface. TMS at GRE-BOLD maxima resulted in higher MEPs which might be attributed to significantly higher electric field strengths. TMS-CoGs were significantly anterior to fMRI-CoGs but distances were not statistically different across sequences. Our findings imply that spatial differences between fMRI and TMS are unlikely to be caused by spatial unspecificity of GRE-BOLD fMRI but might be attributed to other factors, e.g., interactions between TMS-induced electric field and neural tissue. Differences between techniques should be kept in mind when using fMRI coordinates as TMS (intervention) targets. *Hum Brain Mapp 32:341–357, 2011.* © 2010 Wiley-Liss, Inc.

Key words: perfusion; CBF; BOLD; GRE; SE; ASL; spatial; transcranial magnetic stimulation; functional magnetic resonance imaging; motor mapping

INTRODUCTION

Gradient-Echo (GRE) echo planar imaging (EPI) is by far the most widely used technique for functional magnetic resonance imaging (fMRI) due to high data acquisition efficiency and high sensitivity to T_2^* effects [Liu and Brown, 2007]. The underlying blood oxygen level-dependent (BOLD) contrast relies on alterations of local magnetic susceptibility mainly caused by changes in deoxyhemoglobin level reflecting the increased metabolic demands due to enhanced neural activity (for a recent review see: Logothetis [2008]). However, such changes do not only occur in small blood vessels in brain parenchyma (e.g., gray matter) but also in large draining veins [Buxton et al. 1998]. GRE-BOLD signal has been shown to be sensitive to both T_2^* changes in parenchyma as well as in and around large draining veins [Boxerman et al., 1995; Frahm et al., 1994; Uludag et al., 2009] and hence GRE-BOLD signal changes may show a spatial displacement from actual neuronal activities, reducing the specificity for functional localization. Spin-Echo (SE) EPI is an alternative BOLD sequence which is sensitive to T_2 and has been suggested to be more accurate in functional localization at higher field strengths, i.e., from 3 Tesla (T) upwards [Duong et al., 2002; Lee et al., 2002; Thulborn et al., 1997; for review see: Norris, 2003; Uludag et al., 2009]. Decreased sensitivity of SE-BOLD for macrovasculature is achieved by an additional 180° refocusing pulse after half echo time refocusing static dephasing effects caused by local field inhomogenities around large vessels [Ye et al., 2009]. Along with SE-BOLD, Arterial Spin-Labeling (ASL) is an attractive alternative to GRE-BOLD. ASL allows measuring both, cerebral blood flow (CBF) as well as BOLD signal simultaneously. The signal type depends on the contrast calculated in the subsequent analysis, i.e., the BOLD contrast is the standard "activation vs. baseline" contrast, whereas the ASL-CBF contrast is the interaction between ASL-CBF time series (created by calculating control—tag differences) and the "activation vs. baseline" contrast. The ASL signal related to CBF (ASL-CBF) arises from magnetically labeled (i.e., tagged) arterial blood that has passed through the capillary walls into the tissue or is still located within capillaries [Silva et al., 1997]. A number of studies demonstrated that ASL-CBF is well co-localized with neuronal activity [Duong et al., 2000; Luh et al., 2000; Tjandra et al., 2005; Zappe et al., 2008; for reviews see: Liu and Brown, 2007; Silva, 2005].

Spatial accuracy of fMRI is especially important for fMRI informed (i.e., stereotaxically neuronavigated) transcranial magnetic stimulation (TMS). TMS is a well-established tool in neurosciences allowing noninvasive focal brain stimulation via externally applied magnetic fields [Barker et al., 1985]. Within the last decade, neuronavigation systems emerged allowing precise online monitoring of coil positions with reference to underlying brain structures and their functional properties assessed with anatomical or functional MRI, respectively. The potential of TMS in combination with fMRI is regarded to be high, especially for identification of TMS targets in the "virtual lesion" approach or in therapeutical intervention studies [Walsh and Cowey, 2000].

Several studies have already investigated the spatial congruence between positions yielding highest TMS effects, i.e., motor-evoked potentials (MEP), and positions with highest neural activity, i.e., highest statistical t-values, during hand movements measured by neuroimaging techniques such as positron emission tomography (PET) [Classen et al., 1998; Wassermann et al., 1996] or fMRI [Bastings et al., 1998; Boroojerdi et al., 1999; Herwig et al., 2002; Krings et al., 1997; Lotze et al., 2003; Sparing et al., 2008; Terao et al., 1998]. All studies reported good gross spatial correspondence between TMS and neuroimaging techniques as both techniques localized neural activity during hand movements within the precentral gyrus. However, if mean Euclidean distances between optimal TMS positions and highest neuroimaging signal were reported, they were often relatively large, i.e., 13 (±8.8) mm for ^{15}O PET (four subjects; Wassermann [1998]), 9.8 mm (eight subjects; Herwig et al. [2002]) and 13.9 mm (five subjects; Lotze et al. [2003]) for fMRI. Only one study reported relatively short mean 3D distances, i.e., 3.3 ± 0.8 mm (five subjects; Terao et al. [1998]) between TMS and fMRI. Hence, although all studies reported fairly good correspondence between TMS and fMRI, a considerably large residual mismatch has consistently been demonstrated rising the question whether these differences can be solely attributed to technical issues (e.g., coregistration inaccuracy or spatial unspecificity of fMRI signal) or if both techniques probe different underlying (neuronal) processes. Although relatively small sample sizes (in the majority of studies 4–5 subjects) and technical limitations due to unavailability of neuronagivated stimulation systems [Lotze et al., 2003; Terao et al., 1998; Wassermann, 1998] might have influenced spatial accuracy, the exact cause of the spatial mismatch remains unknown.

In the present study, we aimed to investigate whether displacements between TMS and fMRI might rely on the fMRI sequence used. All studies mentioned above used GRE-BOLD at 1.5 T (except for Krings et al. [1997] who used SE-BOLD at 1.5 T). Thus, all studies employed fMRI sequences that are susceptible to shifts towards large vessels at low field strengths. Hence, the observed mismatch between fMRI and TMS might, at least partially, be explained by inaccurate localization of motor hand area by the fMRI sequences used.

We, therefore, hypothesized that at 3 T, SE-BOLD and ASL-CBF may provide more accurate information in terms of functional localization of the motor hand area than GRE-BOLD. In particular, we aimed to test the hypothesis that spatial differences are functionally relevant by stimulating brain tissue at fMRI peak voxel coordinates with single-pulse neuronavigated TMS. Finally, we aimed to answer the question whether the spatially more accurate

fMRI sequences better match with optimal TMS sites for evoking highest motor responses.

METHODS

Subjects

MRI measurements were performed on 15 healthy subjects (eight males; 21–31 years old; mean age 24.9 ± 2.7). Fourteen subjects were right-handed and one subject was left-handed according to the Edinburgh Handedness Inventory [Oldfield, 1971]. We did not exclude left-handers as we did not expect that handedness impacts on spatial localization accuracy of fMRI sequences. Twelve subjects participated in a subsequent TMS session (seven males; 23–31 years old; mean age 25.1 ± 2.7; all right-handed). None of the subjects had any history of medical or psychiatric disease or contraindication to TMS [Wassermann, 1998]. All subjects gave informed written consent to participate in this study, which was approved by the ethics committee of the Medical Faculty, University of Cologne, Germany (file-no 08-062). All experiments conformed to the Declaration of Helsinki, sixth revision, 2008.

fMRI Motor Paradigm

Subjects were asked to perform visually paced rhythmic right thumb abductions at a frequency of 1.55 Hz. The movement frequency was paced by a red blinking circle on white background presented on a shielded TFT screen at the rear end of the MR scanner visible via a mirror mounted on the MR headcoil. Blocks of thumb movements (20 s) were separated by resting baselines (40 s plus 0–6 s jitter) in which a black screen instructed the subjects to rest still until the next block of movements commenced. One fMRI session consisted of 10 cycles of baseline and movement blocks and lasted approximately 11 min. Each subject underwent three fMRI sessions, i.e., one for each fMRI sequence. The order of fMRI sequences was counterbalanced across subjects. Prior to scanning, subjects were trained until a stable performance was reached, which was monitored by visual inspection.

fMRI Data Acquisition

MR images were acquired on a 3 T Siemens MAGNETOM Trio TIM scanner. High-resolution anatomical T_1-weighted images were acquired using a 3D MP-RAGE (magnetization-prepared, rapid acquisition gradient echo) sequence with the following imaging parameters: Time of Repetition (TR) = 2000 ms, Echo Time (TE) = 3.25 ms, Field of View (FOV) = 256 mm, 176 sagittal slices, slice thickness = 1 mm, in-plane resolution = 1×1 mm^2, flip angle = 9°. Although CBF and BOLD signal changes can be measured simultaneously using ASL, this approach has been shown to result in a reduction of the BOLD signal in the order of 15% compared to conventional BOLD meas-

urements [Luh et al., 2000]. Hence, a separate GRE-BOLD session was conducted in the present study to ensure that each fMRI measurement was conducted under optimal conditions. Altogether, we employed three different fMRI sequences: (i) GRE-BOLD EPI sequence with the following parameters: TR = 2200 ms, TE = 30 ms, FOV = 192 mm, 15 axial slices, slice thickness = 3 mm, in-plane resolution = 3×3 mm^2, distance factor = 10%, flip angle = 90°, (ii) SE-BOLD EPI sequence with identical imaging parameters except for a longer TE of 80 ms, and (iii) PICORE-Q2TIPS (quantitative imaging of perfusion using a single subtraction with thin slice TI_1 periodic saturation—proximal inversion with a control for off-resonance effects) ASL-CBF sequence [Luh et al., 1999] using a Frequency Offset Corrected Inversion pulse for inversion with the following parameters: TI_1 & equals; 700 ms, TI_{1s} = 900 ms, and TI_2 = 1400 ms, TR = 2200 ms, TE = 30 ms, FOV = 192 mm, 15 axial slices, slice thickness = 3 mm, in-plane resolution = 3×3 mm^2, distance factor = 10%, flip angle = 90°. The tag was 10 cm in width positioned at a 1 cm gap inferior to the imaging slices. Two presaturation pulses were applied in the imaging planes immediately before the inversion tag to minimize the impact of the static tissue. A 20-mm thick saturation slab was repeatedly applied for the bolus cutoff [Cavusoglu et al., 2009]. Images were acquired sequentially in ascending direction using a single-shot EPI technique. Slices covered a region extending from the body of the corpus callosum to the top of the parietofrontal vertex, thereby ensuring full coverage of the primary motor cortex along the central sulcus. Each fMRI session consisted of 310 EPI volumes including four "dummy" scans ensuring a steady-state in T_1 tissue contrast. 10 wholebrain EPI volumes (35 slices) were additionally acquired to improve the coregistration with the anatomical T_1 volume in data preprocessing (see below).

Analysis of Individual fMRI Data

For ASL sessions, ASL-CBF time series were created by calculating control-tag difference images (resulting in a total of 153 substraction images) using surround subtraction (i.e., computing the difference between each image and the average of its two nearest neighbors), thereby reducing BOLD signal contamination of the ASL-CBF time course (see Cavusoglu et al. [2009] for details). For image preprocessing and statistical analysis of GRE-BOLD, SE-BOLD, and ASL-CBF data, we used FEAT (FMRI Expert Analysis Tool) Version 5.98, part of FSL (FMRIB's Software Library, www.fmrib.ox.ac.uk/fsl). The following prestatistics processing was applied: motion correction using MCFLIRT [Jenkinson et al., 2002], nonbrain removal using Brain Extraction Tool (BET) [Smith, 2002], and spatial smoothing using a Gaussian kernel of 4-mm full-width half maximum (FWHM). Time-series statistical analysis was carried out using FILM (FMRIB's Improved Linear Model) with local autocorrelation correction [Woolrich

et al., 2001] and a high-pass filter of 1/60 Hz to remove low frequency drifts. Head motion parameters were included as covariates into the model. Z (Gaussianized T/ F) statistic images were thresholded using a voxel-wise corrected significance threshold of $P < 0.001$ [Forman et al., 1995; Friston et al., 1994; Worsley et al., 1992]. ASL-CBF provided much weaker signal intensities than BOLD signal and thus, no correction for multiple comparisons was applied for the identification of peak voxel coordinates ($P < 0.001$, uncorrected). Coregistration to high-resolution images was carried out using FLIRT [Jenkinson et al., 2001, 2002].

Identification of fMRI Peak Voxel

The voxel with the highest statistical *t*-value located within the precentral gyrus near or at the hand knob was identified for each of the three fMRI sessions per subject. The hand knob is shaped like an omega or epsilon in the axial plane and hook-shaped in the sagittal plane, and has been shown to constitute a reliable anatomical landmark for the motor hand area [Yousry et al., 1997]. In two subjects no significant voxel could be observed in the precentral gyrus for the SE-BOLD session after correcting for multiple comparisons, and thus no correction was applied for identification of the peak voxel in these subjects ($P < 0.001$, uncorrected).

Identification of fMRI CoGs

While the peak voxel represents the site of maximal regional activity, the center-of-gravity (CoG) of an fMRI activation cluster considers the spatial distribution of activity in the pericentral region and hence might be less prone to a spatial shift towards large veins which usually produce high levels of activation [Luh et al., 2000]. Therefore, CoGs were computed for each of the three fMRI sessions per subject. In contrast to peak voxel coordinates, CoG coordinates are influenced by the threshold applied and hence a uniform threshold of $P < 0.001$ (uncorrected) was applied to all fMRI data (lower thresholds were found to yield very large activation cluster for BOLD sessions, whereas higher statistical thresholds could not be passed by ASL-CBF activation clusters). After thresholding, the fMRI activation cluster comprising the peak voxel was identified and the CoG was calculated as *t*-value weighted position.

Group Analysis of fMRI Data

EPI volumes were normalized to the standard template (MNI152 at 2-mm resolution) of the Montreal Neurological Institute (MNI, Canada) using FNIRT (FMRIB's Nonlinear Image Registration Tool). A Gaussian kernel of 4-mm FWHM was used for spatial smoothing. For statistical analysis, we applied FLAME 1 (FMRIB's Local Analysis of Mixed Effects). Z (Gaussianized T/F) statistic images were thresholded using clusters determined by $Z > 2.3$ and a

corrected cluster significance threshold of $P < 0.001$. For anatomical assignment, statistics for the contrast "movement vs. baseline" were overlayed with cytoarchitectonic probability maps of the Juelich Histological Atlas [Eickhoff et al., 2007].

Neuronavigated TMS Apparatus

Stereotaxic frameless neuronavigation was performed with the eXimia NBS system Version 2.1.1 (Nexstim, Helsinki, Finland). As subjects performed a thumb abduction task during fMRI, the right abductor pollicis brevis (APB) muscle served as target muscle. Simultaneous electromyographic (EMG) recordings were additionally obtained from the right first dorsal interosseus (FDI) muscle. EMG signals were recorded by Ag/AgCl surface electrodes (Tyco Healthcare, Neustadt, Germany) placed in a belly tendon montage. The EMG signal was amplified, filtered with a 0.5 Hz high-pass filter and digitized using a Power-Lab 26 T Myograph and the "Scope" software package Version 3 (ADInstruments, Dunedin, New Zealand). Prior to the study, TMS coils were X-rayed. Displacements between central positions of the outer plastic case and the inner copper wings occurred solely in anterior–posterior (AP) direction and did not exceed 1 mm.

Motor Hotspot and Resting Motor Threshold

Subjects were comfortably seated in an adjustable armchair with head-rest. The head of the subject was coregistered with the individual high-resolution anatomical MR image via anatomical landmarks (e.g., nasion and crus helicis). Prior to the study, the accuracy of the coregistration procedure was verified by small vitamin E capsules (providing a good MRI T_1 contrast) attached to a volunteer's head at different anatomical positions. The software-depicted and true positions of the capsules did not show mismatches larger than 1 mm for any position. Furthermore, the root mean square difference between positions of landmarks in the MRI volume and at the subjects head was reported to be ≤2 mm for any TMS session of this study (reported by the neuronavigation software). After anatomical coregistration, the motor "hotspot," i.e., the coil position providing highest MEPs of the APB muscle with shortest latencies during single pulse supra-threshold TMS, was identified. Hotspot coil orientations were (nearly) perpendicular (90 ± 10°) to the central sulcus and tangential to the scalp in all investigated subjects (information provided by the neuronavigation software). The resting motor threshold (RMT) was assessed by means of the TMS Motor Threshold Assessment Tool 2.0 (http://www.clinicalresearcher.org/software.htm) suggested by Awiszus [2003]. The software starts with 45% as stimulator output intensity. After being informed via button press whether a TMS effect (in the present study: a MEP with a peak-to-peak amplitude of at least 50 µV) was induced by

the applied stimulus or not, the software suggests a new threshold intensity based on maximum likelihood calculations. In the present study, the procedure was repeated 12 times ensuring a reliable estimation of the motor threshold (MT).

TMS Motor Mapping

TMS mapping of the dominant, i.e., left motor cortex and the surrounding tissue was obtained by stimulation of an area determined by 8 anterior-posterior (AP) × 7 (medial–lateral) positions spaced at intervals of 10 mm. The hand knob structure [Yousry et al., 1997] was located approximately in the center of the grid, and the AP axis was oriented in parallel to the interhemispheric fissure. Classen et al. [1998] showed that increasing the grid size improves the motor mapping accuracy. Hence, we used a relatively large grid resulting in an area of 7 × 6 cm in size being stimulated. With such a large area stimulated we expected that stimulation of several positions at the margins of the grid would not result in MEPs. Classen et al. [1998] demonstrated that 5–6 stimuli per position are sufficient to achieve stable mapping results. Hence, positions not resulting in a MEP after 5 trials (peak-to-peak amplitude >50 μV) were stimulated with five stimuli, whereas positions resulting in at least one MEP after five trials were stimulated with 10 stimuli to achieve a good trade-off between mapping time and accuracy. The order of stimulation was randomized across the 56 positions [120% RMT; inter stimulus interval (ISI) = 1500 ms]. During the mapping procedure coil tilting was tangentially to the scalp and the TMS coil orientation was identical to coil orientation during RMT identification and stimulation at fMRI maxima coordinates. Both parameters were maintained throughout the mapping procedure.

The mean peak-to-peak MEP amplitude of the APB was calculated for each grid position using all EMG recordings obtained from this position (i.e., either 5 or 10) and divided by the largest amplitude obtained within the stimulation area. Based on these data, the CoG of the APB was calculated using the following formula:

$$CoG = \left[\sum_i \frac{\bar{a}(x_i, y_i)x_i}{a_{i,\max}}, \sum_i \frac{\bar{a}(x_i, y_i)y_i}{a_{i,\max}} \right]$$

with a_i being the mean amplitude at position x_i or y_i [Classen et al., 1998]. While the TMS motor hotspot represents the site of maximal neuronal excitability, the CoG takes into account the spatial distribution of excitability in the pericentral region. Spatial differences between hotspot and CoG locations occur if there is an asymmetrical distribution of excitability around the hotspot. Therefore, the information provided by a CoG is not the location of highest excitability, but the weighted average of excitability of the region of interest. CoG coordinates might be less prone to artifacts, e.g., resulting from co-activation of other muscles.

As it is unknown at which position, superficial or deep, TMS-induced neuronal excitation occurs we projected TMS identified positions (i.e., hotspot and CoG positions) onto the cerebral surface. This was done by identifying the individual depth of the cerebral surface by surface peeling of the software generated 3D head model (mean distance from the scalp: 24.5 ± 2.7 mm). Positions with highest electric field (EF) strength at the cerebral surface were recorded during hotspot identification and TMS mapping and used for later analyses. EF_{max} positions were then marked on the individual structural T_1 image and transferred into MNI space by applying the respective nonlinear normalization transform that was also used to transfer individual fMRI activation maps into MNI space.

TMS of Peak Voxel Coordinates at 120% RMT

Brain tissue at fMRI peak voxel coordinates was stimulated with 120% RMT (15 stimuli; ISI = 3000 ms). The order of peak voxels obtained by the three different fMRI sequences was counterbalanced across subjects. The experimenter was blinded to the fMRI sequence. The target entry point for stimulation was identified by bringing the TMS coil in a position in which the distance between fMRI target and EF_{max} value position was found to be minimal (0–2 mm, computed by the software). Then, tilting of the coil was adjusted until the coil was tangential to the scalp (computation and visual feedback provided by the software). TMS coil orientation coincided with TMS coil orientation during RMT identification. In this final position, one stimulus was applied. The coil positioning parameters of this stimulus were used as reference for all subsequent stimuli at this particular target (by means of the "aiming tool" implemented in the neuronavigation software).

RESULTS

fMRI Group Analysis

The fMRI group analysis of the contrast "right thumb movement vs. baseline" revealed a left-lateralized network of cortical areas in left sensorimotor cortex located on the precentral and postcentral gyrus (Fig. 1, $P < 0.001$, cluster-level corrected). SE-BOLD and GRE-BOLD sequences showed additional bilateral activation of the supplementary motor area (SMA), pre-SMA, cingulate motor area, dorsal and superior ventral premotor cortex, and anterior intraparietal cortex. More voxels were activated in the GRE-BOLD cluster as compared to the SE-BOLD cluster, and more for SE-BOLD than for ASL-CBF. The voxel with highest t-value at the precentral gyrus assessed in the voxel-wise group analysis of the spatially normalized GRE-BOLD session was close to the crown of the precentral gyrus (Fig. 1, top right) and assigned to Brodman Area 6 (BA6) by the Juelich Histological Atlas (MNI coordinates: −38, −22, 62). In contrast, the peak voxel of the
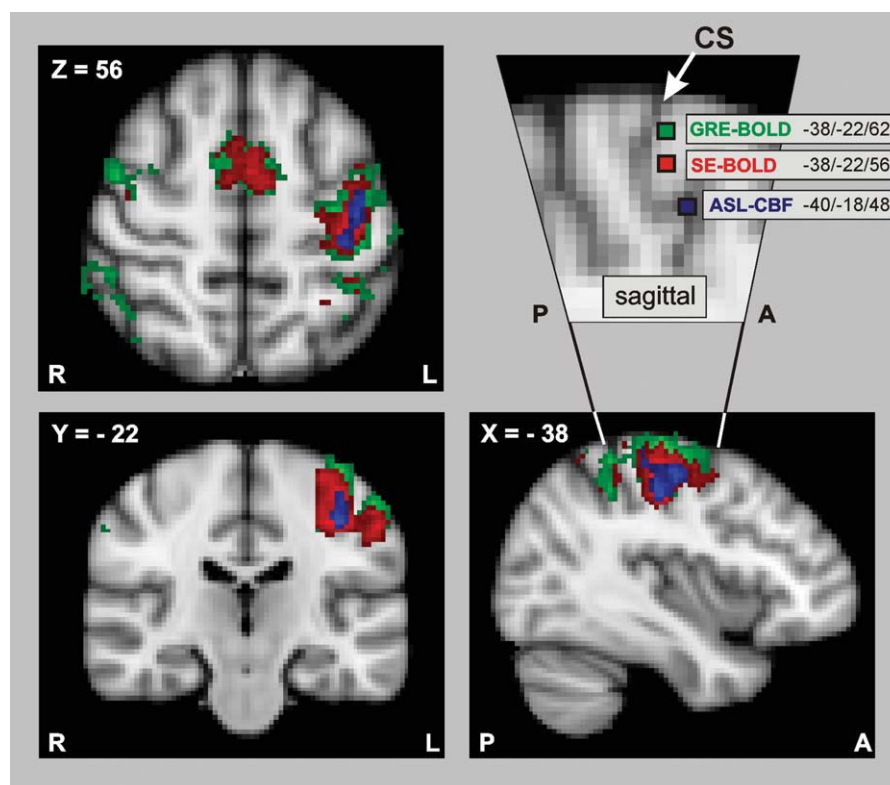
Figure 1.

Results of the fMRI group analysis. Functional magnetic resonance imaging (fMRI) was performed in 15 healthy subjects during right thumb abductions with three different fMRI techniques, i.e., Gradient-Echo (GRE-BOLD, green), Spin-Echo (SE-BOLD, red), and Arterial Spin-Labeling (ASL-CBF, blue). GRE-BOLD and SE-BOLD rely on blood oxygenation level-dependent (=BOLD) contrast, whereas ASL-CBF measures changes in cerebral blood flow (=CBF). "Movement vs. rest" contrasts were superimposed onto the MNI standard template ($P < 0.001$, cluster-level corrected; only voxels exceeding a t-threshold of 3.0 are shown). The detail of the sagittal view (top right) shows the voxel with highest statistical t-value located within the precentral gyrus for each of the three different fMRI techniques (voxels were projected into plane $X = -38$). In line with our hypotheses, SE-BOLD and ASL-CBF yielded more focused activation with higher specificity than GRE-BOLD. The voxel with highest GRE-BOLD signal change was closest to the gyral surface and was assigned to the premotor cortex (Juelich Histological Atlas). Highest SE-BOLD and ASL-CBF signal changes occurred 6 and 14 mm deeper within the central sulcus, respectively and were assigned to the primary motor cortex (Juelich Histological Atlas). The white arrow marks the central sulcus (CS).

SE-BOLD group analysis was 6 mm deeper within the central sulcus and assigned to area BA4a, i.e., the anterior primary motor cortex (MNI coordinates: −38, −22, 56). The peak voxel of the ASL-CBF group analysis was located even deeper in the central sulcus (14 mm deeper than GRE-BOLD, 8 mm deeper than SE-BOLD group fMRI peak voxels) and assigned to area BA4p, i.e., the posterior part of the primary motor cortex (MNI coordinates: −40, −18, 48).

Individual fMRI Peak Voxel Coordinates

The differences found for the fMRI sequences in the fMRI group analysis were confirmed by analyses based on individual activation maps. Movement-related neural activity could be observed with all three fMRI sequences in all subjects. However, sensitivity in terms of t-values of local maxima at the hand knob was significantly different across fMRI sequences [repeated measures ANOVA ($n = 15$)] with the factor "sequence" (levels "GRE-BOLD", "SE-BOLD", and "ASL-CBF"; $F(2, 28) = 64.003$; $P < 0.001$). GRE-BOLD peak voxels had significantly higher t-values (11.4 ± 3.8) than SE-BOLD (5.7 ± 2.3) and ASL-CBF (1.6 ± 0.9) peak voxels. SE-BOLD peak voxels had significantly higher t-values than ASL-CBF peak voxels (post-hoc paired sample t-test, $P < 0.001$, each comparison). However, also the position of the peak voxel coordinates was significantly different across sequences: A repeated
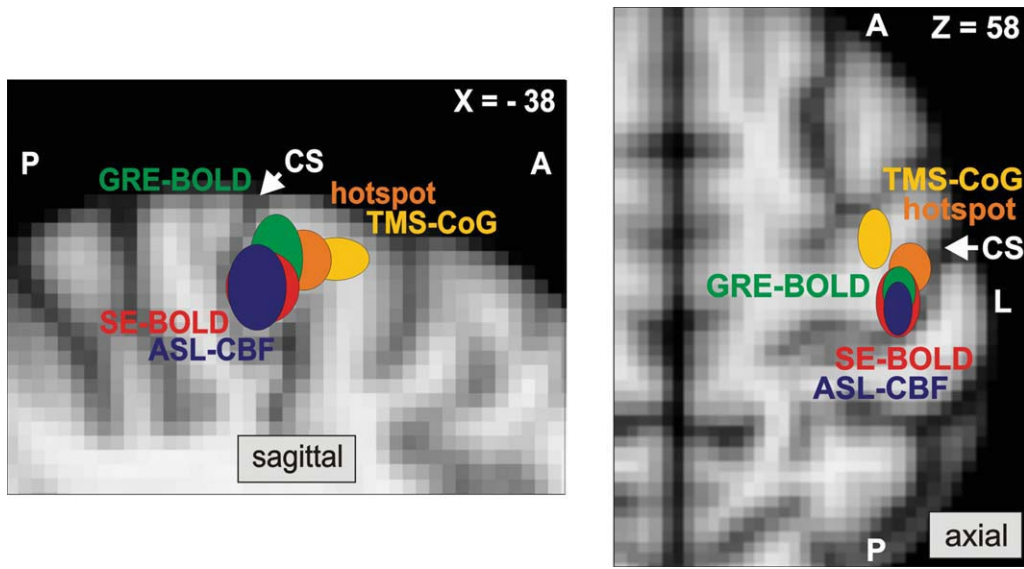
Figure 2.

Localization of the primary motor cortex with fMRI and TMS. Colored ellipsoids indicate mean MNI coordinates ($\pm$SD) of fMRI peak voxels and optimal transcranial magnetic stimulation (TMS) positions located within the precentral gyrus of the left hemisphere ($n = 12$ subjects). fMRI peak voxels were defined as voxel with highest statistical t-value during right thumb abductions measured with GRE-BOLD (green), SE-BOLD (red), and ASL-CBF (blue). Hotspot coordinates refer to stimulation sites resulting in highest abductor pollicis brevis (APB) muscle responses with shortest latencies (orange). CoG coordinates were calculated from a TMS motor mapping, and reflect the motor-evoked potential weighted maximum electric field coordi-

nate (yellow). All coordinates were projected into sagittal plane $X = -38$ for the figure on the left showing the sagittal view and plane $Z = 58$ for the right figure on the right showing the axial view. GRE-BOLD coordinates were significantly more superficial than SE-BOLD and ASL-CBF coordinates (paired-sample t-test, $P < 0.05$, each comparison). Hotspot and CoG coordinates were significantly more anterior than fMRI maxima (paired-sample t-test, $P < 0.05$, each comparison). Euclidean distances to hotspot or CoG coordinates were not statistically different for GRE-BOLD, SE-BOLD, and ASL-CBF coordinates (paired-sample t-test, $P > 0.05$, each comparison). The white arrow marks the central sulcus (CS).

measures ANOVA ($n = 15$) with the factor "sequence" (levels "GRE-BOLD", "SE-BOLD", and "ASL-CBF") showed significant differences between fMRI peak voxel coordinates in MNI coordinate Z [$F(2, 28) = 3.542$, $P < 0.05$; Fig. 2; Table I], i.e., in inferior–superior direction. Post-hoc t-tests revealed that GRE-BOLD coordinates (mean MNI coordinate Z: 60.7 ± 6.3) were significantly more superficial than SE-BOLD coordinates (56.4 ± 5.0) and ASL-CBF coordinates (55.5 ± 6.6), which were on average 4.3 and 5.2 mm deeper within the central sulcus, respectively ($P < 0.05$, for each comparison). SE-BOLD and ASL-CBF peak voxel coordinates were not statistically different ($P > 0.05$). There were no significant differences between sequences in the other two dimensions, i.e., in the medial–lateral (MNI coordinate X; ANOVA, $F(2, 28) = 1.053$; $P > 0.05$) or posterior–anterior direction [MNI coordinate Y; ANOVA, $F(2, 28) = 0.829$; $P > 0.05$].

Individual fMRI CoG Coordinates

Significant spatial differences in depth (i.e., in MNI coordinate Z) were preserved when similar analyses (repeated

measures ANOVA with the factor "sequence") were performed on fMRI CoGs instead of fMRI peak voxels [$F(2, 28) = 4.662$, $P < 0.05$]. Post-hoc t-tests revealed that GRE-BOLD CoG coordinates (mean MNI coordinate Z: 56.5 ± 2.5) were significantly more superficial than SE-BOLD (50.9 ± 5.5) and ASL-CBF (52.2 ± 6.9) CoG coordinates ($P < 0.05$, each comparison), whereas SE-BOLD and ASL-CBF CoG coordinates were not statistically different (paired sample t-test; $P > 0.05$). In addition, there was a significant difference in medial–lateral direction [i.e., in MNI coordinate X; $F(2, 28)$

TABLE I. Positions of highest fMRI signals and highest TMS effects individually identified in 12 subjects and transferred into MNI space using nonlinear normalization

	X	Y	Z
GRE-BOLD	-38.4 ± 3.2	-20.6 ± 4.2	60.7 ± 6.3
SE-BOLD	-37.9 ± 3.9	-21.5 ± 5.6	56.4 ± 5.0
ASL-CBF	-37.6 ± 2.6	-22.9 ± 4.5	55.5 ± 6.6
TMS hotspot	-40.7 ± 4.3	-15.7 ± 3.8	59.7 ± 3.7
TMS CoG$_{APB}$	-33.4 ± 2.7	-10.9 ± 5.0	60.0 ± 2.6

TABLE II. Euclidean distances between fMRI and TMS sites in single subject space

	fMRI peak voxel vs. TMS hotspot			fMRI CoG vs. TMS CoG		
Subjects	GRE	SE	ASL	GRE	SE	ASL
1	11.49	15.10	13.75	42.89	17.80	21.29
2	12.81	4.90	13.56	8.50	14.73	21.00
3	14.59	14.59	13.00	14.18	14.56	15.98
4	13.75	13.75	9.43	14.49	18.60	8.95
5	7.48	7.48	17.80	17.68	24.49	19.78
6	11.00	6.32	11.49	23.86	12.66	3.84
7	8.72	14.70	13.75	25.54	12.22	11.17
8	5.48	17.15	18.47	22.22	25.30	24.58
9	13.19	13.19	16.67	19.25	25.87	23.75
10	11.45	10.77	10.05	5.20	5.85	17.56
11	6.40	6.32	8.94	5.75	11.77	8.89
12	9.38	10.20	6.32	17.93	22.11	20.53
Mean	10.5	11.2	12.8	18.1	17.2	16.4
SD	3.0	4.1	3.7	10.3	6.3	6.7

$= 5.948$, $P < 0.05$] as GRE-BOLD CoGs were significantly more medial than SE-BOLD and ASL-CBF CoG coordinates (paired sample t-tests; $P < 0.05$, each comparison). SE-BOLD and ASL-CBF CoG coordinates were not statistically different in medial–lateral direction (paired sample test; $P > 0.05$). There were no statistically significant differences between sequences in AP localization (i.e., MNI coordinate Y) of CoGs [$F(2, 28) = 0.572$; $P > 0.05$].

Differences in fMRI and TMS Positions

For each subject, the TMS coordinate of the motor "hotspot" i.e., the coil position and tilt for evoking a MEP of 50 μV peak-to-peak amplitude with lowest stimulator output intensity) and the CoG of a systematic TMS mapping of the motor cortex were projected into MNI space applying the individual FNIRT registration transform. MNI coordinates were then compared with the fMRI peak voxel coordinates by computing a repeated measures ANOVA ($n = 12$) with the factor "localization approach" (levels "CoG$_{APB}$," "hotspot," "GRE-BOLD," "SE-BOLD," and "ASL-CBF"). The analyses revealed significant differences in medial–lateral direction, i.e., in MNI coordinate X [$F(4, 44) = 8.705$; $P < 0.001$) and in AP direction, i.e., in MNI coordinate Y [$F(4, 44) = 14.168$; $P < 0.001$]. Differences in inferior-superior direction, i.e., MNI coordinate Z showed a statistical trend [$F(4, 44) = 2.353$; $P = 0.069$; Table I]. Bonferroni-corrected post-hoc t-tests revealed that the motor hotspot was significantly anterior to GRE-BOLD, SE-BOLD, and ASL-CBF coordinates ($P < 0.05$, each comparison; Fig. 2). Displacements between fMRI maxima and the hotspot in medial-lateral direction were less pronounced but there was a statistical trend for hotspot coordinates to be more lateral than fMRI maxima ($P < 0.100$,

each comparison). Hotspot coordinates were assigned to BA6 in all 12 subjects (Juelich Histological Atlas). The CoG$_{APB}$ was significantly anterior to hotspot, GRE-BOLD, SE-BOLD, and ASL-CBF coordinates ($P < 0.05$, each comparison). In addition, CoG$_{APB}$ coordinates were significantly more medial than ASL-CBF, GRE-BOLD, and hotspot coordinates ($P < 0.05$, each comparison) whereas the comparison to SE-BOLD coordinates failed the corrected P-threshold of $P < 0.007$ only marginally ($P = 0.011$, uncorrected). In all 12 subjects the CoG$_{APB}$ was assigned to BA6.

## Euclidean Distances Between fMRI and TMS Positions

Although we found spatial differences between fMRI maxima obtained by different fMRI sequences, Euclidean distances between these maxima and the TMS hotspot were not statistically different across sequences [GRE-BOLD: 10.5 ± 3.0 mm; SE-BOLD: 11.2 ± 4.1 mm; ASL-CBF: 12.8 ± 3.7 mm; $F(2, 22) = 1.360$; $P > 0.05$, repeated measures ANOVA; see also Table II]. The same was true for Euclidean distances between fMRI maxima and the TMS mapping CoG$_{APB}$, which were also not significantly different across sequences [GRE-BOLD: 13.4 ± 5.5 mm; SE-BOLD: 15.3 ± 5.7 mm; ASL-CBF 15.3 ± 7.0 mm; $F(2, 22) = 1.115$; $P > 0.05$, repeated measures ANOVA]. In other words, none of the fMRI sequences localized neural activity systematically closer to the TMS hotspot or the TMS CoG$_{APB}$.

If identical analyses were conducted with fMRI CoGs instead of fMRI peak voxels, results were similar, i.e., none of the fMRI sequences yielded CoG positions systematically closer to the TMS hotspot [$F(2, 22) = 1.151$; $P > 0.05$] or CoG$_{APB}$ [$F(2, 22) = 0.191$; $P > 0.05$; see also Table II].

TMS of fMRI Peak Voxel with 120% RMT

We stimulated brain tissue at the fMRI peak voxel coordinate with single-pulse neuronavigated TMS to investigate whether the spatial differences found for the three different fMRI sequences are functionally relevant, i.e., impact on MEP size of the respective peripheral muscle. A repeated measures ANOVA ($n = 12$) with the factors "sequence" and "muscle" (levels "APB" and "FDI") yielded a significant main effect of sequence [$F(22, 2) = 4.797$; $P < 0.05$] and muscle [$F(11, 1) = 8.506$; $P < 0.05$] but no significant interaction [$F(22, 2) = 0.131$; $P > 0.05$]. Post-hoc t-tests revealed that mean peak-to-peak MEP amplitudes of the APB and the FDI were higher for GRE-BOLD coordinates compared to both SE-BOLD coordinates and ASL-CBF coordinates ($P < 0.05$, each comparison; Fig. 3A). Muscle responses during TMS of SE-BOLD and ASL-CBF coordinates were not statistically different ($P > 0.05$). MEPs of the APB were statistically higher than MEPs of
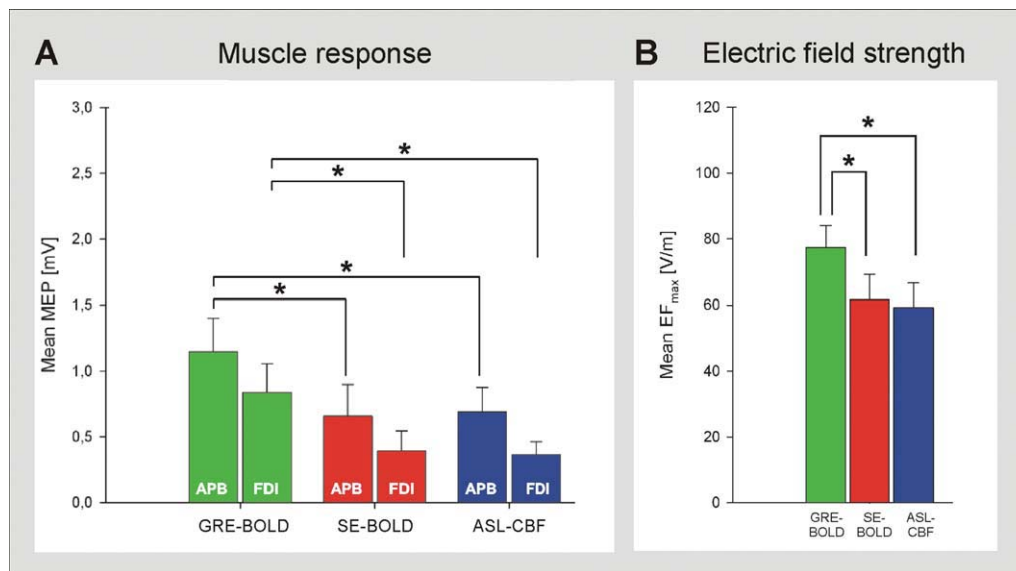
Figure 3.

Stimulation of brain tissue at fMRI peak voxel coordinates with TMS. Neuronavigated TMS (120% resting motor threshold) was used to stimulate brain tissue at fMRI peak voxel coordinates to investigate whether localization differences between fMRI sequences are functionally relevant, i.e., impact on muscle responses ($n = 12$ subjects). **A**: Muscle responses. Peak-to-peak motor-evoked potentials (MEPs) of the abductor pollicis brevis (APB) and the first dorsal interosseus (FDI) hand muscle are shown. MEPs resulting of stimulation at GRE-BOLD coordinates were significantly higher than MEPs resulting of stimulation at SE-BOLD and ASL-CBF coordinates. **B**: Electric field strength at target position. Maximum electric field values (EF_{max}) reaching the fMRI target position during stimulation are shown. GRE-BOLD coordinates were stimulated with significantly higher EF_{max} values than SE-BOLD and ASL-CBF coordinates which were significantly deeper in the central sulcus and hence further away from the TMS coil. Mean EF_{max} values during stimulation at SE-BOLD and ASL-CBF coordinates were not statistically different (paired-sample t-test, $P > 0.05$). Error bars indicate standard errors. Asterisks indicate significant differences in paired sample t-tests (paired-sample t-test, $P < 0.05$, each comparison).

the FDI during stimulation of SE-BOLD and ASL-CBF coordinates ($P < 0.05$, each comparison) but not during stimulation of GRE-BOLD coordinates ($P > 0.05$). In summary, spatial differences of local maxima were matched by functional differences in MEP amplitudes. TMS at GRE-BOLD coordinates was probably more effective than TMS at SE-BOLD or ASL-CBF coordinates because GRE-BOLD coordinates were more superficial and anterior, and hence closer to optimal TMS positions than SE-BOLD and ASL-CBF sites. We correlated individual differences in mean MEPs obtained by stimulation of GRE-BOLD vs. SE-BOLD positions with individual spatial differences of GRE-BOLD vs. SE-BOLD positions in AP direction. The result suggests that TMS over the GRE-BOLD site evoked larger MEPs the more anterior the GRE-BOLD coordinate was (APB: Pearson's $r = 0.67$, $P < 0.05$; FDI: Pearson's $r = 0.63$, $P < 0.05$). However, correlations for differences of GRE-BOLD vs. ASL-CBF positions and SE-BOLD vs. ASL-CBF positions were not statistically significant ($P > 0.05$, each correlation). Differences in medial–lateral or inferior–superior direction were not significantly correlated with differences in MEP amplitudes between the three different fMRI sites ($P > 0.05$, each correlation). However, a significant main

effect of sequence in the repeated measures ANOVA on mean EF_{max} values at the target position during TMS ($F(22, 2) = 5.779$; $P < 0.05$) indicates that due to the physical constraints of TMS, superficial GRE-BOLD coordinates were stimulated with significantly higher mean EF_{max} values (77.4 ± 23.2 V/m) compared to deeper SE-BOLD (61.7 ± 26.5 V/m) and ASL-CBF coordinates (59.2 ± 25.9 V/m; paired sample t-tests, $P < 0.05$, each comparison; Fig. 3B). Differences between SE-BOLD and ASL-CBF coordinates in EF_{max} values were not statistically significant (paired sample t-test, $P > 0.05$).

Tests to Exclude Spatial Errors of the TMS Equipment

Coregistration quality was verified prior to the study and after each session (to verify that the head tracker depicting the subject's head position had not changed its position during the TMS session). Furthermore, for one subject with pronounced anterior shift of the optimal TMS position (Subject 1, see Fig. 4), the complete motor mapping was repeated with the induced current direction as
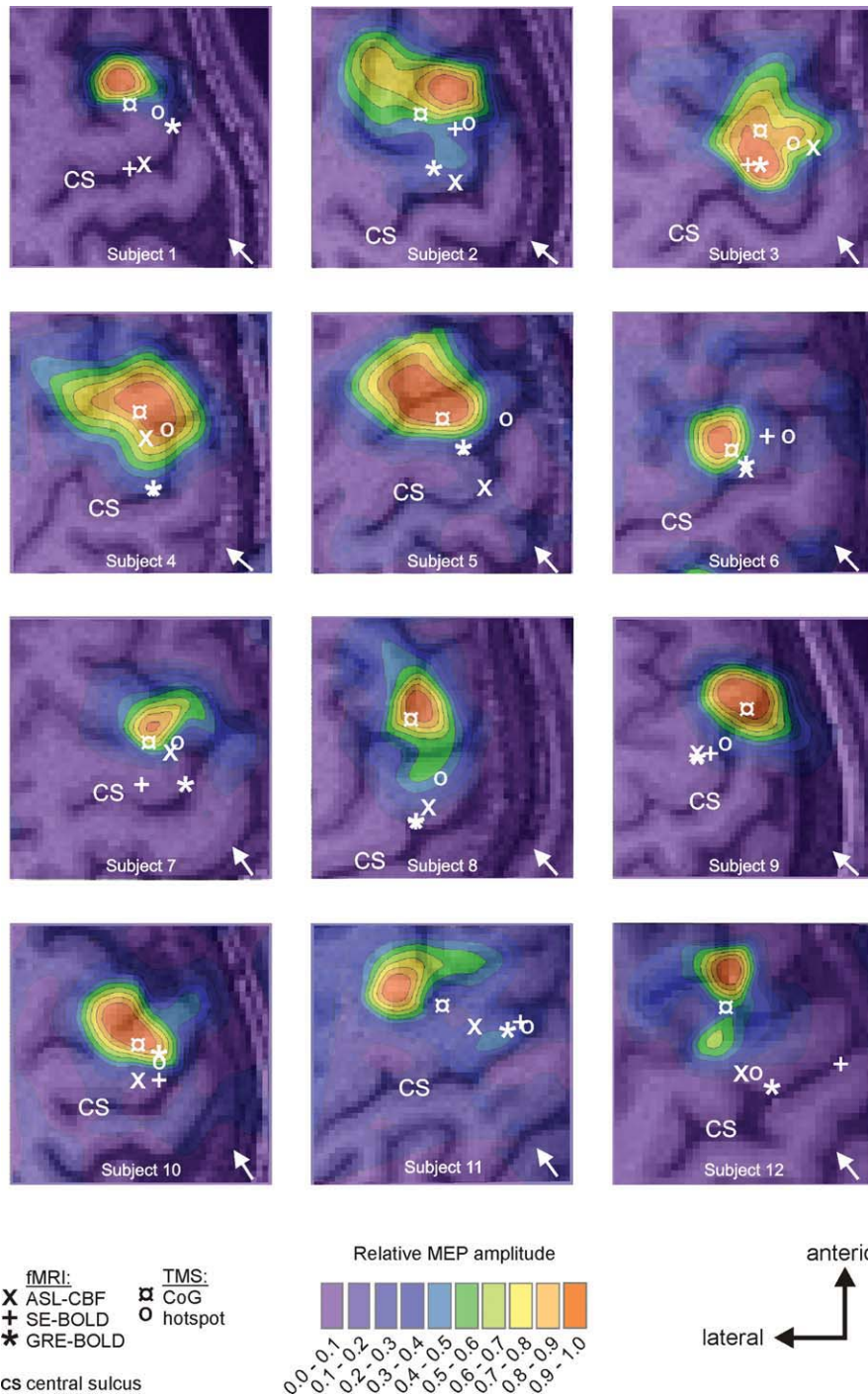
Figure 4.

Results of TMS motor mappings. Eight (anterior–posterior) × seven (medial–lateral) positions spaced at intervals of 10 cm were stimulated with neuronavigated TMS in randomized order (10 stimuli if at least one MEP > 50 μV was recorded after five stimuli; otherwise five stimuli; 120% RMT; ISI = 1500 ms). The hand knob was located approximately in the center of the grid, and the anterior–posterior axis was oriented in parallel to the interhemispheric fissure. Positions refer to electric field maximum (EF_{max}) positions within the cerebral cortex calculated by computerized modeling. Contours represent 10 percentiles of the averaged maximal response of the APB muscle viewed from above. Background images refer to individual structural images showing the corresponding underlying cerebral anatomy. All fMRI and TMS positions (depicted as white symbols) were projected into the slice corresponding to the mean axial depth of all five individual sites (i.e., GRE-BOLD, SE-BOLD, ASL-CBF, hotspot, and CoG).

applied before (i.e., PA, perpendicular to the central sulcus) and additionally with inverted induced current direction (i.e., AP, perpendicular to the central sulcus). If systematic anterior EF distortions due to coil failure or inaccurate computerized modeling accounted for the anterior shift of the optimal TMS position, then the CoG of the mapping with inverted coil orientation (AP-induced current direction) should be located considerably more posterior (i.e., to the amount of the displacement) than with standard coil orientation. The results showed that except for a drop in maximum MEP size, we basically replicated the map recorded with PA-induced current direction with almost identical location of peak excitability and CoG (Supporting Information Fig. 1). Therefore, technical confounds cannot explain the systematic anterior shift of optimal TMS positions when compared to fMRI peak voxels.

DISCUSSION

Localization Differences Between fMRI Sequences

Localization of the motor hand area

The primary motor cortex is a cortical key area for the execution of voluntary movements [Dum and Strick, 2002; Grefkes et al., 2008; Sanes and Donoghue, 2000]. This region is structurally well defined: Human post-mortem studies showed that the primary motor cortex (BA4) is a distinct cytoarchitectonic area characterized by the absence of layer IV and presence of giant Betz cells in layer V [Brodmann, 1909]. At the hand representation area, BA4 is buried within the central sulcus and rarely extends to the gyral surface [Geyer et al., 1996] where it forms a sharp boundary with the premotor cortex. As ASL-CBF and SE-BOLD showed highest signal increase during isolated simple thumb abductions in the rostral wall of the central sulcus, i.e., the location where BA4 has to be expected [Eickhoff et al., 2007], our data suggest that at 3 T these fMRI sequences may correctly locate the primary motor hand area. By contrast, signal increases for the GRE-BOLD sequence were shifted towards the crown of the precentral gyrus, and thus, towards premotor areas.

Systematic Superior Shift of GRE-BOLD

Both, fMRI group analysis as well as single subject fMRI analyses, demonstrated that highest GRE-BOLD signal changes showed a systematic shift in superior direction. These findings suggest that the underlying cause is, at least partially, subject-independent. High susceptibility of GRE-BOLD for large draining veins [Boxerman et al., 1995; Uludag et al., 2009] mainly running on the cerebral surface [Duong et al., 2000] seem to be the most likely explanation for our findings.

Spatial Localization of ASL-CBF (vs. GRE-BOLD) Signal

ASL sequences measure CBF by means of magnetically labeled arterial water that has either passed the capillary wall into tissue or is still located within capillaries [Silva et al., 1997]. Due to the tight neurovascular coupling, ASL-CBF changes have been shown to occur in close proximity to neuronal activity [Duong et al., 2000; Luh et al., 2000; Tjandra et al., 2005]. The main disadvantage of ASL-CBF over GRE-BOLD is decreased sensitivity. We used a robust block design and relatively long scanning durations of 11 min with only one condition to accomplish this problem, but being able to use equal experimental conditions (i.e., scanning times) for all fMRI sequences. Pilot experiments on healthy volunteers showed that shorter scanning times resulted in lower sensitivity whereas longer scanning times rather increased fatigue of the subjects and head movement artifacts with only minor gain in sensitivity (as the signal-to-noise ratio increases in proportion to the square root of the number of acquisitions, i.e., doubling SNR means four times longer scanning times). We, therefore, used a scanning duration of 11 min as trade off between evoking sufficient fMRI signal and duration of the whole fMRI experiments (which was 40 min on average (including structural images and localizers). However, the low sensitivity of ASL-CBF measurements did apparently not affect spatial localization accuracy which was found to be clearly superior over GRE-BOLD. Duong et al. [2000] compared GRE-BOLD and ASL-CBF signal changes during forepaw stimulation in anesthetized rats at 9.4 T and in line with our findings, GRE-BOLD signal was more expanded and located at the cortical surface whereas voxels with highest ASL-CBF percent signal changes showed excellent spatial co-localization with synaptic activity within deeper cortical layers [measured by means of manganese ion (Mn^{2+}) acting as calcium analogue and MRI contrast agent]. Interestingly, Luh et al. [2000] identified tissue types by means of T_1 maps and demonstrated that T_1-values were correlated on a voxel-wise basis with BOLD and ASL-CBF signal changes in healthy subjects at 3 T. For GRE-BOLD especially voxels with highest t-values predominantly contained cerebrospinal fluid (CSF) and/or blood. In contrast, highest relative ASL-CBF signal changes were located in voxels with T_1-values similar to voxels containing predominantly grey matter. In addition, Luh et al. [2000] demonstrated that BOLD and ASL-CBF activation maps showed a fractional overlap of only 40%. In contrast, Tjandra et al. [2005] found no statistical spatial displacement between GRE-BOLD and ASL-CBF statistical t-maps in healthy subjects at 3 T. However, Tjandra et al. [2005] used center-of-gravities (CoGs) instead of peak voxel coordinates. The findings of Luh et al. [2000] that especially voxels with high statistical values may contain signal from large veins and CSF, suggest that a venous

shift might have been evident when comparing peak voxels instead of CoGs. We, however, found no support for this suggestion in the present study as the results of analyses with fMRI peak voxels were preserved in analyses with fMRI CoGs, i.e., fMRI coordinates showed differences in depth but not in Euclidean distances to optimal TMS positions. Nevertheless, Tjandra et al. [2005] also defined the nearest draining vein by MR venograms and found that GRE-BOLD signal was significantly closer to draining veins than ASL-CBF signal. Thus, our data are supported by growing body of evidence that ASL-CBF is better co-localized to neural activity, whereas GRE-BOLD is susceptible to shifts towards large veins or CSF.

Localization of SE-BOLD vs. GRE-BOLD

SE-BOLD and GRE-BOLD fMRI sequences are both sensitive to the BOLD effect—a joint combination of changes in blood volume, CBF, and de-oxygenation level of blood [Buxton et al., 1998]. At 1.5 and 3 T, both sequences have high susceptibility for large draining veins [Kennan et al., 1994; Boxerman et al., 1995; Oja et al., 1999; Uludag et al., 2009]. From 3 T upwards, intravascular signal from veins vanishes for SE-BOLD, but not GRE-BOLD [Uludag et al., 2009]. Intra- and extravascular contributions to SE-BOLD signal changes are equal at 3 T [Norris et al., 2002] but intravascular signals mainly arise from microvasculature (i.e., capillaries, arterioles, and venules). Although intravascular signal also decreases with increasing field strength for GRE-BOLD, there is no field strength at which the BOLD signal from the microvasculature is larger than from the macrovasculature [Uludag et al., 2009]. Recent high magnetic field studies in rats [Lee et al., 2002] and humans [Duong et al., 2002] demonstrated that both SE-BOLD and ASL-CBF located neural activity within grey matter with good spatial correspondence suggesting that SE-BOLD provides comparable high spatial specificity as ASL-CBF. Several studies investigating the laminar specificity of high-resolution SE-BOLD and GRE-BOLD fMRI in primary visual cortex of macaque monkeys [Goense and Logothetis, 2006] and cats [Harel et al., 2006] at 4.7 and 9.4 T, respectively demonstrated laminar specific activation for SE-BOLD yielding highest signal changes in cortical layer IV whereas highest GRE-BOLD signal changes occurred at the cerebral surface. However, studies comparing different fMRI sequences in humans at 3 T are scarce [Thulborn et al., 1997]. Thulborn et al. [1997] measured neural activity during stimulation with different visual stimuli and found that the 10 most significant voxels obtained with SE-BOLD and GRE-BOLD overlapped by only 30–40%. This result suggests that SE-BOLD signal is not just a subset of the more sensitive GRE-BOLD activation, but that both detect spatially different effects. This finding is in good agreement with our data suggesting that already from 3 T on, SE-BOLD signal changes are well localized

with primary motor cortex activity. Uludag et al. [2009] showed that reduced macro-vasculature weighting is achieved if large vessels predominantly run parallel to the main magnetic field as the susceptibility effect equals to zero for this condition. This is, for example, true for the central sulcus and hence for parts of the motor cortex but not, e.g., for the calcarine sulcus where the large vessels are mainly oriented perpendicular to the magnetic field. Therefore, in our study, SE might be more sensitive to gray matter than large vessels.

Taken together our findings strongly encourage considering alternative fMRI sequences such as ASL-CBF and (under certain conditions) SE-BOLD when spatial localization is of high priority. However, decisions may depend on multiple aspects and not only on localization (Table III). For example, ASL-CBF is superior to GRE-BOLD in spatial accuracy, provides lower inter-session and inter-subject variation [Tjandra et al., 2005], and offers quantitative measures, in contrast to GRE-BOLD [Kim et al., 1997; Luh et al., 1999]. However, GRE-BOLD offers highest sensitivity (in terms of contrast-to-noise ratio), temporal resolution (due to faster data acquisition) and finally, a larger number of slices can readily measured with GRE-BOLD, whereas ASL-CBF is limited to fewer slices [Liu and Brown, 2007].

Localization Differences Between fMRI and TMS

Surprisingly, although SE-BOLD and ASL-CBF were more accurate in anatomical localization of the primary motor hand area, they provided significantly lower muscle responses than GRE-BOLD when stimulated with TMS. One explanation may be found in the properties of the EF induced by the magnetic pulse which declines exponentially with increasing distance from the coil [Eaton, 1992]. As GRE-BOLD peak voxel coordinates were significantly more superior (i.e., closer to the TMS coil), they were stimulated with significantly higher EF strengths than SE-BOLD and ASL-CBF peak voxels. In this case, stimulation under equal conditions seems impossible to achieve with TMS, as stimulation of maxima with similar EF values would require stimulation with highly differently stimulator output intensities, thereby enlarging the stimulated area. However, as it is unknown at which position, superficial or deep, excitation occurs accounting for highest TMS effects [Fox et al., 2004; Salinas et al., 2009; Thielscher and Wichmann, 2009], the most likely explanation for our findings is that the GRE-BOLD site was located more anterior (i.e., closer to the TMS hotspot) and thus TMS at the GRE-BOLD site was more effective. However, spatial distances between fMRI peak voxels and optimal TMS positions, i.e., hotspots and mapping CoGs, were not statistically different across fMRI sequences. This finding demonstrates that the mismatch between TMS and fMRI persists even if fMRI sequences with high anatomical accuracy such as ASL-CBF or SE-BOLD are used. Hence, a

TABLE III. Qualitative comparison of different motor mapping approaches

	fMRI			TMS
Aim	Identification of position with highest task-related neural activity			Identification of position with lowest electrophysiological threshold to elicit MEPs of the respective peripheral muscle
Assessed via	Neurovascular coupling			Cortico-spinal excitability
	GRE-BOLD	SE-BOLD	ASL-CBF	
Measured variable(s)	BOLD (Deoxy-Hb, CBF, CBV)	BOLD (Deoxy-Hb, CBF, CBV)	CBF	Peripheral EMG signals
Main advantages	High CNR	High spatial specificity	High spatial specificity	Independent of vascular effects
Main disadvantages	Low spatial specificity	Low CNR	Low CNR	Restricted to superficial areas (limited penetration depth)
Main source of signal	Large draining veins	Microvasculature (≥3 T)	Arterioles and capillaries	Indirect trans-synaptic excitation of cell bodies and direct excitation of axons
Localized structure	BA6	BA4a	BA4p	BA6
Distance to surface	+	++	+++	n/a

Please see text body for references.

potential shift of GRE-BOLD towards superficial veins cannot explain the spatial mismatch observed between TMS and fMRI. Although fMRI and TMS were not expected to yield exactly identical positions due to apparent technical differences underlying these two brain mapping approaches, spatial mismatches were considerably large, i.e, 11.9 mm and optimal TMS positions were located within premotor areas in all 12 subjects [Eickhoff et al., 2007]. These differences are not likely to be caused by technical issues, such as systematic coregistration errors or systematic EF distortions in the posterior direction, since the magnitude of displacements were highly different across subjects (e.g., low in Subject 6, and high in Subject 8; Fig. 4). Furthermore, similar anterior displacements were also reported in previous studies investigating spatial congruency of TMS and neuroimaging data such as PET [Classen et al., 1998] and fMRI [Herwig et al., 2002; Lotze et al., 2003]. Even if no precise specifications were made, figures in papers often suggested anterior displacements of optimal TMS positions relative to PET (Wassermann et al. [1996]; Fig. 2) or fMRI (Bastings et al. [1998]; Figs. 2 and 3) activations.

Possible Explanations for the Anterior Shift of Optimal TMS Positions

Muscle responses evoked by TMS typically have up to 3 ms longer latencies than muscle responses evoked by electrical stimulation, which led to the assumption that TMS activates cortical cells predominantly trans-synaptically, whereas electrical stimuli excite cortical cell bodies or axons directly [Day et al., 1989; Hess et al., 1987; Mills et al., 1992; Rothwell et al., 1991]. However, it is unknown whether the entire synaptic chain (from optimal stimulation position to descending motoneurons) is located within the primary motor cortex or whether it includes (inter-) neurons in other regions, e.g., premotor cortex projecting onto BA4 neurons. Hence, although it seems unlikely, it cannot be ruled out that indirect stimulation of BA4 neurons via trans-synaptic input from BA6 accounts for anterior positions of optimal TMS sites.

Although fMRI and TMS sessions were performed under different functional motor states, ("active" during fMRI sessions, "passive" during TMS sessions) this difference seems unlikely to account for the spatial mismatch observed since previous studies demonstrated that TMS mappings under low-level voluntary contraction (10–20% of maximum contraction) yield CoGs significantly anterior (and non-significantly medial) of CoGs obtained at rest [Lewko et al., 1996; Wilson et al., 1995]. This anterior–medial shift (in the range of 6.6–20 mm) could be caused by decreased thresholds for surrounding premotor and SMAs during muscle pre-activation [Lewko et al., 1996]. However, this anterior–medial shift would have more likely enlarged than shortened the distance between fMRI and TMS positions in the present study, as TMS mapping

CoGs showed already (predominantly) anterior displacements.

We rather assume that EF effects are likely to account for the anterior shift of optimal TMS positions. Like the neuronavigation system used in the present study, most systems compute EF strength based on spherical head models which assume that EF is maximal directly under the junction of the wings and declines exponentially with distance from the coil [Eaton, 1992]. However, there is growing evidence that this simplified model is insufficient, as different tissue types of the head have different conductivities which change the EF considerably. Realistic head models such as tissue-segmented MR images with realistic anatomical features like gyri and sulci demonstrated that the EF forms a complex pattern onto the folded cerebral cortex [Salinas et al., 2009]. For instance, secondary EFs with either decreasing or increasing effects of varying magnitude (20–35% of primary EF) and direction (often opposing the primary EF) occur especially near tissue boundaries [Salinas et al., 2009]. These data show that stimulation with highest EF intensities does not necessarily occur directly under the junction of the coil as proposed by spherical head models. Therefore, it might be that stimulation with highest EF strength did not necessarily occur directly at the CoG position.

The neurophysiology of TMS is still incompletely understood but there is some evidence that medial-lateral induced current directions activate cortical motor neurons directly leading to D-waves whereas PA-induced current directions, as used in the present study, activate cortical motor neurons predominantly indirectly via interneurons leading to I-waves [Di Lazzaro et al., 1998]. However, at stimulus intensities above the MT, as applied in the present study, induced PA current direction can also excite neurons directly generating D-waves [Di Lazzaro et al., 1998]. Hence, for the coil orientation and stimulus intensity used in the present study both types of neuronal excitation (direct and indirect) should be considered. I-wave generation relies on short distance (inter)neuron or even microscopic (dendrite, cell body) geometry [Herbsman et al., 2009], and there is some evidence that especially these short distance neuronal structures are subject to orientation-specific effects [Amassian et al., 1998]. For instance, Fox et al. [2004] demonstrated that the orientation of the EF relative to cortical columns outweighs highest absolute EF strengths, i.e., TMS excitation was optimal within sulci where cortical columns run parallel to EF direction, although the absolute EF was higher at gyral crowns (where orientation to cortical columns is less optimal). Direct excitation on the other hand is mediated by longer neuronal structures, i.e., axons. Here, inhomogenities of the applied electric field caused by changes of the axonal trajectory relative to the EF are the most dominant factor in TMS-induced neuronal excitability [Amassian et al., 1992; Abdeen and Stuchly, 1994; Maccabee et al., 1993]. Axons originating from BA4 first run perpendicular and anterior to the sulcal wall, and then turn approxi-

mately 90° downwards to form the cord fibres and the subcortical bundle in the center of the precentral gyrus [Schmahmann and Pandya, 2006]. Therefore, if for some subjects axonal thresholds were lower due to more abrupt white matter bendings [Fox et al., 2004], these subjects would show an anterior shift of optimal TMS excitation spots. In line with this suggestion are also the results of a very recent study by Herbsman et al. [2009] who investigated the relation between TMS excitability (i.e., MT) and several anatomical parameters in 17 subjects. Approximately 50–60% of the inter-subject variability in MT can be explained by the subjects' individual skull-to-cortex distance [Kozel et al., 2000] but there is also strong evidence that the anterior component of the corticospinal tract is an additional important predictor for MT accounting for ~48% of the variance observed [Herbsman et al., 2009]. Pronounced anterior components of the corticospinal tract were associated with low MT [Herbsman et al., 2009] suggesting that TMS with PA induced current direction may act directly on axons running anterior of BA4 and changing their trajectory relative to the EF.

Implications and Limitations

In summary, we conclude from the findings of the current study that the spatial mismatch between fMRI and TMS is not caused by the venous shift of GRE-BOLD signal. Spatial differences between fMRI and TMS are likely to result from different underlying physiological processes, i.e., fMRI predominantly reflects the position with highest task-related synaptic activity [Duong et al., 2000] at cell bodies, i.e, within grey matter, whereas TMS mappings yield optimal positions for neuronal excitation with applied EFs. These two positions might be different for several reasons including (i) EF distortion (caused by tissue boundaries, etc.) and (ii) direct excitation of axons [Di Lazzaro et al., 1998] which might be distant from cell bodies in white matter. However, if fMRI-based coordinates are more appropriate TMS intervention sites than TMS hotspots remains to be tested in future. One limitation of the present study might be the fact that effects are EF orientation (and hence coil orientation) specific. Our finding that optimal TMS positions were more anterior might not apply to TMS mappings with other coil orientations. EFs in the coronal plane are more likely to act on medial-lateral fiber tract components, and hence might show displacements in medial-lateral direction in contrast to EFs in PA (or AP) directions which predominantly act on AP fiber tract components [Herbsman et al., 2009]. Another limitation of the present study might be that fMRI and TMS sessions were not matched in functional state although fMRI informed TMS lesion studies usually use the same task for the MRI localizer and the TMS experiment. Although this limitation is unlikely to account for the mismatch between fMRI and TMS sites observed in

the present study, it might limit the significance of our findings with respect to previous fMRI-informed (r)TMS studies. Nevertheless, our findings also have implications for studies in which optimal TMS positions cannot be identified as easily as for the motor or visual cortex. Although fMRI-informed TMS might not reflect the optimal position to generate TMS effects, our data indicate that it provides a position resulting in measurable TMS effects, and hence fMRI informed TMS should be preferred to the sole use of structural landmarks. Furthermore, our data imply that if behavioral effects are absent after rTMS over fMRI-based coordinates (e.g., in a cognitive task), missing effects might also result from suboptimal stimulation of the target region due to the spatial mismatch of fMRI coordinates and maximal TMS effects as demonstrated for the motor system in the present study.

ACKNOWLEDGMENTS

REFERENCES

Abdeen MA, Stuchly MA (1994): Modeling of magnetic field stimulation of bent neurons. IEEE Trans Biomed Eng 41:1092–1095.

Amassian VE, Eberle L, Maccabee PJ, Cracco RQ (1992): Modelling magnetic coil excitation of human cerebral cortex with a peripheral nerve immersed in a brain-shaped volume conductor: The significance of fiber bending in excitation. Electroencephalogr Clin Neurophysiol 85:291–301.

Amassian VE, Cracco RQ, Maccabee PJ, Cracco JB, Rudell AP, Eberle L (1998): Transcranial magnetic stimulation in study of the visual pathway. J Clin Neurophysiol 15:288–304.

Awiszus F (2003): TMS and threshold hunting. Suppl Clin Neurophysiol 56:13–23.

Barker AT, Jalinous R, Freeston IL (1985): Non-invasive magnetic stimulation of human motor cortex. Lancet 1:1106–1107.

Bastings EP, Gage HD, Greenberg JP, Hammond G, Hernandez L, Santago P, Hamilton CA, Moody DM, Singh KD, Ricci PE, Pons TP, Good DC (1998): Co-registration of cortical magnetic stimulation and functional magnetic resonance imaging. Neuroreport 9:1941–1946.

Boxerman JL, Bandettini PA, Kwong KK, Baker JR, Davis TL, Rosen BR, Weisskoff RM (1995): The intravascular contribution to fMRI signal change: Monte Carlo modeling and diffusion-weighted studies in vivo. Magn Reson Med 34:4–10.

Buxton RB, Wong EC, Frank LR (1998): Dynamics of blood flow and oxygenation changes during brain activation: the balloon model. Magn Reson Med 39:855–864.

Boroojerdi B, Foltys H, Krings T, Spetzger U, Thron A, Topper R (1999): Localization of the motor hand area using transcranial magnetic stimulation and functional magnetic resonance imaging. Clin Neurophysiol 110:699–704.

Brodmann K (1909): Vergleichende Lokalisationslehre der Grosshirnrinde: In Ihren Principien dargestellt auf Grund des Zellenbaues. Leipzig: Johann Ambrosius Barth Verlag.

Cavusoglu M, Pfeuffer J, Ugurbil K, Uludag K (2009): Comparison of pulsed arterial spin labeling encoding schemes and absolute perfusion quantification. Magn Reson Imaging 27:1039–1045.

Classen J, Knorr U, Werhahn KJ, Schlaug G, Kunesch E, Cohen LG, Seitz RJ, Benecke R (1998): Multimodal output mapping of human central motor representation on different spatial scales. J Physiol 512 (Pt 1):163–179.

Day BL, Dressler D, Maertens de Noordhout A, Marsden CD, Nakashima K, Rothwell JC, Thompson PD (1989): Electric and magnetic stimulation of human motor cortex: surface EMG and single motor unit responses. J Physiol 412:449–473.

Di Lazzaro V, Oliviero A, Profice P, Saturno E, Pilato F, Insola A, Mazzone, Tonali P, Rothwell JC (1998): Comparison of descending volleys evoked by transcranial magnetic and electric stimulation in conscious humans. Electroencephalogr Clin Neurophysiol 109:397–401.

Dum RP, Strick PL (2002): Motor areas in the frontal lobe of the primate. Physiol Behav 77:677–682.

Duong TQ, Silva AC, Lee SP, Kim SG (2000): Functional MRI of calcium-dependent synaptic activity: Cross correlation with CBF and BOLD measurements. Magn Reson Med 43:383–392.

Duong TQ, Yacoub E, Adriany G, Hu X, Ugurbil K, Vaughan JT, Merkle H, Kim SG (2002): High-resolution, spin-echo BOLD, and CBF fMRI at 4 and 7 T. Magn Reson Med 48:589–593.

Eaton H (1992): Electric field induced in a spherical volume conductor from arbitrary coils: Application to magnetic stimulation and MEG. Med Biol Eng Comput 30:433–440.

Eickhoff SB, Paus T, Caspers S, Grosbras MH, Evans AC, Zilles K, Amunts K (2007): Assignment of functional activations to probabilistic cytoarchitectonic areas revisited. Neuroimage 36:511–521.

Forman SD, Cohen JD, Fitzgerald M, Eddy WF, Mintun MA, Noll DC (1995): Improved assessment of significant activation in functional magnetic resonance imaging (fMRI): Use of a cluster-size threshold. Magn Reson Med 33:636–647.

Fox PT, Narayana S, Tandon N, Sandoval H, Fox SP, Kochunov P, Lancaster JL (2004): Column-based model of electric field excitation of cerebral cortex. Hum Brain Mapp 22:1–14.

Frahm J, Merboldt KD, Hanicke W, Kleinschmidt A, Boecker H (1994): Brain or vein—oxygenation or flow? On signal physiology in functional MRI of human brain activation. NMR Biomed 7:45–53.

Friston KJ, Worsley KJ, Frackowiak RSJ, Mazziotta JC, Evans AC (1994): Assessing the significance of focal activations using their spatial extent. Hum Brain Mapp 1:210–220.

Geyer S, Ledberg A, Schleicher A, Kinomura S, Schormann T, Burgel U, Klingberg T, Larsson J, Zilles K, Roland PE (1996): Two different areas within the primary motor cortex of man. Nature 382:805–807.

Grefkes C, Eickhoff SB, Nowak DA, Dafotakis M, Fink GR (2008): Dynamic intra- and interhemispheric interactions during unilateral and bilateral hand movements assessed with fMRI and DCM. Neuroimage 41:1382–1394.

Goense JB, Logothetis NK (2006): Laminar specificity in monkey V1 using high-resolution SE-fMRI. Magn Reson Imaging 24:381–392.

Harel N, Lin J, Moeller S, Ugurbil K, Yacoub E (2006): Combined imaging-histological study of cortical laminar specificity of fMRI signals. Neuroimage 29:879–887.

Herbsman T, Forster L, Molnar C, Dougherty R, Christie D, Koola J, Ramsey D, Morgan PS, Bohning DE, George MS, Nahas Z (2009): Motor threshold in transcranial magnetic stimulation: The impact of white matter fiber orientation and skull-to-cortex distance. Hum Brain Mapp 30:2044–2055.

Herwig U, Kolbel K, Wunderlich AP, Thielscher A, von Tiesenhausen C, Spitzer M, Schonfeldt-Lecuona C (2002): Spatial congruence of neuronavigated transcranial magnetic stimulation and functional neuroimaging. Clin Neurophysiol 113:462–468.

Hess CW, Mills KR, Murray NM (1987): Responses in small hand muscles from magnetic stimulation of the human brain. J Physiol 388:397–419.

Jenkinson M, Bannister P, Brady M, Smith S (2002): Improved optimization for the robust and accurate linear registration and motion correction of brain images. Neuroimage 17:825–841.

Jenkinson M, Smith S (2001): A global optimisation method for robust affine registration of brain images. Med Image Anal 5:143–156.

Kennan RP, Zhong J, Gore JC (1994): Intravascular susceptibility contrast mechanisms in tissues. Magn Reson Med 31:9–21.

Kim SG, Tsekos NV, Ashe J (1997): Multi-slice perfusion-based functional MRI using the FAIR technique: Comparison of CBF and BOLD effects. NMR Biomed 10:191–196.

Kozel FA, Nahas Z, deBrux C, Molloy M, Lorberbaum JP, Bohning D, Risch SC, George MS (2000): How coil–cortex distance relates to age, motor threshold, and antidepressant response to repetitive transcranial magnetic stimulation. J Neuropsychiatry Clin Neurosci 12:376–384.

Krings T, Buchbinder BR, Butler WE, Chiappa KH, Jiang HJ, Cosgrove GR, Rosen BR (1997): Functional magnetic resonance imaging and transcranial magnetic stimulation: Complementary approaches in the evaluation of cortical motor function. Neurology 48:1406–1416.

Lee SP, Silva AC, Kim SG (2002): Comparison of diffusion-weighted high-resolution CBF and spin-echo BOLD fMRI at 9.4 T. Magn Reson Med 47:736–741.

Lewko JP, Stokić DS, Tarkka IM (1996): Dissociation of cortical areas responsible for evoking excitatory and inhibitory responses in the small hand muscles. Brain Topogr 8:397–405.

Liu TT, Brown GG (2007): Measurement of cerebral perfusion with arterial spin labeling: Part 1. Methods. J Int Neuropsychol Soc 13:517–525.

Logothetis NK (2008): What we can do and what we cannot do with fMRI? Nature 453:869–878.

Lotze M, Kaethner RJ, Erb M, Cohen LG, Grodd W, Topka H (2003): Comparison of representational maps using functional magnetic resonance imaging and transcranial magnetic stimulation. Clin Neurophysiol 114:306–312.

Luh WM, Wong EC, Bandettini PA, Hyde JS (1999): QUIPSS II with thin-slice TI1 periodic saturation: A method for improving accuracy of quantitative perfusion imaging using pulsed arterial spin labeling. Magn Reson Med 41:1246–1254.

Luh WM, Wong EC, Bandettini PA, Ward BD, Hyde JS (2000): Comparison of simultaneously measured perfusion and BOLD signal increases during brain activation with T(1)-based tissue identification. Magn Reson Med 44:137–143.

Maccabee PJ, Amassian VE, Eberle LP, Cracco RQ (1993): Magnetic coil stimulation of straight and bent amphibian and mammalian peripheral nerve in vitro: Locus of excitation. J Physiol 460:201–219.

Mills KR, Boniface SJ, Schubert M (1992): Magnetic brain stimulation with a double coil: The importance of coil orientation. Electroencephalogr Clin Neurophysiol 85:17–21.

Norris DG (2003): High field human imaging. J Magn Reson Imaging 18:519–529.

Norris DG, Zysset S, Mildner T, Wiggins CJ (2002): An investigation of the value of spin-echo-based fMRI using a Stroop color-word matching task and EPI at 3 T. Neuroimage 15:719–726.

Oja JM, Gillen J, Kauppinen RA, Kraut M, van Zijl PC (1999): Venous blood effects in spin-echo fMRI of human brain. Magn Reson Med 42:617–626.

Oldfield RC (1971): The assessment and analysis of handedness: The Edinburgh inventory. Neuropsychologia 9:97–113.

Rothwell JC, Thompson PD, Day BL, Boyd S, Marsden CD (1991): Stimulation of the human motor cortex through the scalp. Exp Physiol 76:159–200.

Salinas FS, Lancaster JL, Fox PT (2009): 3D modeling of the total electric field induced by transcranial magnetic stimulation using the boundary element method. Phys Med Biol 54:3631–3647.

Sanes JN, Donoghue JP (2000): Plasticity and primary motor cortex. Annu Rev Neurosci 23:393–415.

Schmahmann JD, Pandya DN (2006): Fiber Pathways of the Brain. Oxford: Oxford University Press, 654 p.

Silva AC (2005): Perfusion-based fMRI: Insights from animal models. J Magn Reson Imaging 22:745–750.

Silva AC, Williams DS, Koretsky AP (1997): Evidence for the exchange of arterial spin-labeled water with tissue water in rat brain from diffusion-sensitized measurements of perfusion. Magn Reson Med 38:232–237.

Smith SM (2002): Fast robust automated brain extraction. Hum Brain Mapp 17:143–155.

Sparing R, Buelte D, Meister IG, Paus T, Fink GR (2008): Transcranial magnetic stimulation and the challenge of coil placement: A comparison of conventional and stereotaxic neuronavigational strategies. Hum Brain Mapp 29:82–96.

Terao Y, Ugawa Y, Sakai K, Miyauchi S, Fukuda H, Sasaki Y, Takino R, Hanajima R, Furubayashi T, Putz B, Kanazawa I (1998): Localizing the site of magnetic brain stimulation by functional MRI. Exp Brain Res 121:145–152.

Thielscher A, Wichmann FA (2009): Determining the cortical target of transcranial magnetic stimulation. Neuroimage 47:1319–1330.

Thulborn KR, Chang SY, Shen GX, Voyvodic JT (1997): High-resolution echo-planar fMRI of human visual cortex at 3.0 Tesla. NMR Biomed 10:183–190.

Tjandra T, Brooks JC, Figueiredo P, Wise R, Matthews PM, Tracey I (2005): Quantitative assessment of the reproducibility of functional activation measured with BOLD and MR perfusion imaging: Implications for clinical trial design. Neuroimage 27:393–401.

Uludag K, Muller-Bierl B, Ugurbil K (2009): An integrative model for neuronal activity-induced signal changes for gradient and spin echo functional imaging. Neuroimage 48:150–165.

Walsh V, Cowey A (2000): Transcranial magnetic stimulation and cognitive neuroscience. Nat Rev Neurosci 1:73–79.

Wassermann EM (1998): Risk and safety of repetitive transcranial magnetic stimulation: Report and suggested guidelines from the International Workshop on the Safety of Repetitive Transcranial Magnetic Stimulation, June 5–7, 1996. Electroencephalogr Clin Neurophysiol 108:1–16.

Wassermann EM, Wang B, Zeffiro TA, Sadato N, Pascual-Leone A, Toro C, Hallett M (1996): Locating the motor cortex on the MRI with transcranial magnetic stimulation and PET. Neuroimage 3:1–9.

Wilson SA, Thickbroom GW, Mastaglia FL (1995): Comparison of the magnetically mapped corticomotor representation of a muscle at rest and during low-level voluntary contraction. Electroencephalogr Clin Neurophysiol 97:246–250.

Woolrich MW, Ripley BD, Brady M, Smith SM (2001): Temporal autocorrelation in univariate linear modeling of FMRI data. Neuroimage 14:1370–1386.

Worsley KJ, Evans AC, Marrett S, Neelin P (1992): A three-dimensional statistical analysis for CBF activation studies in human brain. J Cereb Blood Flow Metab 12:900–918.

Ye Y, Zhuo Y, Xue R, Zhou XJ (2009): BOLD fMRI using a modified HASTE sequence. Neuroimage 49:457–466.

Yousry TA, Schmid UD, Alkadhi H, Schmidt D, Peraud A, Buettner A, Winkler P (1997): Localization of the motor hand area to a knob on the precentral gyrus. A new landmark. Brain 120 (Pt 1):141–157.

Zappe AC, Pfeuffer J, Merkle H, Logothetis NK, Goense JB (2008): The effect of labeling parameters on perfusion-based fMRI in nonhuman primates. J Cereb Blood Flow Metab 28:640–652.

Abbreviations

ACA	anterior cerebral arteries
AM	amplitude modulated
ASL	arterial spin labeling
BASSI	bandwidth-modulated selective saturation and inversion
BOLD	blood oxygenated levele dependent
CASL	continuous arterial spin labeling
CBV	cerebral blood volume
CMRO$_2$	cerebral metobolic rate of oxygen
CSF	cerebrospinal fluid
CT	computerized tomography
DC-CASL	dual coil continuous arterial spin labeling
deHB	deoxyhemoglobin
EPI	echo planar imaging
EPISTAR	echoplanar imaging and signal targeting with alternating radiofrequency
FAIR	flow-sensitive alternating inversion recovery
fMRI	functional magnetic resonance imaging
FOCI	frequency offset controlled inversion
FSL	free surfer library
FOV	field of view
GE	gradient echo
GLM	general linear model
GM	gray matter
HRF	hemodynamic response funtion
HS	hyperbolic secant
LT	local tissue
LVF	lower visual field
MCA	middle cerebral arteries
MP-RAGE	magnetization prepaired rapid acquisition gradient echo
MRI	magnetic resonance imaging
MT	magnetization transfer
NMR	nuclear magnetic resonance
PASL	pulsed arterial spin labeling

PCA	posterior cerebral arteries
pCASL	pseudo-continuous arterial spin labeling
PET	positron emmision tomography
PICORE	proximal inversiob with a control for off-resonance effects
PLD	post labeling delay
QUIPSS	quantitative imaging of perfusion with a single subtraction
Q2TIPS	QUIPSS II with thin-slice TI1 periodic saturation
RF	radio frequency
ROI	region of interest
SAR	specific absorbtion ratio
SE	spin echo
SNR	signal to noise ratio
TILT	transfer insensitive labeling technique
TMS	transcranial magnetic stimulation
TOF	time of flight
UVF	upper visual field
VASO	vascular space occupancy
VS-ASL	velocity selective arterial spin labeling
WM	white matter

List of publications from the thesis

Journal Articles

1. Cavusoglu, M., Pfeuffer, J., Ugurbil, K., Uludag, K., *Comparison of pulsed arterial spin labeling encoding schemes and absolute perfusion quantification.* Magn Reson Imaging, 2009. **27**(8): p. 1039-45

2. Cavusoglu, M., Bartels, A., Yesilyurt, B., Uludag, K., *Retinotopic maps and hemodynamic delays in human visual cortex measured using arterial spin labeling.* Neuroimage, 2011 (doi: 10.1016/j.neuroimage.2011.10.056).

3. Cavusoglu, M., Pohmann, R., Burger, C., Uludag, K., *Reginoal effects of magnetization dispersion on quantitative perfusion imaging for pulsed and continuous arterial spin labeling.* Magnetic Resonance in Medicine, 2011. (submitted).

4. Varkuti, B., Cavusoglu, M., Kullik, A., Schiffler, B., Veit, R., Yilmaz, O., Rosenstiel, W., Braun, C., Uludag, K., Birbaumer, N., Sitaram, R., *Quantifying the link between anatomical connectivity, gray matter volume and regional cerebral blood flow: an integrative MRI study.* Plos One, 2011. **6**(4): p. e14801.

5. Grichisch, Y., Cavusoglu, M., Preissl, H., Uludag, K., Hallschmid, M., Birbaumer, N., Haring, H. U., Fritsche, A., Veit, R., *Differential effects of intranasal insulin and caffeine on cerebral blood flow.* Hum Brain Mapp, 2011.

6. Diekhoff, S., Uludag, K., Sparing, R., Tittgemeyer, M., Cavusoglu, M., von Cramon, D. Y., Grefkes, C., *Functional localization in the human brain: Gradient-Echo, Spin-Echo, and arterial spin-labeling fMRI compared with neuronavigated TMS.* Hum Brain Mapp, 2011. **32**(3): p. 341-57.

Selected Conference Articles

1. Cavusoglu, M., Pohmann, R., Burger, C., Uludag, K., *Reginoal effects of magnetization dispersion on quantitative perfusion imaging for pulsed and continuous arterial spin labeling,* 20th Annual Meeting of the International Society for Magnetic Resonance in Medicine 2012, Melbourne (submitted).

2. Cavusoglu M., Yesilyurt B., Bartels A., Uludag K., *Retinotopic maps and hemodynamic delays in human visual cortex measured using arterial spin labeling*, . 20th Annual Meeting of the International Society for Magnetic Resonance in Medicine 2012, Melbourne (submitted).

3. Cavusoglu M., Yesilyurt B., Bartels A., Uludag K., 'Retinotopy of the human visual cortex with perfusion contrast using arterial spin labeling', 16th Annual Meeting of the Organization for Human Brain Mapping, 2010, Barcelona.

4. Várkuti B., Cavusoglu M., Kullik A., Veit R. Yilmaz O., Rosenstiel W., Braun C., Uludag K., Birbaumer N., Sitaram R., *Quantifying the link between Anatomical Connectivity and regional Cerebral Blood Flow – a combined DTI/ASL study*, 16th Annual Meeting of the Organization for Human Brain Mapping, 2010, Barcelona.

5. Diekhoff S., Uludag K., Sparing R., Cavusoglu M., Cramon D.Y., Grefkes C., *Functional localization in the human brain: Gradient-Echo, Spin-Echo, and Arterial Spin-Labeling fMRI compared with neuronavigated transcranial magnetic stimulation,* 15th Annual Meeting of the Organization for Human Brain Mapping, 2009, San Francisco.

6. Veit R., Cavusoglu M., Grichisch Y., Preissl H., Uludag K., Hallschmid M., Birbaumer N., Haring H.U., Fritsche A., *Intranasal insulin effects on cerebral blood flow and BOLD responses*, 15th Annual Meeting of the Organization for Human Brain Mapping, 2009, San Francisco.

7. Cavusoglu M., Ugurbil K., Uludag K., *Comparison of Pulsed Arterial Spin Labeling Sequences Using Different Absolute Quantification Methods*, 16th Annual Meeting of the International Society for Magnetic Resonance in Medicine 2008, Toronto.